Modelling active electrolocation in weakly electric fishes

Thomas Boulier

THÈSE

Présentée pour obtenir le grade de
DOCTEUR DE L'ÉCOLE POLYTECHNIQUE
Spécialité : Mathématiques Appliquées
par
M. Thomas BOULIER

Modélisation de l'électro-localisation active chez les poissons faiblement électriques.

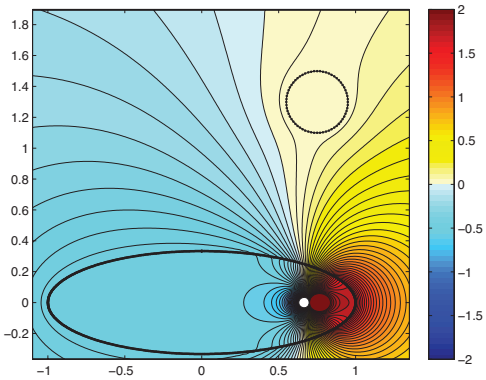

Soutenue le 21 juin 2013 devant le jury composé de:

M. Habib AMMARI	*Directeur de Thèse*
M. Josselin GARNIER	*Directeur de Thèse*
M. Oscar BRUNO	*Rapporteur*
M. Jin Keun SEO	*Rapporteur*
M. Hongkai ZHAO	*Rapporteur*
M. Grégoire ALLAIRE	*Examinateur*
M. Frédéric BOYER	*Examinateur*
M. Stéphane MALLAT	*Examinateur*
Mme Liliana BORCEA	*Invitée*

À ma famille.

Je chante les héros dont Esope est le père,
Troupe de qui l'histoire, encor que mensongère,
Contient des vérités qui servent de leçons.
Tout parle en mon ouvrage, et même les poissons:
Ce qu'ils disent s'adresse à tous tant que nous sommes;
Je me sers d'animaux pour instruire les hommes.

Jean de La Fontaine, Fables.
A Monseigneur le Dauphin, Livre I - Fable 0.

Contents

Remerciements

L'exercice des remerciements est très délicat, d'autant plus que cette page sera sûrement la plus lue de ce présent manuscrit. Plus à l'aise avec les formules qu'avec les mots, je dois cependant trouver ceux qui exprimeront le mieux toute ma gratitude envers les gens qui ont contribué au succès de cette thèse. Je m'excuse par avance pour tous ceux que j'ai oublié, et les remercie pour leur indulgence envers ma mémoire imparfaite.

Je commencerai donc par Habib Ammari, qui m'accompagne depuis bien avant la thèse. Depuis que je l'ai recontré en petites classes à l'X, il m'a aidé à trouver un stage de recherche à New York, a suivi ma scolarité en M2 pour finalement me proposer ce sujet de thèse. Alors merci Habib pour tout ce que tu as fait pour moi. Je n'oublierai jamais ta gentillesse, ta disponibilité, ton enthousiasme toujours intact. J'espère que nos chemins continueront de se croiser à l'avenir.

Josselin Garnier a également été mon directeur de thèse durant ces trois années. Je te remercie pour les séances de travail que nous avons passé ensemble, pour ta disponibilité, ou encore ta patience lorsque ce que je formulais n'était pas assez précis.

I would like to thank the reviewers of this manuscript: Oscar Bruno, Jin Keun Seo and Hongkai Zhao. Your presence in the jury is a honor, and I am proud to have the opportunity to discuss with you about this work.

Un grand merci à Grégoire Allaire, Frédéric Boyer, Stéphane Mallat, et Liliana Borcea d'avoir accepté de faire partie de mon jury de thèse. Je suis très flatté de vous présenter mes travaux de recherche.

Les collaborations auxquelles j'ai participé ont été une source de joie dans mon travail, et j'espère que ma carrière sera jalonnée d'autres rencontres de ce genre. Je pense aux personnes de l'équipe d'imagerie avec qui j'ai eu la chance de travailler (Vincent Jugnon, Abdul Wahab, Élie Bretin, Han Wang, Wenjia Jing, Loc Nguyen, Pierre Millien, Laure Giovangigli, Laurent Seppecher), mais également des travaux avec l'équipe de l'IRCCyN (Frédéric Boyer et Vincent Lebastard : merci pour l'accueil et la confiance que vous m'avez accordée pour la manipulation du robot !), ou encore l'équipe Data au DI (Stéphane Mallat, Laurent Sifre, Irène Waldspurger). In a more international context, I had the pleasure to meet wonderful people in several conferences. I would like to thank especially Hyeonbae Kang for his warmful welcome in Korea, and also Mikyoung Lim, Hyundae Lee. Thank you also to Knut Sølna and Laurent Demanet for the fruitful discussions.

Ces trois ans de thèse n'auraient pas pu se dérouler dans un meilleur contexte que celui du Département de Mathématiques et Applications de l'ENS. Je suis très heureux d'y avoir travaillé, que ce soit pour la recherche, pour l'enseignement, ou tout simplement pour les échanges amicaux avec de nombreux collègues. Je pense notamment aux occupants du bureau 15, passés et présents (outre les membres de l'équipe imagerie cités plus haut, Vincent Duchêne, Cécile Huneau, Hugues Auvray, Quentin Dufour, Yannick Bonthonneau). Que ce soit pour un projet comme le site web de la FIMFA, les exposés de troisième année, les corrections de copies, les cours à préparer, ou simplement pour une discussion autour d'un café ou d'un déjeuner, je ne

manque pas de souligner ma joie d'avoir partagé autant de moments agréables avec mes collègues. Merci donc à Daniel Han Kwan, Thibaut Allemand, Colin Guillarmou, Diogo Arsénio, Benoît Desjardins, David Lannes, Thomas Alazard, Jérémie Szeftel, Anne-Laure Dalibard, Laure Saint-Raymond, Gilles Stoltz, Bénédicte Haas, Laure Dumaz, Nicolas Curien, Thierry Bodineau, Tony Ly, Olivier Benoist. Enfin, merci à Bénédicte Auffray, Zaïna Elmir, Lara Morise, et Laurence Vincent sans qui tout ce petit monde ne pourrait pas travailler dans d'aussi bonnes conditions.

La thèse est un marathon de trois ans, et le travail n'est également possible que parce que l'on est bien soutenu durant ces années. Je profite donc de ces quelques lignes pour remercier mes proches de m'avoir épaulé, encouragé, et aidé dans les moments difficiles. Merci aux copains de l'X (Alexandre, Clément, Cyprien, Jimmy-Jonathan, Kevin, Leonardo, Nicolas, Pierre-Adrien, Stéphane, Youssef), aux plus anciens et toujours fidèles (Geoffrey, Julien, Héloïse, Noémie, Lucie, Sabine, Marion, Antoine, Mathieu). J'ai découvert un groupe de pratiquants d'arts martiaux très soudé au Dojo de la Montagne, et je les remercie de m'avoir permis de me défouler et de changer d'air entre deux simulations numériques. Merci enfin à Bastien et Natcho, qui m'ont supporté pendant deux ans du côté de la Porte de Saint-Ouen, et avec qui j'ai été très heureux de vivre.

Enfin, je voudrais terminer par un hommage à famille, sans qui je ne serai pas là où j'en suis aujourd'hui. Mes parents pour leur soutien et leur motivation sans faille, mes deux soeurs Marion et Louise pour leur bonne humeur, mes grans-parents pour leurs encouragements constants. Je voudrais finalement exprimer ma tendresse à Manon, qui me supporte, me soutient, m'accepte tel que je suis, et bien plus encore.

Résumé

Le sujet de cette thèse est la modélisation mathématique d'un sens particulier chez certaines espèces de poissons, dites faiblement électriques. Ces poissons, qui vivent principalement dans les eaux douces en Afrique et en Amérique du Sud, émettent un champ électrique de très faible intensité afin de se repérer dans l'espace. En effet, lorsqu'un objet se trouve à proximité, la déformation qu'il induit sur le champ est enregistrée à la surface de leur peau, puis analysée afin de l'identifier. En d'autres termes, ces poissons font face à la résolution d'un problème inverse ; ce type de sujet occupe la communauté de l'analyse des équations aux dérivées partielles depuis les années 80. La principale difficulté est le caractère mal-posé de ces problèmes : non-existence, non-unicité, ou instabilité.

Des études comportementales ont montré que ces poissons sont capables de distinguer la localisation, la taille, la forme ainsi que les paramètres électriques (permittivité et conductivité) des objets qui les entourent. A l'heure actuelle, les méthodes de reconstruction d'anomalies ne permettent pas d'extraire autant d'information. L'enjeu est donc de taille, tant d'un point de vue théorique (prouver l'existence, l'unicité et la stabilité du problème) que pratique, avec des applications médicales, industrielles voire environnementales.

Nous proposons ainsi un modèle mathématique permettant de calculer le champ électrique émis par un poisson, et la déformation induite par la présence d'un ou plusieurs objets. Nous avons ensuite développé des algorithmes permettant de localiser un objet, compte tenu du caractère multi-fréquentiel des mesures. Enfin, en utilisant de plus le mouvement du poisson, nous avons montré qu'il est alors possible de différencier des objets de formes différentes.

Ces algorithmes permettent ainsi de montrer la faisabilité physique de l'électro-localisation. Ils ouvrent également la voie à des applications de détection, d'identification et de classification, notamment grâce à une approche théorique permettant la généralisation à d'autres systèmes d'imagerie.

Abstract

The aim of this thesis is to build a mathematical model for a particular sense in certain species of fish, called weakly electric. These fishes, living in the rivers of Africa and South America, emit an electric field with a very low intensity. It allows them to orientate in their surrounding space. Indeed, when an object is situated in its vincinity, the induced distorsion is recorded at the surface of their skin, and then analyzed in order to be identified. In other words, these fishes are dealing with an inverse problem ; this subject has raised interest in the field of partial differential equations analysis since the 80's. The main difficulty is the ill-posedness character of these problems: non-existence, non-uniqueness, or instability.

Behavioral studies have shown that these fishes are able to distinguish the location, the size, the shape and the electrical parameters (conductivity and permittivity) of objects around them. Up to now, it is not possible to extract such information with the usual reconstruction method. The challenge is then huge, both from a theoretical point of view (prove existence, unicity and stability of the problem) and from a practical point of view, with applications in medical sciences, industrial imaging, or environmental issues.

We propose here a mathematical model that allows to compute the electric field emitted by the fish, and the difference induced by the presence of one or several objects. We have then developped algorithms of localization, using the multi-frequency aspect of the measurements. Finally, using the information contained in the movement of the fish, we have shown that it is possible to differentiate between two objects with different shapes.

These algorithms shows the physical feasibility of active electrolocation. They open the door to detection, identification, and classification applications. A theoretical approach gives easily the clue for generalization to other imaging systems.

CHAPTER 1

Introduction and overview

Several species of fish share an uncommon sense, making them able to probe their surrounding environment thanks to a self-generated electric field. Very much like bats, which use a sonar to orient themselves, these fishes are equipped with some sort of radar. Indeed, they are able to create an electric potential thanks to a special organ, which is then recorded by specific sensors located at the surface of their skin. This allows them to perceive the distorsion created by the presence of a target, which gives them access to the size, the shape, and the material of this object. This ability is called *active electrolocation* and was discovered by Hans Lissmann and Ken Machin in 1958 [77].

Since this finding, a huge amount of work has been done in order to understand this sense. However, a quantitative model is lacking to explain the physics that underly within this low-frequency imaging technique. In this perspective, it is interesting to investigate what are the equations involved, the relevant parameters, and the phenomena that could furnish a satisfying explanation.

From a mathematical point of view, this problem is promising since it gives an example of an *inverse problem* solved by the fish. Hence, the study of its behaviors could lead us to invent numerical algorithms that could avoid the ill-posedness of such problems. Biomimetism and bio-inspired technologies are then not very far from this approach.

In this chapter, we will first focus on the electric fishes (section 1.1), and then we will present the main outline of the work presented in this thesis (section 1.2).

1.1 State of the Art

This section presents, in a non-exhaustive way, what is known about electric fishes. The interested reader should refer to [37, 84], two remarkable reviews on the subject from which the following lines have taken their sources.

1.1.1 Discovery of the Electric Sense: a Brief History

The relations between man and electric fishes teach us how the study of these latters improved scientific knowledge, from the invention of the first electric battery to the finding of acetylcholin. This section

Figure 1.1: The Narmer Palette (left), and a zoom on the *serekh* (box containing the name) situated on the top (right) The fish that is represented is probably *Malapterurus electricus* [34, 60].

intends to summarize this long scientific journey, showing that - starting with electrolocation - mysteries to be uncovered still hold. It relies heavily on [52, 84]; the first reference is a must-read which is accessible for any public.

Bioelectrogenesis One of the most ancient trace of knowledge of these fishes can be found on the Narmer Palette, depicting King Narmer (Early Dynastic Period, 31st century BC) whose name is composed by the two symbols *n'r* (catfish) and *mr* (chisel), see Figure 1.1.

The electric shocks were then also used in medicine, as being analgesic; this practice seems to have endured during Ancient Greece.

The link between those shocks and thunders had been a mystery since, until the 18th century, helped by the Leyden jar. Officialy, John Walsh is rewarded for this discovery (receiving the Copley Medal of The Royal Society in 1775). However, a lot of people had recognized the electrical nature of the discharges of the electric eel, the torpedo or the electric catfish: Hunter (1773), van s'Gravesande (1754), van der Lott (1762), Bancroft (1769), Bajon (1774), Williamson (1775) and Cavendish (1776). A surprizing fact tells us that the first electric battery (built by Volta in 1800) was designed to be an electric organ; more details will be given on that point in subsection 1.1.2.

At the end of the 19th century, weakly electric fishes are discovered. In the perspective of the freshly established theory of evolution by Darwin, the question of the use of such a low signal is raised. Indeed, a few millivolts is no use for harming a prey.

At the beginning of the 20th, Fledberg and Fessard study the electric organ of the Torpedo in order to demonstrate that acetylcholine is a neurotransmitter [51].

Electroreception John Walsh and his contemporaries - Ingenhousz (1782), Schilling (1772) and Faraday (1839) - remarked that these fishes "feel" electricity. Electroreceptor organs were discovered by Lorenzini in 1678 but the link between emission and reception is not made; Du Bois-Reymond and Müller went to reject it. It is only in 1958 that Lissmann and Mahcin showed that these organs were part of a complex electroperception system, allowing these fishes not only to probe their environnement, but also to communicate between them.

1.1.2 Weakly Electric Fish

Taxonomy and living conditions

There are dozens of weakly electric species, classified in various families. These families all belong to two different orders: Gymnotiforms in South America and Mormyriforms in Africa (see Figure 1.2).

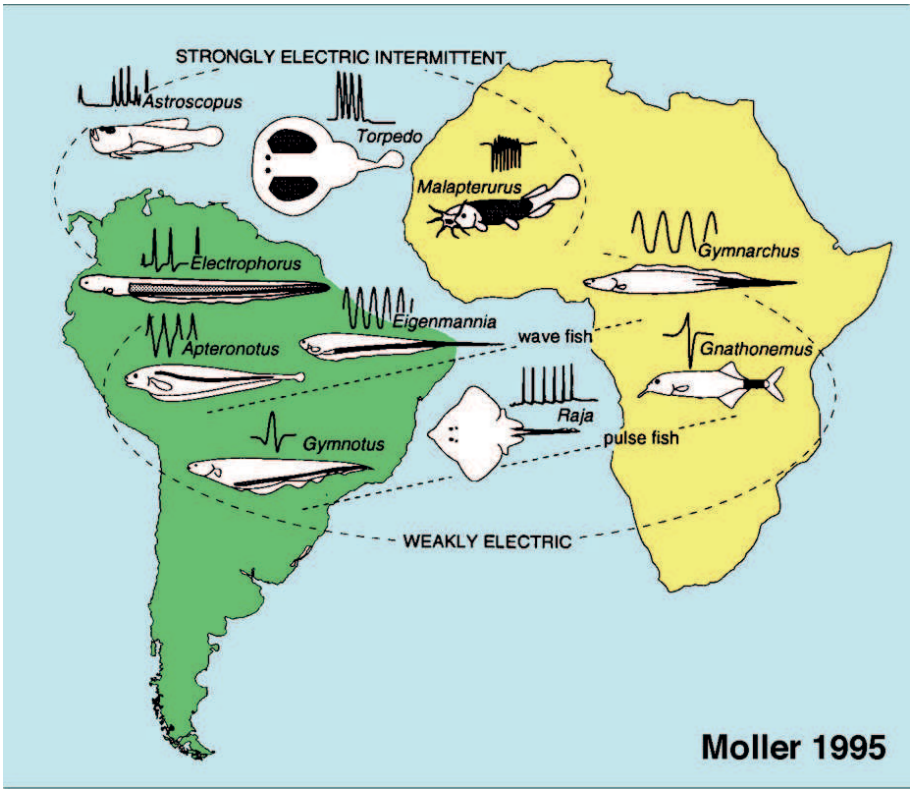

Figure 1.2: Classification and geographic distribution of the different species of weakly electric fish. The species of interest are in the lower circle and the other ones use their electric organ in an aggressive or defensive manner. Taken from [84].

These fishes hunt at night and sleep during the day. They live in muddy rivers, therefore the turbidity of the water is very high. However, as we will see in chapter 2, only conductivity will have an importance on electrolocation. This latter is considered to be homogenized because of the little size of the particles suspended in the water.

The shape and size of these fishes vary considerably from one species to another. Two types are distinguished according to the electric signal emitted: pulse-type species and wave-type species (see Figure 1.3).

Emitting and receiving the electric field

This section will explain the physical, chemical and biological mechanisms involved during *electrogenesis* and *electroreception*.

Whatever the type of specie (wave or pulse), the emission relies on the same principle and is due to a specific organ which is generally situated in the tail; the first paragraph will provide more details. The reception is operated by receptors spreading on the surface of the skin; further explanation will be given later on.

The electric organ Apart from the family Apteronotidae (in the Gymnotiforms order), the Electric Organ (denoted *EO* below) emitting the electric discharges derives from muscular tissues - it is called *myogenic*

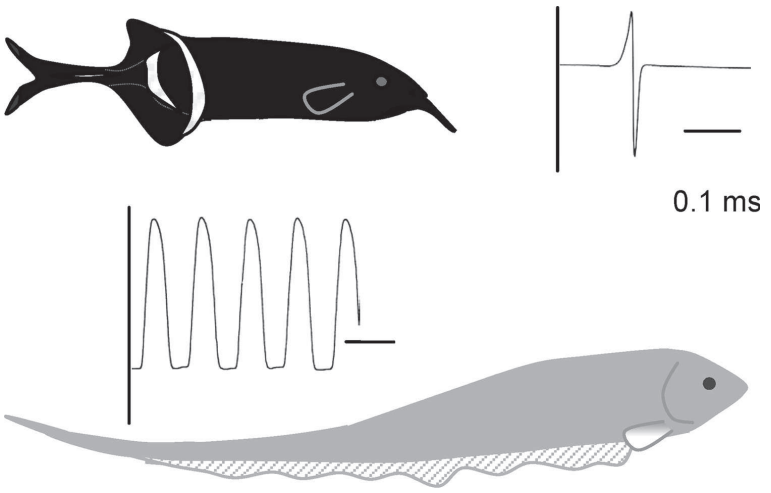

Figure 1.3: Differences between two species: one is pulse-type (top) and the other is wave-type. For each fish, its electric discharge is represented in time scale. Taken from [54].

organ - built in superimposed disks (cf Figure 1.4). These disks are in fact big cells (0.75 mm in *Brachyhypopomus pinnicaudatus* [98]) called *electrocytes*. Their number ranges from hundreds (in Mormyrids) to several millions in strongly electric species.

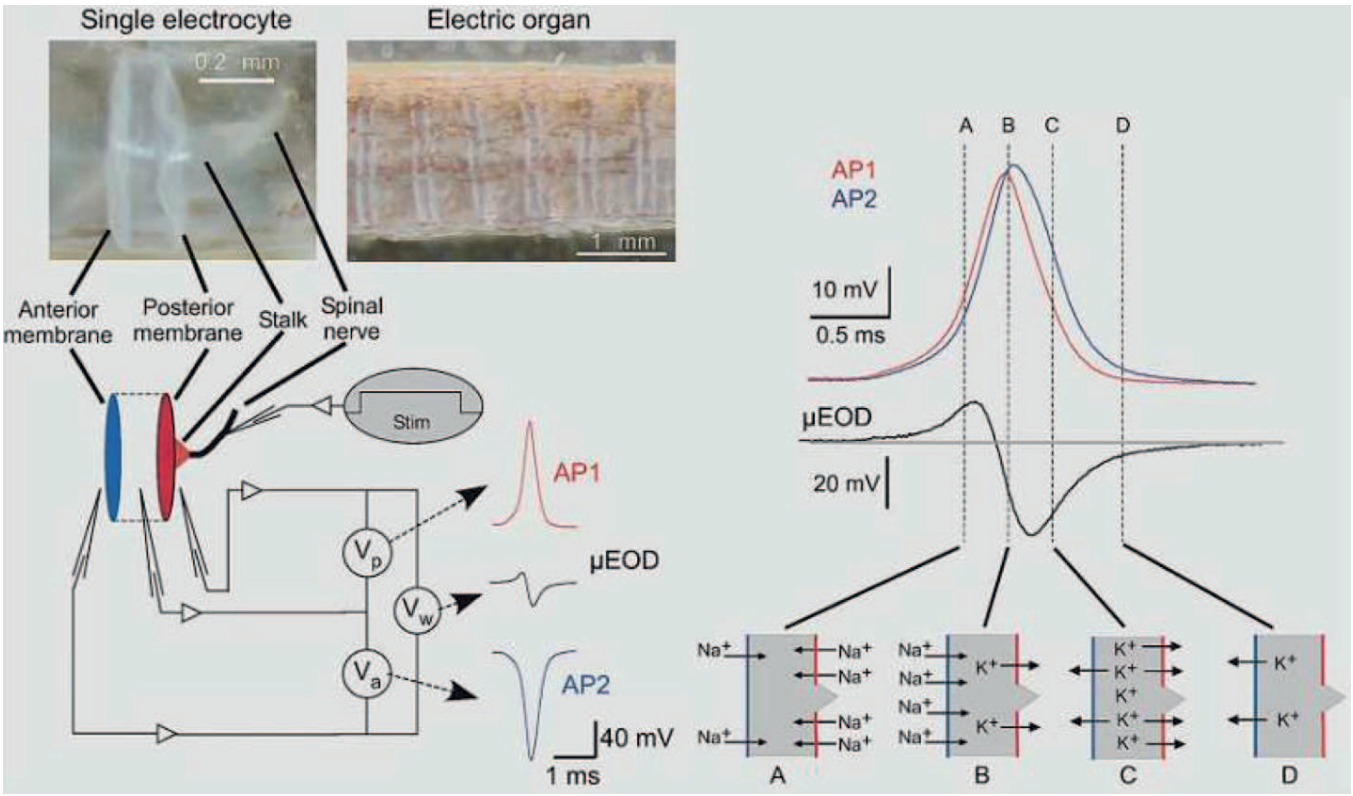

Figure 1.4: A *Brachyhypopomus pinnicaudatus* electrocyte. Taken from [98].

An *Electric Organ Discharge* (denoted *EOD* below) is as follows: first, the brain sends an impulse that goes through a pacemaker in the spinal cord. This pacemaker is connected to every electrocyte by a *spinal nerve*. Each nerve depolarizes the caudal (*i.e.* posterior) part of the cell, which causes the opening of the ionic canals situated on the membrane (they are uniquely sensible to voltage difference between the interior

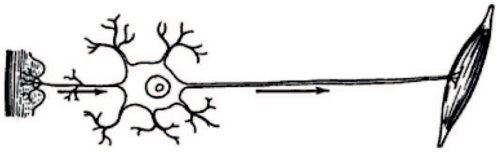

Figure 1.5: An electromotor neuron. The axon connects the body of the neuron (in the center) to the muscular tissues (on the right). Taken from [93].

and the exterior of the cell). It follows a ionic flux (see A, B, C and D in Figure 1.4) that makes the electric current. It should be noted that the great similarity with a battery is historic: indeed, Volta built its first pile in 1800 according to his observations of the eel's organ [107] and named it *Artificial Electric Organ*.

However, in Apteronotidae species the EO derives from neural tissues and therefore is said to be *neurogenic*. In this case, the organ is composed of several presynaptic axons of electromotor nerves (see Figure 1.5) that are not connected at their end. When the brain sends a signal in these neurons, the sum of all the small currents makes the discharge.

Depending on the species, this organ occupies a small part of the body (for example in Mormyrids it is located in the caudal peduncle) or an extended one (for example almost the entire trunk in Gymnarchus niloticus).

Electroreceptors There are thousands of pores - sizing around a millimeter - on its scaleless skin. In each of them can be found an electroreceptor used to measure the voltage difference between the exterior medium and the inside of the fish's body. A receptor is formed by a cavity filled by a conducting material (liquid or fibers): when a potential difference is applied a current appears in this material, which is measured by sensitive cells (see Figure 1.6). Then this information is transmitted to the brain via *afferent neurons*.

Two types of receptors are distinguished according to their shape: *ampullary* receptors and *tuberous* ones. The shape is not the only difference, since the ampullary receptors measure low frequency signals (from 1 to 10 Hz) and the others are sensitive to high frequencies (from a hundred of Hertz to 1 kHz). Moreover, the laters can be either sensitive to the amplitude of the signal (in this case they are called AM for *Amplitude-Modulating units*) or to the frequency (here they are called RT for *Rapid Timing units*).

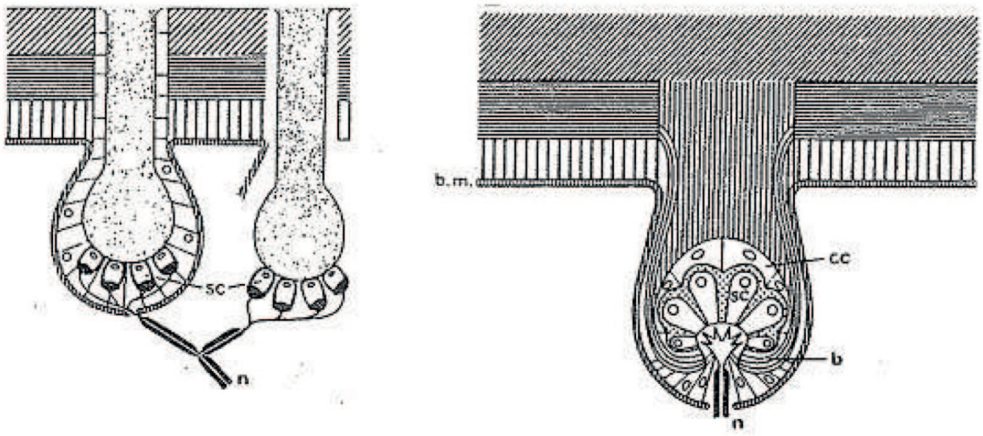

Figure 1.6: Two types of electroreceptors: an ampullary receptor on the left (this shape is common to Mormyrids and Gymnotiforms) and a tuberous one on the right (this shape of organ is from Gymnotiforms). Sensitive cells are indicated by "sc" and the afferent neurons are noted "n". Taken from [84].

However the repartition on the skin depends on the species, there are similarities in each order. Indeed, it is rather uniform in Gymnotiforms (though the density is higher near the head) and it is concentrated on the back and on the ventral part of the body in Mormyriforms (see Figure 1.7).

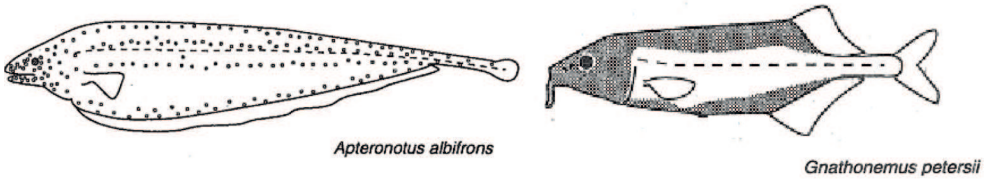

Figure 1.7: Location of the receptors according to the order: *A. albifrons* is a Gymnotiform (each dot represents an ampullary organ - the tuberous ones show the same repartition but are simply in a higher number) and *G. petersii* belongs to the Mormyrifoms order (the receptors are situated in the shaded area). Taken from [84].

1.1.3 Electrolocation

These fishes live in turbid water, mostly at night, and hunt small preys - like insects or small fishes [2, 88]. The vision is useless in these conditions and they rely mainly on their electric sense. Two behaviors are to be described in this section: *passive* electro-location and *active* electro-location.

Passive electro-location

This type of detection is not exclusive to weakly electric fish: for example sharks and rays also use it [1, 64]. From the point of view of evolution, it seems to be anterior to active electro-location [76]. It is based on the detection of the low frequencies of the electric field emitted by external sources (physical, chemical or biological [64]). Experimentally, it can be observed when the fish is in the field of an electric dipole [58]: it tends to align its body with the streamlines and to follow it until the source (see Figure 1.8). Consequently, this behavior does not involve a complex analysis of the electric field and the fish does not seem to know by advance where is the dipole. Since it is well understood, we will not study it.

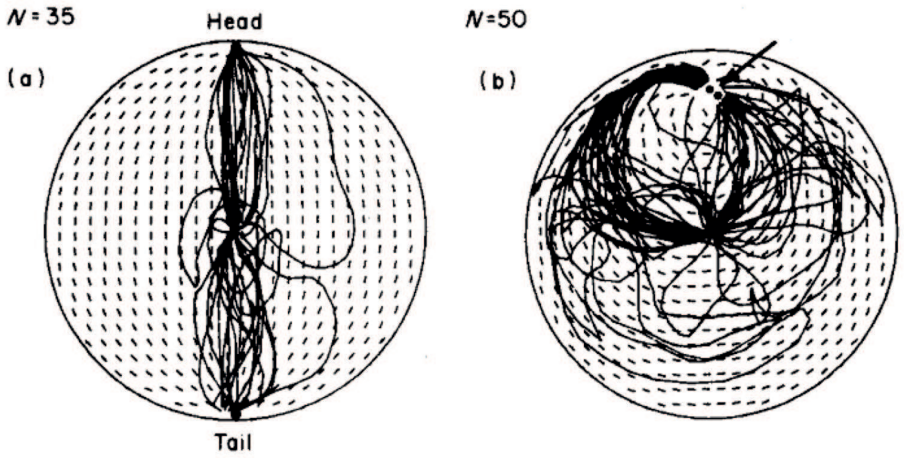

Figure 1.8: Behavior of *G. carapo* in the presence of a dipole, with two different geometries. Full lines correspond to pathway followed by the fish during an essay (N is the number of essays) and doted lines are stremlines of the electric field. Taken from [48].

Active electro-location

Active electro-location is far more complex because the fish seems to know away from the object its location and its properties. It has long been known that weakly electric fishes react strongly when a metallic rod enters the aquarium *. But it took centuries to understand why: in 1958, Hans Lissmann finally connected this fact with their emission of a weak electric field and concluded that they possess an "electric sense". This sense has a range of about one or two body length. Behavioral studies showed that these fishes are able to determine the distance (Figure 1.9A), the size, the shape (Figure 1.9B) and the material (via resistivity and capacitance) of an object [109, 108, 112].

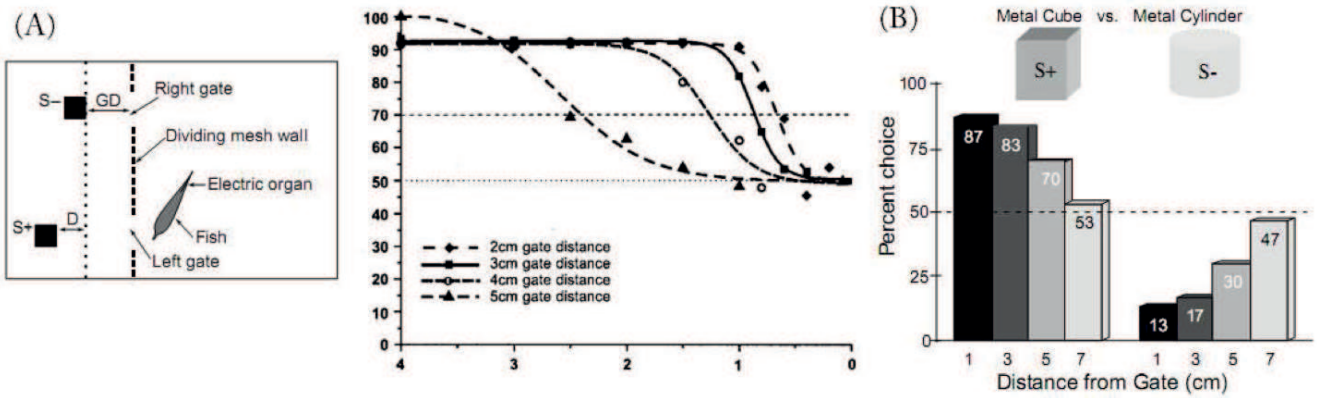

Figure 1.9: (A) Experimental evidence of distance measurement by a *Gnathonemus petersii*. On the left: experimental setup. The fish is forced to enter one of two gates where objects S^+ and S^- are placed. These objects only differ by their distance D with respect to the gate. If the first one is chosen, the fish is rewarded (by feeding) and if not, the fish is punished (by disturbing it). On the right is plotted the rate of correct choice as a function of D. The objects S^+ and S^- are metallic sphere with a volume of 33.5 cm^3. (Taken from [112]).
(B) Experimental evidence of shape discrimination by individuals of the same specie. The experimental setup is the same, except that the difference between the objects is now their shape: one is a metallic cube whereas the other is a metallic cylinder. (Taken from [110]).

The physical principle of electro-location has been known since its discovery by Lissmann in 1958 [77]: the electric field's amplitude and frequency are modified when there is an element in the surrounding with conductivity and capacitance - respectively - different from that of the water. This modification is then felt by tuberous receptors all over the skin and the fish analyzes this data. However, no one knows an algorithm that can translate this data into information on the object.

It should be noticed that when the fish probes its environment, is exhibits an intense activity [71]. Moreover, the swimming patterns are quite uncommon. For example, Gymnotiforms do not have caudal nor dorsal fin so swimming depends entirely on their anal fin; the result is that they can swim either forward or backward without difficulty. The strategy used during exploration has been called *Probing Motor Acts* by Toerring and Belbenoit [102]: see Figure 1.10.

During the exploration, pulse-type species control the EOD rate by stabilizing the frequency (see Figure 1.11). In both types, an amplitude enhancement is also observed. A special care will be made on these strategies when modelling the problem.

*In fact it has been known since the 18^{th} century, when electrogenesis was discovered [84].

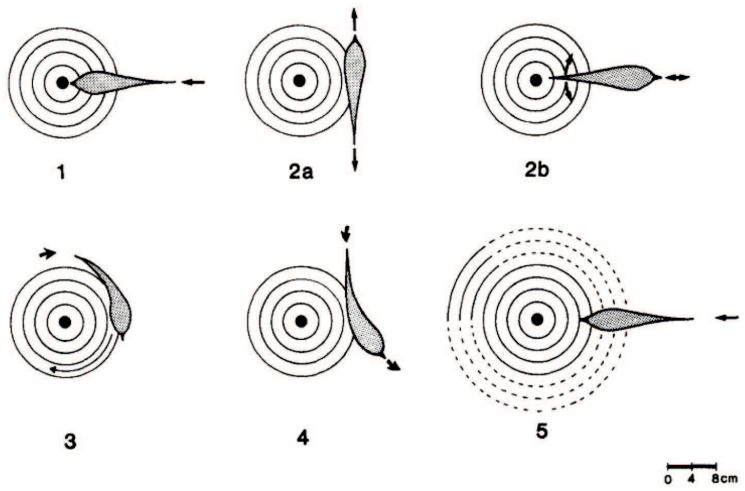

Figure 1.10: PMA: behavior exhibited by mormyrids (*Marcusenius cyprinoides* and *Gnathonemus petersii*) when introducing a metallic - or plastic - object (showed by the black dot). 1. chin probing 2a. lateral "va-et-vient" 2b. radial "va-et-vient" 3. lateral probing 4. tangential probing 5. stationary probing. Taken from [103].

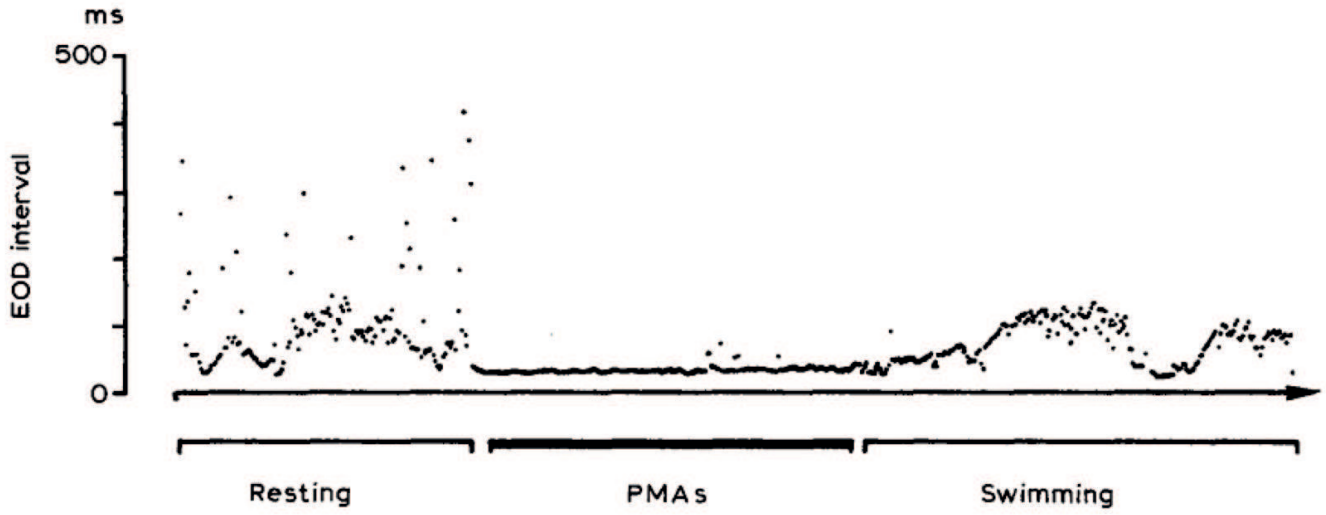

Figure 1.11: EOD rate as a function of the fish's activity. Taken from [103].

Modelling the electric field

Electro-location has been quantitatively investigated since it is known: in their article, Lissmann and Machin tried an analytical approach by calculating the distortion of a dipole's electric field caused by an infinite cylinder [77]. This section will give a brief state-of-the-art of the progress that has been made since then. First, we will focus on analytical results, and various numerical approaches of the electric field will follow.

Formulas have been established to compute the effect of a scatterer in the fish's field by several authors: Lissmann and Machin in 1958 [77], Bacher in 1983 [31] and Rasnow in 1996 [90]. All of them rely on the fact that a sphere placed in a uniform electric field "creates" another field equivalent to a dipole's one. Let us see in detail what are these formulas. In the first article, an infinite cylinder with conductivity σ is illuminated in a medium of conductivity σ_0 by a dipole M. In the plane, the equivalent dipole M' of the cylinder is given by the following expression (with the notation of Figure 1.12):

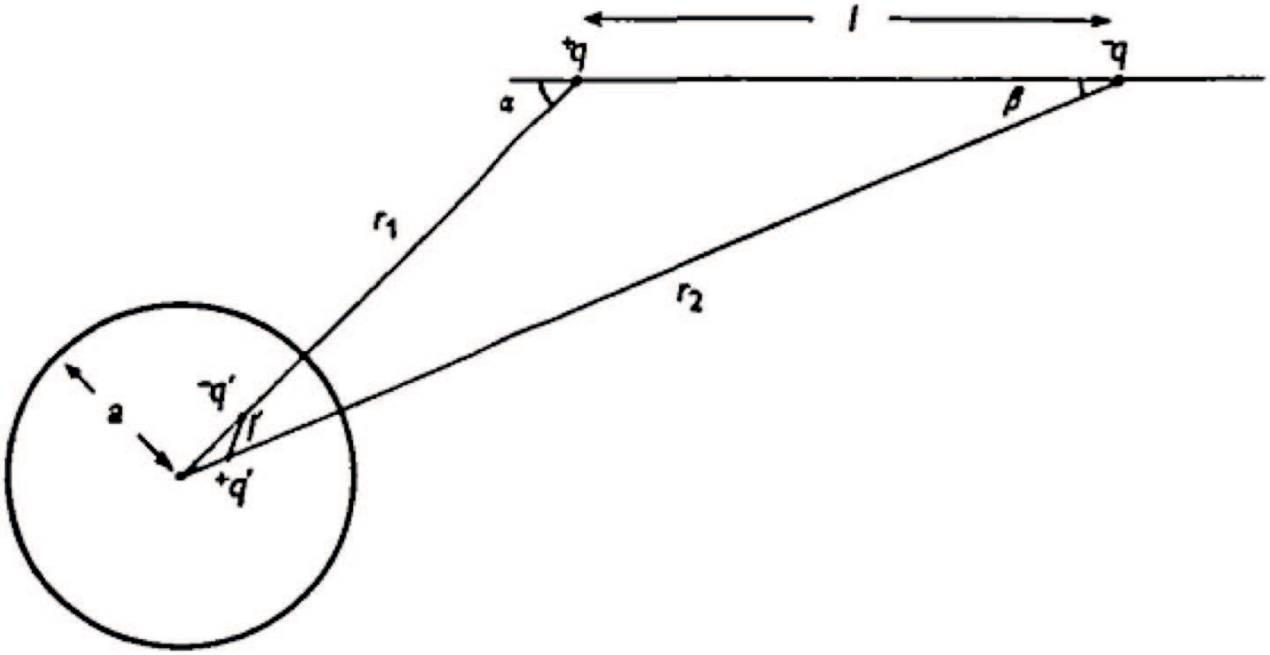

Figure 1.12: Model used by Lissmann and Machin. An infinite cylinder of radius a is in the neighborhood of a dipole formed by two sources $+q$ and $-q$ which are separated by a distance l. Taken from [77].

$$\frac{M'}{M} = a^2 \left(\frac{\sigma_0 - \sigma}{\sigma_0 + \sigma}\right) \frac{1}{r_1 r_2} \tag{1.1}$$

In 1983, Bacher remarks that this formula cannot explain the phase difference observed when the electric permittivity of the target does not equal the water's permittivity [31]. This phase difference is important since it is measured by RT units receptors (see section 1.1.2). He proposes then to take this into account in the equations by considering a non-stationary electric field, but does not give a formula similar to (1.1). Rasnow resolves this problem in 1996 by considering a harmonic regime for the background electric field: in the presence of a sphere of radius a, conductivity σ_1 and permittivity ε_1, a uniform harmonic electric field E_0 with frequency ω is modified in this way:

$$\delta u(\boldsymbol{r}) = \boldsymbol{E_0} \cdot \boldsymbol{r} \left(\frac{a}{r}\right)^3 \frac{(\sigma_1 + i\omega\varepsilon_1) - (\sigma_0 + i\omega\varepsilon_0)}{2\,(\sigma_1 + i\omega\varepsilon_1) + (\sigma_0 + i\omega\varepsilon_0)}, \tag{1.2}$$

where the indices 0 refers to the ambient medium. As we will see in chapter 2, it corresponds to the first order approximation of the potential u that verifies the equation $-\nabla \cdot (\sigma + i\omega\varepsilon)\nabla u = 0$ where σ (resp. ε) is equal to σ_1 (resp. ε_1) in the sphere and σ_0 (resp. ε_0) in the exterior. Let us remark that the factor in formula (1.2) is opposed to the one in (1.1) because the vector $\boldsymbol{r}$ does not point at the same direction, and the factor 2 in the denominator is due to the fact that we are now in the whole space and not only in the plane (see section 2.4.1, Proposition 2.4.1). Even if the model has been improved, it is only correct in an ideal case: the target is a sphere and the field is supposed to be uniform. It is not reasonable because for example the latter assumption is not true around the tail [29, 28]. The next section will show how the tools developed recently in mathematical imaging can handle it.

Numerical approaches have also been made since the 70's: in 1975, Heiligenberg proposes a finite differences scheme to calculate the field created by the fish [57]. In 1980, Hoshimiya *et al.* use finite elements to solve this problem [59]. The geometry of the fish is simplified by an ellipse and is divided

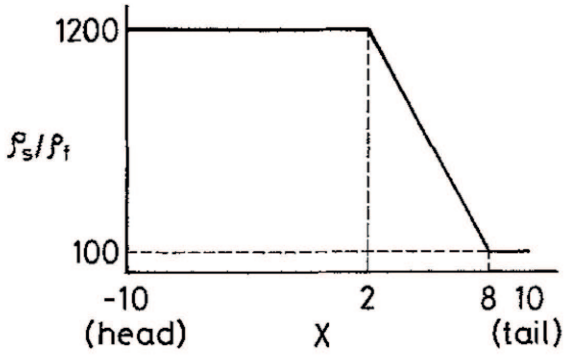

Figure 1.13: Optimal repartition of the ratio between skin resistivity ρ_s and body conductivity ρ_f along the head-tail axis. Taken from [59].

into two areas: the thin skin with low conductivity and the inside of the body. Their aim is to optimize conductivity values to approximate as well as possible the experimentally measured field. The result is that the optimal conductivity is non-uniform, being higher in the tail region (see Figure 1.13).

A lot of improvement has been made since this study (see for example [30, 78, 82, 92]). It is now well-accepted that the skin conductivity is not uniform (higher in the head) but remains low with regards to the water conductivity, and that the body conductivity is high. According to Migliaro *et al.* [82], the first fact increases the sensitivity of the skin by enhancing the voltage difference and the second extends and makes uniform the potential near the skin (which is indeed experimentally measured [87]). The relative error between measures and simulations is around 10%.

Another promising technique is the use of the boundary elements method performed by Assad in 1997 [27]. Indeed the important feature is the electric potential on the skin (because it is the *input* for the fish), so a BEM approach allows us to concentrate the equations on it. Moreover, the speed of calculation is enhanced because the number of nodes is dramatically reduced. The equation considered is here $\Delta u = 0$ on the exterior of the body with Robin boundary conditions on the skin [115]:

$$u - \xi \frac{\partial u}{\partial n} = \psi, \tag{1.3}$$

where ψ is the potential inside the body and $\xi = h\,(\sigma_0/\sigma_s)$ (h being the skin thickness, σ_s the skin conductivity and σ_0 the water conductivity) is the *effective skin thickness*. In the next section we will show the validity of this model, which allows us to easily simulate the PMA(see Figure 1.14).

Let us notice that there are other kinds of simulations, based on a more empirical approach, determining an equivalent electric circuit [36, 39] or an equivalent multipole [42].

To conclude this section, we have seen that weakly electric fish are able to collect data issued from their self-generated electric field, and to analyze them in order to determine features of scatterers around them. So far, numerical studies have been made to compute this electric field but with a lot of differences in their approaches. Our goal here is to analyze quantitatively the equations in order to have a precise forward problem.

1.2 Overview of the Thesis

1.2.1 Interests and Potential Applications

Even if neuroethology of weakly electric fish is well developped [37], knowing the neural mechanisms of active electrolocation is far beyond the scope of mathematical modeling. Instead, we should restrict

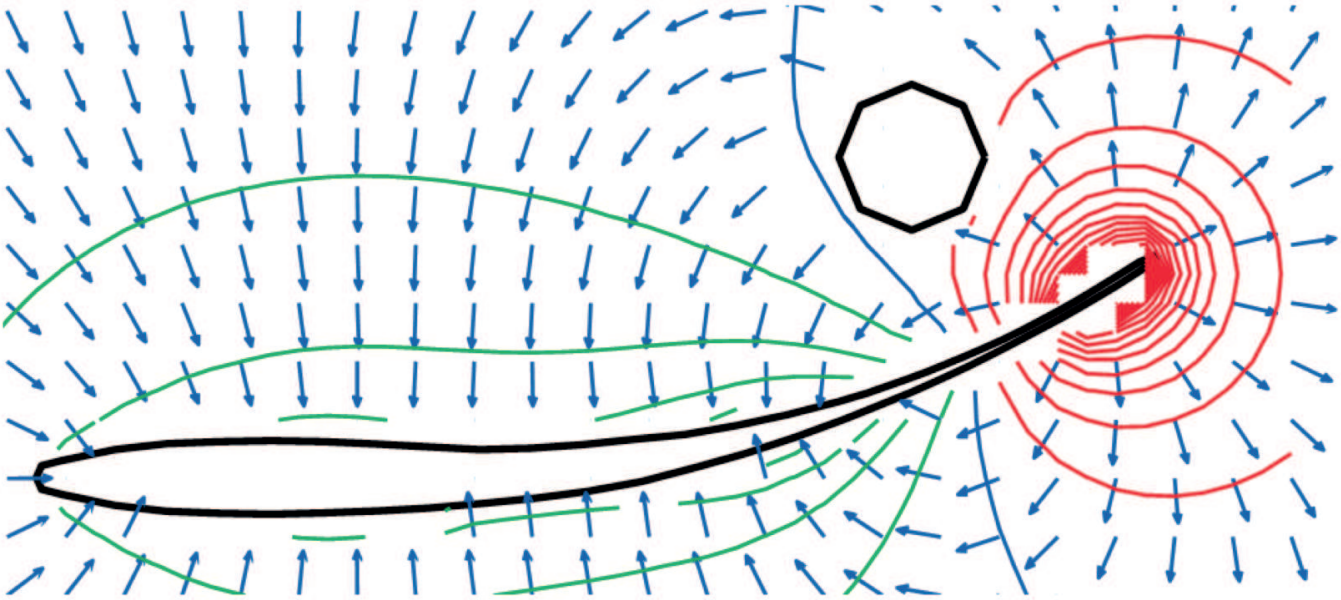

Figure 1.14: BEM simulation of the field with an object, the fish's body being curved. Isopotentials are depicted by lines (1 mV between each one) and the normalized arrows indicate streamlines. Taken from [29].

ourselves to a more accessible question. For example, knowing what could be the physical mechanisms is of major importance for several reasons.

The first one is of course biological. Indeed, it is a sixth sense unknown by a majority of species; its study unravel marvelous mysteries of Nature.

Bio-inspired engineering is the major motivation for such investigation. As a matter of fact, autonomous water navigation is the closest application of study [62]. Indeed, it would have numerous applications, for example for naval mines or UXO (UneXplored Ordnances) detection, oceans and lakes monitoring, etc. But it would have also other applications, going from medical to geophysical imaging. In fact, as it will be shown in chapter 2, we are in the context of Electrical Impedance Tomography. Since it is knwon for poor resolution, the performance of our fishes (see section 1.1.3) are quite impressive. Imitating their strategies would surely made improvements for this field.

And, last but not least, mathematical sciences would benefit for such knowledge, since it is an inverse problem. Indeed, given the current distribution over the skin, the problem is to recover the conductivity distribution in the surrounding space. Due to the ill-posedness character of this type of problems, it is intriguing to see how much information is the fish able to recover. Thus, modelling this "electric sense" (called active electrolocation) is likely to give us insights in this regard.

Hence, this will be the central question of the thesis: how can we explain physically the process of active electrolocation ? How it is possible to locate and differentiate different objects situated near the fish ?

1.2.2 Organization of the Thesis

We propose to answer these questions by means of numerical analysis of the equations involved in the description of the self-generated electric field.

In chapter 2, we derive these equations and reduce them to a simplified model, taking advantage of the highly resistive skin and highly conductive body. A dipolar expansion of the transdermal potential is also computed when a small target is present.

In chapter 3, an algorithm of localization is designed. It uses the fact that the fish emits several frequencies; thus, we can locate a target even if the fish is static.

In chapters 4-6, we develop new tools for extracting the relevant geometrical and physical features of the target. Since it was not performed before, they are described in a more general framework. In chapter 4 the problem of extraction is derived and analyzed. In chapter 5, it is used for shape identification from a pre-computed dictionary. Finally, in chapter 6, it is used for tracking a mobile target.

In chapter 7, we gather all these tools in order to explain how discriminating objects of different shapes could be possible. The key points are the multi-frequency aspect of the electric field, and the movement of the fish, thus giving sense to the PMA described in subsection 1.1.3.

The chronological order of research has been kept on purpose, taking the risk of having to repeat the notation of chapters 2-3 when returning to the physical model in chapter 7. Indeed, since the first two chapters represent modeling and localization, whereas chapters 4-7 deal with shape recognition, this order appears to be more natural.

CHAPTER 2

Mathematical Model

The results of this chapter are published in [4].

Abstract

In this chapter, we provide a mathematical model for the electrolocation problem. We first investigate the forward admittivity equation and derive the approximate boundary conditions on the skin of the fish. Then we provide a dipole approximation for small targets away from the fish. Finally, numerical simulations are performed in order to illustrate these results.

2.1 Introduction

Mathematically speaking, the electrolocation process is an inverse problem for the electric field created by the fish. Indeed, given the current distribution over the skin, the problem is to recover the conductivity distribution in the surrounding space. Hence, in order to lead a quantitative investigation of this process, we have to model the electric field precisely. The aim of this chapter is to do so for the particular case of the electrolocation of an object around the fish.

Two problems arise: the direct problem, *i.e.*, the equations involved and their boundary conditions. Here, we will make precise the model of Assad [27, 116]. As already mentioned in section 1.1.3, if u denotes the scalar potential field, it involves the equation $\Delta u = 0$ on the exterior of the body, and Robin boundary conditions on the skin :

$$u - \xi \frac{\partial u}{\partial \nu} = \psi, \tag{2.1}$$

where ψ is the potential inside the body and $\xi = h(\sigma_0/\sigma_s)$ (h being the skin thickness and σ_s (resp. σ_0) the skin (resp. water) conductivity) is the *effective skin thickness*.

The second problem is to image a target. In this perspective, we generalize formula (1.2) to the case of a non-uniform background electric field, taking into account the distortion induced by the body of the fish, and with any shape of the target. This approximation will be then very useful in chapter 3 and, in some way, re-interpreted in chapters 4 and 7.

This chapter is organized as follows. In section 2.2, the physical model is set up and the equations governing the electric field are introduced and their basic properties analyzed. Using layer potential techniques, the boundary condition (2.1) is rigorously recovered in section 2.3. In subsection 2.4, asymptotic expansions will be carried out for the electric field in the presence of a small and distant target. Finally, numerical simulations of the electric field - with or without a target - are performed in section 2.5. Due to the presence of a hyper-singular operator, a particular attention is paid to the numerical scheme for solving the direct problem.

2.2 Physical modeling

The aim of this section is to formulate the *forward problem*. The electromagnetic formulation is introduced in subsection 2.2.1. The model equations are non-dimensionalized in subsection 2.2.2 and the different scales identified. Subsection 2.2.3 is devoted to the problem setup. Existence, uniqueness and a useful representation formula for the solution of the model equations are proved in subsection 2.2.4.

2.2.1 Electromagnetic formulation

In this subsection, we derive the equations governing the electric field. A formal explanation of the electroquasistatic (or EQS) formulation is given.

The electroquasistatic (or EQS) formulation is a low-frequency limit for the Maxwell system in three dimensions [104]. In the frequency domain, the latter is given by

$$\begin{cases} \nabla \cdot \varepsilon E = \rho, \\ \nabla \cdot B = 0, \\ \nabla \times E = -i\omega B, \\ \nabla \times \dfrac{B}{\mu} = j + i\omega\varepsilon E, \end{cases} \tag{2.2}$$

where E is the electric field, B is the magnetic induction field, ρ and j are the free charges and currents, ω is the frequency, μ is the magnetic permeability, and ε is the electric permittivity. Moreover, in a medium of conductivity σ, Ohm's law connects the electric field to the induced current density ($j_i = \sigma E$) so the total current density can be decomposed as:

$$j = \sigma E + j_s,$$

where j_s is a source of current (in our model, it comes from the electric organ). Then, taking the divergence of the last line in (2.2), we have:

$$\nabla \cdot (\sigma + i\varepsilon\omega)E = -\nabla \cdot j_s. \tag{2.3}$$

The EQS approximation consists of considering the electric field as irrotational because the magnetic field variation is negligible. A sufficient condition for that is given by [104]:

$$\frac{L_{\max}}{\lambda_{\min}} \ll 1, \tag{2.4}$$

where $L_{\max}$ is the maximal length of the problem and $\lambda_{\min}$ the minimal wavelength. Here, we can take $L_{\max} = 1\text{m}$ because the range of electrolocation does not exceed two body lengths [84]. In the water, the minimal wavelength is given by

$$\lambda_{\min} = \frac{1}{\omega_{\max}\sqrt{\mu\varepsilon}},$$

where $\mu \approx \mu_0$, $\varepsilon \approx 80\varepsilon_0$ and $\omega_{\max}$ is the maximal frequency emitted by the fish, which is of the order of 10kHz. Thus, the fraction in (2.4) is of order 10^{-4}, so the EQS approximation is very well suited for our situation.

Going back to the equation of the electric field (2.3), we can now use the fact that E is irrotational to state that it is derived from a scalar potential field u. This finally leads us to the following equation:

$$\nabla \cdot (\sigma + i\varepsilon\omega)\nabla u = -\nabla \cdot j_s. \tag{2.5}$$

To conclude, taking into account the slow variation of the electric field leads us to consider an admittivity equation (the *admittivity* being $\sigma + i\omega\varepsilon$) instead of a conductivity equation (*i.e.* with σ only). However, for the rest of this section, the imaginary part of this admittivity will be neglected; indeed measurements on a *Gnathonemus petersii* showed that the capacitance (*i.e.* $\omega\varepsilon^*$) of the skin, the body, and the water are very small compared to their respective conductivity [39, 94]. Thus, this EQS approximation will be used only in the presence of a target: it will be detected by the phase shift induced by its capacitance.

2.2.2 Non-dimensionalization

In this subsection, the setup of the problem is non-dimensionalized. The first step consists in identifying the different scales of the model problem. The electric potential u, the variables x and ω, and the parameters σ and j_s can be written as follows:

$$u = V_0 u',\ x = Lx',\ \omega = \omega_0\omega',\ \sigma = \sigma_0 k,\ j_s = \frac{I_0}{L^2} j_s',$$

where V_0 is the voltage produced by an *electric organ discharge* (EOD), L is the length of the fish, ω_0 is the fundamental frequency of the EOD, σ_0 is the conductivity of the surrounding water and I_0 is the current intensity inside the electric organ. Moreover, anticipating the next subsection, the conductivity of the body and the skin play an important role in the shape of the electric field. Thus, in the list of parameters we add the conductivity of the body σ_b, the thickness of the skin δ_s and its surface conductivity Σ. The orders of magnitude of these parameters are found in Table 2.1.

Quantity	Order of magnitude	Reference
V_0	10 mV	[29, 99]
L	10 cm	[84]
ω_0	1 kHz	[84]
σ_0	100 μS·cm^{-1}	[79]
I_0	1 mA	[32]
σ_b	1 S·m^{-1}	[94]
Σ	100 μS·cm^{-2}	[39]
δ_s	100 μm	[117]

Table 2.1: Orders of magnitude of the physical quantities involved. These are only scales and not the exact values measured in the cited references. Here S is Siemens ($1S = 1A/1V$).

These $n = 8$ quantities involve $r = 4$ fundamental units of the SI system, so according to the Buckingham-Pi theorem, we need $n - r = 4$ nondimensional quantities to describe the model problem. The first one can be found by rewriting the equation (2.5) in terms of the nondimensional quantities (x', k, u', j_s'):

$$\nabla_{x'} \cdot k\nabla_{x'} u' = -\frac{I_0}{\sigma_0 V_0 L}\nabla \cdot j_s'. \tag{2.6}$$

*It is also called *susceptance* when it does not come from capacitive effects only, as it is the case here.

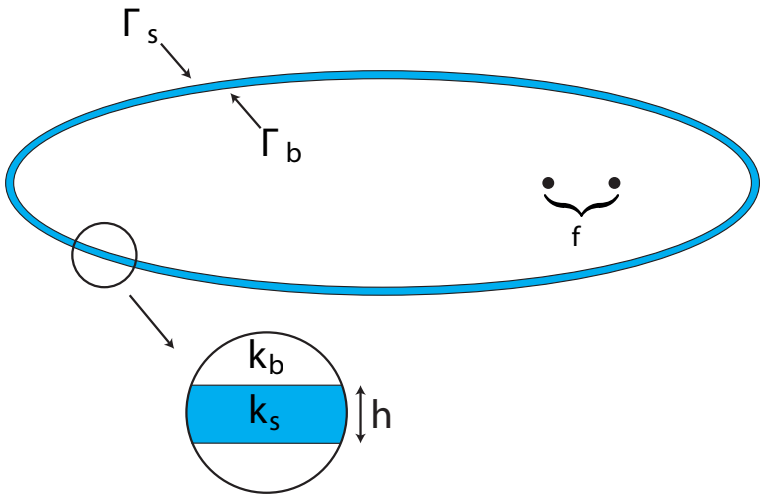

Figure 2.1: Setup of the problem. The conductivities are non-dimensionalized so that $\sigma_0 = 1$. The body Ω_b, with boundary Γ_b and conductivity k_b, is the interior of the ellipse. The skin Ω_s, with exterior boundary Γ_s and conductivity k_s, is represented in blue. The sources J_s are given by the two dots.

The multiplicative term in the right-hand side of the previous equation is not important as the equation is linear. The three other nondimensional quantities come from the parameters of the skin and the body of the fish:

$$k_b := \frac{\sigma_b}{\sigma_0} \sim 10^2,\ k_s := \frac{h\Sigma}{\sigma_0} \sim 10^{-2},\ h := \frac{\delta_s}{L} \sim 10^{-3}.$$

In other words, in nondimensional units, k_b (resp. k_s) is the body (resp. skin) conductivity and h is the skin thickness.

To conclude, omitting the prime symbol for the sake of clarity and denoting by $k_b J_s$ the source term in equation (2.6), the governing PDE is the following

$$\nabla \cdot k \nabla u = k_b J_s, \tag{2.7}$$

where k is piecewise constant, being equal to 1 in the water, k_b inside the body of the fish and k_s in the skin. These domains will be specified in the next subsection.

For the sake of simplicity, from now on, we only consider the model equations in two dimensions.

2.2.3 Problem setup

The setup is as follows: the body occupies a fixed smooth open set Ω_b and the skin with constant thickness is denoted by Ω_s. The source of the electric field is a sum of Dirac functions:

$$J_s = \sum_{j=1}^{m} \alpha_j \delta_{x_s^{(j)}}, \tag{2.8}$$

where, for $1 \leq j \leq m$, $x_s^{(j)} \in \Omega_b$ and J_s satisfies the charge neutrality condition

$$\sum_{j=1}^{m} \alpha_j = 0. \tag{2.9}$$

Although condition (2.9) is the physical condition in our model, we will show how to modify the derivations and the results of the paper in the general case. An illustration is given in Figure 7.3.

Our main purpose is to investigate the behavior of the solution of (2.7) with

$$k(x) = \begin{cases} k_s & \text{if } x \in \Omega_s, \\ k_b & \text{if } x \in \Omega_b, \\ 1 & \text{otherwise,} \end{cases} \tag{2.10}$$

where $k_s \neq 1$ and $k_b \neq k_s$. Let ξ be the effective thickness given by [116]:

$$\xi := \frac{h}{k_s}. \tag{2.11}$$

In order to make the dependence of the solution on h and k_b clear (ξ being fixed), let us denote such a solution by u_{h,k_b}. Adding a far field condition (essential for uniqueness, see subsection 2.2.4), it is the solution of

$$\begin{cases} \nabla \cdot k \nabla u_{h,k_b} = k_b J_s, & x \in \mathbb{R}^2, \\ |u_{h,k_b}| = O(|x|^{-1}), \ |x| \to \infty \text{ uniformly in } \hat{x}, \end{cases} \tag{2.12}$$

where $\hat{x} := x/|x|$ and $k(x)$ is given by (2.10).

In the next subsection, we analyze equation (2.12) and show that there exists a unique solution that can be represented as the sum of a harmonic function and two single-layer potentials.

2.2.4 Existence, uniqueness, and representation of the electric potential

We first prove the uniqueness of the solutions of (2.12) and then we derive a representation formula, which will give us the existence of the solution. For the moment, h and k_b are fixed, but we suppose that:

$$k_s < 1 < k_b. \tag{2.13}$$

Uniqueness

The uniqueness comes from the second line of (2.12) [20]. Indeed, let $v = u_1 - u_2$, where u_1 and u_2 are two solutions of (2.12) and let us show that $v = 0$. From (2.13) we get, for R sufficiently large (so that the ball with center 0 and radius R encompasses Ω_s):

$$\int_{|x|<R} |\nabla v|^2 \leq \frac{1}{k_s} \int_{|x|<R} k(x) |\nabla v|^2 = \frac{1}{k_s} \int_{|x|=R} v \frac{\partial v}{\partial \nu} = -\frac{1}{k_s} \int_{|x|>R} |\nabla v|^2 \leq 0.$$

Here we have used the fact that $\nabla v \in L^2(\mathbb{R}^2 \setminus \overline{\Omega}_s)$, which holds as a consequence of the far field condition. A unique continuation argument shows that $|\nabla v|^2 = 0$ in $\mathbb{R}^2$ and thus v is constant. Then, using the fact that $v \to 0$ as $|x| \to \infty$, we have $v = 0$.

Existence and representation

The existence is given by a representation formula decomposing the solution into a source part and a refraction part. This refraction part implies layer potentials on the boundaries of the body and the skin. Let us define them explicitly and give some well-known results. First, let us introduce the following boundaries:

$$\Gamma_b := \partial\Omega_b \text{ and } \Gamma_s := \partial\Omega_s \setminus \Gamma_b,$$

and assume that they are of class $\mathcal{C}^{1,\eta}$ for some $\eta > 0$. In the following, the index β stands for the subscript b or s. The single- and double-layer potentials on Γ_β are operators that map any $\varphi \in L^2(\Gamma_\beta)$ to $\mathcal{S}_\beta \varphi$ and

$\mathcal{D}_\beta\varphi$, respectively, where

$$\begin{aligned} \mathcal{S}_\beta &:= \mathcal{S}_{\Gamma_\beta} \text{ with } (\mathcal{S}_\Gamma\varphi)(x) := \int_\Gamma G(x-s)\varphi(s)ds, \\ \mathcal{D}_\beta &:= \mathcal{D}_{\Gamma_\beta} \text{ with } (\mathcal{D}_\Gamma\varphi)(x) := \int_\Gamma \frac{\partial G}{\partial \nu_s}(x-s)\varphi(s)ds, \end{aligned} \tag{2.14}$$

where G is the fundamental solution of the Laplacian in $\mathbb{R}^2$:

$$G(x) := \frac{1}{2\pi}\ln|x|, \quad x \neq 0. \tag{2.15}$$

For $\varphi \in L^2(\Gamma_\beta)$, the functions $\mathcal{S}_\beta\varphi$ and $\mathcal{D}_\beta\varphi$ are harmonic functions in $\mathbb{R}^2 \setminus \Gamma_\beta$; their singularities hold on Γ_β. To describe these singularities, we define, for a function w defined in $\mathbb{R}^2 \setminus \Gamma_\beta$ and $x \in \Gamma_\beta$:

$$\begin{aligned} w(x)|_\pm &:= \lim_{t\to 0} w(x \pm t\nu(x)), \\ \left.\frac{\partial w}{\partial \nu}(x)\right|_\pm &:= \lim_{t\to 0} \nabla w(x \pm t\nu(x)) \cdot \nu(x). \end{aligned}$$

Across the boundary Γ_β, the following trace relations hold [20]:

$$\begin{aligned} \mathcal{S}_\beta\varphi|_+ &= \mathcal{S}_\beta\varphi|_-, \\ \left.\frac{\partial \mathcal{S}_\beta\varphi}{\partial \nu}\right|_\pm &= \left(\pm\frac{1}{2}I + \mathcal{K}_\beta^*\right)\varphi, \\ \mathcal{D}_\beta\varphi|_\pm &= \left(\mp\frac{1}{2}I + \mathcal{K}_\beta\right)\varphi, \\ \left.\frac{\partial \mathcal{D}_\beta\varphi}{\partial \nu}\right|_+ &= \left.\frac{\partial \mathcal{D}_\beta\varphi}{\partial \nu}\right|_-. \end{aligned} \tag{2.16}$$

Here, for a $\mathcal{C}^{1,\eta}$-boundary Γ_β, the operator $\mathcal{K}_\beta$ and its L^2-adjoint $\mathcal{K}_\beta^*$ are given by

$$\begin{aligned} \mathcal{K}_\beta &:= \mathcal{K}_{\Gamma_\beta} \text{ with } (\mathcal{K}_{\Gamma_\beta}\varphi)(x) := \frac{1}{2\pi}\int_{\Gamma_\beta} \frac{\langle (s-x), \nu(s)\rangle}{|x-s|^2}\varphi(s)ds \quad , \ x \in \Gamma_\beta, \\ \mathcal{K}_\beta^* &:= \mathcal{K}_{\Gamma_\beta}^* \text{ with } (\mathcal{K}_{\Gamma_\beta}^*\varphi)(x) := \frac{1}{2\pi}\int_{\Gamma_\beta} \frac{\langle (s-x), \nu(x)\rangle}{|x-s|^2}\varphi(s)ds \quad , \ x \in \Gamma_\beta, \end{aligned} \tag{2.17}$$

where $\langle , \rangle$ denotes the scalar product in $\mathbb{R}^2$. From (2.16) it follows that the following jump formulas hold:

$$\left.\frac{\partial \mathcal{S}_\beta\varphi}{\partial \nu}\right|_+ - \left.\frac{\partial \mathcal{S}_\beta\varphi}{\partial \nu}\right|_- = \varphi \quad \text{and} \quad \mathcal{D}_\beta\varphi|_+ - \mathcal{D}_\beta\varphi|_- = -\varphi.$$

The following invertibility result is useful [50, 68, 105].

Theorem 2.2.1. *Suppose that Γ_β is $\mathcal{C}^{1,\eta}$ for some $\eta > 0$. Then the operator $\lambda I - \mathcal{K}_\beta^*$ is invertible on $L_0^2(\Gamma_\beta) := \{\varphi \in L^2(\Gamma_\beta) : \int_{\Gamma_\beta}\varphi = 0\}$ if $|\lambda| \geq 1/2$, and for $\lambda \in (-\infty, -1/2] \cup (1/2, +\infty)$, $\lambda I - \mathcal{K}_\beta^*$ is invertible on $L^2(\Gamma_\beta)$.*

Let us remark here that, when $\partial\Omega$ is connected, it is admitted to use the simplified notations $\mathcal{S}_\Omega$, $\mathcal{D}_\Omega$ and $\mathcal{K}_\Omega$ [23].

With these essentials tools, we can now prove the following decomposition formula in the same spirit as in [66]:

Lemma 2.2.2. *The solution of problem (2.12), with J_s given by (2.8), can be written as*

$$u(x) = p_s(x) + (\mathcal{S}_s\tilde{\varphi}_s)(x) + (\mathcal{S}_b\varphi_b)(x), \tag{2.18}$$

where

$$p_s(x) = \sum_{j=1}^{m} \alpha_j G(x - x_s^{(j)}), \tag{2.19}$$

and the pair $(\tilde{\varphi}_s, \varphi_b) \in L^2(\Gamma_s) \times L^2(\Gamma_b)$ is uniquely determined by the system

$$\begin{cases} (\lambda_s I - \mathcal{K}_s^*)\tilde{\varphi}_s - \dfrac{\partial \mathcal{S}_b\varphi_b}{\partial \nu} = \dfrac{\partial p_s}{\partial \nu}, \; x \in \Gamma_s, \\ (\lambda_b I - \mathcal{K}_b^*)\varphi_b - \dfrac{\partial \mathcal{S}_s\tilde{\varphi}_s}{\partial \nu} = \dfrac{\partial p_s}{\partial \nu}, \; x \in \Gamma_b. \end{cases} \tag{2.20}$$

Here, λ_b and λ_s are given by

$$\lambda_s := \frac{k_s + 1}{2(k_s - 1)} \text{ and } \lambda_b := \frac{k_s + k_b}{2(k_s - k_b)}. \tag{2.21}$$

Moreover, the decomposition (2.18) of u into a source part p_s and a refraction part $\mathcal{S}_s\tilde{\varphi}_s + \mathcal{S}_b\varphi_b$ is unique.

Proof. The system (2.12) is equivalent to the following transmission problem [3]:

$$\begin{cases} \Delta u = J_s, & x \in \mathbb{R}^2 \setminus (\Gamma_b \cup \Gamma_s), \\ u|_+ - u|_- = 0, & x \in \Gamma_b \cup \Gamma_s, \\ k_s \dfrac{\partial u}{\partial \nu}\Big|_+ - k_b \dfrac{\partial u}{\partial \nu}\Big|_- = 0, & x \in \Gamma_b, \\ \dfrac{\partial u}{\partial \nu}\Big|_+ - k_s \dfrac{\partial u}{\partial \nu}\Big|_- = 0, & x \in \Gamma_s, \\ |u| = O(|x|^{-1}), \; |x| \to \infty, \text{ uniformly in } \hat{x}. \end{cases} \tag{2.22}$$

The existence of a solution $(\tilde{\varphi}_s, \varphi_b)$ to (2.20) comes from the fact that $|\lambda_s|, |\lambda_b| \in (1/2, +\infty)$ and Theorem 2.2.1. On the other hand, the functions $\mathcal{S}_s\tilde{\varphi}_s$ and $\mathcal{S}_b\varphi_b$ are harmonic in Ω_b, and according to the definition of p_s, we have $\Delta u = J_s$ in Ω_b. In Ω_s and $\mathbb{R}^2 \setminus \overline{\Omega}_s \cup \overline{\Omega}_b$, all these functions are harmonic so we have $\Delta u = 0$. The trace relations on Γ_b and Γ_s are then given by the singularities (2.16) of $\mathcal{S}_s$ and $\mathcal{S}_b$ (see [20]) since p_s is smooth away from the points $x_s^{(j)}$. Finally, all these functions are controlled by $|x|^{-1}$ when $|x| \to \infty$. In this way, the existence of a solution to (2.12) is proved.

To prove the uniqueness of the decomposition, let us take $\tilde{\varphi}_s{}'$ and φ_b' such that

$$p_s + \mathcal{S}_s\tilde{\varphi}_s + \mathcal{S}_b\varphi_b = p_s + \mathcal{S}_s\tilde{\varphi}_s{}' + \mathcal{S}_b\varphi_b'.$$

Because of the location of the singularities, the function $\mathcal{S}_s(\tilde{\varphi}_s - \tilde{\varphi}_s{}') = \mathcal{S}_b(\varphi_b' - \varphi_b)$ is harmonic in $\Omega_s \cup \overline{\Omega}_b$, which gives by the jump formula for the normal derivative of $\mathcal{S}_b$ on Γ_b that $\varphi_b = \varphi_b'$. Finally, applying the jump formula for the normal derivative of $\mathcal{S}_s$ on Γ_s, we have $\tilde{\varphi}_s = \tilde{\varphi}_s{}'$. □

2.3 Thin resistive skin and highly conductive body asymptotic

In this section, we derive the appropriate boundary conditions associated with the presence of a very thin and very resistive skin. Robin boundary conditions will be found after an asymptotic analysis of the layer potentials involved.

We assume that Ω_s is described as:

$$\Omega_s := \big\{x + t\nu(x), \; x \in \partial\Omega_b, \; 0 < t < h\big\},$$

where ν is the outward normal unit vector and consider the following asymptotic regime:

$$k_s = \frac{h}{\xi}, \quad \xi \text{ is fixed}, \quad h \to 0, \text{ and } k_b \to \infty \quad (\text{so } k_s \to 0), \tag{2.23}$$

where ξ is the effective thickness. We compute the first-order asymptotic $u_{0,\infty}$ of u_{h,k_b} as $h \to 0$ and $k_b \to +\infty$ and see that it is the solution of the following system:

$$\begin{cases} \Delta u_{0,\infty} = J_s, & x \in \Omega_b, \\ \Delta u_{0,\infty} = 0, & x \in \mathbb{R}^2 \setminus \overline{\Omega}_b, \\ u_{0,\infty}|_+ - u_{0,\infty}|_- = \xi \left.\dfrac{\partial u_{0,\infty}}{\partial \nu}\right|_+, & x \in \partial\Omega_b, \\ \left.\dfrac{\partial u_{0,\infty}}{\partial \nu}\right|_- = 0, & x \in \partial\Omega_b, \\ |u_{0,\infty}| = O(|x|^{-1}), \quad |x| \to \infty, \text{ uniformly in } \hat{x}. \end{cases} \tag{2.24}$$

Here, the subscripts + and − represent the limit from outside and inside Ω_b, respectively. Note that in the limiting model (2.24), the role of J_s is to fix the potential $u_{0,\infty}|_-$ on $\partial\Omega_b$.

For the system (2.24), Lemma 2.2.2 yields the following result.

Lemma 2.3.1. *Assume that (2.9) holds. The solution of problem (2.24) can be written as*

$$u(x) = p_s(x) - \frac{1}{\xi}(\mathcal{S}_b\varphi)(x) + (\mathcal{D}_b\varphi)(x), \tag{2.25}$$

where ξ is defined by (2.11), p_s is given by (2.19), and $\varphi \in L^2_0(\Gamma_b) := \{\phi \in L^2(\Gamma_b) : \int_{\Gamma_b} \phi = 0\}$ is given by the following integral equation:

$$\frac{1}{\xi}\left(\frac{1}{2}I - \mathcal{K}_b^*\right)\varphi + \frac{\partial \mathcal{D}_b\varphi}{\partial \nu} = -\frac{\partial p_s}{\partial \nu}, \quad x \in \Gamma_b. \tag{2.26}$$

The decomposition (2.25) of u into a source part and a refraction part is unique.

The proof of this lemma involves exactly the same arguments as in the previous one: jump formulas applied to the operators.

The decomposition formulas (2.18) and (2.25) will be essential in the next part to derive an asymptotic expansion of u_{h,k_b} as $h \to 0$ and $k_b \to \infty$. To be more precise, we prove the following theorem:

Theorem 2.3.2. *There exists a constant C independent of h and k_b such that the following inequality holds for h and $1/k_b$ small enough:*

$$\|u_{h,k_b} - u_{0,\infty}\|_{L^\infty(\mathbb{R}^2)} \leq C\left(h + \frac{1}{k_b}\right), \tag{2.27}$$

where u_{h,k_b} and $u_{0,\infty}$ are the solutions of (2.12) and (2.24), respectively.

For doing so, we will perform asymptotic analysis of the layer potentials introduced in the representation formula (2.25) as $h \to 0$ and $k_b \to +\infty$ and show that the limiting function is the solution of (2.24). We will adapt the work done by Zribi in his thesis [118] and by Zribi and Khelifi in [69]. We will use the decomposition formula for u_{h,k_b} and compute asymptotic expansions of the refraction part. The limiting solution will then be $u_{0,\infty}$. This latter is well defined if the limits $h \to 0$ and $k_b \to \infty$ are independent, so we must seek the two following limits:

$$\lim_{k_b \to \infty} \lim_{h \to 0} u_{h,k_b} \text{ and } \lim_{h \to 0} \lim_{k_b \to \infty} u_{h,k_b},$$

and show that they are the same. Zribi [118, chapter 3] studied the case when k_b remains fixed, with non-uniform thickness of the skin Ω_s; the limit $u_{0,1}$ is the solution of the system:

$$\begin{cases} \Delta u_{0,1} = J_s, & x \in \Omega_b, \\ \Delta u_{0,1} = 0, & x \in \mathbb{R}^2 \setminus \overline{\Omega}_b, \\ u_{0,1}|_+ - u_{0,1}|_- = -\xi \left.\dfrac{\partial u_{0,1}}{\partial \nu}\right|_+, & x \in \partial\Omega_b, \\ \left.\dfrac{\partial u_{0,1}}{\partial \nu}\right|_+ - k_b \left.\dfrac{\partial u_{0,1}}{\partial \nu}\right|_- = 0, & x \in \Omega_b, \\ |u_{0,1}| = O(|x|^{-1}), \quad |x| \to \infty, \text{ uniformly in } \hat{x}. \end{cases} \tag{2.28}$$

Here, we will follow the same outline for the proof: first we will remind the asymptotic expansions of the operators involved in (2.20), and then we will match the asymptotic expansions for $\tilde{\varphi}_s$ and φ_b.

2.3.1 Asymptotic expansions of the operators

In the decomposition formula (2.18), p_s is independent of h and k_b; we just have to analyze the dependence of $\tilde{\varphi}_s$ and φ_b. Remark that from (2.20)

- the dependence on k_b is carried only by λ_b since $\mathcal{S}_b$ and $\mathcal{K}_b^*$ depend only on the shape of Ω_b;
- the dependence on h is carried by λ_s, $\mathcal{S}_s$, $\mathcal{K}_s^*$ and $\partial/\partial\nu(x)$ for $x \in \Gamma_s$.

In this subsection, we will focus on the asymptotic expansions of the operators (the limits of λ_s and λ_b are obvious). They have been performed in [25, 118]; in order to apply this proof, we first need some assumptions.

Suppose Γ_b is defined in the following way:

$$\Gamma_b := g\left(\partial B\right),$$

where g is a $\mathcal{C}^{3,\eta}$ diffeomorphism of the unit sphere $\partial B := \partial B(0,1)$ for some $\eta > 0$. Moreover, we suppose that the function $X_g : [0, 2\pi] \to \mathbb{R}^2$ defined by

$$X_g = g\left(\begin{pmatrix} \cos t \\ \sin t \end{pmatrix}\right),$$

is such that $\left|X_g'(t)\right| = 1$ for all $t \in [0, 2\pi]$. Thus, X_g is a $\mathcal{C}^{2,\eta}$ arclength counterclockwise parametrization of Γ_b. Then the outward unit normal to Ω_b, $\nu(x)$ at $x = X_g(t)$, is given by

$$\nu(x) = R_{-\frac{\pi}{2}} X_g'(t),$$

where $R_{-\frac{\pi}{2}}$ is the rotation by $-\pi/2$. The tangential vector $T(x)$ at $x = X_g(t)$ is defined by

$$T(x) = X_g'(t),$$

and $X_g'(t) \perp X_g''(t)$. The curvature $\tau(x)$ at $x = X_g(t)$ is defined by

$$X_g''(t) = \tau(x)\nu(x).$$

Let Ψ_h be the diffeomorphism from Γ_b onto Γ_s given by

$$\Psi_h(x) = x + h\nu(x). \tag{2.29}$$

With these assumptions, the following regularity result holds [72]:

Theorem 2.3.3. *Let $\eta > 0$. Let, for a Lipschitz function $g \in \mathcal{C}^{0,1}\left(\partial B, \mathbb{R}^2\right)$,*

$$l_{\partial B}[g] := \inf_{x \neq y \in \partial B} \left| \frac{g(x) - g(y)}{x - y} \right|.$$

Introduce the set $\mathcal{A}_{\partial B}$ of admissible diffeomorphisms of the unit sphere:

$$\mathcal{A}_{\partial B} := \left\{ g \in \mathcal{C}^1(\partial B, \mathbb{R}^2), l_{\partial B}[g] > 0 \right\}.$$

Then, for any integer $m > 0$, the operators S and D defined on $\left(\mathcal{C}^{m,\eta}(\partial B, \mathbb{R}^2) \cap \mathcal{A}_{\partial B}\right) \times \mathcal{C}^{m-1,\eta}(\partial B)$ ($\left(\mathcal{C}^{m,\eta}(\partial B, \mathbb{R}^2) \cap \mathcal{A}_{\partial B}\right) \times \mathcal{C}^{m,\eta}(\partial B)$, respectively) to $\mathcal{C}^{m,\eta}(\partial B)$ by

$$\begin{aligned} S[g, \varphi](x) :=& \mathcal{S}_{g(\partial B)}(\varphi \circ g^{-1}) \circ g(x), x \in \partial B, \\ D[g, \varphi](x) :=& \mathcal{D}_{g(\partial B)}(\varphi \circ g^{-1}) \circ g(x), x \in \partial B, \end{aligned}$$

are real analytic in joint variables g and φ.

Moreover, we have explicit formulas for the derivatives with respect to the variable g [72].

Then, we have the following asymptotic expansions [25, 118]:

Proposition 2.3.4. *Let $\varphi \in \mathcal{C}^{1,\eta}(\Gamma_b)$ and $\tilde{\psi} \in \mathcal{C}^{1,\eta}(\Gamma_s)$ for some $\eta > 0$. Then, we have the following asymptotic expansions for $x \in \Gamma_b$:*

$$\begin{aligned} \left(\mathcal{K}_s^* \tilde{\psi}\right) \circ \Psi_h(x) &= \mathcal{K}_b^* \psi(x) + h \mathcal{K}_b^{(1)} \psi(x) + O(h^2), \\ \frac{\partial \mathcal{S}_b \varphi}{\partial \nu} \circ \Psi_h(x) &= \left(\frac{1}{2} I + \mathcal{K}_b^*\right) \varphi(x) + h \mathcal{R}_b \varphi(x) + O(h^{1+\eta}), \\ \frac{\partial \mathcal{S}_s \tilde{\psi}}{\partial \nu}(x) &= \left(-\frac{1}{2} I + \mathcal{K}_b^*\right) \psi(x) + h \mathcal{L}_b \psi(x) + O(h^{1+\eta}), \end{aligned} \tag{2.30}$$

where $\psi := \tilde{\psi} \circ \Psi_h$, Ψ_h being defined by (2.29), and

$$\begin{aligned} \mathcal{K}_b^{(1)} \psi(x) &= \tau(x) \mathcal{K}_b^* \psi(x) - \mathcal{K}_b^*(\tau \psi)(x) - \frac{d^2 \mathcal{S}_b \psi}{dt^2}(x) + \frac{\partial \mathcal{D}_b \psi}{\partial \nu}(x), \\ \mathcal{R}_b \varphi(x) &= \tau(x) \left(\frac{1}{2} I + \mathcal{K}_b^*\right) \varphi(x) - \frac{d^2 \mathcal{S}_b \varphi}{dt^2}(x), \\ \mathcal{L}_b \psi(x) &= \left(\frac{1}{2} I - \mathcal{K}_b^*\right)(\tau \psi)(x) + \frac{\partial \mathcal{D}_b \psi}{\partial \nu}(x), \end{aligned} \tag{2.31}$$

where d/dt is the tangential derivative in the direction of $T(x) = X_g' \circ X_g^{-1}(x)$.

Note that, according to Theorem 2.3.3, the constants in the $O(h^{1+\eta})$ terms depend on $\|g\|_{\mathcal{C}^{3,\eta}}$.

Moreover, since the thickness of Ω_s is uniform, we have $\nu \circ \Psi_h(x) = \nu(x)$, and a Taylor expansion of p_s gives, for $x \in \Gamma_b$:

$$\frac{\partial p_s}{\partial \nu} \circ \Psi_h(x) = \frac{\partial p_s}{\partial \nu}(x) + h \nu(x) \cdot \left[D^2 p_s(x) \nu(x)\right] + O(h^2), \tag{2.32}$$

where $D^2 p_s$ denotes the Hessian of p_s.

2.3.2 Asymptotic expansions on the layers

In order to prove Theorem 2.3.2, we will first show the convergence on the layers (see next lemma). Then, in the next subsection, we will extend the domain of validity by application of the maximum principle.

The following lemma holds.

Lemma 2.3.5. *There exist constants C and C' independent of h and k_b such that the following inequalities hold for h and $1/k_b$ small enough:*

$$\begin{aligned} \|u_{h,k_b} - u_{0,\infty}\|_{L^\infty(\Gamma_b)} &\leq C\left(h + \frac{1}{k_b}\right), \\ \|u_{h,k_b} - u_{0,\infty}\|_{L^\infty(\Gamma_s)} &\leq C'\left(h + \frac{1}{k_b}\right), \end{aligned} \tag{2.33}$$

where u_{h,k_b} and $u_{0,\infty}$ are solutions of (2.12) and (2.24), respectively.

Proof. Only the first limit will be shown, the second one being very similar. For this purpose, we must show that the limits $h \to 0$ and $k_b \to \infty$ are independent, *i.e.*, they commute. First, let us compute the limit of u_{h,k_b} when $h \to 0$, and then the limit $k_b \to \infty$ (which will be much easier). Then, we will invert this process.

This first limit is the main problem in [118, chapter 3], except that, in that study, $k_b = 1$ and the thickness of Ω_s is non-uniform. According to theorem 2.3.3, the formulas in [72], and by composition with the regular diffeomorphism Ψ_h from Γ_s to Γ_b, we have

$$\left\| \mathcal{S}_s\tilde{\varphi}_s - \mathcal{S}_b\varphi_s - h\left[\left(-\frac{1}{2}I + \mathcal{K}_b\right)\varphi_s - \mathcal{S}_b(\tau\varphi_s)\right] \right\|_{\mathcal{C}^{2,\eta}(\Gamma_b)} \leq Ch^2,$$

where $\varphi_s := \tilde{\varphi}_s \circ \Psi_h$. Hence, with the help of the decomposition formula (2.18), we have the following asymptotic expansion uniformly on Γ_b:

$$u_{h,k_b}(x) = p_s(x) + \mathcal{S}_b(\varphi_b + \varphi_s)(x) + h\left[\left(-\frac{1}{2}I + \mathcal{K}_b\right)\varphi_s(x) - \mathcal{S}_b(\tau\varphi_s)\right](x) + O(h^2), \tag{2.34}$$

We now look for expansions of the functions φ_s and φ_b when $h \to 0$ that will be re-injected in this equation. Using Proposition 2.3.4 and (2.20), these functions are solutions of the following system:

$$\left\{ \begin{aligned} &\frac{k_s}{k_s - 1}\varphi_s - \left(\frac{1}{2}I + \mathcal{K}_b^*\right)(\varphi_s + \varphi_b) + h\left[-\mathcal{K}_b^{(1)}\varphi_s - \mathcal{R}_b\varphi_b\right] + O(h^{1+\eta}) = \\ &\qquad\qquad \frac{\partial p_s}{\partial \nu} + h\big[\nu \cdot D^2 p_s \nu\big] + O(h^2), \\ &\frac{k_s}{k_s - k_b}\varphi_b + \left(-\frac{1}{2}I + \mathcal{K}_b^*\right)(\varphi_s + \varphi_b) + h\mathcal{L}_b\varphi_s + O(h^{1+\eta}) = -\frac{\partial p_s}{\partial \nu}. \end{aligned} \right. \tag{2.35}$$

Let us define the formal asymptotic expansions:

$$\left\{ \begin{aligned} \varphi_s &= \frac{1}{h}\varphi_s^{(-1)} + \varphi_s^{(0)} + h\varphi_s^{(1)} + \dots, \\ \varphi_b &= \frac{1}{h}\varphi_b^{(-1)} + \varphi_b^{(0)} + h\varphi_b^{(1)} + \dots. \end{aligned} \right.$$

Aiming to have the 0-order term in the expansion (2.34), here we seek for the terms of order -1 and 0. By substitution into (2.35) and identification of the leading-order terms in the first line, we get:

$$\left(\frac{1}{2}I + \mathcal{K}_b^*\right)\left(\varphi_s^{(-1)} + \varphi_b^{(-1)}\right) = 0,$$

so that, by Theorem 2.2.1, we have:

$$\varphi_s^{(-1)} + \varphi_b^{(-1)} = 0. \tag{2.36}$$

Let us now look at the 0-order terms; summing the two lines of (2.35), we get:

$$\frac{1}{\xi}\left(\varphi_s^{(-1)} + \frac{1}{k_b}\varphi_b^{(-1)}\right) + (\varphi_s^{(0)} + \varphi_b^{(0)}) + \left[\mathcal{K}_b^{(1)}\varphi_s^{(-1)} + \mathcal{R}_b\varphi_b^{(-1)} - \mathcal{L}_b\varphi_s^{(-1)}\right] = 0,$$

which gives, with the help of (2.31) and (2.36),

$$\varphi_s^{(0)} + \varphi_b^{(0)} = \left[\left(\frac{1}{k_b} - 1\right)\frac{1}{\xi} + \tau\right]\varphi_s^{(-1)}. \tag{2.37}$$

This quantity is what we need in (2.34); thus, only $\varphi_s^{(-1)}$ remains to be found. This can be done by matching 0-order terms in the first line of (2.35) and using the definitions of $\mathcal{K}_b^{(1)}$ and $\mathcal{R}_b$ given by (2.31):

$$\frac{1}{\xi}\varphi_s^{(-1)} + \frac{1}{\xi}\left(\frac{1}{k_b} - 1\right)\left(\frac{1}{2}I + \mathcal{K}_b^*\right)\varphi_s^{(-1)} + \frac{\partial \mathcal{D}_b \varphi_s^{(-1)}}{\partial \nu} = -\frac{\partial p_s}{\partial \nu}. \tag{2.38}$$

Finally, the expansion (2.34) yields:

$$u_{h,k_b}(x) = p_s(x) + \left[\frac{1}{\xi}\left(\frac{1}{k_b} - 1\right)\mathcal{S}_s + \left(-\frac{1}{2}I + \mathcal{K}_b\right)\right]\varphi_s^{(-1)}(x) + O(h). \tag{2.39}$$

This leading-order term (denoted u_{0,k_b}) verifies (2.28) according to (2.38) and jump formulas (2.16).

The asymptotic $k_b \to \infty$ does not add further difficulty. Indeed, let us define the following asymptotic:

$$\varphi_s^{(-1)} = \varphi_s^{(-1,0)} + \frac{1}{k_b}\varphi_s^{(-1,1)} + \dots.$$

By substitution into equation (2.38) and identification of the leading-order terms, we get:

$$\frac{1}{\xi}\left(\frac{1}{2}I - \mathcal{K}_b^*\right)\varphi_s^{(-1,0)} + \frac{\partial \mathcal{D}_b \varphi_s^{(-1,0)}}{\partial \nu} = -\frac{\partial p_s}{\partial \nu},$$

and then the expansion (2.39) becomes:

$$u_{h,k_b}(x) = p_s(x) - \frac{1}{\xi}\mathcal{S}_s\varphi_s^{(-1,0)}(x) + \left(-\frac{1}{2}I + \mathcal{K}_b\right)\varphi_s^{(-1,0)}(x) + O\left(h\right), \tag{2.40}$$

which is (2.25) applied on Γ_b according to the jump formula of $\mathcal{D}_b$ (2.16). Hence, according to lemma 2.3.1, the first-order asymptotic of u_{h,k_b} is $u_{0,\infty}$.

Let us now show that the limits $h \to 0$ and $k_b \to \infty$ commute: unlike in the previous subsection, we will first perform the limit $k_b \to \infty$ and then the limit $h \to 0$. Given the fact that

$$\lambda_b = -\frac{1}{2} + O\left(\frac{1}{k_b}\right),$$

the definition of $\tilde{\varphi}_s$ and φ_b in (2.20) will be affected only in the second line. Indeed, with the following expansions:

$$\begin{cases} \tilde{\varphi}_s = \tilde{\varphi}_s^{(0)} + \dfrac{1}{k_b}\tilde{\varphi}_s^{(1)} + \dots, \\ \varphi_b = \varphi_b^{(0)} + \dfrac{1}{k_b}\varphi_b^{(1)} + \dots, \end{cases}$$

this second line becomes, at the leading order:

$$\left(-\frac{1}{2}I + \mathcal{K}_b^*\right)(\varphi_s^{(0)} + \varphi_b^{(0)}) + h\mathcal{L}_b\varphi_s^{(0)} + O(h^{1+\eta}) = -\frac{\partial p_s}{\partial \nu},$$

where $\varphi_s^{(0)} := \tilde{\varphi_s}^{(0)} \circ \Psi_h$. With the expansion:

$$\begin{cases} \varphi_s^{(0)} = \dfrac{1}{h}\varphi_s^{(0,-1)} + \varphi_s^{(0,0)} + h\varphi_s^{(0,1)} + \dots, \\ \varphi_b^{(0)} = \dfrac{1}{h}\varphi_b^{(0,-1)} + \varphi_b^{(0,0)} + h\varphi_b^{(0,1)} + \dots, \end{cases}$$

the identifications (2.36), (2.37), and (2.38) respectively become:

$$\varphi_s^{(0,-1)} + \varphi_b^{(0,-1)} = 0, \tag{2.41}$$

$$\varphi_s^{(0,0)} + \varphi_b^{(0,0)} = \left[\tau - \frac{1}{\xi}\right] \varphi_s^{(0,-1)}, \tag{2.42}$$

$$\frac{1}{\xi}\left(\frac{1}{2}I - \mathcal{K}_b^*\right) \varphi_s^{(0,-1)} + \frac{\partial \mathcal{D}_b \varphi_s^{(0,-1)}}{\partial \nu} = -\frac{\partial p_s}{\partial \nu}. \tag{2.43}$$

Finally, recalling that the expansion of u_{h,k_b} in (2.34) is conductivity-independent, we obtain the same expansion (2.40). □

2.3.3 Proof of Theorem 2.3.2

With the estimates (2.33) on the layers Γ_b and Γ_s, we are now ready to prove the estimate (2.27) on the whole space applying the maximum principle.

For the sets Ω_b and Ω_s, it is straightforward: the function $u_{h,k_b} - u_{0,\infty}$ is harmonic in these bounded domains, so the maximum is reached on the boundaries [101]. And, since this maximum is dominated by h and $1/k_b$, we have:

$$\|u_{h,k_b} - u_{0,\infty}\|_{L^\infty(\bar{\Omega}_b \cup \Omega_s)} \leq C\left(h + \frac{1}{k_b}\right).$$

For the exterior domain, we cannot apply directly the maximum principle since this domain is unbounded. However, the conditions at infinity in the systems (2.12) and (2.24) allow us to have a similar control. Indeed, this condition tells us that

$$\|u_{h,k_b} - u_{0,\infty}\|_{L^\infty(B(0,R))} = O(R^{-1}). \tag{2.44}$$

We take:

$$\varepsilon := \frac{1}{2}\|u_{h,k_b} - u_{0,\infty}\|_{L^\infty(\bar{\Omega}_b \cup \Omega_s)},$$

and choose R_0 such that, for $R \geq R_0$, the right-hand side of (2.44) is bounded by ε. Then, we have:

$$\|u_{h,k_b} - u_{0,\infty}\|_{L^\infty(\mathbb{R}^2 \setminus B(0,R_0))} \leq \varepsilon.$$

Now, only the bounded domain $B(0,R_0) \setminus \left(\overline{\Omega}_b \cup \Omega_s\right)$ remains, where we can apply the maximum principle. Thus, Theorem 2.3.2 is proved.

2.3.4 Final formulation and notation

In the previous subsections, we have performed a multi-scale analysis of the problem to identify the effective equations with boundary conditions. In order to make things clear, let us summarize the results and simplify the notation.

The electric potential emitted by the fish is the solution of the complex-conductivity equation (2.7) with boundary conditions given by the system (2.24). It is easy to see that in the case of an inhomogeneity outside the body, these boundary conditions will not be changed because the asymptotics are done with the layer potentials of the domains defining the fish.

Hence, we conclude this section by summing up the results: omitting all the subscripts, the electric potential u is the solution of the system

$$\begin{cases} \Delta u = J_s, & x \in \Omega, \\ \nabla \cdot (1 + (k - 1 + i\varepsilon\omega)\chi_D)\nabla u = 0, & x \in \mathbb{R}^2 \setminus \overline{\Omega}, \\ u\big|_+ - u\big|_- - \xi \left.\dfrac{\partial u}{\partial \nu}\right|_+ = 0, & x \in \Gamma, \\ \left.\dfrac{\partial u}{\partial \nu}\right|_- = 0, & x \in \Gamma, \\ |u| = O(|x|^{-1}),\ |x| \to \infty, \text{ uniformly in } \hat{x}, \end{cases} \tag{2.45}$$

where $\Gamma := \partial\Omega$, χ_D is the characteristic function of the target D, $k + i\varepsilon\omega$ is the conductivity inside D, ω is the frequency, and k and ε are positive constants. Here, we have assumed that $\sum_{j=1}^m \alpha_j = 0$.

2.3.5 The case of non-neutral charges in the body

We conclude this section by listing the modifications to our results and formulas in the case where the neutral charge condition (2.9) does not hold.

First, the far field condition in (2.12) should be replaced with

$$\left| u_{h,k_b} - (\sum_{j=1}^m \alpha_j) \frac{(\lambda_b + 1/2)(\lambda_s + 1/2)}{2\pi(\lambda_b - 1/2)(\lambda_s - 1/2)} \log|x| \right| = O(|x|^{-1}), \quad |x| \to \infty \text{ uniformly in } \hat{x}, \tag{2.46}$$

where the parameters λ_s and λ_b are given by (2.21). In order to check this far field condition, recall that $\mathcal{K}_b(1) = \mathcal{K}_s(1) = 1/2$. From

$$\int_{\Gamma_b} \left.\frac{\partial \mathcal{S}_b \varphi_b}{\partial \nu}\right|_+ = \int_{\Gamma_b} \varphi_b, \quad \int_{\Gamma_s} \left.\frac{\partial \mathcal{S}_s \tilde{\varphi}_s}{\partial \nu}\right|_- = 0, \quad \int_{\Gamma_s} \frac{\partial p_s}{\partial \nu} = \int_{\Gamma_b} \frac{\partial p_s}{\partial \nu} = \sum_{j=1}^m \alpha_j,$$

by integrating the two equations in (2.20) on Γ_s and Γ_b, respectively, we find that

$$\int_{\Gamma_s} \tilde{\varphi}_s = (\sum_{j=1}^m \alpha_j) \frac{(\lambda_b + 1/2)}{(\lambda_s - 1/2)(\lambda_b - 1/2)} \quad \text{and} \quad \int_{\Gamma_b} \varphi_b = \frac{\sum_{j=1}^m \alpha_j}{\lambda_b - 1/2},$$

and therefore, from the representation formula (2.18) it follows that

$$\left| u_{h,k_b} - (\sum_{j=1}^m \alpha_j) \frac{(\lambda_b + 1/2)(\lambda_s + 1/2)}{2\pi(\lambda_b - 1/2)(\lambda_s - 1/2)} \log|x| \right| = O(|x|^{-1}), \quad |x| \to \infty \text{ uniformly in } \hat{x}.$$

Note that in the limit $h \to 0$ and $k_b \to \infty$, it follows from (2.21) that $\lambda_b \to -1/2, \lambda_s \to -1/2$, and hence, the far field condition above yields

$$|u_{0,\infty}| = O(|x|^{-1}), \quad |x| \to \infty \text{ uniformly in } \hat{x}, \tag{2.47}$$

as stated in (2.24).

Moreover, in the case of non-neutral charges in the body, Lemma 2.2.2 holds, where the solution of (2.22) verifies the far field condition

$$\left| u - (\sum_{j=1}^m \alpha_j) \frac{(\lambda_b + 1/2)(\lambda_s + 1/2)}{2\pi(\lambda_b - 1/2)(\lambda_s - 1/2)} \log|x| \right| = O(|x|^{-1}), \quad |x| \to \infty \text{ uniformly in } \hat{x}.$$

Analogously, Lemma 2.3.1 holds. However, (2.26) should be replaced with

$$\frac{1}{\xi}\left(\frac{1}{2}I - \mathcal{K}_b^*\right)\varphi + \frac{\partial \mathcal{D}_b\varphi}{\partial\nu} = -\frac{\partial p_s}{\partial\nu} + \frac{1}{|\Gamma_b|}\sum_{j=1}^{m}\alpha_j, \quad x \in \Gamma_b.$$

Note that since

$$\int_{\Gamma_b}\frac{\partial p_s}{\partial\nu} = \sum_{j=1}^{m}\alpha_j,$$

the far field condition (2.47) is satisfied for the limiting solution $u_{0,\infty}$ in the non-neutral case.

On the other hand, if the assumption (2.9) does not hold, then the boundary condition on $\partial u_{0,\infty}/\partial\nu\big|_-$ should be replaced with

$$\left.\frac{\partial u_{0,\infty}}{\partial\nu}\right|_- = \frac{1}{|\partial\Omega_b|}\sum_{j=1}^{m}\alpha_j.$$

Analogously, we should replace in (2.45) the boundary condition $\partial u/\partial\nu\big|_- = 0$ on Γ with

$$\frac{\partial u}{\partial\nu}\big|_- = \frac{1}{|\Gamma|}\sum_{j=1}^{m}\alpha_j.$$

From now on, we restrict ourselves to the case $\sum_{j=1}^{m}\alpha_j = 0$. Note that taking two points z_1 and $z_2 \in \Omega$ close enough and $\alpha_1 = -\alpha_2 \neq 0$ yields an approximation of a dipole at $(z_1+z_2)/2$ of moment $|\alpha_1|$ and direction orthogonal to $(z_1 - z_2)$.

2.3.6 Multi-frequency measurements

Let us suppose that the electric current produced by the electric organ, (*i.e.*, the source term J_s in equation (2.45)) is time periodic and separable, that is

$$J_s(x,t) = J_s(x)h(t),$$

where J_s is a sum of Dirac functions and $h(t)$ is periodic with fundamental frequency ω_0. Hence, we set

$$h(t) = \sum_{f=1}^{N_f} h_f e^{in\omega_0 t}, \tag{2.48}$$

so that all frequencies involved are less than $N_f\omega_0$, assuming that we remain in the low-frequency regime, see [84]. According to the previous section, the electric potential u is then given by

$$u(x,t) = \sum_{f=1}^{N_f} h_f u_f e^{in\omega_0 t}, \tag{2.49}$$

where u_f, for $f = 1,\dots,N_f$, is solution of the following system

$$\begin{cases} \Delta u_f = J_s, & x \in \Omega, \\ \nabla\cdot(1+(k-1+i\varepsilon f\omega_0)\chi_D)\nabla u_f = 0, & x \in \mathbb{R}^2\setminus\overline{\Omega}, \\ u_f\big|_+ - u_f\big|_- - \xi\left.\dfrac{\partial u_f}{\partial\nu}\right|_+ = 0, & x \in \Gamma, \\ \left.\dfrac{\partial u_f}{\partial\nu}\right|_- = 0, & x \in \Gamma, \\ |u_f| = O(|x|^{-1}),\ |x|\to\infty, \text{ uniformly in } \hat{x}, \end{cases} \tag{2.50}$$

2.4 Perturbation Induced by the Presence of a Target

In this section, we derive useful formulas in order to simplify the data. For the sake of simplicity, only one target D will be considered. However, we will see in section 2.5 that it can be easily extended to the case of several inclusions.

2.4.1 A Dipolar Expansion in the Presence of a Target

The first formula, given in Proposition 2.4.1, is often called a *dipolar expansion*; indeed, in the presence of a small inhomogeneity, the perturbation of the electric potential looks like the electric potential of a dipole [19, 40]. More precisely, using exactly the same arguments as in [19, Chapter 4] and in [17] we have the following result.

Proposition 2.4.1. *Let us denote U the static background solution,* i.e.*, the electric potential without any target which does not depend on the frequency. To be more precise, it is the solution of (2.50) with a constant conductivity equal to* 1 *outside the body Ω.*

If $D := z + \delta B$ with $dist(z, \Gamma) \gg 1$, $\delta \ll 1$ and B is an open set, then we have, for $x \in \partial\Omega$,

$$\left.\frac{\partial(u_f - U)}{\partial\nu}\right|_+ (x) \simeq \delta^2 \nabla U(z)^T \mathbf{M}(\lambda_f, B) \nabla_z \left(\left.\frac{\partial G_R}{\partial \nu_x}\right|_+ \right)(x, z), \tag{2.51}$$

where T denotes the transpose, $k_f = k + i\varepsilon\omega_0 f$ is the admittivity of the target at the frequency $f\omega_0$, $\mathbf{M}(\lambda_f, B) = (M_{\alpha\beta}(\lambda_f, B))_{\alpha,\beta=1,2}$ is the first-order polarization tensor associated to B with admittivity k_f [20]:

$$M_{\alpha\beta}(\lambda_f, B) := \int_{\partial B} (\lambda_f I - \mathcal{K}_B^*)^{-1}(\nu_\alpha) y_\beta \, ds(y), \quad \lambda_f := \frac{k_f + 1}{2(k_f - 1)}, \quad \alpha, \beta = 1, 2,$$

and G_R is the Green function associated to Robin boundary conditions, which is defined for $z \in \mathbb{R}^2 \setminus \overline{\Omega}$ by

$$\begin{cases} \Delta_x G_R(x, z) = \delta_z(x), & x \in \mathbb{R}^2 \setminus \overline{\Omega}, \\ G_R|_+ - \xi \left.\dfrac{\partial G_R}{\partial \nu_x}\right|_+ = 0, & x \in \Gamma, \\ \left| G_R + \dfrac{1}{2\pi} \log|x| \right| = O(|x|^{-1}), \ |x| \to \infty, \ \textit{uniformly in } \hat{x}. \end{cases} \tag{2.52}$$

Proof. Let

$$H_f = -\mathcal{S}_\Gamma(\tfrac{\partial u_f}{\partial \nu}|_+) + \mathcal{D}_\Gamma(u_f|_+).$$

We have

$$u_f - U = -(k_f - 1) \int_D \nabla u_f \cdot \nabla G_R,$$

and on the other hand,

$$u_f - H_f = -(k_f - 1) \int_D \nabla u_f \cdot \nabla G.$$

From the transmission condition

$$\tfrac{\partial u_f}{\partial \nu}|_+ - k_f \tfrac{\partial u_f}{\partial \nu}|_- = 0 \quad \text{on } \partial D,$$

it follows that

$$u_f - U = \int_{\partial D} (\lambda_f I - \mathcal{K}_{\partial D}^*)^{-1} (\tfrac{\partial H_f}{\partial \nu}) G_R. \tag{2.53}$$

Since

$$\|\nabla H_f - \nabla U\|_{L^\infty(D)} \leq C\delta^2,$$

for some constant C, provided that $\mathrm{dist}(D, \partial\Omega) \gg \delta$, see [19, Proposition 4.6], a scaling of the integral in (2.53) together with a Taylor expansion of G_R gives the desired asymptotic expansion. Note that the approximation in (2.51) is uniform in x and k_f [20]. □

2.4.2 Post-processing

Now, we will carry on a second formula in order to simplify this equation. Indeed, the Green function associated to Robin boundary conditions is tedious to compute. Instead, we will post-process the data thanks to the following lemma which generalizes Lemma 2.15 in [19].

Lemma 2.4.2. *Let G denote the fundamental solution defined by (2.15). For $z \in \mathbb{R}^2 \setminus \overline{\Omega}$ and $x \in \Gamma$, let $G_z(x) = G(x - z)$ and $G_{R,z}(x) = G_R(x - z)$. Then*

$$\left(\frac{1}{2}I - \mathcal{K}_\Gamma^* - \xi\frac{\partial\mathcal{D}_\Gamma}{\partial\nu}\right)\left(\frac{\partial G_{R,z}}{\partial\nu_x}\right)(x) = \frac{\partial G_z}{\partial\nu_x}(x).$$

Proof. Employing the same argument as in Lemma 2.3.1 yields

$$G_{R,z} = G_z + \frac{1}{\xi}(\mathcal{S}_\Gamma\varphi) + \mathcal{D}_\Gamma\varphi - \mathcal{S}_\Gamma(\frac{\partial G_z}{\partial\nu}) - \xi\mathcal{D}_\Gamma(\frac{\partial G_z}{\partial\nu}),$$

where $\varphi = \xi\frac{\partial G_{R,z}}{\partial\nu}\big|_+$. Therefore, taking the normal derivative of the above identity and using the trace relations (2.16) give the result. □

2.5 Numerical simulations

This section is devoted to the computation of the electric field around the fish.

2.5.1 Direct Solver

The case without target

The electric field U generated by the fish is the function $u_{0,\infty}$ treated in section 2.2. Let us recall that it is the solution of the following system:

$$\begin{cases} \Delta U = J_s, & x \in \Omega, \\ \Delta U = 0, & x \in \mathbb{R}^2 \setminus \overline{\Omega}, \\ U\big|_+ - U\big|_- - \xi\left.\dfrac{\partial U}{\partial\nu}\right|_+ = 0, & x \in \Gamma, \\ \left.\dfrac{\partial U}{\partial\nu}\right|_- = 0, & x \in \Gamma, \\ |U| = O(|x|^{-1}),\ |x| \to \infty, \text{ uniformly in } \hat{x}. \end{cases} \tag{2.54}$$

Numerical simulations will be done using a boundary element method (BEM). Indeed, we need accuracy on the skin of the fish, and the jumps at the boundaries are too difficult to handle with a finite element method. Moreover, it reduces the number of discretization points, resulting in a much faster algorithm.

This BEM simulation relies on the representation formula for U in terms of the layer potentials. From Lemma 2.3.1, we have $U = p_s + \mathcal{S}_\Gamma\psi + \mathcal{D}_\Gamma\varphi$, where $\Delta p_s = J_s$ in the whole space, and the potentials are solutions of the system:

$$\begin{cases} \varphi = -\xi\psi, & x \in \Gamma, \\ \left(\dfrac{I}{2} - \mathcal{K}_\Gamma^* + \xi\dfrac{\partial\mathcal{D}_\Gamma}{\partial\nu}\right)\psi = \dfrac{\partial p_s}{\partial\nu}, & x \in \Gamma. \end{cases} \tag{2.55}$$

Note that we have changed a little bit the notation, in order to be able to test the case $\xi = 0$. On smooth domains, the operator $\mathcal{K}_\Gamma^*$ is easy to handle because its kernel has integrable singularity, whereas the operator $\partial\mathcal{D}_\Gamma/\partial\nu$ is an *hypersingular operator*. Thus, one has to perform a integration by parts in order to regularize it: for two smooth functions v_1 and v_2, we have (for example from [86, Theorem 1] and [97, Theorem 6.15]):

$$\int_\Gamma \frac{\partial\mathcal{D}_\Gamma v_1}{\partial\nu}\cdot v_2 = \int_\Gamma\int_\Gamma G(x-y)\mathrm{curl}_\Gamma v_1(x)\cdot\mathrm{curl}_\Gamma v_2(y)\,ds(x)\,ds(y), \tag{2.56}$$

where curl_Γ is the surface rotational, defined in the following way in dimension 2. First, let us define the vector:

$$\underline{\mathrm{curl}}_\Gamma\tilde{v} = \begin{pmatrix} \dfrac{\partial\tilde{v}}{\partial x_2} \\ -\dfrac{\partial\tilde{v}}{\partial x_1}\end{pmatrix},$$

where $\tilde{v}$ is an extension of v into a neighborhood of Γ, *i.e.*, $\tilde{v}(x) = v\left(\mathcal{P}(x)\right)$ with the local projection $\mathcal{P}$ onto Γ. Then curl_Γ is defined by

$$\mathrm{curl}_\Gamma v(x) := \nu(x)\cdot\underline{\mathrm{curl}}_\Gamma\tilde{v}(x).$$

In our context, this can be made much easier. Recalling the notation of subsection 2.3, we have

$$\Gamma = \left\{ x = X(t) = \begin{pmatrix} X_1(t) \\ X_2(t)\end{pmatrix},\ t\in[0,2\pi]\right\}.$$

Thus we have, for $x\in\Gamma$,

$$\begin{aligned}\mathrm{curl}_\Gamma v(x) &= \nu_1(x)\frac{\partial\tilde{v}}{\partial x_2}(x) - \nu_2(x)\frac{\partial\tilde{v}}{\partial x_1}(x)\\ &= X_2'(t)\frac{\partial v}{\partial x_2}(X(t)) + X_1'(t)\frac{\partial v}{\partial x_1}(X(t)),\quad t = X^{-1}(x),\\ &= \frac{d}{dt}\left[v(X(t))\right].\end{aligned}$$

Hence, denoting by v' the curvilinear derivative of v on Γ, formula (2.56) becomes

$$\int_\Gamma \frac{\partial\mathcal{D}_\Gamma v_1}{\partial\nu}\cdot v_2 = \int_\Gamma \mathcal{S}_\Gamma v_1'\cdot v_2'.$$

This enables us to derive a BEM formulation of the system (2.55); however one has to perform it with $\mathbb{P}_1$ elements instead of simple $\mathbb{P}_0$ elements in the case of $\xi = 0$.

The discretization of (2.55) is classical [97]. We do have to penalize equation (2.55) to deal with the far field condition by adding the term: $\left|\int_\Gamma\psi\right|^2$. The effect of the penalty term is to fix an additive constant. It is worth mentioning that this boundary element formulation can be extended to the three-dimensional case (see [86]).

The case with a target

In this subsection, we derive the modification induced on the system (2.55) in the presence of a target $D \Subset \mathbb{R}^2 \setminus \overline{\Omega}$ of admittivity k. The system (2.54) becomes:

$$\begin{cases} \Delta u = J_s, & x \in \Omega, \\ \Delta u = 0, & x \in \mathbb{R}^2 \setminus \left(\overline{\Omega} \cup \partial D\right), \\ u\big|_+ - u\big|_- - \xi \left.\dfrac{\partial u}{\partial \nu}\right|_+ = 0, & x \in \Gamma, \\ \left.\dfrac{\partial u}{\partial \nu}\right|_- = 0, & x \in \Gamma, \\ u\big|_+ - u\big|_- = 0, & x \in \partial D, \\ \left.\dfrac{\partial u}{\partial \nu}\right|_+ - k \left.\dfrac{\partial u}{\partial \nu}\right|_- = 0, & x \in \partial D, \\ |u| = O(|x|^{-1}),\ |x| \to \infty, \text{ uniformly in } \hat{x}. \end{cases} \tag{2.57}$$

Thus, u can be written as

$$u(x) = p_s(x) + \mathcal{S}_\Gamma \psi(x) + \mathcal{D}_\Gamma \varphi(x) + \mathcal{S}_{\partial D} \phi(x). \tag{2.58}$$

The absence of $\mathcal{D}_{\partial D}$ is justified by the continuity across the boundary of D. From the jump formulas (2.16), the conditions on the boundaries Γ and ∂D given in (2.57) leads us to the following system:

$$\begin{cases} \varphi = -\xi\psi, \quad x \in \Gamma, \\ \left(\dfrac{I}{2} - \mathcal{K}_\Gamma^* + \xi \dfrac{\partial \mathcal{D}_\Gamma}{\partial \nu}\right)\psi - \dfrac{\partial}{\partial \nu}\left(\mathcal{S}_{\partial D}\phi\right)\big|_\Gamma = \left.\dfrac{\partial p_s}{\partial \nu}\right|_\Gamma, \quad x \in \Gamma, \\ -\dfrac{\partial}{\partial \nu}\left(\mathcal{S}_\Gamma \psi\right)\big|_{\partial D} - \xi \dfrac{\partial}{\partial \nu}\left(\mathcal{D}_\Gamma \psi\right)\big|_{\partial D} + \left(\lambda I - \mathcal{K}_{\partial D}^*\right)\phi = \left.\dfrac{\partial p_s}{\partial \nu}\right|_{\partial D}, \quad x \in \partial D, \end{cases} \tag{2.59}$$

where

$$\lambda := \frac{k+1}{2(k-1)}.$$

System (2.59) can be rewritten as follows:

$$\mathbb{M}\begin{pmatrix} \psi \\ \phi \end{pmatrix} = \begin{pmatrix} \left.\dfrac{\partial p_s}{\partial \nu}\right|_\Gamma \\ \left.\dfrac{\partial p_s}{\partial \nu}\right|_{\partial D} \end{pmatrix},$$

with

$$\mathbb{M} := \begin{pmatrix} \left(\dfrac{I}{2} - \mathcal{K}_\Gamma^* + \xi \dfrac{\partial \mathcal{D}_\Gamma}{\partial \nu}\right) & \left(-\left.\dfrac{\partial \mathcal{S}_{\partial D}}{\partial \nu}\right|_\Gamma\right) \\ -\left(\left.\dfrac{\partial \mathcal{S}_\Gamma}{\partial \nu}\right|_{\partial D} + \xi \left.\dfrac{\partial \mathcal{D}_\Gamma}{\partial \nu}\right|_{\partial D}\right) & \left(\lambda I - \mathcal{K}_{\partial D}^*\right) \end{pmatrix}.$$

The BEM formulation is then also classical, because the only difficulty is due to the hypersingular operator in the upper left term. Hence, we discretize $\psi \in L_0^2(\Gamma)$ with $\mathbb{P}_1$ elements and $\phi \in L_0^2(\partial D)$ with $\mathbb{P}_0$ elements.

In the case of several objects D_j, $j = 1 \dots N$, the above system becomes:

$$\mathbb{M} \begin{pmatrix} \psi \\ \phi_1 \\ \vdots \\ \phi_N \end{pmatrix} = \begin{pmatrix} \left.\frac{\partial p_s}{\partial \nu}\right|_{\Gamma} \\ \left.\frac{\partial p_s}{\partial \nu}\right|_{\partial D_1} \\ \vdots \\ \left.\frac{\partial p_s}{\partial \nu}\right|_{\partial D_N} \end{pmatrix},$$

with

$$\mathbb{M} := \begin{pmatrix} \left(\frac{I}{2} - \mathcal{K}_\Gamma^* + \xi \frac{\partial \mathcal{D}_\Gamma}{\partial \nu}\right) & \left(-\left.\frac{\partial \mathcal{S}_{\partial D_1}}{\partial \nu}\right|_{\Gamma}\right) & \dots & \left(-\left.\frac{\partial \mathcal{S}_{\partial D_N}}{\partial \nu}\right|_{\Gamma}\right) \\ \left(-\left.\frac{\partial \mathcal{S}_\Gamma}{\partial \nu}\right|_{\partial D_1} + \xi \left.\frac{\partial \mathcal{D}_\Gamma}{\partial \nu}\right|_{\partial D_1}\right) & (\lambda_1 I - \mathcal{K}_{\partial D_1}^*) & \dots & \left(-\left.\frac{\partial \mathcal{S}_{\partial D_N}}{\partial \nu}\right|_{\partial D_1}\right) \\ \vdots & \vdots & \vdots & \vdots \\ \left(-\left.\frac{\partial \mathcal{S}_\Gamma}{\partial \nu}\right|_{\partial D_N} + \xi \left.\frac{\partial \mathcal{D}_\Gamma}{\partial \nu}\right|_{\partial D_N}\right) & \left(-\left.\frac{\partial \mathcal{S}_{\partial D_1}}{\partial \nu}\right|_{\partial D_N}\right) & \dots & (\lambda_N I - \mathcal{K}_{\partial D_N}^*) \end{pmatrix},$$

and the field is given by a slight modification of 2.58, namely:

$$u(x) = p_s(x) + \mathcal{S}_\Gamma \psi(x) + \mathcal{D}_\Gamma \varphi(x) + \sum_{j=1}^{N} \mathcal{S}_{\partial D_j} \phi_j(x). \tag{2.60}$$

2.5.2 Results

We present here the results of the simulation, using the methods described above. We approximate the shape of the fish by an ellipse with semi-axes of lengths 1 and 0.3; the electric organ is a dipole in the x_1-direction of moment 1, placed at $z_0 = (0.7, 0)$ and the impedance is $\xi = 0.1$. A ball of infinite conductivity (more precisely, with $\sigma = 10^{10}$ and $\varepsilon = 0$) and radius $r = 0.05$ is located at $(1.5\cos(\pi/3), 1.5\sin(\pi/3))$. Figure 2.2(b) shows the isopotentials. In Figure 2.2(c) it can be seen that the isopotentials avoid the target since it is of infinite conductivity. In Figure 2.2(d), we have perform the same simulation, with a star-shaped domain.

In Figure 2.3, we have placed two disks of conductivity 3 and 5, at the points $(\cos(\pi/3), \sin(\pi/3))$ and $(0, \sin(\pi/3))$, respectively. The electric field u is plotted in Figure 2.3(a), the difference $u - U$ in Figure 2.3(b), and finally the field of the equivalent dipole in Figure 2.3(c). This latter is given by the formula shown in Proposition 2.4.1.

2.6 Conclusion

In this chapter, we have proposed a complex conductivity model for the electric field emitted by the fish. We have rigorously derived the boundary conditions to be used, and the leading order terms of the transdermial currents when an object is located in the vincinity of the fish. Finally, we have performed numerical simulations.

In the next chapter, we will use the approximation formulas derived in section 2.4 in order to localize the target.

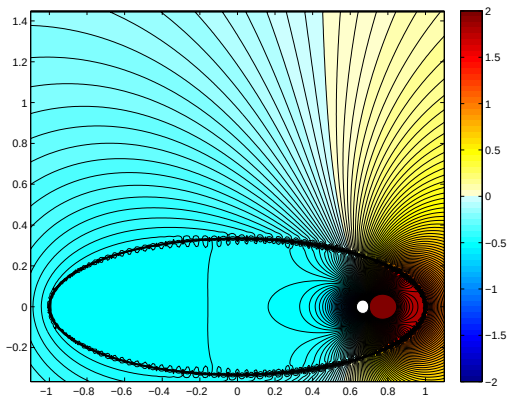

(a) Global overview, without anomaly

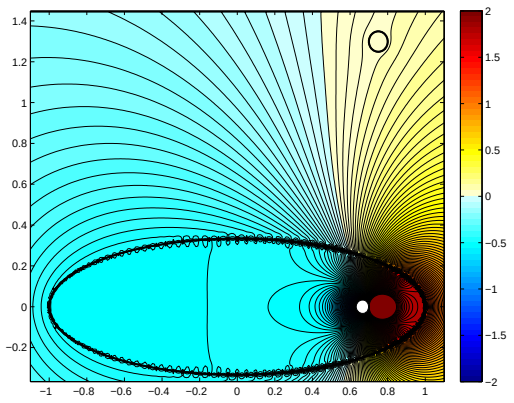

(b) Global overview, with the anomaly

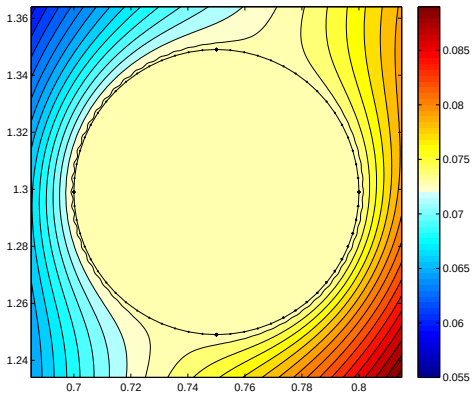

(c) Zoom on the target

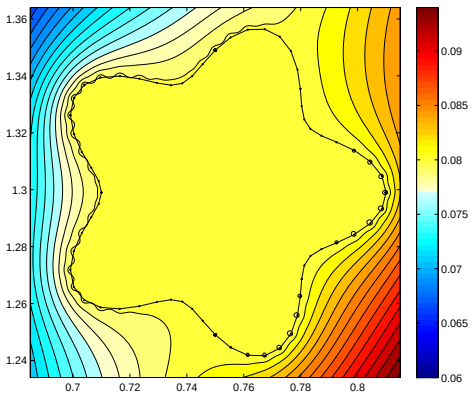

(d) Zoom on a target with different shape

Figure 2.2: Isopotentials for the cases described.

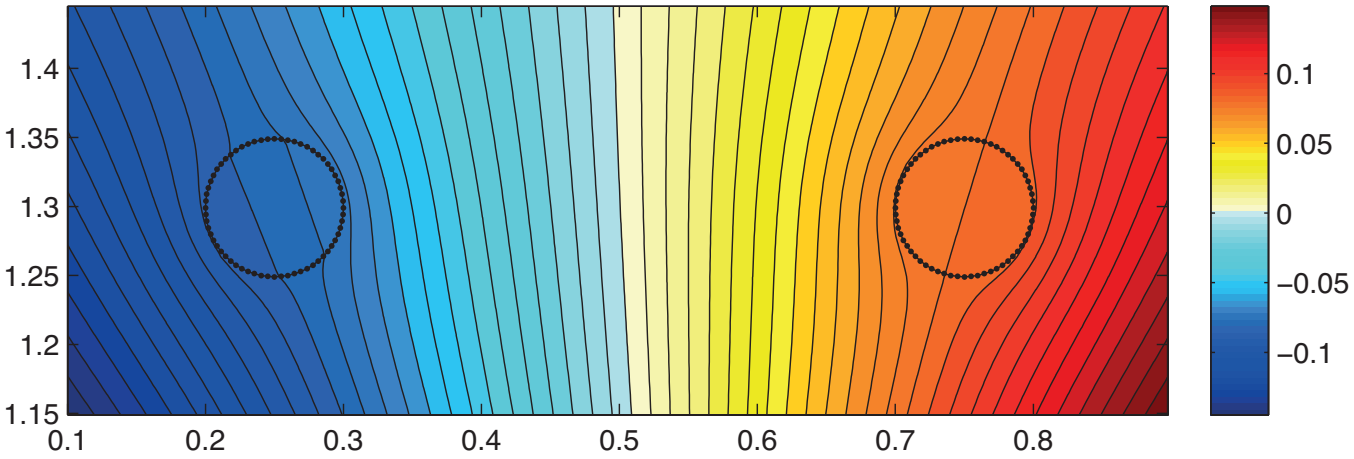

(a) Electric potentiel u

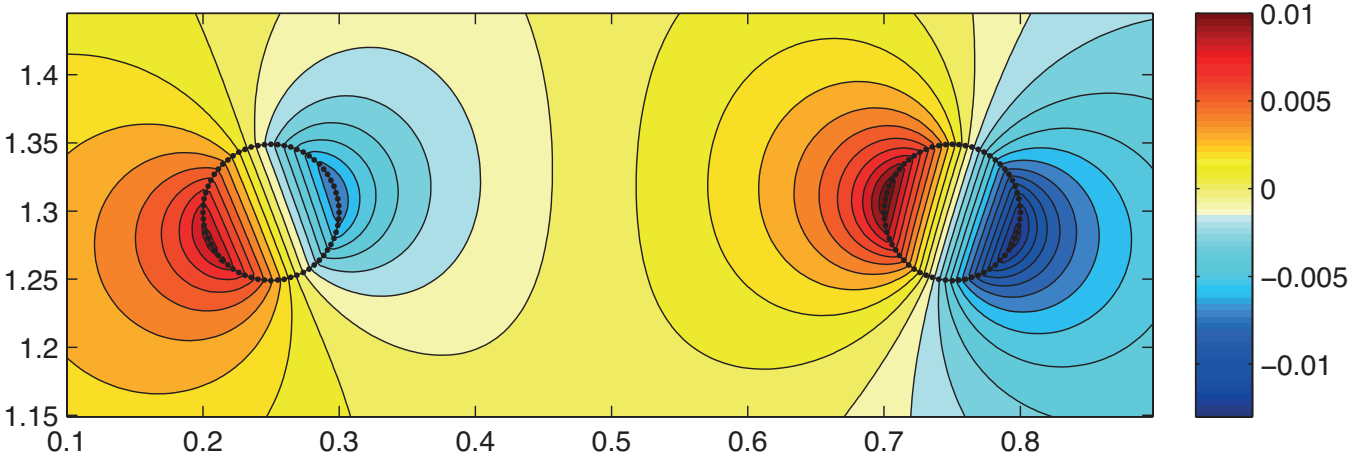

(b) Difference $u - U$

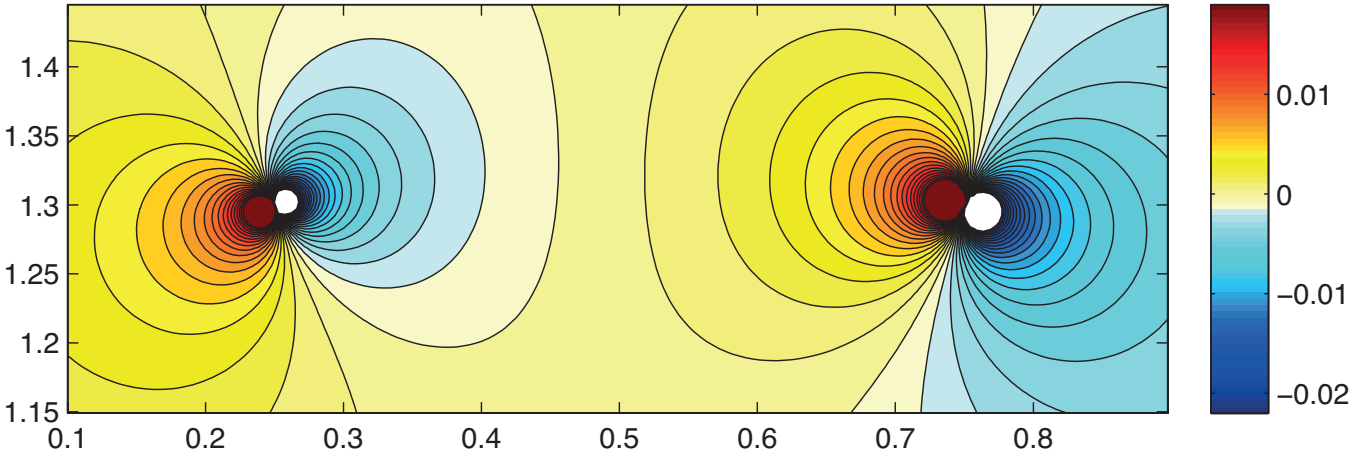

(c) Equivalent dipoles

Figure 2.3: Isopotentials for several objects.

CHAPTER 3

A Space-Frequency Localization Algorithm

The results of this chapter are published in [4].

Abstract

Based on the dipole approximation shown in the previous chapter, we obtain here a non-iterative location search algorithm using multi-frequency measurements. We present numerical experiments to illustrate the performance and the stability of the algorithm. In the case of disk- and ellipse-shaped targets, we provide a method to reconstruct separately the conductivity, the permittivity, and the size of the targets from multi-frequency measurements.

3.1 Introduction

For the inverse problem, little is known in the complex admittivity case [33]. Here, we take advantage of the smallness of the targets to use the framework of small volume asymptotic expansions (see section 2.4.1) for target location and characterization [19, 20]. However, since the electric current is generated by only one emitter at the tail of the fish (the electric organ) and measured by many receptors on the skin, standard non-iterative algorithms such as MUSIC (standing for MUltiple Signal Classification) cannot be applied for location search. In standard MUSIC, the data (called multistatic response matrix) form a matrix and its singular value decomposition leads to an efficient imaging function by projecting the Green function of the medium onto the significant image space [13, 16, 22, 35, 41, 43, 70]. Here, roughly speaking, one has only a column of the response matrix. However, using the fact that the electric current produced by the electric organ is time-harmonic with a known fundamental frequency, we extend MUSIC approach to multi-frequency measurements by constructing an efficient and robust multi-frequency MUSIC imaging function. We perform numerical simulations in order to validate both the direct model and the multi-frequency MUSIC algorithm. We also illustrate the robustness with respect to measurement noise and the sensitivity with respect to the number of frequencies, the number of sensors, and the distance to the target of the location search algorithm. Finally, in the case of disk- and ellipse-shaped targets, we provide a method to reconstruct separately the conductivity, the permittivity, and the size of the targets from multi-frequency

measurements. We mention that this is possible only because of multi-frequency measurements which yield polarization tensors with complex admittivty. It is well-known that polarization tensors for vanishing capacitance (*i.e.* real-valued admittivity) cannot separate the size from material properties of the target [20]. We also mention that the use of different values for the frequencies is more crucial for the material and size reconstruction procedure than for the location step. In fact, in the presence of measurement noise, location with N_f realizations with one frequency is comparable to the one with N_f different frequency values.

3.2 Detection algorithm for multi-frequency measurements

Scholz described in [96] a way to recover the location of a target from multi-frequency measurements. The paper focuses on an application in electrical impedance tomography (EIT) for breast cancer detection; the algorithm was called "Space-Frequency MUSIC". Indeed, it is based on the so-called MUSIC algorithm, which is a standard tool in signal theory for the identification of several signals with an additive noise [95, 49]. It has then been applied to identify small conductivity inhomogeneities in [15, 22, 35]. In this section, we apply a similar approach for our model.

In this section, we develop an algorithm to recover (from a single measurement) the location of a small object located far away from the fish. This algorithm is based on multi-frequency measurements defined in subsection 3.2.1, and the algorithm will be explained in detail in subsection 3.2.2.

3.2.1 Response matrix

The electroreceptors of the fish measure the electric current at the surface of the skin [84]. Hence, from a single measurement, we can construct the Space-Frequency Response (SFR) matrix $\mathbf{V}$, whose terms are given by

$$V_{rf} = \left(\frac{\partial u_f}{\partial \nu}\bigg|_+ - \frac{\partial U}{\partial \nu}\bigg|_+ \right)(x_r), \quad \text{for } 1 \leq f \leq N_f \text{ and } 1 \leq r \leq N_r,$$

where $(x_r)_{1\leq r\leq N_r}$ are points on the boundary Γ and U is the static background solution, *i.e.*, the electric potential without any target which does not depend on f. It is the solution of (2.50) with a constant conductivity equal to 1 outside the body Ω.

Recalling from section 2.4, after a calculation of $\frac{\partial u_f}{\partial \nu}\Big|_+ - \frac{\partial U}{\partial \nu}\big|_+$ on Γ, we will apply the post-processing operator given in Lemma 2.4.2. The modified matrix will still be denoted A.

Thus, the location of the target D is going to be recovered from the knowledge of the following data

$$V_{rf} = \left(\frac{1}{2}I - \mathcal{K}_\Gamma^* - \xi\frac{\partial \mathcal{D}_\Gamma}{\partial \nu}\right)\left(\frac{\partial u_f}{\partial \nu}\bigg|_+ - \frac{\partial U}{\partial \nu}\bigg|_+ \right)(x_r), \quad 1 \leq r \leq N_r, 1 \leq f \leq N_f, \tag{3.1}$$

which is approximately equal to

$$V_{rf} \simeq \delta^2 \nabla U(z)^T \mathbf{M}(\lambda_f, B)\nabla_z \left(\frac{\partial G}{\partial \nu_x}\bigg|_+ \right)(x_r, z), \tag{3.2}$$

when the characteristic size of the target δ is small. It is worth mentioning that the polarization tensor $\mathbf{M}(\lambda_f, B)$ is symmetric (but not Hermitian) [20].

3.2.2 A location search algorithm

As we can see in formula (3.2), the rows of the SFR matrix are - to leading-order - linear combinations of the derivatives of $\partial G/\partial \nu_x$. Moreover, one has to distinguish whether the target is a disk or not. Indeed,

in dimension 2 and in the case of an ellipse whose semi-axes are on the x_i-axis and of length a and b, the polarization tensor $\mathbf{M}(\lambda, B)$, for $k \in \mathbb{C}$, takes the form [83]

$$\mathbf{M}(\lambda, B) = (k-1)|B| \begin{pmatrix} \frac{a+b}{a+kb} & 0 \\ 0 & \frac{a+b}{b+ka} \end{pmatrix}.$$

Hence, the polarization tensor is proportional to the identity matrix if and only if $a = b$, *i.e.*, B is a disk; this result remains true in dimension 3 [20]. This changes dramatically the range of A: if B is a disk, the response matrix has rank 1 and if it is an ellipse, it has rank 2.
For the sake of simplicity, let us suppose that B is the unit disk. The identification process will be based on the following fact

Lemma 3.2.1. *The following map*

$$\begin{aligned} \Lambda : \quad & \mathbb{R}^2 \setminus \overline{\Omega} \to L^2(\Gamma) \\ & z \mapsto \nabla U(z)^T \nabla_z \frac{\partial G}{\partial \nu_x}(\cdot, z), \end{aligned}$$

is one-to-one.

Proof.

Suppose that z and z' are points on $\mathbb{R}^2 \setminus \overline{\Omega}$ such that $\Lambda(z) = \Lambda(z') := \varphi$. Let us define the two following functions

$$\begin{aligned} v_z : \quad & \mathbb{R}^2 \setminus \overline{\Omega} \cup \{z\} \to \mathbb{R} \\ & x \mapsto \nabla U(z)^T \nabla_z G(x, z), \end{aligned}$$

$$\begin{aligned} v_{z'} : \quad & \mathbb{R}^2 \setminus \overline{\Omega} \cup \{z'\} \to \mathbb{R} \\ & x \mapsto \nabla U(z')^T \nabla_{z'} G(x, z'). \end{aligned}$$

Thus, these two functions both solve the following boundary value problem

$$\begin{cases} \Delta v = 0, \quad x \in \mathbb{R}^2 \setminus \overline{\Omega} \cup \{z\} \cup \{z'\}, \\ \dfrac{\partial v}{\partial \nu} = \varphi, \qquad\qquad\qquad\qquad x \in \Gamma, \\ \quad v \to 0 \ \ |x| \to \infty, \ \text{uniformly in } \hat{x}. \end{cases}$$

Hence, by the uniqueness of the solution for this problem, we have

$$\nabla U(z) \cdot \nabla_z G(x, z) = \nabla U(z') \cdot \nabla_{z'} G(x, z'), \ \text{for all } x \in \mathbb{R}^2 \setminus \overline{\Omega} \cup \{z\} \cup \{z'\}.$$

Relying on the singularity of $G(\cdot, z)$ at the point z, this is only possible if $z = z'$.

□

However, we do not have access to the complete function (because there is only a finite number of electroreceptors on the body), and the formula for Λ is only an approximation, based on (3.2). The location of the target will then be approximated as follows. In the following we suppose for the sake of simplicity that $x_1, \ldots, x_L$ are equi-distributed on Γ.

Proposition 3.2.2 (Space-Frequency MUSIC)**.** *Define the vector*

$$\tilde{g}(z) := \left(\nabla U(z) \cdot \nabla_z \left(\frac{\partial G}{\partial \nu_x} \right)(x_1, z), \ldots, \nabla U(z) \cdot \nabla_z \left(\frac{\partial G}{\partial \nu_x} \right)(x_{N_r}, z) \right)^T, \tag{3.3}$$

and its normalized version $g = \tilde{g}/|\tilde{g}|$. Then, in the limit $N_r \to +\infty$ and $\delta \to 0$, the following imaging functional will have a large peak at z:

$$\mathcal{I}(z_s) := \frac{1}{|(I - P)g(z_s)|}, \tag{3.4}$$

where P is the orthogonal projection onto the first singular vector of the SFR matrix A.

Proof.

First of all, let us rewrite (just for this proof) the projection $P_\delta^{N_r}$ and the illumination vector g^{N_r}, in order to take into account the dependence with respect to N_r. When N_r goes to infinity, quadrature formulas show us that

$$|(I - P_\delta^{N_r}) g^{N_r}(z_s)|_{\mathbb{R}^{N_r}} \to \left| (I - P_\delta) \frac{\Lambda(z_s)}{|\Lambda(z_s)|_{L^2(\Gamma)}} \right|_{L^2(\Gamma)}.$$

Here, P_δ is the projection onto the first singular vector of the operator $\mathbb{A}_\delta$, acting on the space of functions that have the form (2.48)

$$\begin{aligned} \mathbb{A}_\delta : L^2[0, 2\pi/\omega_0] &\to L^2[0, 2\pi/\omega_0] \times L^2(\Gamma) \\ h = \sum_{f=1}^{N_f} h_r e^{if\omega_0 t} &\mapsto \left(\frac{1}{2} I - \mathcal{K}_\Gamma^* - \xi \frac{\partial \mathcal{D}_\Gamma}{\partial \nu} \right) \left(\left. \frac{\partial u}{\partial \nu} \right|_+ - \left. \frac{\partial U}{\partial \nu} \right|_+ \right), \end{aligned}$$

where u is given by (2.49) and U is the background solution (*i.e.*, the solution of (2.50) with $\chi_D = 0$).

In the limit $\delta \to 0$, $\mathbb{A}_\delta$ is approximated by the operator $\mathbb{A} : h \mapsto \Lambda(z)h$, which is obviously of rank one. By theory of perturbation [67], one has therefore

$$\left| (I - P_\delta) \frac{\Lambda(z_s)}{|\Lambda(z_s)|_{L^2(\Gamma)}} \right|_{L^2(\Gamma)} \to \left| (I - P) \frac{\Lambda(z_s)}{|\Lambda(z_s)|_{L^2(\Gamma)}} \right|_{L^2(\Gamma)}, \ \delta \to 0,$$

where P is the projector onto the first significant singular vector of $\mathbb{A}$. Then, from Lemma 3.2.1, this functional is zero if and only if $z_s = z$.

□

Moreover, in order to have a general algorithm which is robust with respect to the background solution, we will plot the following imaging functional:

$$\mathcal{I}(z_s) := \max \left(\frac{1}{\sum_{i=1}^2 \left| (I - P) g_i^{\mathcal{E}}(z_s) \right|}, \frac{1}{\sum_{i=1}^2 \left| (I - P) g_i^{\mathcal{D}}(z_s) \right|} \right), \tag{3.5}$$

where $g^{\mathcal{D}} = (g_1^{\mathcal{D}}, g_2^{\mathcal{D}})^T$ is defined in Proposition 3.2.2 and $g_i^{\mathcal{E}}(z_s)$, for $i = 1, 2$, is the normalization of the following vector

$$\tilde{g}_i^{\mathcal{E}}(z) = \left(e_i \cdot \nabla_z \left(\frac{\partial G}{\partial \nu_x} \right)(x_1, z), \ldots, e_i \cdot \nabla_z \left(\frac{\partial G}{\partial \nu_x} \right)(x_{N_r}, z) \right)^T,$$

with (e_1, e_2) being an orthonormal basis of $\mathbb{R}^2$. Numerical localization results for targets with different shapes will be given in section 3.3.

3.3 Numerical simulations

In this section, numerical results are presented in order to illustrate the multi-frequency location search algorithm introduced in the previous section. The computed electric field in the presence of the target, computed in 2.5 is the input of our location search algorithm that is performed here.

3.3.1 Target location

In this subsection, we show numerical target location results using the multi-frequency imaging function (3.5). With the same parameters used for Figure 2.2(b) for the fish, but with a small target of electric parameters $\sigma = 2$ and $\varepsilon = 1$ and fundamental frequency $\omega_0 = 1$, we obtain the imaging functional plotted

in Figure 3.1 (a). We use 10 frequencies equidistributed from ω_0 to $10\omega_0$. In Figure 3.1 (b) and (c), we have tested other shapes for the target.

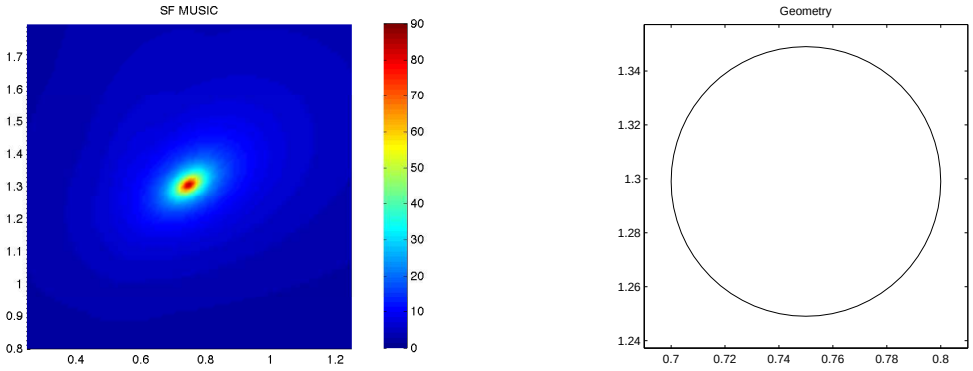

(a)

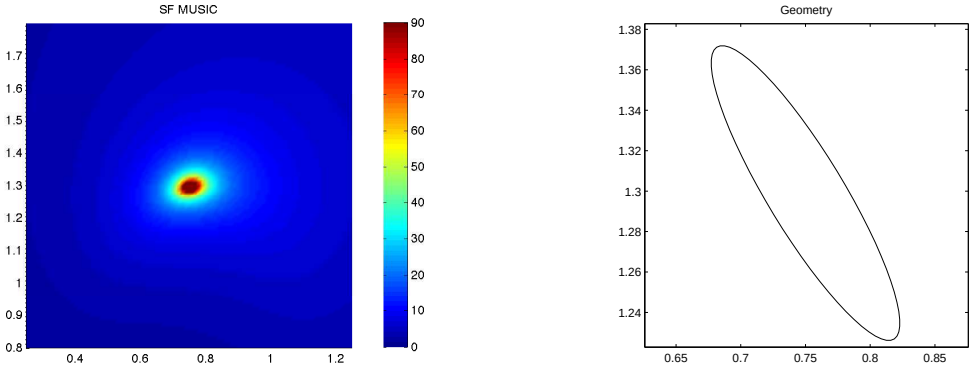

(b)

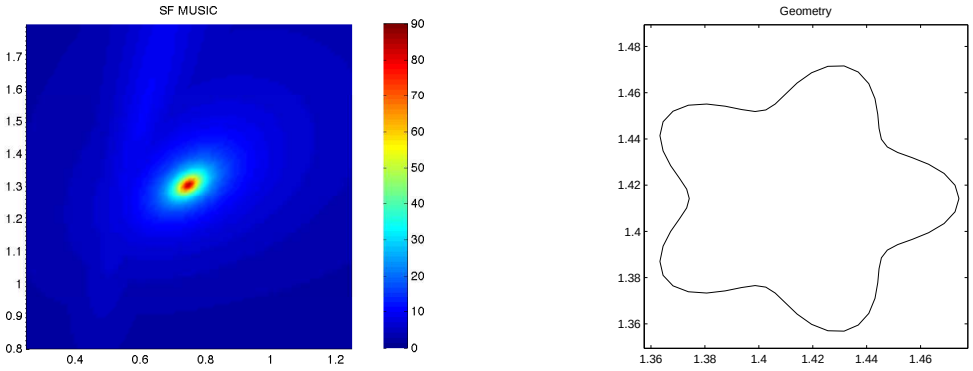

(c)

Figure 3.1: Detection (left) of the target with the SF-MUSIC algorithm, for different target shapes (right). Here, the number of used frequencies is 10, equidistributed from ω_0 to $10\omega_0$, and there are 64 equidistant sensors on the fish.

For multiple targets, we only have developped the algorithm for disks, and we suppose that we know in advance their number, see Figure 3.2. We can see in Figure 3.2(b) that if the disks are too close, we cannot distinguish them.

The generalization for other shapes would involve first to count the number of objects, by counting the number of significant singular values [19]. Then, we would have to check for each singular value - or each pair of singular values for non-isotropic objects - if it corresponds to an abject or not. An example of such algorithm can be found in [85], where it has been called *Recursively Applied and Projected (RAP) MUSIC*.

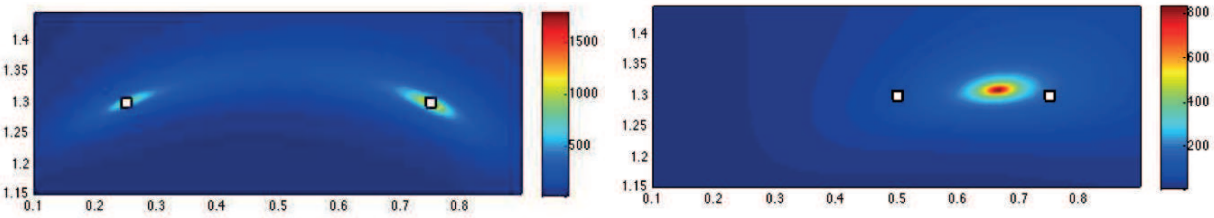

(a) $t = (-0.5, 0)$ (b) $t = (-0.25, 0)$

Figure 3.2: Detection of two disks, the first one being the same as in 3.1(a), with conductivity $\sigma = 5$ and permittivity $\varepsilon = 2$. The second one has the same radius, and is translated by the vector t indicated below each figure. It has conductivity $\sigma = 3$ and permittivity $\varepsilon = 1$. Their centers are indicated by a square

Let us notice that, in the absence of noise, the number of used frequencies does not change significantly the image. Indeed, we can see in Figure 3.3(a)(a) that we can recover the location of the target with only one frequency for a single disk. For several disks, one needs the same number of frequencies as the number of disks, see Figure 3.3(b) and Figure 3.3(c).

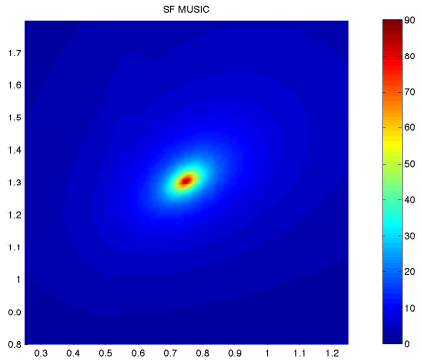

(a)

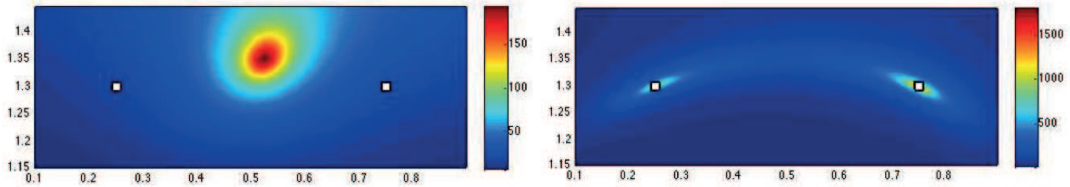

(b) (c)

Figure 3.3: Target detection in the absence of noise. (a)The target is the disk in Figure 3.1(a), with only one frequency $\omega_0 = 1$. (b) The two disks of Figure 3.2(a), with only one frequency $\omega_0 = 1$. (c) The two disks of Figure 3.2(a), with two frequencies $\omega_0 = 1$ and $\omega_0 = 2$. In all these experiments, the number of sensors stay the same.

Stability estimates with respect to measurement noise

Let us now consider the effect of measurement noise on the performance of the location search algorithm. We add to the entries of the SFR matrix A defined in (3.2) independent Gaussian random variables of mean 0 and standard deviation

$$\sqrt{\zeta}\max_{r,f}\left|\left(\frac{\partial u_f}{\partial \nu}\bigg|_+ - \frac{\partial U}{\partial \nu}\bigg|_+\right)(x_r)\right|.$$

The parameter ζ is the relative strength of the noise, and will be given in percentage.

In Figure 3.4, one can see that even with 1% of noise level, we cannot discriminate two disks that are well separated. Hence, we will focus in this subsection on the stability for only one object.

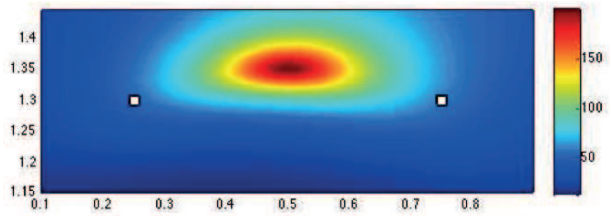

Figure 3.4: Target detection for the two disks of Figure 3.2(a) with 1% noise.

Figure 3.5 shows that increasing the number of frequencies stabilizes the image. The image on the left in Figure 3.5 corresponds to the same configuration as in Figure 3.3(a), but with 10% of noise.

Figure 3.6 shows the performance of the imaging algorithms for a target of a noncircular shape.

More quantitatively, we have computed the empirical root mean square location error (between the exact location of the target and the maximum of the imaging functional), for $N_r = 250$ realizations. The root mean square location error is defined by $\sqrt{\mathbb{E}(|z^{\text{est}} - z|^2)}$ with $\mathbb{E}$ standing for the expectation (mean value) and z^{est} (resp. z) being the estimated location (resp. the exact one).

Here, the same target as in Figure 3.3(a) is considered. Results are shown in Figure 3.7.

A natural question is whether taking different values for the frequencies plays a role in the multi-frequency imaging procedure. In order to answer this question, we construct an SFR matrix using the same frequency for all the columns and compare the resulting image with the one obtained using different

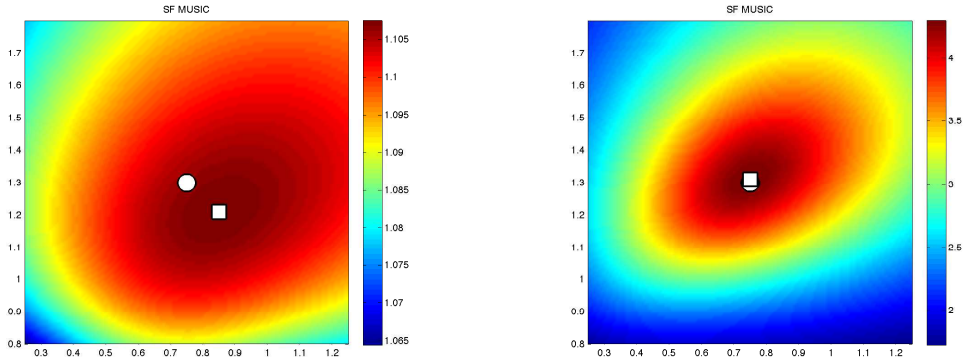

Figure 3.5: Influence of the number of used frequencies on the stability. Here, the same target as in Figure 3.3(a) is imaged with 10% of noise and only one frequency $\omega_0 = 1$ (left), 100 frequencies equidistributed from ω_0 to $100\omega_0$ (right), with 64 sensors. The disks plot the exact position, and the squares plot the location of the maximum of the imaging functional.

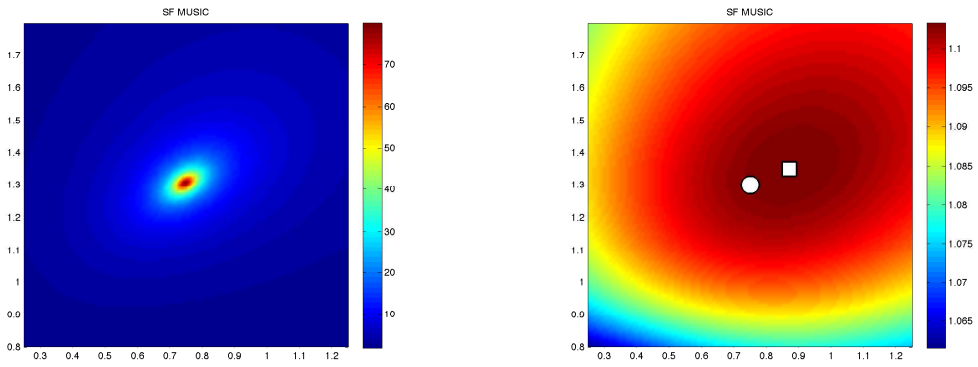

Figure 3.6: The same target as in Figure 3.1(c) is imaged with only one frequency $\omega_0 = 1$ and without noise (left), with 10% of noise (right). The disks plot the exact position, and the squares plot the location of the maximum of the imaging functional.

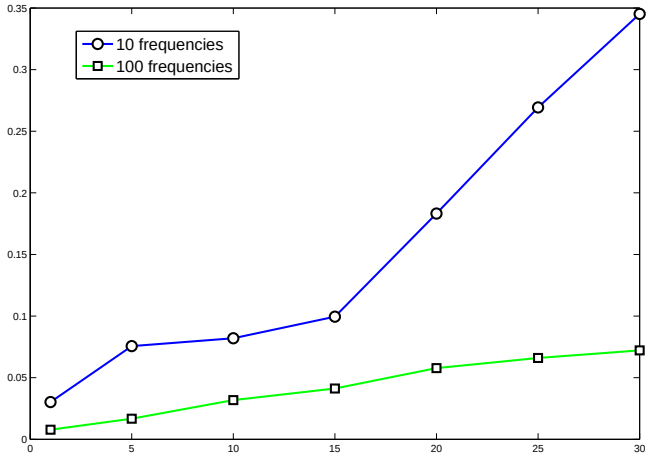

Figure 3.7: Influence of the number of frequencies on the root mean square location error for 250 realizations. Here, the horizontal axis is for the measurement noise level in percentage and the vertical axis is for the root mean square location error.

frequencies (one for each column). In Figure 3.8, we use the data obtained by 100 trials (making measurements 100 times using the same frequency ω_0) for 10% of noise, 64 sensors, and a single frequency $\omega_0 = 1$. Here, the entries of each of the 100 columns are corrupted (independently) with 10% of noise. Figure 3.8 shows that the values of the frequencies do not play a crucial role in the location procedure. In fact, the location result is similar to the one in Figure 3.5. However, from a practical point of view, using simultaneously N_f different frequencies yields a faster robust location procedure than repeating N_f times the data acquisition procedure with the same frequency. In subsection 3.3.2, we also identify the more fundamental role of the values of the frequencies in the characterization procedure.

The number of sensors is also crucial in the stability of the algorithm. Figure 3.9 compares the root mean square location error with 100 frequencies equidistributed from ω_0 to $100\omega_0$ for 64 and 8 sensors for different measurement noise levels.

The same type of statistics is possible for the detection as function of the distance between the fish from the target. In Figure 3.10, we have plotted the root mean square location errors, with 15 frequencies equidistributed from ω_0 to $15\omega_0$ and 5% of noise, for disks with radius 0.05 placed at $(t\cos(\pi/3), t\sin(\pi/3))$

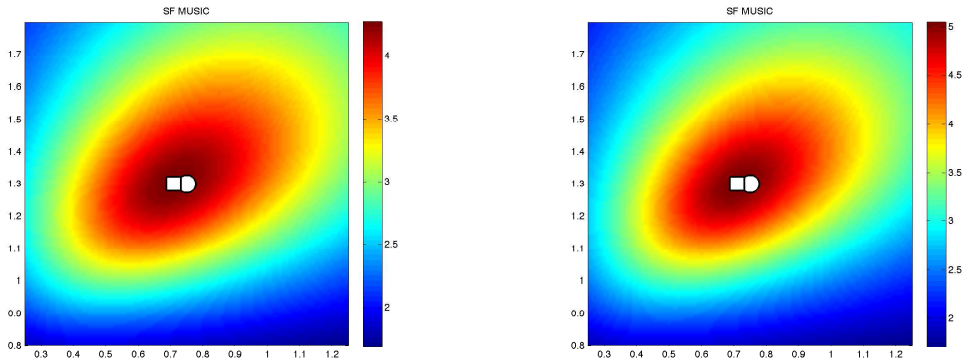

Figure 3.8: Influence of the values of used frequencies on the stability. Imaging using the data obtained by 100 trials with 10% of noise, 64 sensors, and frequency $\omega_0 = 1$: Left: the same target as in Figure 3.1(a); Right: the same target as in Figure 3.1(c). The disks plot the exact position, and the squares plot the location of the maximum of the imaging functional.

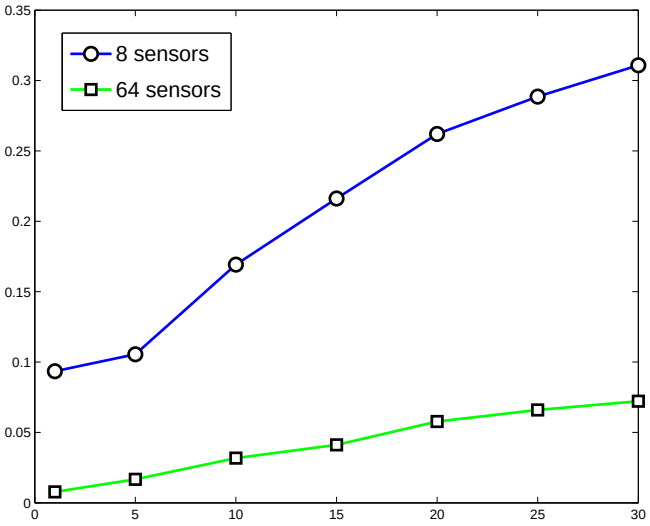

Figure 3.9: Influence of the number of sensors on the root mean square location error for 250 trials. Here, the horizontal axis is for the noise level in percentage and the vertical axis is for the root mean square location error.

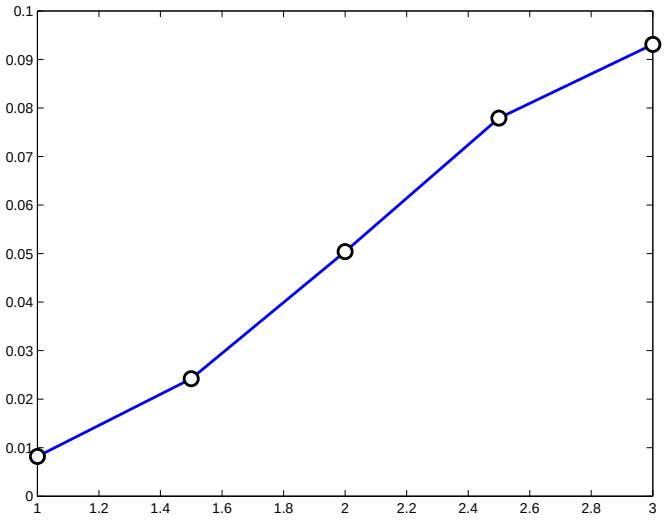

Figure 3.10: Influence of the distance to the fish on the mean square location error for 250 trials. Here, the horizontal axis is for the distance to the fish and the vertical axis is for the root mean square location error.

for $t = 1, 1.5, 2, 2.5,$ and 3.

3.3.2 Target characterization

Once the target is located, one can use (3.2) to estimate the electromagnetic parameters and the size of the target. Assume that the target is a disk of radius δ, placed at z. From (3.2) it follows that $\delta^2(k_f-1)/(k_f+1)$ can be estimated for $1 \leq f \leq N_f$ from the measurement matrix A. Here, $k_f = k + i\varepsilon\omega_0 f$ with ω_0 being known. Let τ_r^{est} be the estimated values of $\delta^2(k_f - 1)/(k_f + 1)$ from A. To characterize the target and approximate its size, one minimizes the following quadratic misfit functional:

$$\sum_{1\leq f\leq N_f} \left| \frac{\delta^2(k_f - 1)}{k_f + 1} - \tau_r^{\text{est}} \right|^2, \tag{3.6}$$

over k, ε, and δ.

Table 3.1 gives the result of the optimization algorithm for a disk-shaped target with center center $(1.5\cos(\pi/3), 1.5\sin(\pi/3))$ and radius δ^{true}. The electromagnetic parameters are $(\sigma^{\text{true}}, \varepsilon^{\text{true}})$. The initial guess is $\delta^{\text{init}} = 0.01, \sigma^{\text{init}} = 1, \varepsilon^{\text{init}} = 1$. The data is collected for 100 frequencies equidistributed from ω_0 to $100\omega_0$. The reconstructed results are accurate.

δ^{true}	σ^{true}	$\varepsilon^{\text{true}}$	δ^{est}	σ^{est}	ε^{est}
0.05	5	1	0.0506	4.9882	1.0004
0.05	4	1	0.0506	3.9993	0.9998
0.05	5	2	0.0506	4.9868	2.0017
0.06	5	1	0.0607	4.9878	1.0003
0.04	3	2	0.0404	2.9614	1.9806

Table 3.1: Target characterization by minimizing the quadratic misfit functional (3.6) using data collected for 100 frequencies equidistributed from ω_0 to $100\omega_0$. Here, true: true values, est: estimated values. The initial values are $\delta^{\text{init}} = 0.01, \sigma^{\text{init}} = 1, \varepsilon^{\text{init}} = 1$.

When the target is an ellipse, the measurement matrix A may not be sufficient to characterize the electromagnetic parameters and the size of the target. At least two different positions of the fish (or equivalently two different locations of the target in the fish frame of reference) are needed in order to generate non-parallel dipole directions $\nabla U/|\nabla U|$ at the location z of the target and consequently lead to the extraction of the polarization tensor $\mathbf{M}(\lambda_f, D)$ of the ellipse-shaped target D. Consider two target locations z_1 and z_2 in the fish frame of reference. Multi-frequency measurements lead to two SFR matrices, $V_{rf}^{(1)}$ and $V_{rf}^{(2)}$ with $1 \leq r \leq N_r$ and $1 \leq f \leq N_f$. Define the following linear application from the set $\mathcal{M}$ of complex symmetric 2×2 matrices to $\mathbb{C}^{2N}$

$$F : \mathbf{M} \mapsto \begin{pmatrix} \nabla U(z_1)^T \mathbf{M} \nabla_z \left(\frac{\partial G}{\partial \nu_x}\Big|_+ \right)(x_1, z_1) \\ \vdots \\ \nabla U(z_1)^T \mathbf{M} \nabla_z \left(\frac{\partial G}{\partial \nu_x}\Big|_+ \right)(x_{N_r}, z_1) \\ \nabla U(z_2)^T \mathbf{M} \nabla_z \left(\frac{\partial G}{\partial \nu_x}\Big|_+ \right)(x_1, z_2) \\ \vdots \\ \nabla U(z_2)^T \mathbf{M} \nabla_z \left(\frac{\partial G}{\partial \nu_x}\Big|_+ \right)(x_{N_r}, z_2) \end{pmatrix}.$$

For a fixed f, we define the data

$$b_f := \begin{pmatrix} \mathbf{V}_{1f}^{(1)} \\ \vdots \\ \mathbf{V}_{Nrf}^{(1)} \\ \mathbf{V}_{1f}^{(2)} \\ \vdots \\ \mathbf{V}_{Nrf}^{(2)} \end{pmatrix}.$$

By a least-squares method, we recover an estimation of the polarization tensor $\mathbf{M}(\lambda_f, D)$:

$$\mathbf{M}_f^{\text{est}} := \arg \min_{\mathbf{M} \in \mathcal{M}} \|F(\mathbf{M}) - b_f\|.$$

Again, once $\mathbf{M}(\lambda_f, D)$ is estimated, a minimization approach yields correct parameter and size values. Since for any f, the eigenvectors of the matrix $\mathbf{M}(\lambda_f, D)$ are the ellipse axes, denoting $\tau_{f,1}^{\text{est}}$ and $\tau_{f,2}^{\text{est}}$ the estimated complex eigenvalues of $\mathbf{M}(\lambda_f, D)$, one minimizes the following quadratic misfit functional

$$\sum_{1 \leq f \leq N_f} \left| \frac{ab(k_f - 1)(a+b)}{ak_f + b} - \tau_{f,1}^{\text{est}} \right|^2 + \left| \frac{ab(k_f - 1)(a+b)}{bk_f + a} - \tau_{f,2}^{\text{est}} \right|^2,$$

over a, b, k, and ε, in order to reconstruct the semi-axis lengths a and b and the material parameters k and ε of the ellipse-shaped target D.

If N_f is large enough, then semi-analytical formulas to estimate the semi-axis lengths a, b and the material parameters k, ε hold. Since

$$\tau_{N_f,1}^{\text{est}} \approx \pi a(a+b), \quad \tau_{N_f,2}^{\text{est}} \approx \pi b(a+b),$$

one can estimate a and b as follows:

$$a^{\text{est}} = \frac{\tau_{N_f,1}^{\text{est}}}{\sqrt{\pi \left(\tau_{N_f,1}^{\text{est}} + \tau_{N_f,2}^{\text{est}} \right)}}, \quad b^{\text{est}} = \frac{\tau_{N_f,2}^{\text{est}}}{\sqrt{\pi \left(\tau_{N_f,1}^{\text{est}} + \tau_{N_f,2}^{\text{est}} \right)}}. \tag{3.7}$$

Table 3.2 gives estimations of a and b. The target is centered at $z_1 = 1.5(\cos(\pi/3), \sin(\pi/3))$ and the fish moves in the horizontal axis so that $z_2 = (1.5\cos(\pi/3) - 1, 1.5\sin(\pi/3))$. The material parameters of the target are $k = 2$ and $\varepsilon = 1$. The data is collected for 10 frequencies equidistributed from ω_0 to $10\omega_0$. The reconstructed results are accurate.

a^{true}	b^{true}	a^{est}	b^{est}
0.04	0.04	0.0390	0.0405
0.05	0.05	0.0497	0.0516
0.05	0.06	0.0586	0.0608
0.03	0.06	0.0313	0.0567
0.06	0.05	0.0406	0.0487
0.01	0.03	0.0108	0.0273

Table 3.2: Estimations of the semi-axis lengths of ellipse-shaped targets using (3.7).

Moreover, once the geometric parameters a and b are estimated, it is straightforward to recover k and ε. Introduce

$$\mu_f^{(1)} := \frac{\tau_{N_f,1}^{\text{est}}}{\pi ab(a+b)} = \frac{k_f - 1}{a + k_f b}.$$

From

$$k_f = k + i\varepsilon f\omega_0 = \frac{1 + a\mu_f^{(1)}}{1 - b\mu_f^{(1)}},$$

one can estimate k and ε as the real and imaginary parts of k_f. However, as shown in Figure 3.11, one can see that the error on the real part is growing with the frequency. Therefore, in order to increase the robustness of the material parameter estimations, we estimate k using the lowest frequencies (for example the first three) and ε using all the frequencies:

$$k^{\text{est}} := \frac{1}{3}\sum_{f=1}^{3} \Re\left(\frac{1 + a^{\text{est}}\mu_f^{(1)}}{1 - b^{\text{est}}\mu_f^{(1)}}\right), \quad \varepsilon^{\text{est}} := \frac{1}{N_f}\sum_{f=1}^{N_f} \frac{1}{\omega_0 f} \Im\left(\frac{1 + a^{\text{est}}\mu_f^{(1)}}{1 - b^{\text{est}}\mu_f^{(1)}}\right). \tag{3.8}$$

Table 3.3 gives the material estimations using formula (3.8) for a disk and an ellipse. Once again the results are accurate. Nevertheless, for high contrasts between the real and imaginary parts of the admittivity the results of reconstruction are less satisfactory (see also Figure 3.11).

	k^{true}	$\varepsilon^{\text{true}}$	k^{est}	ε^{est}
disk	2	1	1.9167	1.0661
	3	2	2.8481	2.0516
	5	1	5.8884	1.4668
ellipse	2	1	1.7943	1.0473
	3	2	2.7208	2.0415
	5	1	6.0886	1.5828

Table 3.3: Estimations of the material parameters based on formula (3.8). The disk has radius $0,05$ and the ellipse has semi-axis lengths $0,025$ and $0,1$ and orientation angle $\pi/3$. Both targets are placed at $z_1 = 1.5(\cos(\pi/3), \sin(\pi/3))$ and then at $z_2 = (1.5\cos(\pi/3) - 1, 1.5\sin(\pi/3))$, and are illuminated with 10 frequencies equidistributed from ω_0 to $10\omega_0$ (with $\omega_0 = 1$).

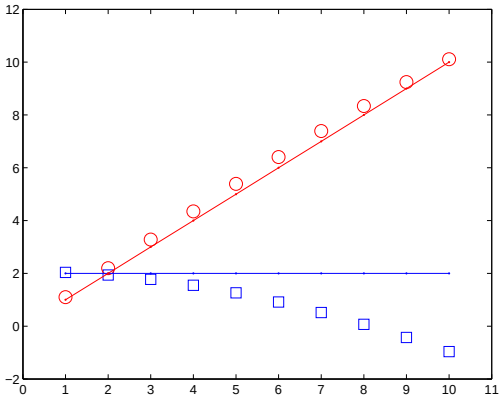

Figure 3.11: Conductivity, k^{est}, and capacitance, $f\omega_0\varepsilon^{\text{est}}$, of the reconstructed conductivity (respectively represented by squares and circles) for a disk-shaped target as functions of f (*i.e.*, the frequency). Here, $\omega_0 = 1$ and the target is with (true) material parameters $k = 2$ and $\varepsilon = 1$, radius $0,05$, and placed at $z_1 = 1.5(\cos(\pi/3), \sin(\pi/3))$ and then at $z_2 = (1.5\cos(\pi/3) - 1, 1.5\sin(\pi/3))$. The solid lines are the theoretical values.

3.4 Concluding remarks

In this chapter, we have proposed a non-iterative location search algorithm based on multi-frequency measurements. We have presented some numerical results which are promising. We have seen that increasing the number of frequencies (with not necessary different values) improves the stability. In fact, using multi-frequency measurements increases the signal-to-noise ratio. On the other hand, using different frequencies yields a faster robust location algorithm than repeating the data acquisition procedure with the same frequency. We have also proposed a procedure to reconstruct the electromagnetic parameters and the size of disk- and ellipse-shaped targets. This has been possible only because of multi-frequency measurements corresponding here to different frequency values. The use of multi-frequency measurements is fundamental in the characterization procedure. It has been known that polarization tensor for real admittivities (*i.e.* for vanishing capacitance) cannot separate the size from material properties of the target [20].

For arbitrary-shaped targets, many important questions remain. In particular, it would be interesting to know how much parameter and size information one can extract from its polarization tensors for different admittivities. A numerical answer will be provided in chapter 7, but theoretical questions remain [65]. It is also worth mentioning that limiting our asymptotic expansions with respect to the target size to the first-order term (the dipole approximation) does not give us the shape of the target. Hence, in the next chapters we will investigate how much information can be acquired in the near field by approaching the fish next to the target and developing the asymptotic expansions with high-order generalized polarization tensors [19].

It is worth mentioning that in three dimensions the model problem and the detection algorithm derived in this chapter is exactly the same as in Proposition 3.2.2, see [19].

CHAPTER 4

Extraction of Generalized Polarization Tensors

The results of this chapter have been submitted in [5] and [7].

Abstract

In order to recognize the shape of a target, we will need to develop tools that are not available in the literature. This will not only help us for the electrolocation problem, but it will also advance the more general field of mathematical imaging and numerical inverse problems. Hence, in chapters 4-6, we will take away from the electrolocation problem to go to a canonical setting in electro-sensing.

In this chapter, we will develop tools to extract, from multi-static measurements, physically relevant features called Generalized Polarization Tensors (GPTs). The system has the remarkable property that low order generalized polarization tensors are not affected by the error caused by the instability of higher orders in the presence of measurement noise. This will later enables us to identify an object thanks to a dictionary (chapter 5) and tracking it when moving (chapter 6). We will study the full-view and partial-aperture problems, since they will be important for later application on active electrolocation (chapter 7).

4.1 Introduction

With each domain and material parameter, an infinite number of tensors, called the Generalized Polarization Tensors (GPTs), is associated. The concept of GPTs was introduced in [17, 19]. The GPTs contain significant information on the shape of the domain [18]. It occurs in several interesting contexts, in particular, in low-frequency scattering [46, 19], asymptotic models of dilute composites (see [83] and [26]), in invisibility cloaking in the quasi-static regime [24] and in potential theory related to certain questions arising in hydrodynamics [89].

In fact, the GPTs are the basic building blocks for the asymptotic expansions of the boundary voltage perturbations due to the presence of small conductivity inclusions inside a conductor [53, 40, 17]. In other

words, the dipole approximation computed in section 2.4 is the first order approximation of a more general expansion involving these GPTs that will be expressed here.

The GPTs can be accurately obtained from multistatic measurements by solving a linear system. We provide here a stability analysis for the reconstruction of the GPTs in the presence of measurement noise and with respect to the aperture angle formed by the sources/receptors array. This will quantify the ill-posedness of the imaging problem.

The chapter is organized as follows. In section 4.2, we introduce a particular linear combination of the GPTs to obtain what we call the contracted GPTs (CGPTs) [24]. In Section 4.3, we investigate the reconstruction of contracted GPTs, defined in (4.14)–(4.17) below, from the multistatic response matrix of a conductivity problem. We also consider the effect of the presence of measurement noise in the MSR (subsection 4.3.2) and aperture (subsection 4.3.3) on the reconstruction of the CGPTs. Given a signal-to-noise ratio, we determine the statistical stability in the reconstruction of the CGPTs, and show that such inverse problem is exponentially unstable. This is the well-known ill-posedness of the inverse conductivity problem. Numerical results are summarized in section 4.4.

4.2 Structure of the Multistatic Response Matrix

Here we propose to reconstruct CGPTs from the multistatic response (MSR) matrix, which measures the change in potential field due to a conductivity inclusion. In this section, we present the toy model for MSR and write it in terms of the CGPTs associated to the conductivity inclusion.

In order to take into account the similarity between the EIT setting and the electrolocation problem, the notations will be quite the same as in chapter 2. We consider a two dimensional conductivity medium with uniform conductivity equal to one, except in an inclusion where the conductivity is $k > 1$; we denote by λ the contrast of this inclusion, that is, $\lambda = (k+1)/(2(k-1))$. To this point, let us remark that for application to the electrolocation problem, we will need $k \in \mathbb{C}$. This problem will be tackled in chapter 7, but for the moment we will restrict ourselves to the real case, since in this case we have much more properties (such as symmetry for example [20]). Let $D = z + \delta B = \{x = z + \delta y \mid y \in B\}$ model the conductivity inclusion. Here, B is some $\mathcal{C}^2$ and bounded domain in $\mathbb{R}^2$ whose typical length scale is of order one; z is a point in $\mathbb{R}^2$ and is taken here to be an estimation of the location of the inclusion; δ is the typical length scale of the inclusion. We refer to [19] for efficient location search algorithms and to [10] for correcting the effect of measurement noise on the localization procedure.

The MSR matrix is constructed as follows. Let $\{x_r\}_{r=1}^{N_r}$ and $\{x_s\}_{s=1}^{N_s}$ model a set of electric potential point detectors and electric point sources. We assume in this chapter that the two sets of locations coincide and $N_r = N_s = N$ (see an example in Figure 4.1). The MSR matrix $\mathbf{V}$ is an N-by-N matrix whose rs-element is the difference of electric potentials with and without the conductivity inclusions:

$$V_{rs} = u_s(x_r) - G_s(x_r), \quad r, s = 1, \dots, N. \tag{4.1}$$

Here, $G_s(x) = G(x - x_s)$ and $G(x) = \frac{1}{2\pi} \log |x|$ is the fundamental solution of the Laplace equation in $\mathbb{R}^2$, and $u_s(x)$ is the solution to the transmission problem

$$\begin{cases} \nabla \cdot (1 + (k-1)\chi_D)\nabla u_s(x) = \delta_{x_s}(x), & x \in \mathbb{R}^2 \backslash \partial D, \\ u_s(x)\big|_+ = u_s(x)\big|_-, & x \in \partial D, \\ \nu_x \cdot (\nabla u_s)\big|_+ = k\nu_x \cdot (\nabla u_s)\big|_-, & x \in \partial D, \\ u_s(x) - G_s(x) = \mathcal{O}(|x|^{-1}), & |x - x_s| \to \infty. \end{cases} \tag{4.2}$$

In the second and third equations above, the notation $\phi\big|_\pm(x)$ denotes the limit $\lim_{t \downarrow 0} \phi(x \pm t\nu_x)$, where $x \in \partial D$ and ν_x is the outward unit normal of ∂D at x.

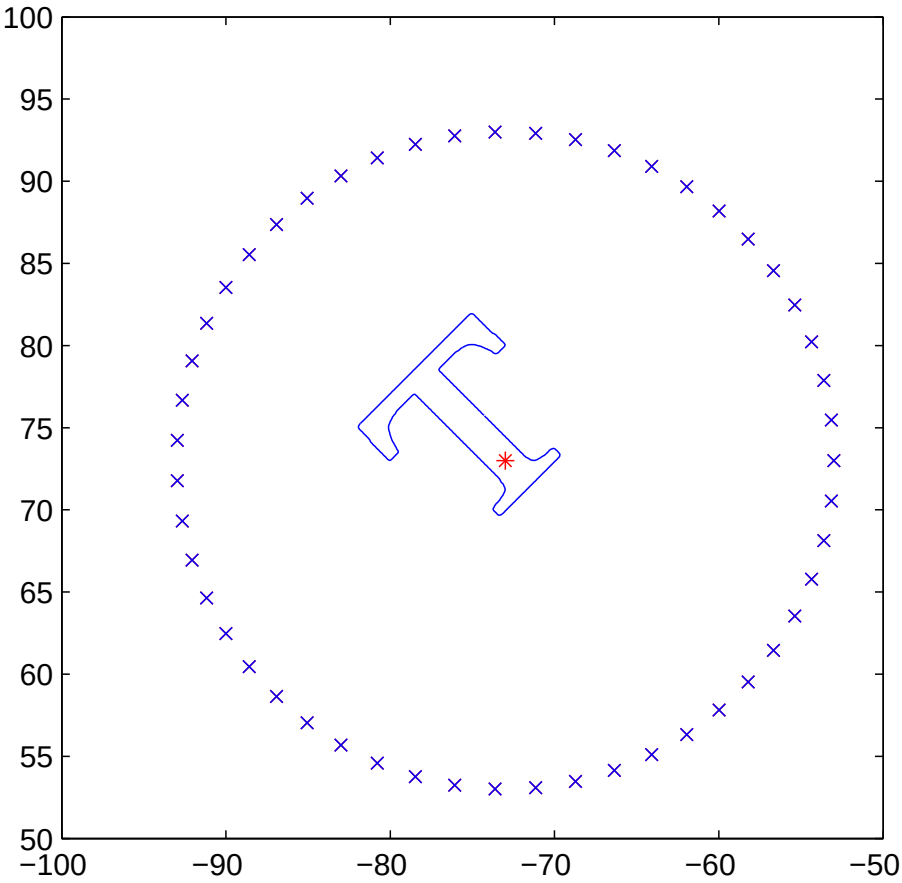

Figure 4.1: An example of configuration for MSR data simulation. Here, the unknown shape is a rotated letter "T". $N = 51$ sources/receivers marked by "x" are equally placed on a circle of radius $R = 20$ centered at $z_0 = [-73, 73]$ which is marked by "*".

Let us remark that the system (4.2) is closely related to system (2.45) of chapter 2. Indeed, here u_s is the electric potential coming from a point source at x_s whereas in system (2.45), u is the electric potential given by the sum of Dirac masses (or the dipole) denoted J_s. Hence, the difference is here that we have several sources ; as mentioned in section 3.1, this was the major difficulty in chapter 3.

4.2.1 The asymptotic expansion of the perturbed potential field

As modeled above, the MSR matrix characterizes the perturbed potential field $u_s(x_r) - G_s(x_r)$. In this section we recall, from [19], the asymptotic expansion of this perturbation and that generalize those in chapter 2.

First, let us explicit the layer potential operators (define section 2.2.4) with these new notations. Let $\mathcal{S}_D$ be the single layer potential associated with D, that is,

$$\mathcal{S}_D[\phi](x) := \int_{\partial D} G(x-y)\phi(y)ds(y), \quad x \in \mathbb{R}^2, \tag{4.3}$$

and let $\mathcal{K}_D : L^2(\partial D) \to L^2(\partial D)$ denote the Poincaré-Neumann operator

$$\mathcal{K}_D[\phi](x) := \frac{1}{2\pi} \int_{\partial D} \frac{\langle y - x, \nu_y \rangle}{|x-y|^2} \phi(y)ds(y), \quad x \in \partial D. \tag{4.4}$$

Here ν_y is the unit normal vector along the boundary at y. Relation 2.16 gives us $\mathcal{S}_D[\phi]\big|_- = \mathcal{S}_D[\phi]\big|_+$ and the jump condition

$$\frac{\partial}{\partial\nu}\mathcal{S}_D[\phi]\Big|_\pm = \left(\pm\frac{1}{2}I + \mathcal{K}_D^*\right)[\phi], \tag{4.5}$$

where $\mathcal{K}_D^*$ is the adjoint operator of $\mathcal{K}_D$; it has a similar expression as (4.4) with the numerator of the integrand replaced by $\langle x-y, \nu_x\rangle$. Using (4.5), we verify that $G_s(x) + \mathcal{S}_D[\phi_s]$ with $\phi_s \in L^2(\partial D)$ solving

$$(\lambda I - \mathcal{K}_D^*)[\phi_s] = \frac{\partial G_s}{\partial\nu}\Big|_{\partial D}, \tag{4.6}$$

is a solution to the transmission problem (4.2). In fact, this solution is unique and we conclude that

$$u_s(x) - G_s(x) = \mathcal{S}_D[\phi_s] = \int_{\partial D} G(x-y)(\lambda I - \mathcal{K}_D^*)^{-1}\left[\frac{\partial G_s}{\partial\nu}\Big|_{\partial D}\right](y)ds(y). \tag{4.7}$$

To verify the formal derivation above, we refer the reader to Section 2.4 of [19].

Throughout this section, we use Greek letters to denote double indices: $\alpha = (\alpha_1, \alpha_2) \in \mathbb{N}^2$, $\alpha! = \alpha_1!\alpha_2!$, $|\alpha| = \alpha_1 + \alpha_2$, $x^\alpha = x_1^{\alpha_1}x_2^{\alpha_2}$, and $\partial^\alpha = \partial_1^{\alpha_1}\partial_2^{\alpha_2}$, with $\partial_j = \partial/\partial x_j$.

We assume that the inclusion D and the point z is away from the sources. As a result, the functions $G(x_r - y)$ and $G_s(y)$ are smooth for $y \in \overline{D}$, and the perturbed field (4.7) is well defined. For $y \in \partial D$ and z away from x, the K-th order Taylor expansion formula with remainder e_K states

$$G(x-y) = G(x-z-(y-z)) = \sum_{|\alpha|=0}^{K}\frac{(-1)^{|\alpha|}}{\alpha!}\partial^\alpha G(x-z)(y-z)^\alpha + e_K. \tag{4.8}$$

Substitution of this expansion into (4.7) yields the following expansion of V_{rs} plus an error term denoted by E_{rs}:

$$V_{rs} = \sum_{|\alpha|,|\beta|=1}^{K}\frac{(-1)^{|\alpha|}}{\alpha!\beta!}\partial^\alpha G(x_r - z)Q_{\alpha\beta}(z)\partial^\beta G(z - x_s) + E_{rs},$$

with

$$Q_{\alpha\beta}(z) = \int_{\partial D}(y-z)^\alpha(\lambda I - \mathcal{K}_D^*)^{-1}\left[\frac{\partial}{\partial\nu}(\cdot - z)^\beta\right](y)ds(y).$$

The zeroth order term with $\beta = 0$ vanishes because the differentiation $\partial/\partial\nu$; the zeroth order term corresponding to $\alpha = 0$ vanishes because $(\lambda I - \mathcal{K}_D^*)^{-1}$ maps a zero mean value function on ∂D to another zero mean value function.

For a generic conductivity inclusion D with the contrast factor λ, the GPT of order $\alpha\beta$ associated with the inclusion is defined by [20]

$$M_{\alpha\beta}(\lambda, D) := \int_{\partial D} y^\beta(\lambda I - \mathcal{K}_D^*)^{-1}[\frac{\partial}{\partial\nu}y^\alpha]\,ds(y). \tag{4.9}$$

Using the change of variable $y - z \mapsto \tilde{y}$, the integral term $Q_{\alpha\beta}(z)$ inside the expansion of V_{rs} above can be written as

$$Q_{\alpha\beta}(z) = \int_{\partial(\delta B)}\tilde{y}^\alpha(\lambda I - \mathcal{K}_{\delta B}^*)^{-1}[\frac{\partial}{\partial\nu}\tilde{y}^\beta]\,ds(\tilde{y}), \tag{4.10}$$

which is independant of z. Moreover, by the definition of GPT, this term is $M_{\beta\alpha}(\lambda, \delta B)$. As a result, we have

$$V_{rs} = \sum_{|\alpha|,|\beta|=1}^{K}\frac{1}{\alpha!\beta!}\partial^\alpha G(z - x_s)M_{\alpha\beta}(\lambda, \delta B)\partial^\beta G(z - x_r) + E_{rs}, \tag{4.11}$$

where E_{rs} is the truncation error resulted from the finite expansion. Note also that we have switched the indices α and β.

The MSR matrix $\mathbf{V}$ consisting of $u_s(x_r) - G_s(x_r)$ depends only on the inclusion (λ, D). However, the GPTs involved in the representation (4.11) depend on the (non-unique) characterization $(z, \delta B)$ of D. We note that the remainder e_K and the truncation error E_{rs} can be evaluated; see Appendix A.1. Moreover, since the sensors and the receivers coincide, the MSR matrix is symmetric; see (A.2).

4.2.2 Expansion for MSR using contracted GPT

In this section, we further simplify the expression of MSR using the notion of contracted GPT (CGPT), which has been introduced in [24]. Using CGPT, we can write the MSR matrix $\mathbf{V}$ as a product of a CGPT matrix with coefficient matrices, which is a very convenient form for inversion.

Let $P_m(x)$ be the complex valued polynomial

$$P_m(x) = (x_1 + ix_2)^m := \sum_{|\alpha|=m} a_\alpha^m x^\alpha + i \sum_{|\beta|=m} b_\beta^m x^\beta. \tag{4.12}$$

Using polar coordinate $x = re^{i\theta}$, the above coefficients a_α^m and b_β^m can also be characterized by

$$\sum_{|\alpha|=m} a_\alpha^m x^\alpha = r^m \cos m\theta, \text{ and } \sum_{|\alpha|=m} b_\alpha^m x^\beta = r^m \sin m\theta. \tag{4.13}$$

For a generic conductivity inclusion D with contrast λ, the associated GPT $M_{\alpha\beta}(\lambda, D)$ is defined as in (4.9). The associated CGPT is the following combination of GPTs using the coefficients in (4.12):

$$M_{mn}^{cc} = \sum_{|\alpha|=m} \sum_{|\beta|=n} a_\alpha^m a_\beta^n M_{\alpha\beta}, \tag{4.14}$$

$$M_{mn}^{cs} = \sum_{|\alpha|=m} \sum_{|\beta|=n} a_\alpha^m b_\beta^n M_{\alpha\beta}, \tag{4.15}$$

$$M_{mn}^{sc} = \sum_{|\alpha|=m} \sum_{|\beta|=n} b_\alpha^m a_\beta^n M_{\alpha\beta}, \tag{4.16}$$

$$M_{mn}^{ss} = \sum_{|\alpha|=m} \sum_{|\beta|=n} b_\alpha^m b_\beta^n M_{\alpha\beta}. \tag{4.17}$$

Using the complex coordinate $x = r_x e^{i\theta_x}$, we have (see Appendix A.2) that

$$\frac{(-1)^{|\alpha|}}{\alpha!} \partial^\alpha G(x) = \frac{-1}{2\pi|\alpha|} \left[a_\alpha^{|\alpha|} \frac{\cos|\alpha|\theta_x}{r_x^{|\alpha|}} + b_\alpha^{|\alpha|} \frac{\sin|\alpha|\theta_x}{r_x^{|\alpha|}} \right]. \tag{4.18}$$

Recall that $\{x_r\}_{r=1}^N$ and $\{x_s\}_{s=1}^N$ denote the locations of the receivers and electric sources. Define R_r and θ_r so that the complex representation of $x_r - z$ is $R_r e^{i\theta_r}$ with z being the location of the target. Similarly define R_s and θ_s. Substituting formula (4.18) into the expression (4.11) of the MSR, we get

$$\begin{aligned} V_{rs} &= \sum_{|\alpha|=1,|\beta|=1}^{K} \frac{a_\alpha^{|\alpha|}\cos|\alpha|\theta_s + b_\alpha^{|\alpha|}\sin|\alpha|\theta_s}{2\pi|\alpha|R_s^{|\alpha|}} M_{\alpha\beta}(\lambda, \delta B) \frac{a_\beta^{|\beta|}\cos|\beta|\theta_r + b_\beta^{|\beta|}\sin|\beta|\theta_r}{2\pi|\beta|R_r^{|\beta|}} + E_{rs} \\ &= \sum_{m,n=1}^{K} \underbrace{\begin{pmatrix} \frac{\cos m\theta_s}{2\pi m R_s^m} & \frac{\sin m\theta_s}{2\pi m R_s^m} \end{pmatrix}}_{\mathbf{A}_{sm}} \underbrace{\begin{pmatrix} M_{mn}^{cc} & M_{mn}^{cs} \\ M_{mn}^{sc} & M_{mn}^{ss} \end{pmatrix}}_{M_{mn}} \underbrace{\begin{pmatrix} \cos n\theta_r \\ \sin n\theta_r \end{pmatrix} \frac{1}{2\pi n R_r^n}}_{(\mathbf{A}_{rn})^T} + E_{rs}. \end{aligned} \tag{4.19}$$

Here, the short-hand notations M_{mn} and $\mathbf{A}_{sm}$ represent the two-by-two and one-by-two matrices respectively, and $(\mathbf{A}_{rn})^T$ is the transpose. As m, n run from one to K, which is the truncation order of CGPT, and r, s run from one to N, which is the number of receivers (sources), these matrices build up the $2K \times 2K$ CGPT block matrix $\mathbf{M}$ and the $N \times 2K$ coefficient matrix $\mathbf{A}$ as follows:

$$\mathbf{M} = \begin{pmatrix} M_{11} & M_{12} & \cdots & M_{1K} \\ M_{21} & M_{22} & \cdots & M_{2K} \\ \cdots & \cdots & \ddots & \cdots \\ M_{K1} & M_{K2} & \cdots & M_{KK} \end{pmatrix}; \mathbf{A} = \begin{pmatrix} \mathbf{A}_{11} & \mathbf{A}_{12} & \cdots & \mathbf{A}_{1K} \\ \mathbf{A}_{21} & \mathbf{A}_{22} & \cdots & \mathbf{A}_{2K} \\ \cdots & \cdots & \ddots & \cdots \\ \mathbf{A}_{N1} & \mathbf{A}_{N2} & \cdots & \mathbf{A}_{NK} \end{pmatrix}. \tag{4.20}$$

Note that, when $K = 1$, the notation $\mathbf{M}$ coincides with the definition given in proposition 2.4.1.

Using these notations, the MSR matrix $\mathbf{V}$ can be written as

$$\mathbf{V} = \mathbf{A}\mathbf{M}\mathbf{A}^T + \mathbf{E}, \tag{4.21}$$

where $\mathbf{A}^T$ denotes the transpose of $\mathbf{A}$ and the matrix $\mathbf{E} = (E_{rs})$ represents the truncation error. We precise again that the CGPT above is for the "shifted" inclusion δB. We note also that the dimension of $\mathbf{V}$ depends on the number of sources/receivers but does not depend on the expansion order K in (4.11).

Due to the symmetry of harmonic combination of GPTs [20], the matrix $\mathbf{M}$ is symmetric. Since $\mathbf{V}$ is symmetric as shown in (A.2), the truncation error $\mathbf{E}$ is also symmetric.

4.3 Reconstruction of CGPTs and Stability Analysis

The first step in the target identification procedure is to reconstruct CGPTs from the MSR matrix $\mathbf{V}$, which has expression (4.21). Define the linear operator $L : \mathbb{R}^{2K\times 2K} \to \mathbb{R}^{N\times N}$ by

$$L(\mathbf{M}) := \mathbf{A}\mathbf{M}\mathbf{A}^T. \tag{4.22}$$

We reconstruct CGPTs as the least squares solution of the above linear system, *i.e.*,

$$\mathbf{M}^{\text{est}} = \min_{\mathbf{M}^{\text{test}} \perp \ker(L)} \|\mathbf{V} - L(\mathbf{M}^{\text{test}})\|_F, \tag{4.23}$$

where $\ker(L)$ denotes the kernel of L and $\|\cdot\|_F$ denotes the Frobenius norm of matrices [73]. In general we take N large enough so that $2K < N$. When $\mathbf{A}$ has full rank $2K$, L is rank preserving and $\ker(L)$ is trivial; in that case, the admissible set above can be replaced by $\mathbb{R}^{2K\times 2K}$ and

$$\mathbf{M}^{\text{est}} = (\mathbf{A}^T\mathbf{A})^{-1}\mathbf{A}^T\mathbf{V}\mathbf{A}(\mathbf{A}^T\mathbf{A})^{-1}.$$

From the structure of the matrix $\mathbf{A}$ in (4.20) and the expression of the MSR matrix, we observe that the contribution of a CGPT decays as its order grows. Consequently, one does not expect the inverse procedure to be stable for higher order CGPTs. The remainder of this section is devoted to such stability analysis.

4.3.1 Analytical formula in the concentric setting

To simplify the analysis, we assume that the receivers (sources) are evenly distributed along a circle of radius R centered at z. That is, $\theta_r = 2\pi r/N$, $r = 1, 2, \ldots, N$, and $R_r = R$. In this setting, we have $\mathbf{A} = \mathbf{C}\mathbf{D}$, where $\mathbf{C}$ is an $N \times 2K$ matrix constructed from the block $\mathbf{C}_{rm} = (\cos m\theta_r \ \ \sin m\theta_r)$ and $\mathbf{D}$ is

$2K \times 2K$ diagonal matrix:

$$\mathbf{C} = \begin{pmatrix} \mathbf{C}_{11} & \mathbf{C}_{12} & \cdots & \mathbf{C}_{1K} \\ \mathbf{C}_{21} & \mathbf{C}_{22} & \cdots & \mathbf{C}_{2K} \\ \cdots & \cdots & \ddots & \cdots \\ \mathbf{C}_{N1} & \mathbf{C}_{N2} & \cdots & \mathbf{C}_{NK} \end{pmatrix}; \mathbf{D} = \frac{1}{2\pi} \begin{pmatrix} \mathbf{I}_2/R & & & \\ & \mathbf{I}_2/(2R^2) & & \\ & & \ddots & \\ & & & \mathbf{I}_2/(KR^K) \end{pmatrix}. \tag{4.24}$$

Here $\mathbf{I}_2$ is the 2×2 identity matrix. We note that $\mathbf{C}$ and $\mathbf{D}$ account for the angular and radial coefficients in the expansion of MSR, respectively. The matrix $\mathbf{C}$ satisfies the following important property; see Appendix A.3.

Proposition 4.3.1. *Suppose that $2K < N$ holds. Then*

$$\mathbf{C}^T\mathbf{C} = \frac{N}{2}\mathbf{I}_{2K}. \tag{4.25}$$

Henceforth, we assume that the number of receivers is large enough so that $2K < N$. In this setting, the least squares problem (4.23) admits an analytical expression as follows.

Lemma 4.3.2. *In the above concentric setting with sufficiently many receivers,* i.e., *$2K < N$, the least squares estimation* (4.23) *is given by*

$$\mathbf{M}^{\text{est}} = (\frac{2}{N})^2\mathbf{D}^{-1}\mathbf{C}^T\mathbf{V}\mathbf{C}\mathbf{D}^{-1}. \tag{4.26}$$

Proof. Firstly, (4.25) implies that $\mathbf{A}$ has full rank, so $\ker(L) = \{0\}$. Moreover,

$$(\mathbf{A}^T\mathbf{A})^{-1} = \frac{2}{N}\mathbf{D}^{-2}.$$

Hence,

$$\mathbf{M}^{\text{est}} = (\frac{2}{N})^2\mathbf{D}^{-2}\mathbf{D}\mathbf{C}^T\mathbf{V}\mathbf{C}\mathbf{D}\mathbf{D}^{-2},$$

which yields (4.26). □

Furthermore, the reconstruction problem is exponentially ill-posed. To be more precise, we first rewrite $\mathbf{M}^{\text{est}} = Ł^{\dagger}(\mathbf{V})$, with $Ł^{\dagger}$ being the pseudo-inverse of Ł provided in this case by lemma 4.3.2 :

$$Ł^{\dagger}(\mathbf{V}) = \frac{4}{N^2}\mathbf{D}^{-1}\mathbf{C}^{\top}\mathbf{V}\mathbf{C}\mathbf{D}^{-1}. \tag{4.27}$$

Hence, the following result holds.

Proposition 4.3.3. *Let $\mathbf{e}_{ab}$ be the $2K \times 2K$ matrix whose elements are all zero but the (a,b)th element is equal to 1. In the circular and full-view setting with $N \geq 2K$, the (a,b)-th singular value of the operator L, for $a, b = 1, \ldots, 2K$, is*

$$\lambda_{ab} = N/(8\pi^2\lceil a/2\rceil\lceil b/2\rceil\rho^{\lceil a/2\rceil+\lceil b/2\rceil}), \tag{4.28}$$

with the matrix $\mathbf{e}_{ab}$ as the right singular vector, and $\mathbf{f}_{ab} = \lambda_{ab}^{-1}L(\mathbf{e}_{ab})$ as the left singular vector. In particular, the condition number of the operator L is $K^2\rho^{2(K-1)}$.

Proof. Using the fact that $\mathbf{C}^{\top}\mathbf{C} = \frac{N}{2}\mathbf{I}$, we have, for any square matrices $\mathbf{U}$ and $\mathbf{V}$,

$$\langle L(\mathbf{U}), L(\mathbf{V})\rangle = \frac{N^2}{4}\langle \mathbf{D}\mathbf{U}\mathbf{D}, \mathbf{D}\mathbf{V}\mathbf{D}\rangle, \tag{4.29}$$

where $\langle\cdot,\cdot\rangle$ is the termwise inner product. Since $\mathbf{D}$ is diagonal and invertible, we conclude that the matrix $\mathbf{e}_{ab}$ is a right singular vector of L associated to the singular value $\|L(\mathbf{e}_{ab})\|_F = \|\mathbf{D}\mathbf{e}_{ab}\mathbf{D}\|_F N/2 =$

$N/(8\pi^2\lceil a/2\rceil\lceil b/2\rceil\rho^{\lceil a/2\rceil+\lceil b/2\rceil})$. □ As a simple consequence, we have $L^\dagger(\mathbf{W})_{ab} = \lambda_{ab}^{-1}\langle \mathbf{W}, f_{ab}\rangle$. When K is sufficiently large, the truncation error $\mathbf{E}$ is $O(\rho^{-K-2})$ and can be neglected if compared to $\mathbf{W}$ [5], and then by the property of white noise

$$\sqrt{\mathbb{E}(((\mathbf{M}^{\text{est}})_{ab} - (\mathbf{M})_{ab})^2)} \lesssim \sqrt{\mathbb{E}(\left(L^\dagger(\mathbf{W})_{ab}^2\right))} = \lambda_{ab}^{-1}\sigma_{\text{noise}},$$

which is the result already established in [5]. Hence, it follows from (4.28) that the reconstruction of high order CGPTs is an ill-posed problem. Nonetheless the system has the remarkable property that low order CGPTs are not affected by the error caused by the instability of higher orders as the following proposition shows.

Proposition 4.3.4. *Let $\mathbf{M}_K$ denote the CGPTs of order up to K, and let L_K be the corresponding linear operator in* (4.19)*. Then, for any order $K_1 \le K_2 < N/2$, the submatrix of $L_{K_2}^\dagger(\mathbf{V})$ formed by the first $2K_1$ columns and rows is identical to the minimal norm solution $L_{K_1}^\dagger(\mathbf{V})$.*

Proof. Let the $N \times 2K$ matrix J_K be the row concatenation of the $2K \times 2K$ identity matrix $\mathbf{I}_{2K}$ and a zero matrix. We have $\mathbf{J}_K^\top \mathbf{J}_K = \mathbf{I}_{2K}$ and $\mathbf{J}_{K_1}^\top L_{K_2}^\dagger(\mathbf{V})\mathbf{J}_{K_1}$ is the submatrix of $L_{K_2}^\dagger(\mathbf{V})$ formed by the first $2K_1$ columns and rows. Let $\mathbf{D}_K$ and $\mathbf{C}_K$ be the matrices defined in (4.24). Because of (4.27), we have

$$\mathbf{J}_{K_1}^\top L_{K_2}^\dagger(\mathbf{V})\mathbf{J}_{K_1} = \frac{4}{N^2}\mathbf{J}_{K_1}^\top \mathbf{D}_{K_2}^{-1}\mathbf{C}_{K_2}^\top \mathbf{V}\mathbf{C}_{K_2}\mathbf{D}_{K_2}^{-1}\mathbf{J}_{K_1}.$$

One can easily see that

$$\mathbf{C}_{K_2}\mathbf{D}_{K_2}^{-1}\mathbf{J}_{K_1} = \mathbf{C}_{K_1}\mathbf{D}_{K_1}^{-1}.$$

Thus, we have

$$\mathbf{J}_{K_1}^\top L_{K_2}^\dagger(\mathbf{V})\mathbf{J}_{K_1} = L_{K_1}^\dagger(\mathbf{V}).$$

□ Numerically, $L^\dagger$ can be implemented through either the formula (4.27) or the Conjugated Gradient (CG) method using (4.23). Simulations in section 4.4 confirm that in typical situations, say, with $K = 5$ and 10% noise, the reconstructed CGPT is sufficiently accurate for a task such as identification of a target in a dictionary (performed then in chapter 5), or tracking (chapter 6).

4.3.2 Measurement noise and stability analysis

We develop in this subsection a stability analysis for the least squares reconstruction of CGPT from the MSR matrix, in the setting of concentric receivers (sources).

Counting some additive measurement noise, we modify the expression of MSR to

$$\mathbf{V} = \mathbf{C}\mathbf{D}\mathbf{M}\mathbf{D}\mathbf{C}^T + \mathbf{E} + \zeta\mathbf{W}. \tag{4.30}$$

Here, $\mathbf{E}$ is the truncation error due to the finite order K in expansion (4.11), $\mathbf{W}$ is an $N \times N$ real valued random matrix with independent and identically Gaussian entries with mean zero and unit variance, and ζ is a small positive number modeling the standard deviation of the noise.

Recall that the unknown $\mathbf{M}$ consists of CGPTs of order up to K of the relative domain $\delta B = D - z$, where δ denote the typical length scale of the domain D. The receivers and sources are located along a circle of radius R centered at z. Let $\rho = \delta/R$ be the ratio between the two scales, and it is assumed to be smaller than one. Due to the scaling property of CGPT (see (5.3), shown in the next chapter), the entries of the CGPT block $\mathbf{M}_{mn}(\delta B)$ is $\delta^{m+n}\mathbf{M}_{mn}(B)$. Consequently, the size of $\mathbf{V}$ itself is of order ρ^2, which is the order of the first term in the expansion (4.19). The truncation error $\mathbf{E}$ is of order ρ^{K+2}; see Appendix A.1.

According to the above analysis, we assume that the size of the noise satisfies

$$N\rho^{K+2} \ll \zeta \ll \rho^2. \tag{4.31}$$

This is the regime where the measurement noise is much smaller than the signal but much larger than the truncation error. The presence of N in (4.31) will be clear later; see remark 4.3.6. We define the signal-to-noise ratio (SNR) to be

$$\mathrm{SNR} = \frac{\rho^2}{\zeta}.$$

We will investigate the error made by the least squares estimation of the CGPT matrix, in particular the manner of its growth with respect to the order of the CGPTs. Given a SNR and a tolerance number τ_0, we can define the resolving order m_0 to be

$$m_0 = \min\left\{1 \le m \le K \ : \ \sqrt{\frac{\mathbb{E}\|\mathbf{M}^{\mathrm{est}}_{mm} - \mathbf{M}_{mm}\|_F^2}{\|\mathbf{M}_{mm}\|_F^2}} \le \tau_0\right\}. \tag{4.32}$$

We are interested in the growth of m_0 with respect to SNR.

We have used the notation $\mathbf{M}_{mn}$, $m, n = 1, \dots, K$, to denote the building block of the CGPT matrix $\mathbf{M}$ in (4.20). In the following, we also use the notation $(\mathbf{M})_{jk}$, $j, k = 1, \dots, 2K$, to denote the real valued entries of the CGPT matrix.

Theorem 4.3.5. *Assume that the condition of Lemma 4.3.2 holds; assume also that the additive noise is in the regime* (4.31)*, Then for j, k so that $(\mathbf{M})_{jk}$ is non-zero, the relative error in its reconstructed CGPT satisfies*

$$\sqrt{\frac{\mathbb{E}|(\mathbf{M}^{\mathrm{est}})_{jk} - (\mathbf{M})_{jk}|^2}{|(\mathbf{M})_{jk}|^2}} \le C\frac{\zeta}{N}\rho^{-\lceil j/2\rceil - \lceil k/2\rceil}\left\lceil\frac{j}{2}\right\rceil\left\lceil\frac{k}{2}\right\rceil. \tag{4.33}$$

Here, the symbol $\lceil l\rceil$ is the smallest natural number larger than or equal to l. For vanishing $(\mathbf{M})_{jk}$, the error $\sqrt{\mathbb{E}|(\mathbf{M}^{\mathrm{est}})_{jk} - (\mathbf{M})_{jk}|^2}$ can be bounded by the right-hand side above with ρ replaced by R^{-1}. In particular, the resolving order m_0 satisfies

$$(m_0\rho^{1-m_0})^2 \simeq \tau_0\mathrm{SNR}, \tag{4.34}$$

where τ_0 is the tolerance number.

Proof. From the analytical formula of the least squares reconstruction (4.26) and the expression of $\mathbf{V}$ (4.30), we see that for each fixed $j, k = 1, \dots, 2K$,

$$(\mathbf{M}^{\mathrm{est}} - \mathbf{M})_{jk} = \frac{2^2\zeta}{N^2}(\mathbf{D}^{-1}\mathbf{C}^T\mathbf{W}\mathbf{C}\mathbf{D}^{-1})_{jk} + \frac{2^2}{N^2}(\mathbf{D}^{-1}\mathbf{C}^T\mathbf{E}\mathbf{C}\mathbf{D}^{-1})_{jk}.$$

Let us denote these two terms by $\mathcal{I}_{jk1}$ and $\mathcal{I}_{jk2}$ respectively. For the first term, define $\widetilde{\mathbf{W}}$ to be $(\sqrt{2/N}\mathbf{C})^T\mathbf{W}(\sqrt{2/N}\mathbf{C})$, which is an $N \times N$ random matrix. Due to the orthogonality (4.25), $\widetilde{\mathbf{W}}$ remains to have mean zero Gaussian entries with unit variance. Because $\mathbf{D}$ is diagonal, we have for each $j, k = 1, \dots, 2K$,

$$\mathbb{E}(\mathcal{I}_{jk1})^2 = \frac{2^2\sigma^2_{\mathrm{noise}}}{N^2}(\mathbf{D}_{jj})^{-2}\mathbb{E}|\widetilde{\mathbf{W}}_{jk}|^2(\mathbf{D}_{kk})^{-2} = \frac{2^6\pi^4\sigma^2_{\mathrm{noise}}}{N^2}R^{2(\lceil j/2\rceil + \lceil k/2\rceil)}\left\lceil\frac{j}{2}\right\rceil^2\left\lceil\frac{k}{2}\right\rceil^2.$$

Note that $\lceil j/2\rceil\lceil k/2\rceil$ is the order of CGPT element $(\mathbf{M})_{jk}$; see (4.20). It is known that $(\mathbf{M})_{jk}(\delta B) = \delta^{\lceil j/2\rceil + \lceil k/2\rceil}(\mathbf{M})_{jk}(B)$. When this term is non-zero, it is of order $\delta^{\lceil j/2\rceil + \lceil k/2\rceil}$. This fact and the above control of $\mathcal{I}_{jk1}$ show that $\sqrt{\mathbb{E}|\mathcal{I}_{jk1}|^2/|(\mathbf{M})_{jk}|^2}$ satisfies the estimate in (4.33).

For the second term, since $\mathbf{E}$ is symmetric, it has the decomposition $\mathbf{E} = \mathbf{P}^T\mathcal{E}\mathbf{P}$, where $\mathbf{P}$ is an $N \times N$ orthonormal matrix, and $\mathcal{E}$ is an $N \times N$ diagonal matrix consisting of eigenvalues of $\mathbf{E}$. Then $(\sqrt{2/N}\mathbf{C})^T\mathbf{E}(\sqrt{2/N}\mathbf{C})$ can be written as $\mathbf{Q}^T\mathcal{E}\mathbf{Q}$ where $\mathbf{Q} = \sqrt{2/N}\mathbf{P}\mathbf{C}$ is an $N \times 2K$ matrix satisfying $\mathbf{Q}^T\mathbf{Q} = \mathbf{I}_{2K}$. Then the calculation for $\mathcal{I}_{jk1}$ shows that

$$(\mathcal{I}_{jk2})^2 = \frac{2^6\pi^4}{N^2}R^{2(\lceil j/2\rceil+\lceil k/2\rceil)}\left\lceil\frac{j}{2}\right\rceil^2\left\lceil\frac{k}{2}\right\rceil^2\left(\sum_{l=1}^{N}\mathcal{E}_{ll}\mathbf{Q}_{jl}^T\mathbf{Q}_{lk}\right)^2.$$

Since $\mathbf{E}$ is of order ρ^{K+2} as shown in (A.1), the sum is of order $N\rho^{K+2}$. Therefore, we have

$$\sqrt{\mathbb{E}|\mathcal{I}_{jk2}|^2} \leq C\rho^{K+2-\lceil j/2\rceil-\lceil k/2\rceil}\lceil\frac{j}{2}\rceil\lceil\frac{k}{2}\rceil.$$

Since we assumed that (4.31) holds, this error is dominated by the one due to the noise. Hence, (4.33) is proved.

For diagonal blocks $\mathbf{M}_{mm}$, their Frobenius norms do not vanish and (4.32) is well defined. In particular, (4.33) applied to the case $j, k = 2m-1, 2m$, shows that the relative error made in the block $\mathbf{M}_{mm}$ is of order $\zeta m^2\rho^{-2m}$. Using the definition of SNR, we verify (4.34). □

Remark 4.3.6. If $\mathbf{E}$ has only several (of order one) non-zero eigenvalues, then the preceding calculation shows that $(\mathcal{I}_{jk2})^2 \leq C\rho^{2(K+2)}$ and condition (4.31) can be replaced with $\rho^{K+2} \ll \zeta \ll \rho^2$.

4.3.3 CGPT reconstruction in the limited-view setting

In this section we study the stability of CGPTs reconstruction problem in the case $0 < \gamma < 2\pi$, always under the condition that $N > 2K$, *i.e.*, the number of sources/receivers is two times larger than the highest order of CGPTs to be reconstructed. Unlike in the full-view case, here $\mathbf{C}$ is no longer orthogonal in general, nonetheless one can still establish the SVD of L similarly as in Proposition 4.3.3.

Proposition 4.3.7. *Consider the concentric and limited-view setting with $N \geq 2K$, and suppose that $\mathbf{C}$ is of maximal rank. Let $\{\mu_n\}$ be the n-th largest eigenvalue of the matrix $\mathbf{D}\mathbf{C}^\top\mathbf{C}\mathbf{D}$ and let $\{v_n\}$ be the associated orthonormal eigenvector. Then the (a,b)-th singular value of the operator L is $\lambda_{ab} = \sqrt{\mu_a\mu_b}$, with the associated left singular vector the matrix $\mathbf{g}_{ab} = v_a v_b^\top$. In particular, the condition number of the operator L is*

$$\mathrm{cond}(L) = \mathrm{cond}(\mathbf{D}\mathbf{C}^\top\mathbf{C}\mathbf{D}) \leq \mathrm{cond}(\mathbf{C})^2K^2\rho^{2(K-1)}, \tag{4.35}$$

with $\mathrm{cond}(\mathbf{C})$ *being the condition number of the matrix $\mathbf{C}$.*

Proof. We first note that for any matrices $\mathbf{U}, \mathbf{V}$ we have:

$$\langle L(\mathbf{U}), L(\mathbf{V})\rangle = \langle \mathbf{U}, (\mathbf{D}\mathbf{C}^\top\mathbf{C}\mathbf{D})\mathbf{V}(\mathbf{D}\mathbf{C}^\top\mathbf{C}\mathbf{D})\rangle.$$

Taking $\mathbf{g}_{ab} = v_a v_b^\top$, and $\mathbf{g}_{a'b'} = v_{a'}v_{b'}^\top$, we get

$$\begin{aligned}\langle L(\mathbf{g}_{ab}), L(\mathbf{g}_{a'b'})\rangle &= \mu_{a'}\langle v_a v_b^\top, v_{a'}v_{b'}^\top(\mathbf{D}\mathbf{C}^\top\mathbf{C}\mathbf{D})\rangle = \mu_{a'}\mu_{b'}\langle v_a v_b^\top, v_{a'}v_{b'}^\top\rangle \\ &= \delta_{aa'}\delta_{bb'}\mu_a\mu_b,\end{aligned}$$

where $\delta_{aa'}$ is the Kronecker's symbol, which implies that $\|L(\mathbf{g}_{ab})\|_F = \sqrt{\mu_a\mu_b}$ is the (a,b)-th singular value of L. If we denote by $\rho_{\max}(\cdot)$ and $\rho_{\min}(\cdot)$ the maximal and the minimal singular values of a matrix, then

$$\begin{aligned}\rho_{\max}(\mathbf{D}\mathbf{C}^\top\mathbf{C}\mathbf{D}) = \rho_{\max}(\mathbf{C}\mathbf{D})^2 \leq \rho_{\max}(\mathbf{C})^2\rho_{\max}(\mathbf{D})^2, \\ \rho_{\min}(\mathbf{D}\mathbf{C}^\top\mathbf{C}\mathbf{D}) = \rho_{\min}(\mathbf{C}\mathbf{D})^2 \geq \rho_{\min}(\mathbf{C})^2\rho_{\min}(\mathbf{D})^2,\end{aligned}$$

and the condition number of L is therefore bounded by $\mathrm{cond}(\mathbf{C})^2K^2\rho^{2(K-1)}$. □

Injectivity of C

We denote by V_K the vector space of functions of the form

$$f(\theta) = \sum_{k=-K}^{K} c_k e^{ik\theta}, \tag{4.36}$$

with $c_k \in \mathbb{C}$, and V_K^0 the subspace of V_K such that $c_0 = 0$. Functions of V_K^0 can be written as

$$f(\theta) = \sum_{k=1}^{K} \alpha_k \cos(k\theta) + \beta_k \sin(k\theta), \tag{4.37}$$

with $\alpha_k, \beta_k \in \mathbb{C}$. Observe that taking discrete samples of (4.37) at $\theta_s = \gamma s/N$ is nothing but applying the matrix $\mathbf{C}$ on a coefficient vector $(\alpha_1, \beta_1 \dots \alpha_K, \beta_K)$. We have the following result.

Proposition 4.3.8. *For any $N \geq 2K$, the matrix $\mathbf{C}$ is of maximal rank.*

Proof. Multiplying $f \in V_K^0$ in (4.36) by $e^{iK\theta}$, and using the fact that $c_0 = 0$, we have

$$\begin{aligned} e^{iK\theta} f(\theta) &= \sum_{k=0}^{K-1} c_{k-K} e^{ik\theta} + \sum_{k=K+1}^{2K} c_{k-K} e^{ik\theta} \\ &= \sum_{k=0}^{K-1} c_{k-K} e^{ik\theta} + \sum_{k=K}^{2K-1} e^{i\theta} c_{k+1-K} e^{ik\theta} = \sum_{k=0}^{2K-1} \tilde{c}_k e^{ik\theta}, \end{aligned} \tag{4.38}$$

where $\tilde{c}_k = c_{k-K}$ for $k = 0, \dots, K-1$, and $\tilde{c}_k = e^{i\theta} c_{k+1-K}$ for $k = K, \dots, 2K-1$. The N vectors $v_s := (e^{ik\theta_s})_{k=0\dots 2K-1}$ are linearly independent since they are the first $2K \leq N$ rows of a $N \times N$ Vandermonde matrix. Therefore, $f(\theta_s) = 0$ for $s = 1 \dots N$ implies that $\tilde{c}_k = 0$ for all $k = 0, \dots, 2K-1$, which means that $\mathbf{C}$ is of maximal rank. □

Consequently, for arbitrary range $0 < \gamma \leq 2\pi$, a sufficient condition to uniquely determine the CGPTs of order up to K is to have $N \geq 2K$ sources/receivers.

Explicit left inverse of C

We denote by $D_K(\theta)$ the Dirichlet kernel of order K:

$$D_K(\theta) = \sum_{k=-K}^{K} e^{ik\theta} = \frac{\sin((K+1/2)\theta)}{\sin(\theta/2)}. \tag{4.39}$$

We state without proof the following well known result about V_K [119].

Lemma 4.3.9. *The functions $\{D_K(\theta - \frac{2\pi n}{2K+1})\}_{n=0,\dots,2K}$ is an orthogonal basis of V_K. For any $f, g \in V_K$, the following identity holds:*

$$\frac{1}{2\pi} \int_0^{2\pi} f(\theta) g^*(\theta) d\theta = \frac{1}{2K+1} \sum_{n=1}^{2K+1} f\left(\frac{2\pi n}{2K+1}\right) g\left(\frac{2\pi n}{2K+1}\right), \tag{4.40}$$

where * denotes the complex conjugate. In particular, we have for $n = 0, \dots, 2K$

$$\frac{1}{2\pi} \int_0^{2\pi} f(\theta) D_K\left(\theta - \frac{2\pi n}{2K+1}\right) d\theta = f\left(\frac{2\pi n}{2K+1}\right). \tag{4.41}$$

Lemma 4.3.10. *Given a set of $N > 2K$ different points $0 < \theta_1 < \ldots < \theta_N \leq 2\pi$, there exist interpolation kernels $h_s \in V_{\lfloor N/2 \rfloor}$ for $s = 1 \ldots N$, such that:*

$$f(\theta) = \sum_{s=1}^{N} f(\theta_s) h_s(\theta) \quad \textit{for any } f \in V_K. \tag{4.42}$$

Proof. When the number of points N is odd, it is well known [119] that h_s takes the form

$$h_s(\theta) = \prod_{t=1, t\neq s}^{N} \frac{\sin\left(\frac{\theta-\theta_t}{2}\right)}{\sin\left(\frac{\theta_s-\theta_t}{2}\right)}. \tag{4.43}$$

When N is even, by a result established in [81]

$$h_s(\theta) = \cos\left(\frac{\theta-\theta_s}{2}\right) \prod_{t=1, t\neq s}^{N} \frac{\sin\left(\frac{\theta-\theta_t}{2}\right)}{\sin\left(\frac{\theta_s-\theta_t}{2}\right)}. \tag{4.44}$$

It is easy to see that in both cases h_s belongs to $V_{\lfloor N/2 \rfloor}$. □

Now we can find explicitly a left inverse for $\mathbf{C}$.

Proposition 4.3.11. *Under the same condition as in Lemma 4.3.10, we denote by h_s the interpolation kernel and define the matrix $\tilde{\mathbf{C}} = (\tilde{\mathbf{C}}_{ks})_{k,s}$ as*

$$\tilde{\mathbf{C}}_{2k-1,s} = \frac{1}{\pi} \int_0^{2\pi} h_s(\theta) \cos(k\theta) d\theta, \quad \tilde{\mathbf{C}}_{2k,s} = \frac{1}{\pi} \int_0^{2\pi} h_s(\theta) \sin(k\theta) d\theta. \tag{4.45}$$

Then $\tilde{\mathbf{C}}\mathbf{C} = \mathbf{I}$. In particular, if N is odd, the matrix $\tilde{\mathbf{C}}$ can be calculated as

$$\tilde{\mathbf{C}}_{2k-1,s} = \frac{2}{N} \sum_{n=1}^{N} h_s\left(\frac{2\pi n}{N}\right) \cos\left(\frac{2\pi k n}{N}\right), \quad \tilde{\mathbf{C}}_{2k,s} = \frac{2}{N} \sum_{n=1}^{N} h_s\left(\frac{2\pi n}{N}\right) \sin\left(\frac{2\pi k n}{N}\right). \tag{4.46}$$

Proof. Given $v = (\alpha_1, \beta_1 \ldots \alpha_K, \beta_K) \in \mathbb{C}^{2K}$, and f the associated function defined by (4.37), we have $(\mathbf{C}v)_n = f(\theta_n)$ for $n = 1, \ldots, N$. Using (4.42) and (4.45), we find that

$$(\tilde{\mathbf{C}}\mathbf{C}v)_{2k-1} = \frac{1}{\pi} \int_0^{2\pi} f(\theta) \cos(k\theta) d\theta = \alpha_k, \tag{4.47}$$

$$(\tilde{\mathbf{C}}\mathbf{C}v)_{2k} = \frac{1}{\pi} \int_0^{2\pi} f(\theta) \sin(k\theta) d\theta = \beta_k, \tag{4.48}$$

and therefore, $\tilde{\mathbf{C}}\mathbf{C}v = v$. Observe that $h_s(\theta)$, $\cos(k\theta)$, and $\sin(k\theta)$ all belong to $V_{\lfloor N/2 \rfloor}$, so when N is odd, we easily deduce (4.46) using (4.40). □

Remark 4.3.1. In general, the left inverse $\tilde{\mathbf{C}}$ in (4.45) is not the pseudo-inverse of $\mathbf{C}$, and by definition, we have $\mathbf{C}^\dagger = \tilde{\mathbf{C}}$ if $\mathbf{C}\tilde{\mathbf{C}}$ is symmetric. If $P_{V_K^0}(h_s)$ is the orthogonal projection of h_n onto V_K^0, *i.e.*,

$$P_{V_K^0}(h_s)(\theta) = \sum_{k=1}^{K} \tilde{\mathbf{C}}_{2k-1,s} \cos(k\theta) + \tilde{\mathbf{C}}_{2k,s} \sin(k\theta), \tag{4.49}$$

then, $P_{V_K^0}(h_s)(\theta_t) = (\mathbf{C}\tilde{\mathbf{C}})_{st}$. Therefore, $\tilde{\mathbf{C}}$ is the pseudo-inverse of $\mathbf{C}$ if and only if the interpolation kernel h_s satisfies:

$$P_{V_K^0}(h_s)(\theta_t) = P_{V_K^0}(h_t)(\theta_s), \quad \text{for } s, t = 1 \ldots N. \tag{4.50}$$

Remark 4.3.12. Proposition 4.3.11 can be used in the noiseless limited-view case to reconstruct the CGPT matrix $\mathbf{M}$ from the MSR measurements $\mathbf{V}$. In fact, from (4.22) it immediately follows that

$$\mathbf{M} = \mathbf{D}^{-1}\tilde{\mathbf{C}}\mathbf{V}\tilde{\mathbf{C}}^{\top}\mathbf{D}^{-1}.$$

This shows that in the noiseless case, the limited-view aspect has no effect on the reconstruction of the GPTs, and consequently on the location and orientation tracking. In the presence of noise, the effect, as will be shown in the next subsection, is dramatic. A small amount of measurement noise significantly changes the performance of our algorithm unless the arrays of receivers and transmitters offer a directional diversity, see Figure 6.3.

Ill-posedness in the limited-view setting

We undertake a numerical study to illustrate the ill-posedness of the linear system (4.30) in the case of limited-view data. Figure 4.2 shows the distribution of eigenvalues of the matrix $\mathbf{C}^{\top}\mathbf{C}$ and $\mathbf{D}\mathbf{C}^{\top}\mathbf{C}\mathbf{D}$ at different values of γ with $N = 101$ and $K = 50$. In Figure 4.3, we calculate the condition number of $\mathbf{C}^{\top}\mathbf{C}$ and L (which is equal to that of $\mathbf{D}\mathbf{C}^{\top}\mathbf{C}\mathbf{D}$ by (4.35)) for different orders K. From these results, we see clearly the effect of the limited-view aspect. First, the tail of tiny eigenvalues in Figure 4.2.(a) suggests that the matrix $\mathbf{C}^{\top}\mathbf{C}$ is numerically singular, despite the fact that $\mathbf{C}$ is of maximal rank. Secondly, both $\mathbf{C}^{\top}\mathbf{C}$ and L rapidly become extremely ill-conditioned as K increases, so the maximum resolving order of CGPTs is very limited. Furthermore, this limit is intrinsic to the angle of view and cannot be improved by increasing the number of sources/receivers, see Figure 4.3 (c) and (d).

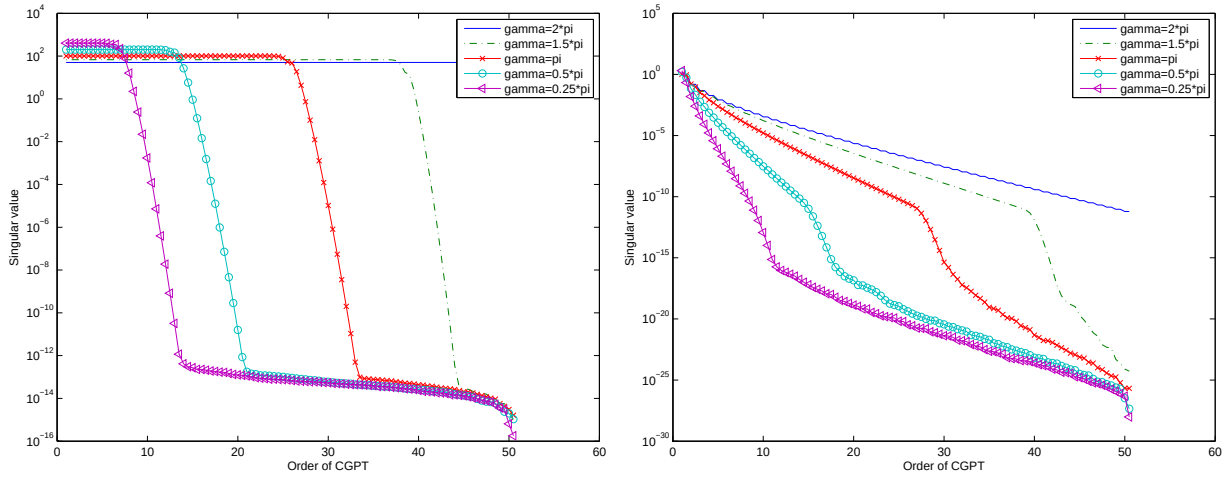

(a) Eigenvalues of $\mathbf{C}^{\top}\mathbf{C}$

(b) Eigenvalues of $\mathbf{D}\mathbf{C}^{\top}\mathbf{C}\mathbf{D}$

Figure 4.2: Distribution of eigenvalues (in log scale) of the matrix $\mathbf{C}^{\top}\mathbf{C}$ (a) and $\mathbf{D}\mathbf{C}^{\top}\mathbf{C}\mathbf{D}$ (b). $N = 101$ sources are equally spaced between $[0, \gamma)$ on a circle of radius $\rho = 1.2$, and $K = 50$. Each curve corresponds to a different value of γ. The matrix $\mathbf{C}^{\top}\mathbf{C}$ and $\mathbf{D}\mathbf{C}^{\top}\mathbf{C}\mathbf{D}$ are calculated from these parameters and their eigenvalues are sorted in decreasing order.

4.4 Numerical Results

In this section we present a variety of numerical results on the theoretical framework discussed in this chapter with noisy MSR measurements. Given a shape D_0 of characteristic size δ, the procedure of our numerical experiment can be summarized as follows:

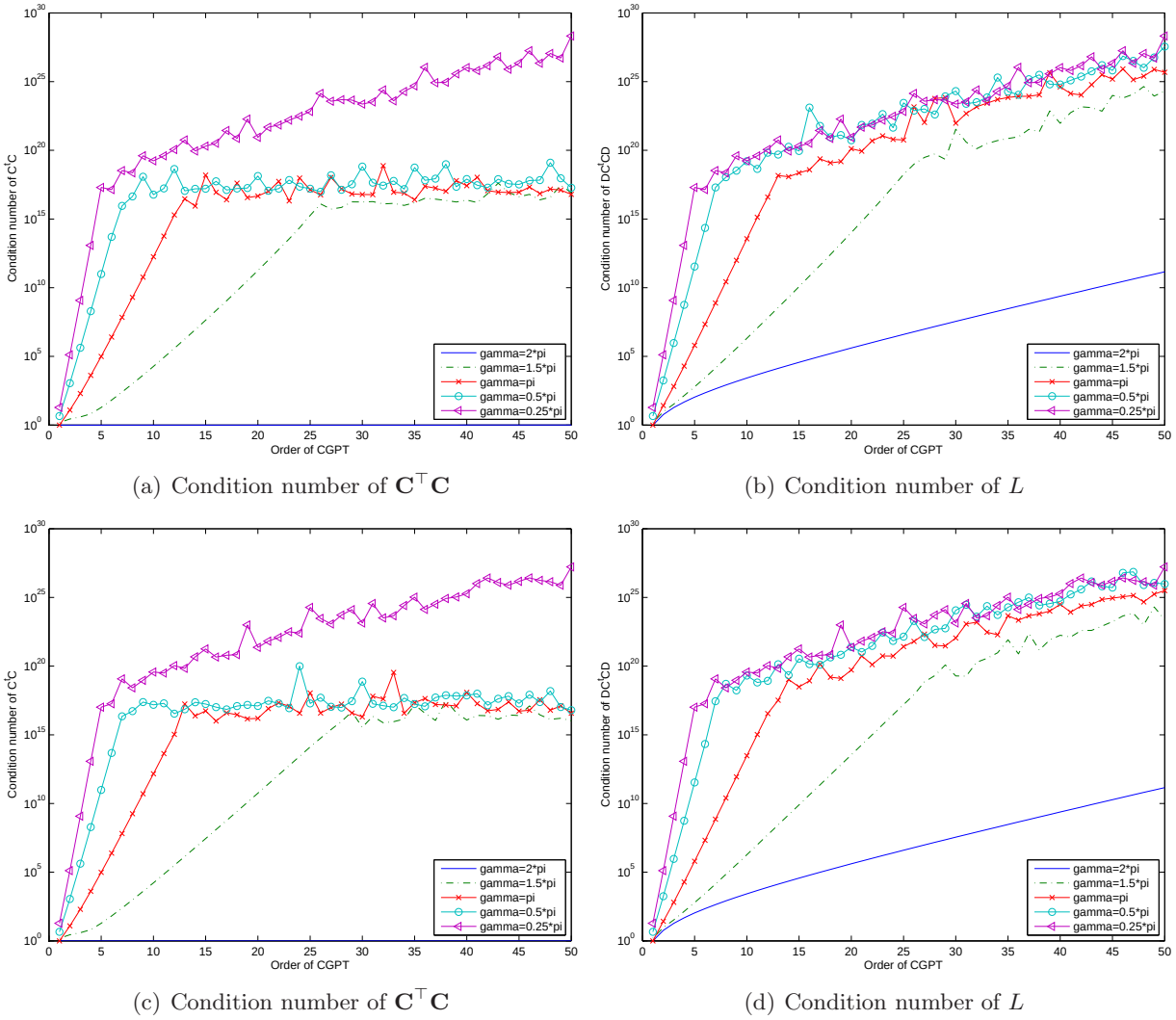

(a) Condition number of $\mathbf{C}^\top\mathbf{C}$

(b) Condition number of L

(c) Condition number of $\mathbf{C}^\top\mathbf{C}$

(d) Condition number of L

Figure 4.3: Condition numbers (in log scale) of the matrix $\mathbf{C}^\top\mathbf{C}$ (a) and the operator L (b) for different orders K between $[1, 50]$. As in Figure 4.2, $N = 101$ sources are equally spaced between $[0, \gamma)$ on a circle of radius $\rho = 1.2$. Figure(c) and (d) are the same experiment as Figure(a) and (b) but with $N = 1001$.

1. Data simulation. N sources (and also receivers) are equally distributed on a circle of radius R, which is centered at an arbitrary point $z_0 \in D_0$ and includes D_0, see Figure 4.4. The MSR matrix is obtained by evaluating numerically its integral expression (4.7) then adding a white noise of variance ζ^2. For simplicity, here we suppose that the reference point $z_0 \in D_0$ can be estimated by means of algorithms such as MUSIC (standing for MUltiple SIgnal Classification) [10, 20].

2. Reconstruction of the CGPTs of $D = D_0 - z_0$ using formula (4.26) or the least squares algorithm (4.23).

We emphasize that the reconstructed CGPTs of shape D depend on the reference point z_0. We fix the conductivity parameter $k = 4/3$ throughout this section.

4.4.1 Reconstruction of CGPTs

The theoretical analysis presented in section 4.3 suggests the following two steps method for the reconstruction of CGPTs. First we apply (4.26) (or equivalently solve the least squares problem (4.23)) by fixing

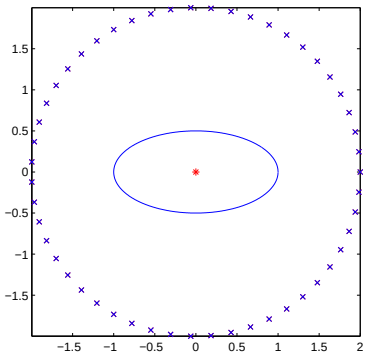

Figure 4.4: An example of the configuration for MSR data simulation. The unknown shape is an ellipse whose long and short axes are 2 and 1, respectively. $N = 51$ sources/receivers (marked by "x") are equally placed on a circle of radius $R = 2$ centered at $z_0 = [0, 0]$ (marked by "*").

the truncation order K as in (4.31):

$$K \leq \min\left(\frac{\log(\zeta/N)}{\log\rho} - 2, N/2\right). \tag{4.51}$$

Then, we keep only the first m_0 orders in the reconstructed CGPTs, with m_0 being the resolving order deduced from estimation (4.34):

$$m_0 = \frac{\log\zeta - \log\tau_0}{2\log\rho}, \tag{4.52}$$

and $\tau_0 \leq 1$ is the tolerance number introduced in (4.32). In all our numerical experiments we set the noise level ζ to:

$$\zeta = (\mathbf{V}_{\max} - \mathbf{V}_{\min})\sigma_0, \tag{4.53}$$

with a positive constant σ_0 and $\mathbf{V}_{\max}$ and $\mathbf{V}_{\min}$ being the maximal and the minimal coefficient in the MSR matrix $\mathbf{V}$. Using the configuration given in Figure 4.4 and for various noise level, we reconstruct the CGPTs of the ellipse up to a truncation order K which is determined as in (4.51). For each $k \leq K$, the relative error of the first k-th order reconstructed CGPTs is evaluated by comparing with their theoretical value ([20, Proposition 4.7]). The results are shown in Figure 4.5. In Figure 4.6 we plot the resolving order m_0 given by (4.52) and the relative error of the reconstruction within this order, for σ_0 in the range $[10^{-3}, 1]$.

4.4.2 Partial View Setting

The analysis performed in subsection 4.3.3 suggests that the least-squares problem (4.23) is not adapted to the CGPT reconstruction in a limited-view setting. Actually, the truncation error or the noise of measurement will be amplified by the tiny singular values of L, and yields extremely instable reconstruction of high-order CGPTs, *e.g.*, $K \geq 2$. Instead, we use Thikhonov regularization and propose to solve

$$\min_{\mathbf{M}} \|L(\mathbf{M}) - \mathbf{V}\|_F^2 + \mu\|\mathbf{M}\|_F^2, \tag{4.54}$$

with $\mu > 0$ a small regularization constant. It is well known that the effect of the regularization term is to truncate those singular values of L smaller than μ, which consequently stabilizes the solution. The optimal

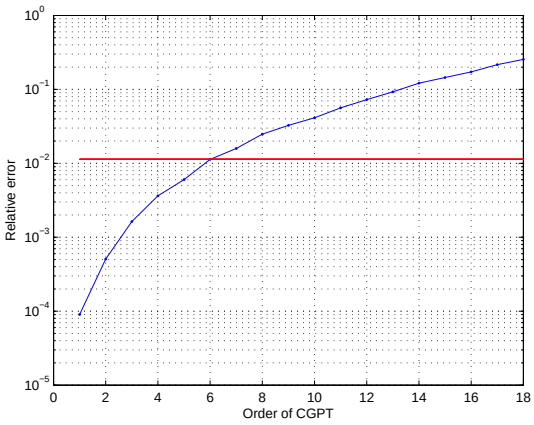

(a) $\sigma_0 = 0.01, m_0 = 6$

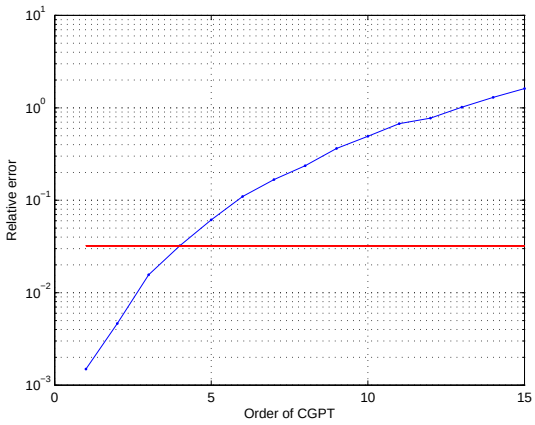

(b) $\sigma_0 = 0.1, m_0 = 4$

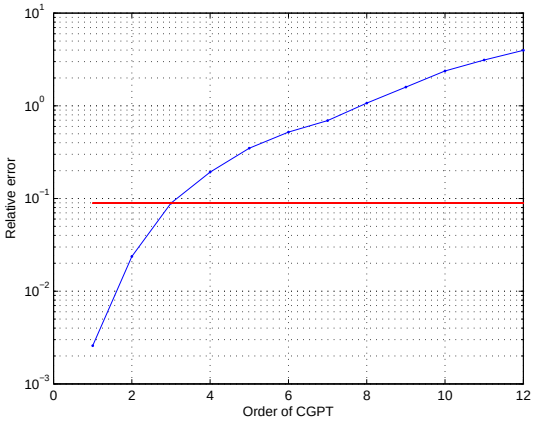

(c) $\sigma_0 = 0.5, m_0 = 3$

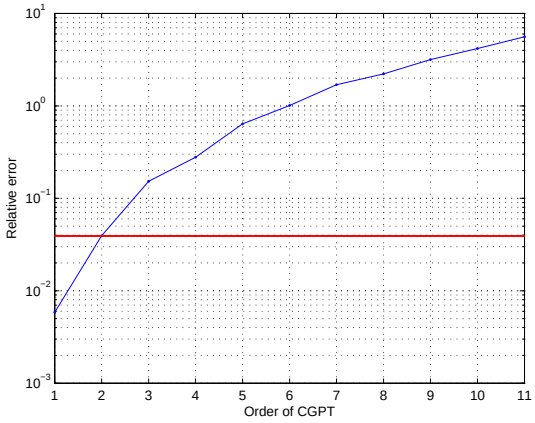

(d) $\sigma_0 = 1.0, m_0 = 2$

Figure 4.5: Relative error of the reconstructed CGPTs. For each noise level, we repeat the experiment 100 times (corresponding to 100 realizations of the noise) and the reconstruction is taken as their mean value. The horizontal solid line in each figure indicates the resolving order m_0 given by (4.52) with the tolerance number $\tau_0 = 10^{-1}$.

choice of μ depends on the noise level, and here we determine it from the range $[10^{-6}, 10^{-1}]$ by comparing the solution of (4.54) with the true CGPTs.

Here we reconstruct the CGPTs of an ellipse with the parameter $N = 101, K = 50$, and γ varying between 0 and 2π. The major and minor axis of the ellipse are 1 and 0.5 respectively. In Figure 4.7 we show the error of the first 2 order CGPTs reconstructed through (4.54) and (4.23) at three different noise levels. It can be seen that, for small γ, the error obtained by (4.54) is substantially smaller.

4.5 Conclusion

In this chapter, we have proposed a general framework for extraction of GPTs from multi-static measurements. From a least-squares formulation, we are able to extract those tensors from multi-static measurements. We have analyzed the stbility of our algorithms with respect to measurement noise, in the cases of full-view and partial-view setting.

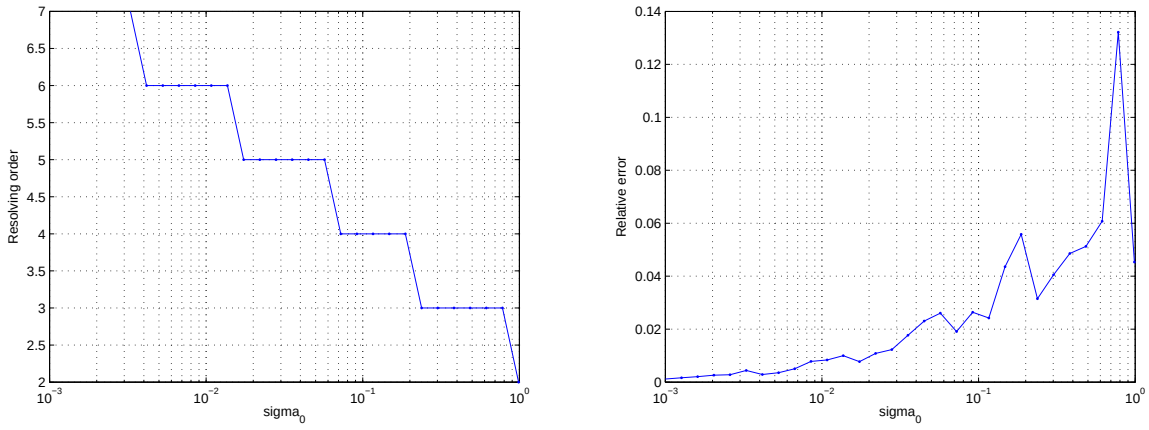

(a) Resolving order (b) Relative error

Figure 4.6: The resolving order m_0, for $\sigma_0 \in [10^{-3}, 1], \tau_0 = 10^{-1}$, and the relative error of the reconstruction within this order. As in Figure 4.5, we repeat the experiment 100 times and the reconstruction is taken as their mean value. The large variations of the relative error in (b) for $\sigma_0 > 10^{-1}$ indicate the instability of the reconstruction for very noisy data.

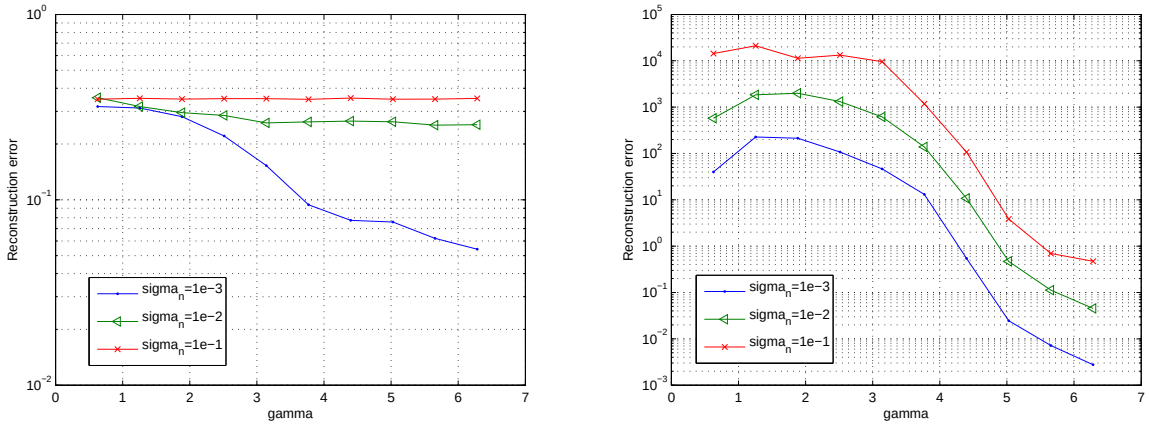

(a) (b)

Figure 4.7: Error of reconstructed CGPT of an ellipse compared with true CGPT values at different noise levels. We solve (4.54) and (4.23) with $N = 101, K = 50$, and compare the first two orders with the true CGPT. The x-axis is the angle of view γ. Figure(a): results of (4.54), Figure(b): results of (4.23).

CHAPTER 5

Dictionary Matching

The results of this chapter have been submitted in [5].

Abstract

The aim of this chapter is to provide a fast and efficient procedure for (real-time) target identification in imaging based on matching on a dictionary of precomputed generalized polarization tensors. The approach is based on some important properties of the GPTs and new invariants. A new shape representation is given and numerically tested in the presence of measurement noise. The stability and resolution of the proposed identification algorithm is numerically quantified.

5.1 Introduction

An important use of the concept of GPT is for imaging diametrically small inclusions from boundary measurements. Based on the multipolar expansion computed in section 4.2.1, efficient algorithms to determine the location and some geometric features of the inclusions have been proposed in previous works (see [19, 20] and the references therein for recent developments of this theory).

In [25], a recursive optimal control scheme to recover fine shape details of a given domain using GPTs is proposed. In [12], it is shown that high-frequency oscillations of the boundary of a domain are only contained in its high-order GPTs. Moreover, by developing a level set version of the recursive optimization scheme, it is also shown that the GPTs can capture the topology of the domain. An efficient algorithm for computing the GPTs has been presented in [38].

The aim of this chapter is to show that the GPTs can be used for shape identification from imaging data. Based on the results of chapter 4, we design a fast algorithm which identifies a target using a dictionary of precomputed GPTs data. Suppose that we have a dictionary which is a collection of standard shapes (for example alphabetic letters or flowers). Our aim is to identify from imaging data a shape which is obtained from one element of the dictionary after some rotation, scaling and translation. We design a dictionary matching procedure which operates directly in the GPTs data. Our procedure is based on some important properties of the GPTs and new invariants. We test the robustness of our procedure with respect to a

measurement noise in the imaging data. Our approach is quite natural since it uses geometric quantities obtained from the imaging data by simply inverting a linear system. Moreover, there is an infinite number of invariants associated with the GPTs. Furthermore, for a given dictionary, the GPT-based representation may lead to better distinguishibility between the dictionary elements.

Over the last decades, a considerable amount of work has been devoted to nonlinear optimization techniques for solving the imaging problem; see, for instance, [55, 100, 106] and the references therein. More recently, new regularized optimal control formulations for target imaging have been proposed in [9, 11]. As far as we know, our approach in this chapter provides for the first time an alternative approach to solving the full inverse problem for target identification and characterization. It opens a way for real-time target identification and tracking algorithms in wave imaging.

The chapter is organized as follows. In section 5.2 it is shown that the CGPTs have some nice properties, such as simple rotation and translation formulas and simple relation with shape symmetry. In section 5.3 we derive two algorithms for shape identification based on those relations. Section 5.4 presents a variety of numerical results for the target identification problem and shows the viability of the proposed procedure.

5.2 Complex CGPTs under Rigid Motions and Scaling

As we will see later, a complex combination of CGPTs is most convenient when we consider the transforms of CGPTs under dilatation and rigid motions, *i.e.*, shift and rotation. Therefore, for a double index mn, with $m, n = 1, 2, \ldots$, we introduce the following complex combination of CGPTs:

$$\begin{aligned} N^{(1)}_{mn}(\lambda, D) &= (M^{cc}_{mn} - M^{ss}_{mn}) + i(M^{cs}_{mn} + M^{sc}_{mn}), \\ N^{(2)}_{mn}(\lambda, D) &= (M^{cc}_{mn} + M^{ss}_{mn}) + i(M^{cs}_{mn} - M^{sc}_{mn}). \end{aligned} \tag{5.1}$$

Then, from (4.9), we observe that

$$\begin{aligned} N^{(1)}_{mn}(\lambda, D) &= \int_{\partial D} P_n(y)(\lambda I - \mathcal{K}^*_D)^{-1}[\langle \nu, \nabla P_m \rangle](y)\, ds(y), \\ N^{(2)}_{mn}(\lambda, D) &= \int_{\partial D} P_n(y)(\lambda I - \mathcal{K}^*_D)^{-1}[\langle \nu, \nabla \overline{P_m} \rangle](y)\, ds(y), \end{aligned}$$

where P_n and P_m are defined by (4.12). In order to simplify the notation, we drop λ in the following and write simply $N^{(1)}_{mn}(D), N^{(2)}_{mn}(D)$.

We consider the translation, the rotation and the dilatation of the domain D by introducing the following notation:

- Shift: $T_z D = \{x + z, \text{ for } x \in D\}$, for $z \in \mathbb{R}^2$;
- Rotation: $R_\theta D = \{e^{i\theta} x, \text{ for } x \in D\}$, for $\theta \in [0, 2\pi)$;
- Scaling: $sD = \{sx, \text{ for } x \in D\}$, for $s > 0$.

Proposition 5.2.1. *For all integers m, n, and geometric parameters θ, s, and z, the following holds:*

$$N^{(1)}_{mn}(R_\theta D) = e^{i(m+n)\theta} N^{(1)}_{mn}(D), \qquad N^{(2)}_{mn}(R_\theta D) = e^{i(n-m)\theta} N^{(2)}_{mn}(D), \tag{5.2}$$

$$N^{(1)}_{mn}(sD) = s^{m+n} N^{(1)}_{mn}(D), \qquad N^{(2)}_{mn}(sD) = s^{m+n} N^{(2)}_{mn}(D), \tag{5.3}$$

$$N^{(1)}_{mn}(T_z D) = \sum_{l=1}^{m} \sum_{k=1}^{n} \mathbf{C}^z_{ml} \mathbf{N}^{(1)}_{lk}(D) \mathbf{C}^z_{nk}, \quad N^{(2)}_{mn}(T_z D) = \sum_{l=1}^{m} \sum_{k=1}^{n} \overline{\mathbf{C}^z_{ml}} N^{(2)}_{lk}(D) \mathbf{C}^z_{nk}, \tag{5.4}$$

where $\mathbf{C}^z$ *is a lower triangle matrix with the* m, n*-th entry given by*

$$\mathbf{C}^z_{mn} = \binom{m}{n} z^{m-n}, \tag{5.5}$$

and $\overline{\mathbf{C}^z}$ *denotes its conjugate. Here, we identify* $z = (z_1, z_2)$ *with* $z = z_1 + iz_2$*.*

An ingredient that we will need in the proof is the following chain rule between the gradient of a function and its push forward under transformation. In fact, for any diffeomorphism T from $\mathbb{R}^2$ to $\mathbb{R}^2$ and any scalar-valued differentiable map f on $\mathbb{R}^2$, we have

$$\mathrm{d}(f \circ T)\big|_x(h) = \left(\mathrm{d}f\big|_{T(x)} \circ \mathrm{d}T\big|_x\right)(h), \tag{5.6}$$

for any tangent vector $h \in \mathbb{R}^2$, with $\mathrm{d}T$ being the differential of T.

Proof of Proposition 5.2.1. We will follow proofs of similar relations that can be found in [12]. Let us first show (5.2) for the rotated domain $D_\theta := R_\theta D$. For a function $\varphi(y), y \in \partial D$, we define a function $\varphi^\theta(y_\theta)$, $y_\theta := R_\theta y \in \partial D_\theta$ by

$$\varphi^\theta(y_\theta) = \varphi \circ R_{-\theta}(y_\theta) = \varphi(y).$$

It is proved in [12] that $\lambda I - \mathcal{K}^*_D$ is invariant under the rotation map, that is,

$$(\lambda I - \mathcal{K}^*_{D_\theta})[\varphi^\theta](y_\theta) = (\lambda I - \mathcal{K}^*_D)[\varphi](y). \tag{5.7}$$

We also check that $P_m(R_\theta y) = e^{im\theta} P_m(y)$.

We will focus on the relation for $N^{(1)}_{mn}$, the other one can be proved in the same way. By definition, we have

$$\begin{aligned} N^{(1)}_{mn}(D) &= \int_{\partial D} P_n(y)\varphi_{D,m}(y)ds(y), \\ N^{(1)}_{mn}(D_\theta) &= \int_{\partial D_\theta} P_n(y_\theta)\varphi_{D_\theta,m}(y_\theta)ds(y_\theta), \end{aligned} \tag{5.8}$$

where

$$\begin{aligned} \varphi_{D,m}(y) &= (\lambda I - \mathcal{K}^*_D)^{-1}[\langle \nu, \nabla P_m\rangle](y), \\ \varphi_{D_\theta,m}(y_\theta) &= (\lambda I - \mathcal{K}^*_{D_\theta})^{-1}[\langle \nu, \nabla P_m\rangle](y_\theta). \end{aligned}$$

Note that the last function differs from $\varphi^\theta_{D,m}$. By the change of variables $y_\theta = R_\theta y$ in the first expression of (5.8), we obtain

$$\begin{aligned} N^{(1)}_{mn}(D) &= \int_{\partial D_\theta} P_n(R_{-\theta}y_\theta)\varphi_{D,m}(R_{-\theta}y_\theta)ds(y_\theta) \\ &= e^{-in\theta}\int_{\partial D_\theta} P_n(y_\theta)\varphi^\theta_{D,m}(y_\theta)ds(y_\theta). \end{aligned}$$

From (5.7), we have

$$\begin{aligned} (\lambda I - \mathcal{K}^*_{D_\theta})[\varphi^\theta_{D,m}](y_\theta) &= (\lambda I - \mathcal{K}^*_D)[\varphi_{D,m}](y) \\ &= \langle \nu_y, \nabla P_m(y)\rangle. \end{aligned}$$

Moreover, $P_m(y) = e^{-im\theta}P_m(y_\theta)$ so that, by applying the chain rule (5.6) with $f = P_m$, $T = R_\theta$, $x = y$ and $h = \nu_y$, we can conclude that

$$\begin{aligned} \langle \nu_y, \nabla P_m(y)\rangle &= e^{-im\theta}\langle R_\theta \nu_y, \nabla P_m(y_\theta)\rangle \\ &= e^{-im\theta}\langle \nu_{y_\theta}, \nabla P_m(y_\theta)\rangle. \end{aligned}$$

Therefore, $\varphi^\theta_{D,m} = e^{-im\theta}\varphi_{D_\theta,m}$, and we conclude that $N^{(1)}_{mn}(D_\theta) = e^{i(m+n)\theta}N^{(1)}_{mn}(D)$.

The second identity in (5.2) results from the same computation as above (the minus sign comes form the conjugate in the definition of $\mathbf{N}^{(2)}$), and the two equations in (5.3) are proved in the same way, replacing the transformed function φ^θ by

$$\varphi^s(sy) = \varphi(y).$$

Thus, only (5.4) remains. Since the difference between these two comes from the conjugation, we will focus only on the first identity in (5.4). The strategy will be once again the following: for a function $\varphi(y), y \in \partial D$, we define a function $\varphi^z(y_z), y_z = y + z \in \partial D_z$, with $D_z := T_z D$, by

$$\varphi^z(y_z) = \varphi \circ T_{-z}(y_z) = \varphi(y),$$

which also verifies an invariance relation similar to (5.7)

$$(\lambda I - \mathcal{K}^*_{D_z})[\varphi^z](y_z) = (\lambda I - \mathcal{K}^*_D)[\varphi](y). \tag{5.9}$$

Moreover, for every integer $q \in \mathbb{N}$ one has the following

$$P_q(y_z) = (y+z)^q = \sum_{r=0}^{q} \binom{q}{r} y^r z^{q-r}. \tag{5.10}$$

Equations (5.8) become

$$N^{(1)}_{mn}(D) = \int_{\partial D} P_n(y)\varphi_{D,m}(y)ds(y),$$
$$N^{(1)}_{mn}(D_z) = \int_{\partial D_z} P_n(y_z)\varphi_{D_z,m}(y_z)ds(y_z),$$

where

$$\varphi_{D,m}(y) = (\lambda I - \mathcal{K}^*_D)^{-1}[\langle \nu, \nabla P_m\rangle](y),$$
$$\varphi_{D_z,m}(y_z) = (\lambda I - \mathcal{K}^*_{D_z})^{-1}[\langle \nu, \nabla P_m\rangle](y_z).$$

Thus, combining (5.9) and (5.10) leads us to

$$\begin{aligned}(\lambda I - \mathcal{K}^*_{D_z})[\varphi_{D_z,m}](y_z) &= \langle \nu_{y_z}, \nabla P_m(y_z)\rangle \\ &= \langle \nu_y, \sum_{l=1}^{m} \binom{m}{l} z^{m-l} \nabla P_l(y)\rangle \\ &= \sum_{l=1}^{m} \binom{m}{l} z^{m-l} (\lambda I - \mathcal{K}^*_D)[\varphi_{D,l}](y) \\ &= \sum_{l=1}^{m} \binom{m}{l} z^{m-l} (\lambda I - \mathcal{K}^*_{D_z})[\varphi^z_{D,l}](y_z),\end{aligned}$$

so that we have

$$\varphi_{D_z,m}(y) = \sum_{l=1}^{m} \binom{m}{l} z^{m-l} \varphi^z_{D,l}(y_z).$$

Hence, returning to the definition of $N^{(1)}_{mn}(D_z)$ with the substitution $y_z \leftrightarrow y$, we obtain

$$\begin{aligned}N^{(1)}_{mn}(D_z) &= \sum_{l=1}^{m} \binom{m}{l} z^{m-l} \int_{\partial D_z} P_n(y_z)\varphi^z_{D,l}(y_z)ds(y_z), \\ &= \sum_{l=1}^{m}\sum_{k=1}^{n} \binom{m}{l}\binom{n}{k} z^{m-l} z^{n-k} \mathbf{N}^{(1)}_{lk}(D),\end{aligned}$$

which is the desired result. Note that the index k begins with $k = 1$ because $\int_{\partial D_z} \varphi^z_{D,l} = 0$. This completes the proof. □

5.2.1 Some properties of complex CGPTs

We define the complex CGPT matrices by $\mathbf{N}^{(1)} := (N^{(1)}_{mn})_{m,n}$ and $\mathbf{N}^{(2)} := (N^{(2)}_{mn})_{m,n}$. We set $w = se^{i\theta}$ and introduce the diagonal matrix $\mathbf{G}^w$ with the m-th diagonal entry given by $s^m e^{im\theta}$. Proposition 5.2.1 implies immediately that

$$\mathbf{N}^{(1)}(T_z s R_\theta D) = \mathbf{C}^z \mathbf{G}^w \mathbf{N}^{(1)}(D) \mathbf{G}^w (\mathbf{C}^z)^T, \tag{5.11}$$

$$\mathbf{N}^{(2)}(T_z s R_\theta D) = \overline{\mathbf{C}^z \mathbf{G}^w} \mathbf{N}^{(2)}(D) \mathbf{G}^w (\mathbf{C}^z)^T, \tag{5.12}$$

where $\mathbf{C}^z$ is defined by (5.5). Relations (5.11) and (5.12) still hold for the truncated CGPTs of finite order, due to the triangular shape of the matrix $\mathbf{C}^z$. Using the symmetry of the CGPTs ([20, Theorem 4.11]) and the positivity of the GPTs as proved in [20], we easily establish the following result.

Proposition 5.2.2. *The complex CGPT matrix $\mathbf{N}^{(1)}$ is symmetric: $(\mathbf{N}^{(1)})^T = \mathbf{N}^{(1)}$, and $\mathbf{N}^{(2)}$ is Hermitian: $(\mathbf{N}^{(2)})^H = \mathbf{N}^{(2)}$. Consequently, the diagonal elements of $\mathbf{N}^{(2)}$ are strictly positive if $\lambda > 0$ and strictly negative if $\lambda < 0$.*

Furthermore, the CGPTs of rotation invariant shapes have special structures:

Proposition 5.2.3. *Suppose that D is invariant under rotation of angle $2\pi/p$ for some integer $p \geq 2$,* i.e., *$R_{2\pi/p} D = D$, then*

$$N^{(1)}_{mn}(D) = 0 \text{ if } p \text{ does not divide } (m+n), \tag{5.13}$$

$$N^{(2)}_{mn}(D) = 0 \text{ if } p \text{ does not divide } (m-n). \tag{5.14}$$

Proof. Suppose that p does not divide $(m+n)$, and define $r := 2\pi(n+m)/p \bmod 2\pi$. Then by the rotation symmetry of D and the symmetry property of the CGPTs, we have

$$N^{(1)}_{mn}(D) = N^{(1)}_{mn}(R_{2\pi/p} D) = e^{i(m+n)2\pi/p} N^{(1)}_{mn}(D) = e^{ir} N^{(1)}_{mn}(D).$$

Since $r < 2\pi$ and $r \neq 0$, we conclude that $N^{(1)}_{mn}(D) = 0$. The proof of (5.14) is similar. □

5.3 Shape Identification by the CGPTs

We call a *dictionary* $\mathcal{D}$ a collection of standard shapes, which are centered at the origin and with characteristic sizes of order 1. Given the CGPTs of an unknown shape D, and assuming that D is obtained from a certain element $B \in \mathcal{D}$ by applying some unknown rotation θ, scaling s and translation z, *i.e.* , $D = T_z s R_\theta B$, our objective is to recognize B from $\mathcal{D}$. For doing so, one may proceed by first reconstructing the shape D using its CGPTs through some optimization procedures as proposed in [25], and then match the reconstructed shape with $\mathcal{D}$. However, such a method may be time-consuming and the recognition efficiency depends on the shape reconstruction algorithm.

We propose in subsections 5.3.1 and 5.3.2 two shape identification algorithms using the CGPTs. The first one matches the CGPTs of data with that of the dictionary element by estimating the transform parameters, while the second one is based on a transform invariant shape descriptor obtained from the CGPTs. The second approach is computationally more efficient. Both of them operate directly in the data domain which consists of CGPTs and avoid the need for reconstructing the shape D. The heart of our

approach is some basic algebraic equations between the CGPTs of D and B that can be deduced easily from (5.11) and (5.12). Particularly, the first four equations read:

$$N_{11}^{(1)}(D) = w^2 N_{11}^{(1)}(B), \tag{5.15}$$
$$N_{12}^{(1)}(D) = 2N_{11}^{(1)}(D)z + w^3 N_{12}^{(1)}(B), \tag{5.16}$$
$$N_{11}^{(2)}(D) = s^2 N_{11}^{(2)}(B), \tag{5.17}$$
$$N_{12}^{(2)}(D) = 2N_{11}^{(2)}(D)z + s^2 w N_{12}^{(2)}(B), \tag{5.18}$$

where $w = se^{i\theta}$.

5.3.1 CGPTs matching

Determination of transform parameters

Suppose that the complex CGPT matrices $\mathbf{N}^{(1)}(B), \mathbf{N}^{(2)}(B)$ of the true shape B are given. Then, from (5.17), we obtain that

$$s = \sqrt{N_{11}^{(2)}(D)/N_{11}^{(2)}(B)}. \tag{5.19}$$

Case 1: Rotational symmetric shape. If the shape B has rotational symmetry, *i.e.* , $R_{2\pi/p}B = B$ for some $p \geq 2$, then from Proposition 5.2.3 we have $N_{12}^{(2)}(B) = 0$ and the translation parameter z is uniquely determined from (5.18) by

$$z = \frac{N_{12}^{(2)}(D)}{2N_{11}^{(2)}(D)}. \tag{5.20}$$

On the contrary, the rotation parameter θ (or $e^{i\theta}$) can only be determined up to a multiple of $2\pi/p$, from CGPTs of order $\lceil p/2 \rceil$ at least. Although explicit expressions of $e^{ip\theta}$ can be deduced from (5.15) - (5.18) (or higher order equations if necessary), we propose to recover $e^{ip\theta}$ by solving the least squares problem:

$$\min_{\theta} \left(\|\mathbf{N}^{(1)}(T_z s R_\theta B) - \mathbf{N}^{(1)}(D)\|_F^2 + \|\mathbf{N}^{(2)}(T_z s R_\theta B) - \mathbf{N}^{(2)}(D)\|_F^2 \right). \tag{5.21}$$

Here, s and z are given by (5.19) and (5.20) respectively, and $\mathbf{N}^{(1)}(D)$ and $\mathbf{N}^{(2)}(D)$ are the truncated complex CGPTs matrices of dimension $\lceil p/2 \rceil \times \lceil p/2 \rceil$.

Case 2: Non rotational symmetric shape. Consider a non rotational symmetric shape B which satisfies the assumption:

$$N_{11}^{(1)}(B) \neq 0 \quad \text{and} \quad \det \begin{pmatrix} N_{11}^{(1)}(B) & N_{11}^{(2)}(B) \\ N_{12}^{(1)}(B) & N_{12}^{(2)}(B) \end{pmatrix} \neq 0. \tag{5.22}$$

From (5.16) and (5.18), it follows that we can uniquely determine the translation z and the rotation parameter $w = e^{i\theta}$ from CGPTs of orders one and two by solving the following linear system:

$$\begin{aligned} N_{12}^{(1)}(D)/N_{11}^{(1)}(D) &= 2z + w N_{12}^{(1)}(B)/N_{11}^{(1)}(B), \\ N_{12}^{(2)}(D)/N_{11}^{(2)}(D) &= 2z + w N_{12}^{(2)}(B)/N_{11}^{(2)}(B). \end{aligned} \tag{5.23}$$

Debiasing by least squares solutions

In practice (for both the rotational symmetric and non rotational symmetric cases), the value of the parameters z, s and θ provided by the analytical formulas and numerical procedures above may be inexact, due to the noise in the data and the ill-conditioned character of the linear system (6.3). Let z^*, s^*, θ^* be the true transform parameters, which can be considered as perturbations around the estimations z, s, θ obtained above:

$$z^* = z + \delta_z,\ s^* = s\delta_s,\ \text{and}\ \theta^* = \theta + \delta_\theta, \tag{5.24}$$

for δ_z, δ_θ small and δ_s close to 1. To find these perturbations, we solve a nonlinear least squares problem:

$$\min_{z',s',\theta'} \left(\|\mathbf{N}^{(1)}(T_{z'}s'R_{\theta'}B) - \mathbf{N}^{(1)}(D)\|_F^2 + \|\mathbf{N}^{(2)}(T_{z'}s'R_{\theta'}B) - \mathbf{N}^{(2)}(D)\|_F^2 \right), \tag{5.25}$$

with (z, s, θ) as an initial guess. Here, the order of the CGPTs in (5.25) is taken to be 2 in the non rotational case and $\max(2, [p/2])$ in the rotational symmetric case. Thanks to the relations (5.11) and (5.12), one can calculate explicitly the derivatives of the objective function, therefore can solve (5.25) by means of standard gradient-based optimization methods.

First algorithm for shape identification

For each dictionary element, we determine the transform parameters as above, then measure the similarity of the complex CGPT matrices using the Frobenius norm, and choose the most similar element as the identified shape. Intuitively, the true dictionary element will give the correct transform parameters hence the most similar CGPTs. This procedure is described in Algorithm 1.

Algorithm 1 Shape identification based on CGPT matching

Input: the first k-th order CGPTs $\mathbf{N}^{(1)}(D), \mathbf{N}^{(2)}(D)$ of an unknown shape D
for $B_n \in \mathcal{D}$ **do**
1. Estimation of z, s, θ using the procedures described in subsections 5.3.1 and 5.3.1;
2. $\tilde{D} \leftarrow R_{-\theta}s^{-1}T_{-z}D$, and calculate $\mathbf{N}^{(1)}(\tilde{D})$ and $\mathbf{N}^{(2)}(\tilde{D})$;
3. $E^{(1)} \leftarrow \mathbf{N}^{(1)}(B_n) - \mathbf{N}^{(1)}(\tilde{D})$, and $E^{(2)} \leftarrow \mathbf{N}^{(2)}(B_n) - \mathbf{N}^{(2)}(\tilde{D})$;
4. $e_n \leftarrow (\|E^{(1)}\|_F^2 + \|E^{(2)}\|_F^2)^{1/2}/(\|\mathbf{N}^{(1)}(B_n)\|_F^2 + \|\mathbf{N}^{(2)}(B_n)\|_F^2)^{1/2}$;
5. $n \leftarrow n + 1$;

end for
Output: the true dictionary element $n^* \leftarrow \text{argmin}_n e_n$.

5.3.2 Transform invariant shape descriptors

From (5.17) and (5.18) we deduce the following identity:

$$\frac{N_{12}^{(2)}(D)}{2N_{11}^{(2)}(D)} = z + se^{i\theta}\frac{N_{12}^{(2)}(B)}{2N_{11}^{(2)}(B)}, \tag{5.26}$$

which is well defined since $N_{11}^{(2)} \neq 0$ thanks to the Proposition 5.2.2. Identity (5.26) shows a very simple relationship between $\frac{N_{12}^{(2)}(B)}{2N_{11}^{(2)}(B)}$ and $\frac{N_{12}^{(2)}(D)}{2N_{11}^{(2)}(D)}$ for $D = T_z s R_\theta B$. .

Let $u = \frac{N_{12}^{(2)}(D)}{2N_{11}^{(2)}(D)}$. We first define the following quantities which are translation invariant:

$$\mathcal{T}^{(1)}(D) = \mathbf{N}^{(1)}(T_{-u}D) = \mathbf{C}^{-u}\mathbf{N}^{(1)}(D)(\mathbf{C}^{-u})^T, \tag{5.27}$$

$$\mathcal{T}^{(2)}(D) = \mathbf{N}^{(2)}(T_{-u}D) = \overline{\mathbf{C}^{-u}}\mathbf{N}^{(2)}(D)(\mathbf{C}^{-u})^T, \tag{5.28}$$

with the matrix $\mathbf{C}^{-u}$ being the same as in Proposition 5.2.1. From $\mathcal{T}^{(1)}(D) = (\mathcal{T}^{(1)}_{mm}(D))_{m,n}$ and $\mathcal{T}^{(2)}(D) = (\mathcal{T}^{(2)}_{mm}(D))_{m,n}$, we define, for any indices m, n, the scaling invariant quantities:

$$\mathcal{S}^{(1)}_{mn}(D) = \frac{\mathcal{T}^{(1)}_{mn}(D)}{\left(\mathcal{T}^{(2)}_{mm}(D)\mathcal{T}^{(2)}_{nn}(D)\right)^{1/2}},\ \mathcal{S}^{(2)}_{mn}(D) = \frac{\mathcal{T}^{(2)}_{mn}(D)}{\left(\mathcal{T}^{(2)}_{mm}(D)\mathcal{T}^{(2)}_{nn}(D)\right)^{1/2}}. \tag{5.29}$$

Finally, we introduce the CGPT-based shape descriptors $\mathcal{I}^{(1)} = (\mathcal{I}^{(1)}_{mn})_{m,n}$ and $\mathcal{I}^{(2)} = (\mathcal{I}^{(2)}_{mn})_{m,n}$:

$$\mathcal{I}^{(1)}_{mn}(D) = |\mathcal{S}^{(1)}_{mn}(D)|,\ \mathcal{I}^{(2)}_{mn}(D) = |\mathcal{S}^{(2)}_{mn}(D)|, \tag{5.30}$$

where $|\cdot|$ denotes the modulus of a complex number. Constructed in this way, $\mathcal{I}^{(1)}$ and $\mathcal{I}^{(2)}$ are clearly invariant under translation, rotation, and scaling.

It is worth emphasizing the symmetry property, $\mathcal{I}^{(1)}_{mn} = \mathcal{I}^{(1)}_{nm}, \mathcal{I}^{(2)}_{mn} = \mathcal{I}^{(2)}_{nm}$, and the fact that $\mathcal{I}^{(2)}_{mm} = 1$ for any m.

Second algorithm for shape identification

Thanks to the transform invariance of the new shape descriptors, there is no need now for calculating the transform parameters, and the similarity between a dictionary element and the unknown shape can be directly measured from $\mathcal{I}^{(1)}$ and $\mathcal{I}^{(2)}$. As in Algorithm 1, we use the Frobenius norm as the distance between two shape descriptors and compare with all the elements of the dictionary. We propose a simplified method for shape identification, as described in Algorithm 2.

Algorithm 2 Shape identification based on transform invariant descriptors

Input: the first k-th order shape descriptors $\mathcal{I}^{(1)}(D), \mathcal{I}^{(2)}(D)$ of an unknown shape D
for $B_n \in \mathcal{D}$ **do**
1. $e_n \leftarrow \left(\|\mathcal{I}^{(1)}(B_n) - \mathcal{I}^{(1)}(D)\|_F^2 + \|\mathcal{I}^{(2)}(B_n) - \mathcal{I}^{(2)}(D)\|_F^2\right)^{1/2}$;
2. $n \leftarrow n + 1$;

end for
Output: the true dictionary element $n^* \leftarrow \text{argmin}_n e_n$.

5.4 Numerical Experiments

In this section, we will present the results of identification that were theoretically shown in the previous sections.

The identification process will be as follows (note that the first two are the same as in section 4.4).

1. Data simulation (see setting in Figure 5.1)
2. Reconstruction of the CGPTs of $D = D_0 - z_0$ using formula (4.26) or the least squares algorithm (4.23).
3. For a given dictionary $\mathcal{D}$, apply Algorithm 1 (or Algorithm 2) using the CGPTs of D and identify the true shape from $\mathcal{D}$.

As in chapter 4, the conductivity parameter is fixed to $k = 4/3$.

Unless specified, in the following we suppose that the unknown shape of the target D_0 is an exact copy of some element from the dictionary, up to a rigid transform and dilatation. As examples, we consider a dictionary of flowers and a dictionary of Roman letters. The aim is to identify the target D_0 from imaging data if it belongs to one of the dictionaries.

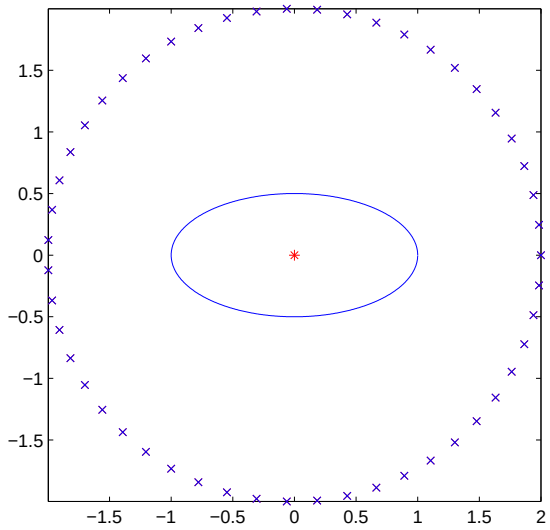

Figure 5.1: An example of the configuration for MSR data simulation. The unknown shape is an ellipse whose long and short axes are 2 and 1, respectively. $N = 51$ sources/receivers (marked by "x") are equally placed on a circle of radius $R = 2$ centered at $z_0 = [0, 0]$ (marked by "*").

5.4.1 Matching on a dictionary of flowers

We start by considering a simple dictionary of rotation invariant "flowers", on which the shape identification algorithm can be greatly simplified. The boundary of the p-th flower B_p is defined as a small perturbation of the standard disk:

$$\partial B_p(\xi) = x(\xi)(1 + \eta\cos(p\xi)),\ x(\xi) = \begin{pmatrix}\cos\xi\\ \sin\xi\end{pmatrix}, \tag{5.31}$$

where $p \geq 2$ is the number of petals and $\eta > 0$ is a small constant. According to Proposition 5.2.3, $N^{(1)}_{mn}(B_p)$ is zero if p does not divide $m+n$. For an unknown shape $D = T_z s R_\theta B_p$, the translation parameter is given by $z = \frac{N^{(2)}_{12}(D)}{2N^{(2)}_{11}(D)}$. Moreover, simple calculations show that $\mathcal{I}^{(1)}(D)$ and $\mathbf{N}^{(1)}(B_p)$ have exactly the same zero patterns.

Therefore, we can find the true number of petals by searching the first nonzero anti-diagonal entry in $\mathcal{I}^{(1)}(D)$.

We fix $\eta = 0.3$ (the amplitude of the perturbation introduced in (5.31)) and $\delta/R = 0.5$. The unknown shape D_0 is obtained by applying the transform parameters $z = [16.3, -46.7], s = 7.5, \theta = 2.69$ on B_p, and the reference point for data acquisition is $z_0 = [15, -45.5]$. The results for two flowers of 5 and 7 petals are shown in Figure 5.2, where we plot the mean absolute value of the anti-diagonal entries mn, for $m + n = l, l = 2, \ldots, 11$, in $\mathcal{I}^{(1)}(D)$ by varying the noise level σ_0. One can clearly distinguish the peak which indicates the true number of petals for σ_0 up to 10^{-2}.

Stability. Let us consider now the model (5.31) with a general $\mathcal{C}^1$ function $h(\xi)$ in place of $\cos(p\xi)$. It was proven in [12] that:

$$N^{(1)}_{mn}(B_p) = 2\pi\eta\frac{mn}{\lambda^2}\hat{h}_{m+n} + O(\eta^2). \tag{5.32}$$

Therefore as long as the perturbation $h(\xi)$ is close to $\cos(p\xi)$, the significant nonzero coefficients in $\mathcal{I}^{(1)}(D)$ will concentrate on the same anti-diagonals. We confirm this observation by applying the same procedure

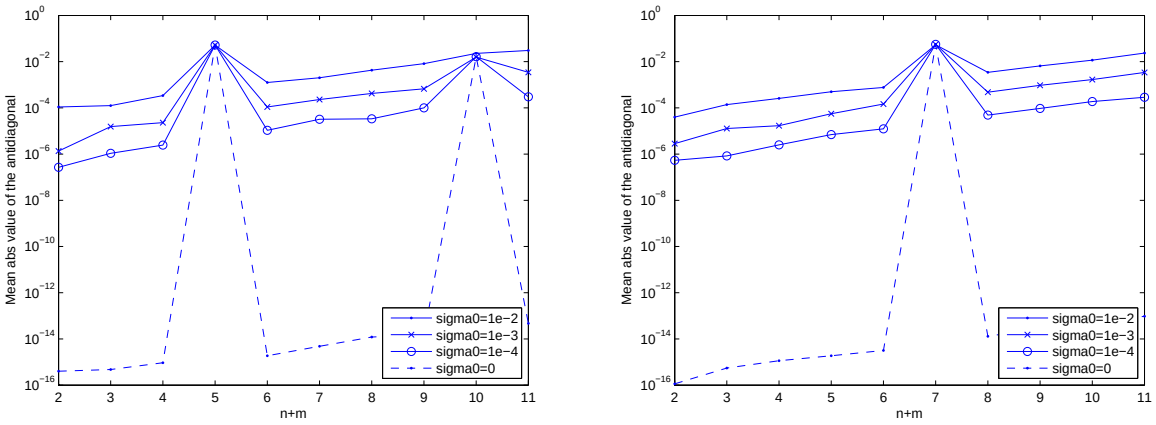

(a) $p = 5$ (b) $p = 7$

Figure 5.2: Mean values of the anti-diagonal entries of $\mathcal{I}^{(1)}$ for the flowers of 5 and 7 petals at different noise levels.

above on a flower with one damaged petal:

$$\partial B_p(\xi) = \begin{cases} x(\xi) f(\xi, t) & \text{for } \xi \in [0, 2\pi/p), \\ x(\xi)(1 + \eta \cos(p\xi)) & \text{for } \xi \in [2\pi/p, 2\pi). \end{cases} \tag{5.33}$$

Here, $f(\cdot, t) : \mathbb{R} \mapsto \mathbb{R}$ is a polynomial of order 6, constructed such that ∂B_p is $\mathcal{C}^2$-smooth, and $t \in (0, 1)$ is the percentage of the damage; see Figure 5.3. In Figure 5.4 we plot the mean value of the anti-diagonal entries at different noise levels. Compared to Figure 5.2, we see that the effect of the damage in the petal dominates the measurement noise. Nonetheless, the peak indicating the true number of petals is still visible.

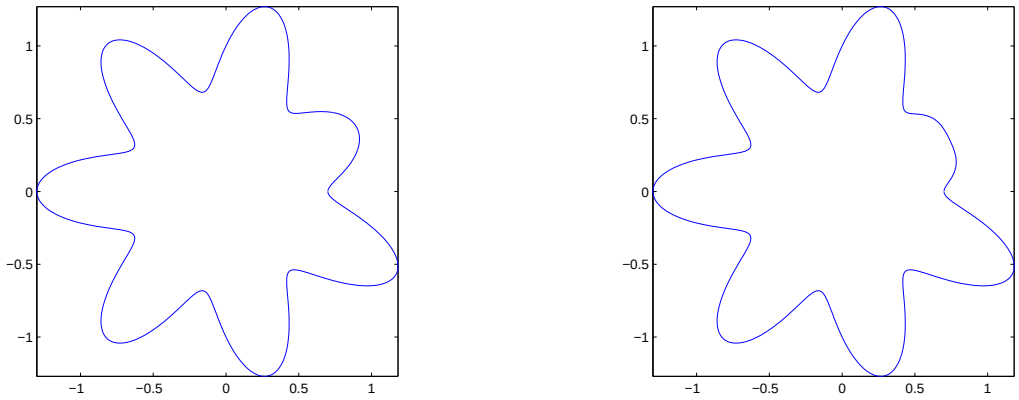

(a) $t = 0.5$ (b) $t = 0.8$

Figure 5.3: Flowers with one damaged petal. The following parameters are used in (5.33): $p = 7$, $\eta = 0.3$, $t = 0.5$ for (a) and $t = 0.8$ for (b).

5.4.2 Dictionary of letters

Next we consider here a dictionary consisting of 26 Roman capital letters without rotational symmetry. The shapes are defined in such a way that the holes inside the letters are filled, see Figure 5.10. We set

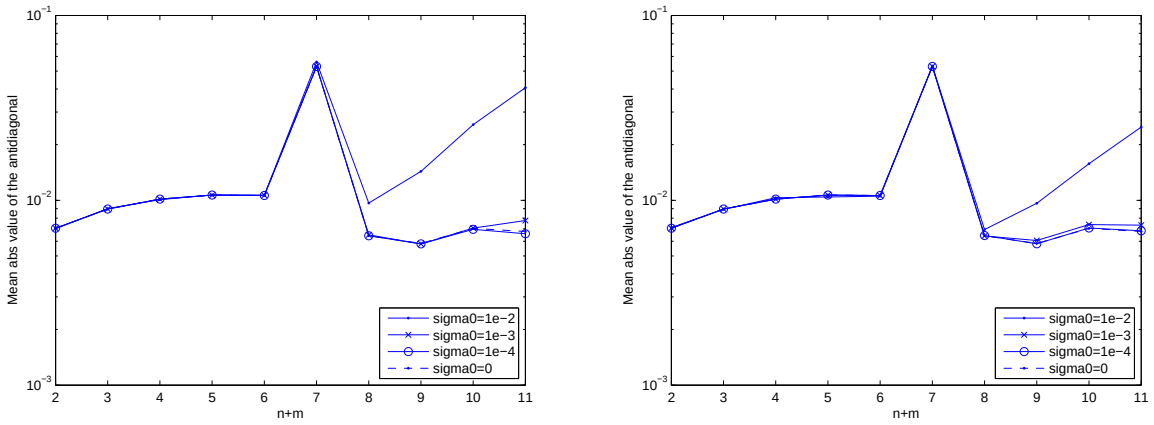

(a) $t = 0.5$ (b) $t = 0.8$

Figure 5.4: Mean value of the anti-diagonal entries of $\mathcal{I}^{(1)}$ for the flowers of Figure 5.3 at different noise levels. The peaks indicate the number of petals.

$\delta/R = 0.5$, $s = 2.47, \theta = 6.08, z = [33.35, 73.84]$ and the center of mass of the target at $[33.40, 73.86]$.

Performance of Algorithm 1. First we test Algorithm 1 on the letter "P". For the noiseless case ($\sigma_0 = 0$), the values of e_n defined in Algorithm 1 are plotted in Figure 5.5 (a) and (b). These results suggest that the high order CGPTs can better distinguish similar shapes such as "P" and "R", since they contain more high frequency information [12]. Nonetheless, the advantage of using high order CGPTs drops quickly when the data are contaminated by noise, and low order CGPTs provide more stable results in this situation, see Figure 5.5 (c) and (d).

By repeating the same procedure as above, we apply Algorithm 1 on all letters at noise levels $\sigma_0 = 0$ and $\sigma_0 = 0.1$, and show the result in Figure 5.6 (a) and (c). At the coordinate (m, n), the unknown shape is the m-th letter and the color represents the relative error (in logarithmic scale) of the CGPTs when compared with the n-th standard letter of the dictionary.

Stability. In real world applications we would like to have Algorithm 1 work also on shapes which are not exact copies of the dictionary, such as handwriting letters (in the case of the present dictionary). In the case of electrolocation, this is motivated by the fact that the targets for the fish do not share exactly the same shape. Figure 5.11 shows the letters obtained by perturbing and smoothing the dictionary elements. With these letters as unknown shapes, we repeat the experiment of Figure 5.6 (a) and (c) by applying Algorithm 1 on the standard dictionary and show the results in Figure 5.6 (b) and (d). Comparing with the results of Figure 5.6 (a) and (c), we see that Algorithm 1 remains quite stable, despite of some slight degradations.

Performance of Algorithm 2. In the case of noiseless data, Algorithm 2 provides correct results with low computational cost. Here we repeat the experiment in Figure 5.5 (a) and (c) using Algorithm 2, and plot the error e_n defined in Algorithm 2 in Figure 5.7. Nonetheless, when data are noisy, Algorithm 1 performs significantly better than Algorithm 2, as shown by Figure 5.8 where we compare the two algorithms for identifying letter "P" at various noise levels. Thanks to the debiasing step (5.25), Algorithm 1 is much more robust with respect to noise than Algorithm 2, in which there is no debiasing and the invariance of the shape descriptors $\mathcal{I}^{(1)}$ and $\mathcal{I}^{(2)}$ may be severely affected by noise (see Figure 5.8).

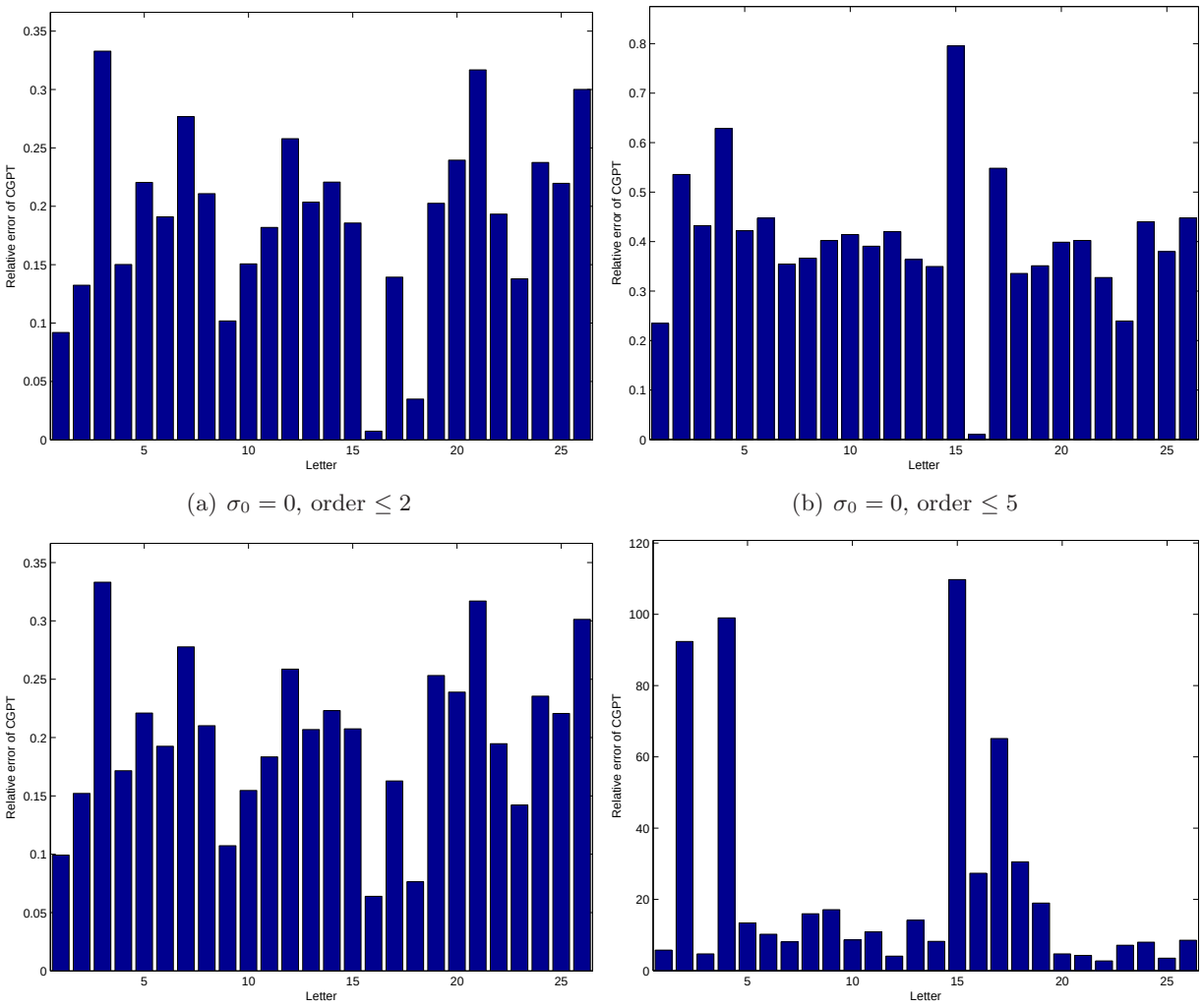

(a) $\sigma_0 = 0$, order ≤ 2

(b) $\sigma_0 = 0$, order ≤ 5

(c) $\sigma_0 = 0.1$, order ≤ 2

(d) $\sigma_0 = 0.1$, order ≤ 5

Figure 5.5: The identification of the letter "P" using the first 2, and 5 orders CGPTs at noise levels $\sigma_0 = 0$ and $\sigma_0 = 0.1$. The bar represents the relative error e_n between the CGPTs of the n-th letter and that of the data, as defined in Algorithm 1, and the shortest one in each figure corresponds to the identified letter. For (c) and (d), the experiment has been repeated for 100 times, using independent draws of white noise, and the results are the mean values of all experiments.

Performance of Algorithm 2 with partial aperture We also studied the influence of a limited angle of view on the matching of dictionary, with the two following configurations. In the first configuration, $N = 51$ sources/receivers are equally distributed between $[0, \pi)$, see Figure 5.9(a). In the second configuration, we divide the sources/receivers into 5 groups placed in a nonuniform way on $[0, 2\pi)$, and each group covers only an angle range of 0.2π, see Figure 5.9(b). As we can see in Figures 5.9(c) and 5.9(c), it is not possible to recover the shape, even without noise. Thus, we will not study the effect of noise. Let us remark that this will be a obstacle in applying these algorithm for electrolocation. We will see in chapter 7 that we can avoid this problem using multi-frequency measurements.

5.5 Conclusion

In this chapter, we have designed two fast algorithms which identify a target using a dictionary of pre-computed GPTs data. The first algorithm matches the computed GPTs (as specified in chapter 4) to

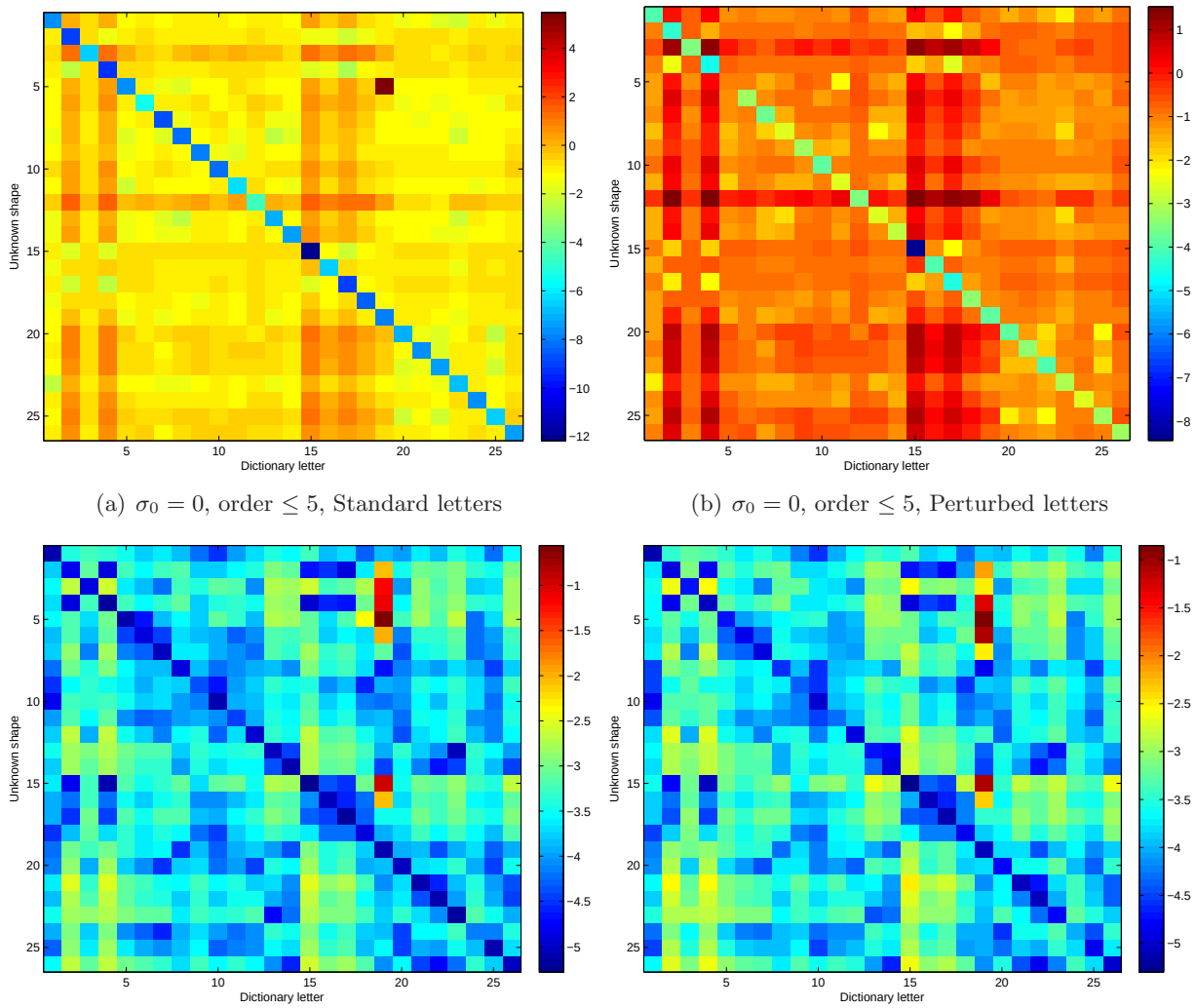

(a) $\sigma_0 = 0$, order ≤ 5, Standard letters

(b) $\sigma_0 = 0$, order ≤ 5, Perturbed letters

(c) $\sigma_0 = 0.1$, order $= 1$, Standard letters

(d) $\sigma_0 = 0.1$, order $= 1$, Perturbed letters

Figure 5.6: Algorithm 1 applied on the all 26 letters using the standard dictionary (Figure 5.10) at noise level $\sigma_0 = 0$ (first column) and $\sigma_0 = 0.1$ (second column), with the color indicating the relative error e_n in logarithmic scale. The unknown shapes in the first row are exact copies of the standard dictionary, and in the second row are those of Figure 5.11. In (a) all letters are correctly identified, while in (b) letters 'E' is identified as 'H'. For the noisy case, the experiment has been repeated 100 times, using independent draws of white noise, and the results in (c) and (d) are the mean values of all experiments, where only the first order CGPT is taken into account. 22 and 21 letters are correctly identified in (c) and (d), respectively.

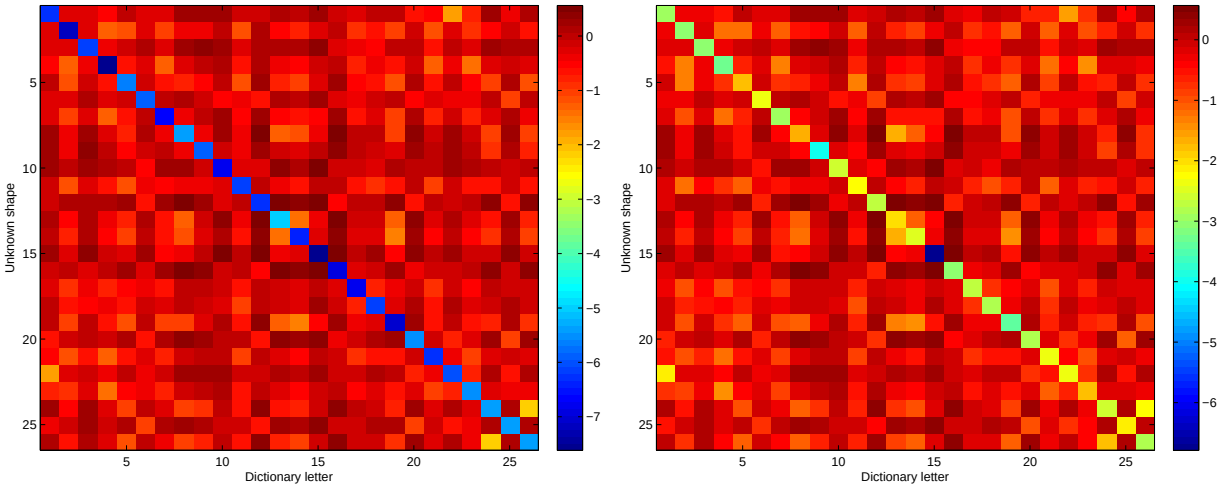

(a) $\sigma_0 = 0$, order ≤ 5, Standard letters

(b) $\sigma_0 = 0$, order ≤ 5, Perturbed letters

Figure 5.7: Algorithm 2 applied on the all 26 letters using the standard dictionary (Figure 5.10) at noise level $\sigma_0 = 0$. The unknown shapes in (a) are exact copies of the standard dictionary, while in (b) are those of Figure 5.11. The color indicates the error e_n in logarithmic scale. All letters are correctly identified in both (a) and (b).

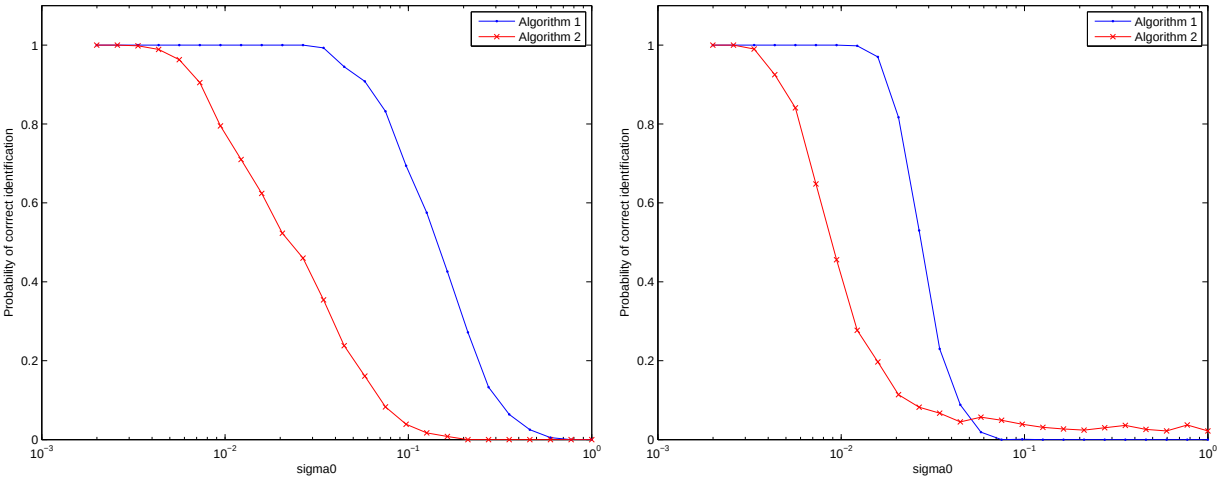

(a) order ≤ 2

(b) order ≤ 3

Figure 5.8: Comparison of Algorithm 2 and Algorithm 1 on identification of the standard letter "P". At each noise level, the experiment has been repeated 1000 times, using independent draws of white noise. For each algorithm, the curve represents the percentage of experiments where the letter "P" is correctly identified.

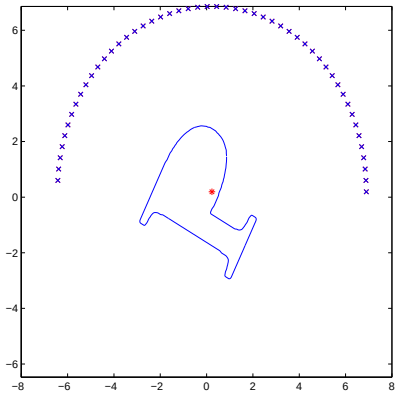

(a) Setup of first configuration

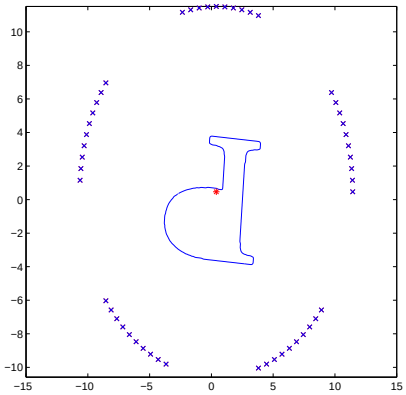

(b) Setup of second configuration

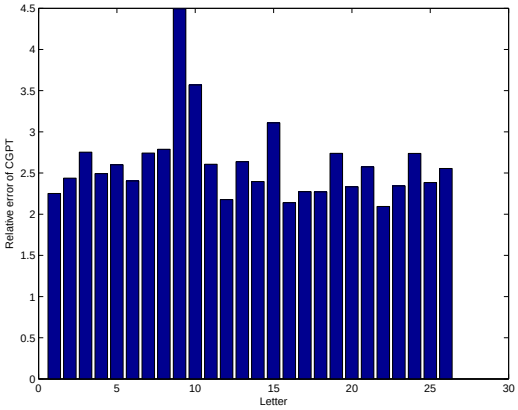

(c) Results for first configuration

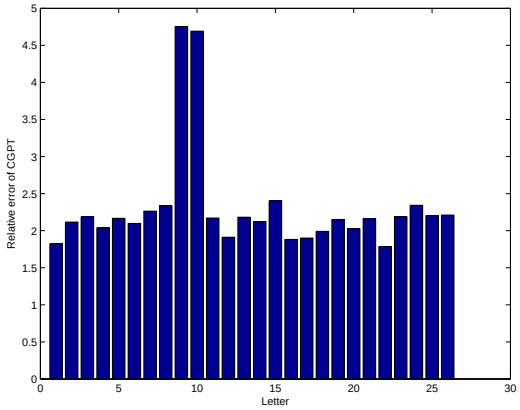

(d) Results for second configuration

Figure 5.9: Two configurations were considered in the study of limited aperture.

precomputed ones (the dictionary elements) by finding rotation, scaling, and translation parameters and therefore, identifies the true target shape. The second algorithm is based on new invariants for the CGPTs. We have provided new shape descriptors which are invariant under translation, rotation, and scaling. The stability (in the presence of additive noise in multistatic measurements) and the resolution issues for both algorithms have been numerically investigated. The second algorithm is computationally much cheaper than the first one. However, it is more sensitive to measurement noise in the imaging data. To the best of our knowledge, our procedure is the first approach for real-time target identification in imaging using dictionary matching. It shows that GPT-based representations are an appropriate and natural tool for imaging. Our approach can be extended to electromagnetic and elastic imaging as well [21, 14]. In [8], shape desciptors in $\mathbb{R}^3$ were derived, allowing us to extend our approach to $3D$ problems.

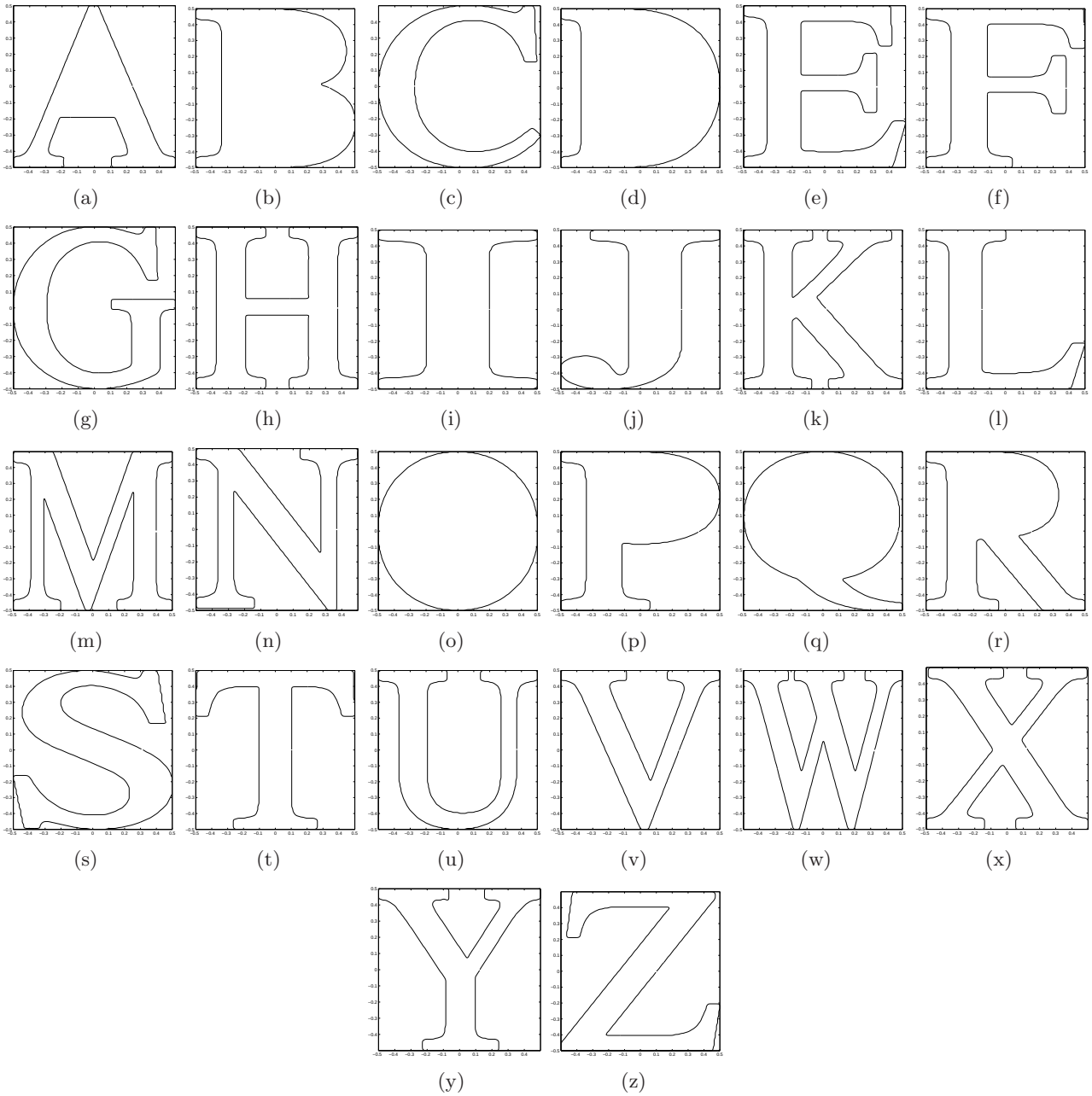

Figure 5.10: Dictionary of standard letters.

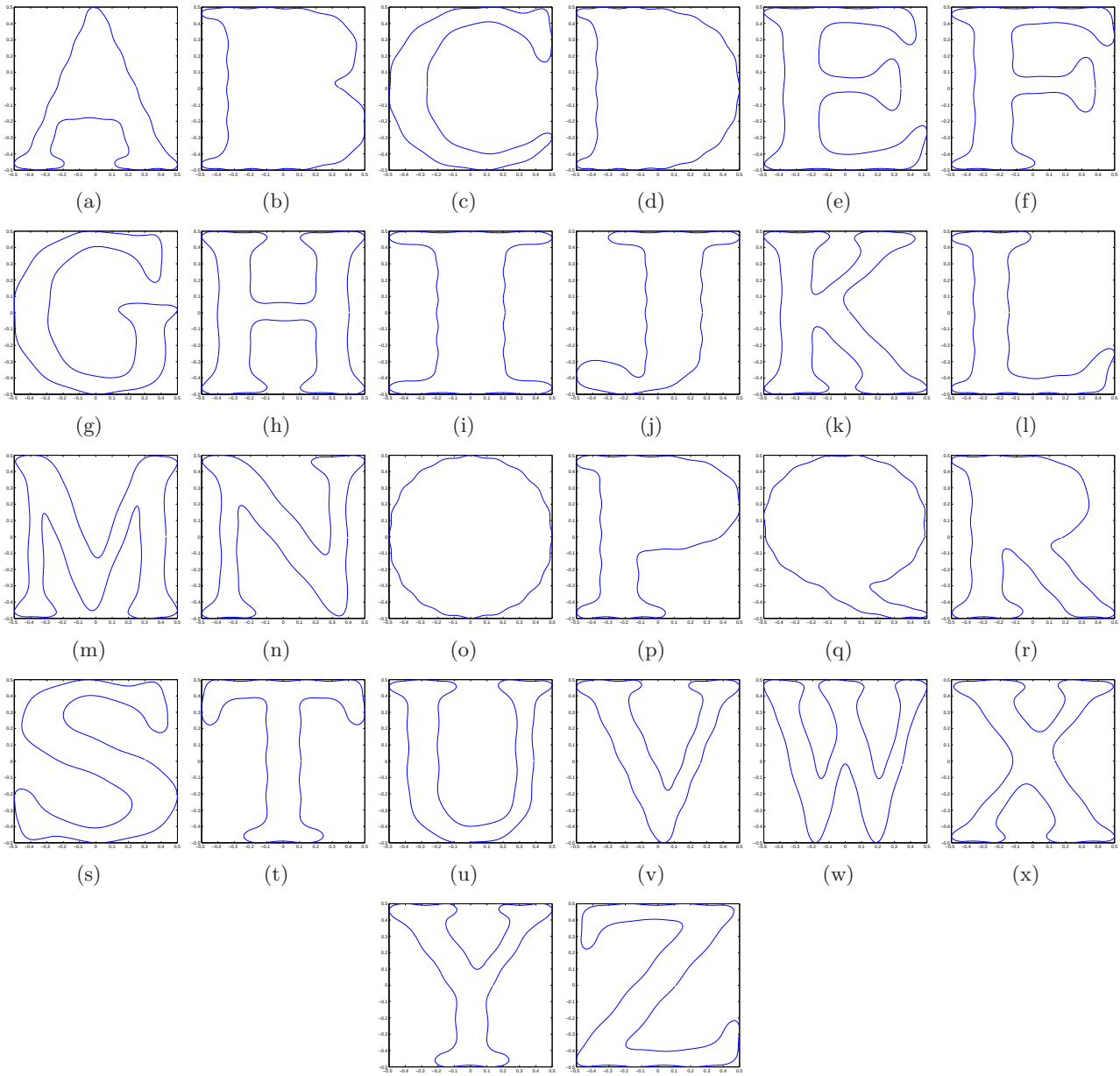

Figure 5.11: Non standard letters obtained by perturbing and smoothing those in Figure 5.10.

CHAPTER 6

Tracking of a Mobile Target

The results of this chapter have been submitted in [7]

Abstract

In this chapter we apply an extended Kalman filter to track both the location and the orientation of a mobile target from the multistatic response measurements described in chapter 4. We also analyze the effect of the limited-view aspect on the stability and the efficiency of our tracking approach.

6.1 Introduction

In this chapter we apply an extended Kalman filter to track both the location and the orientation of a mobile target directly from MSR measurements.

The Extended Kalman Filter (EKF) is a generalization of the Kalman Filter (KF) to nonlinear dynamical systems. It is robust with respect to noise and computationally inexpensive, therefore is well suited for real-time applications such as tracking [114].

Target tracking is an important task in sonar and radar imaging, security technologies, autonomous vehicle, and robotics. The use of Kalman-type filtering for target tracking is quite standard, see, for instance, [44, 45, 47, 56, 61, 113].

However, to the best of our knowledge, this is the first time where tracking of the orientation of a target is provided. Moreover, we analyze the ill-posed character of both the location and orientation tracking in the case of limited-view data. In practice, it is quite realistic to have the sources/receivers cover only a limited angle of view. In this case, the reconstruction of the GPTs becomes more ill-posed than in the full-view case.

It is the aim of this chapter to provide a fast algorithm for tracking both the location and the orientation of a mobile target, in the toy model described in chapter 4.

The chapter is organized as follows. In section 6.2 we present a GPT-based location and orientation tracking algorithm using an extended Kalman filter and show the numerical results in the full-view setting. The chapter ends with a few concluding remarks. A brief review of the extended Kalman filter is given in appendix B.1.

6.2 Tracking of a mobile target

In this section, we describe the setting of the tracking problem, and define in detail the algorithm that will be used.

6.2.1 Time dependent data acquisition

Except for the few modifications below, we keep the notations that have been used throughout chapters 4-5.

At the instant $t \geq 0$, we denote by $z_t = [x_t, y_t]^\top \in \mathbb{R}^2$ the location and $\theta_t \in [0, 2\pi)$ the orientation of a target D_t.

$$D_t = z_t + R_{\theta_t} D, \tag{6.1}$$

where R_{θ_t} is the rotation by θ_t. Let $\mathbf{M}_t$ be the CGPT of D_t, and $\mathbf{M}_D$ be the CGPT of D. Then the equation (4.30) becomes

$$\mathbf{V}_t = L(\mathbf{M}_t) + \mathbf{E}_t + \mathbf{W}_t, \tag{6.2}$$

where $\mathbf{E}_t$ is the truncation error, and $\mathbf{W}_t$ the measurement noise at time t.

The objective of *tracking* is to estimate the target's location z_t and orientation θ_t from the MSR data stream $\mathbf{V}_t$. We emphasize that these informations are contained in the first two orders CGPTs as shown in chapter 5. Precisely, let $\Delta x_t = x_t - x_{t-1}$, $\Delta y_t = y_t - y_{t-1}$ and $\Delta\theta_t = \theta_t - \theta_{t-1}$, then equations in proposition 5.2.1 become :

$$\begin{aligned} \mathbf{N}_{12}^{(1)}(D_t)/\mathbf{N}_{11}^{(1)}(D_t) &= 2(\Delta x_t + i\Delta y_t) + e^{i\Delta\theta_t}\mathbf{N}_{12}^{(1)}(D_{t-1})/\mathbf{N}_{11}^{(1)}(D_{t-1}), \\ \mathbf{N}_{12}^{(2)}(D_t)/\mathbf{N}_{11}^{(2)}(D_t) &= 2(\Delta x_t + i\Delta y_t) + e^{i\Delta\theta_t}\mathbf{N}_{12}^{(2)}(D_{t-1})/\mathbf{N}_{11}^{(2)}(D_{t-1}). \end{aligned} \tag{6.3}$$

Hence when the linear system (6.3) is solvable, one can estimate z_t, θ_t by solving and accumulating $\Delta x_t, \Delta y_t$ and $\Delta\theta_t$. However, such an algorithm will propagate the error over time, since the noise presented in data is not properly taken into account here.

In the following we develop a CGPT-based tracking algorithm using the Extended Kalman Filter, which handles correctly the noise. We recall first the definition of complex CGPT, with which a simple relation between $\mathbf{M}_t$ and $\mathbf{M}_D$ can be established.

6.2.2 Time relationship between CGPTs

Let $u = (1, i)^\top$. The complex CGPTs $\mathbf{N}^{(1)}, \mathbf{N}^{(2)}$ defined in (5.1) then verify :

$$\begin{aligned} N_{mn}^{(1)} &= (M_{mn}^{cc} - M_{mn}^{ss}) + i(M_{mn}^{cs} + M_{mn}^{sc}) = u^\top M_{mn} u, \\ N_{mn}^{(2)} &= (M_{mn}^{cc} + M_{mn}^{ss}) + i(M_{mn}^{cs} - M_{mn}^{sc}) = u^H M_{mn} u, \end{aligned}$$

where M_{mn} is the 2×2 matrix defined by

$$M_{mn} = \begin{pmatrix} M_{mn}^{cc} & M_{mn}^{cs} \\ M_{mn}^{sc} & M_{mn}^{ss} \end{pmatrix},$$

and H denotes the Hermitian transpose. Therefore, we have

$$\mathbf{N}^{(1)} = \mathbf{U}^\top \mathbf{M}\mathbf{U} \quad \text{and} \quad \mathbf{N}^{(2)} = \mathbf{U}^H \mathbf{M}\mathbf{U}, \tag{6.4}$$

where the matrix $\mathbf{U}$ of dimension $2K \times K$ over the complex fields is defined by

$$\mathbf{U} = \begin{pmatrix} u & 0 & \dots & 0 \\ 0 & u & \dots & 0 \\ \vdots & & \ddots & \vdots \\ 0 & \dots & 0 & u \end{pmatrix}, \tag{6.5}$$

and $\mathbf{M}$ is the matrix whose (m,n) block is given by M_{mn}.

To recover the CGPT $\mathbf{M}$ from the complex CGPTs $\mathbf{N}^{(1)}, \mathbf{N}^{(2)}$, we simply use the relations

$$\begin{aligned} M^{cc}_{mn} &= \frac{1}{2}\Re(N^{(1)}_{mn} + N^{(2)}_{mn}),\ M^{cs}_{mn} = \frac{1}{2}\Im(N^{(1)}_{mn} + N^{(2)}_{mn}), \\ M^{sc}_{mn} &= \frac{1}{2}\Im(N^{(1)}_{mn} - N^{(2)}_{mn}),\ M^{ss}_{mn} = \frac{1}{2}\Re(N^{(2)}_{mn} - N^{(1)}_{mn}), \end{aligned} \tag{6.6}$$

where $\Re, \Im$ are the real and imaginary part of a complex number, respectively. For two targets D_t, D satisfying (6.1), equations (5.11) and (5.12) give us

$$\mathbf{N}^{(1)}(D_t) = \mathbf{F}_t^\top \mathbf{N}^{(1)}(D)\mathbf{F}_t, \tag{6.7a}$$

$$\mathbf{N}^{(2)}(D_t) = \mathbf{F}_t^H \mathbf{N}^{(2)}(D)\mathbf{F}_t, \tag{6.7b}$$

where $\mathbf{F}_t$ is a upper triangle matrix with the (m,n)-th entry given by

$$(\mathbf{F}_t)_{mn} = \binom{n}{m}(x_t + iy_t)^{n-m}e^{im\theta_t}. \tag{6.8}$$

Linear operator $\mathbf{T}_t$:

Now one can find explicitly a linear operator $\mathbf{T}_t$ (the underlying scalar field is $\mathbb{R}$) which depends only on z_t, θ_t, such that $\mathbf{M}_t = \mathbf{T}_t(\mathbf{M}_D)$, and the equation (6.2) becomes

$$\mathbf{V}_t = L(\mathbf{T}_t(\mathbf{M}_D)) + \mathbf{E}_t + \mathbf{W}_t. \tag{6.9}$$

For doing so, we set $\mathbf{J}_t := \mathbf{U}\mathbf{F}_t$, where $\mathbf{U}$ is given by (6.5). Then, a straightforward computation using (6.4), (6.6), and (6.7) shows that

$$\begin{aligned} \mathbf{M}^{cc}(D_t) &= \Re\mathbf{J}_t^\top \mathbf{M}_D \Re\mathbf{J}_t,\ \mathbf{M}^{cs}(D_t) = \Re\mathbf{J}_t^\top \mathbf{M}_D \Im\mathbf{J}_t, \\ \mathbf{M}^{sc}(D_t) &= \Im\mathbf{J}_t^\top \mathbf{M}_D \Re\mathbf{J}_t,\ \mathbf{M}^{ss}(D_t) = \Im\mathbf{J}_t^\top \mathbf{M}_D \Im\mathbf{J}_t, \end{aligned} \tag{6.10}$$

where $\mathbf{M}^{cc}(D_t), \mathbf{M}^{cs}(D_t), \mathbf{M}^{sc}(D_t), \mathbf{M}^{ss}(D_t)$ are the matrices with coefficients (m,n) defined in (4.14)-(4.14). Therefore, we get the operator $\mathbf{T}_t$:

$$\begin{aligned} \mathbf{T}_t(\mathbf{M}_D) = \Re\mathbf{U}(\Re\mathbf{J}_t^\top \mathbf{M}_D \Re\mathbf{J}_t)\Re\mathbf{U}^\top + \Re\mathbf{U}(\Re\mathbf{J}_t^\top \mathbf{M}_D \Im\mathbf{J}_t)\Im\mathbf{U}^\top + \\ \Im\mathbf{U}(\Im\mathbf{J}_t^\top \mathbf{M}_D \Re\mathbf{J}_t)\Re\mathbf{U}^\top + \Im\mathbf{U}(\Im\mathbf{J}_t^\top \mathbf{M}_D \Im\mathbf{J}_t)\Im\mathbf{U}^\top = \mathbf{M}_t. \end{aligned} \tag{6.11}$$

6.2.3 Tracking by the Extended Kalman Filter

The EKF is a generalization of the KF to nonlinear dynamical systems. Unlike KF which is an optimal estimator for linear systems with Gaussian noise, EKF is no longer optimal, but it remains robust with respect to noise and computationally inexpensive, therefore is well suited for real-time applications such as tracking. We establish here the *system state* and the *observation* equations which are fundamental to EKF, and refer readers to Appendix B.2 for its algorithmic details.

System state observation equations

We assume that the position of the target is subjected to an external driving acceleration that has the form of a white noise. In other words the velocity $(V(\tau))_{\tau\in\mathbb{R}^+}$ of the target is given in terms of a two-dimensional Brownian motion $(W_a(\tau))_{\tau\in\mathbb{R}^+}$ and its position $(Z(\tau))_{\tau\in\mathbb{R}^+}$ is given in terms of the integral of this Brownian motion:

$$V(\tau) = V_0 + \sigma_a W_a(\tau), \qquad Z(\tau) = Z_0 + \int_0^\tau V(s)ds.$$

The orientation $(\Theta(\tau))_{\tau\in\mathbb{R}^+}$ of the target is subjected to random fluctuations and its angular velocity is given in terms of an independent white noise, so that the orientation is given in terms of a one-dimensional Brownian motion $(W_\theta(\tau))_{\tau\in\mathbb{R}^+}$:

$$\Theta(\tau) = \Theta_0 + \sigma_\theta W_\theta(\tau).$$

We observe the target at discrete times $t\Delta\tau$, $t \in \mathbb{N}$, with time step $\Delta\tau$. We denote $z_t = Z(t\Delta\tau)$, $v_t = V(t\Delta\tau)$, and $\theta_t = \Theta(t\Delta\tau)$. They obey the recursive relations

$$\begin{aligned} v_t &= v_{t-1} + a_t, & a_t &= \sigma_a\big(W_a(t\Delta\tau) - W_a((t-1)\Delta\tau)\big), \\ z_t &= z_{t-1} + v_{t-1}\Delta\tau + b_t, & b_t &= \sigma_a \int_{(t-1)\Delta\tau}^{t\Delta\tau} W_a(s) - W_a((t-1)\Delta\tau)ds, \\ \theta_t &= \theta_{t-1} + c_t, & c_t &= \sigma_\theta\big(W_\theta(t\Delta\tau) - W_\theta((t-1)\Delta\tau)\big). \end{aligned} \tag{6.12}$$

Since the increments of the Brownian motions are independent from each other, the vectors $(U_t)_{t\geq 1}$ given by

$$U_t = \begin{pmatrix} a_t \\ b_t \\ c_t \end{pmatrix}$$

are independent and identically distributed with the multivariate normal distribution with mean zero and covariance matrix $\mathbf{\Sigma}$ given by

$$\mathbf{\Sigma} = \Delta\tau \begin{pmatrix} \sigma_a^2\mathbf{I}_2 & \frac{\sigma_a^2}{2}\Delta\tau\mathbf{I}_2 & 0 \\ \frac{\sigma_a^2}{2}\Delta\tau\mathbf{I}_2 & \frac{\sigma_a^2}{3}\Delta\tau^2\mathbf{I}_2 & 0 \\ 0 & 0 & \sigma_\theta^2 \end{pmatrix} \tag{6.13}$$

The evolution of the state vector

$$X_t = \begin{pmatrix} v_t \\ z_t \\ \theta_t \end{pmatrix}$$

takes the form

$$X_t = \mathbf{F}X_{t-1} + U_t, \qquad \mathbf{F} = \begin{pmatrix} \mathbf{I}_2 & 0 & 0 \\ \Delta\tau\mathbf{I}_2 & \mathbf{I}_2 & 0 \\ 0 & 0 & 1 \end{pmatrix} \tag{6.14}$$

The observation made at time t is the MSR matrix given by (6.9), where the system state X_t is implicitly included in the operator $\mathbf{T}_t$. We suppose that the truncation error $\mathbf{E}_t$ is small compared to the measurement noise so that it can be dropped in (6.9), and that the Gaussian white noise $\mathbf{W}_t$ of different time are mutually independent. We emphasize that the velocity vector v_t of the target does not contribute to (6.9), which can be seen from (6.1). To highlight the dependence upon z_t, θ_t, we introduce a function $\mathbf{h}$ which is nonlinear in z_t, θ_t, and takes $\mathbf{M}_D$ as a parameter, such that

$$\mathbf{h}(X_t; \mathbf{M}_D) = \mathbf{h}(z_t, \theta_t; \mathbf{M}_D) = L(\mathbf{T}_t(\mathbf{M}_D)). \tag{6.15}$$

Then together with (6.14) we get the following *system state* and *observation* equations:

$$X_t = \mathbf{F}X_{t-1} + U_t, \tag{6.16a}$$
$$\mathbf{V}_t = \mathbf{h}(X_t; \mathbf{M}_D) + \mathbf{W}_t. \tag{6.16b}$$

Note that (6.16a) is linear, so in order to apply EKF on (6.16), we only need to linearize (6.16b), or in other words, to calculate the partial derivatives of $\mathbf{h}$ with respect to x_t, y_t, θ_t.

Linearization of the observation equation

Clearly, the operator L contains only the information concerning the acquisition system and does not depend on x_t, y_t, θ_t. So by (6.15), we have

$$\partial_{x_t}\mathbf{h} = L(\partial_{x_t}\mathbf{T}_t(\mathbf{M}_D)), \tag{6.17}$$

while the calculation for $\partial_{x_t}\mathbf{T}_t$ is straightforward using (6.11). We have

$$\begin{aligned}\partial_{x_t}\mathbf{T}_t(\mathbf{M}_D) =& \Re\mathbf{U}\partial_{x_t}(\Re\mathbf{J}_t^\top\mathbf{M}_D\Re\mathbf{J}_t)\Re\mathbf{U}^\top + \Re\mathbf{U}\partial_{x_t}(\Re\mathbf{J}_t^\top\mathbf{M}_D\Im\mathbf{J}_t)\Im\mathbf{U}^\top + \\ & \Im\mathbf{U}\partial_{x_t}(\Im\mathbf{J}_t^\top\mathbf{M}_D\Re\mathbf{J}_t)\Re\mathbf{U}^\top + \Im\mathbf{U}\partial_{x_t}(\Im\mathbf{J}_t^\top\mathbf{M}_D\Im\mathbf{J}_t)\Im\mathbf{U}^\top,\end{aligned} \tag{6.18}$$

where the derivatives are found by the chain rule:

$$\begin{aligned}\partial_{x_t}(\Re\mathbf{J}_t^\top\mathbf{M}_D\Re\mathbf{J}_t) &= \Re(\partial_{x_t}\mathbf{J}_t^\top)\mathbf{M}_D\Re\mathbf{J}_t + \Re\mathbf{J}_t^\top\mathbf{M}_D\Re(\partial_{x_t}\mathbf{J}_t),\\ \partial_{x_t}(\Re\mathbf{J}_t^\top\mathbf{M}_D\Im\mathbf{J}_t) &= \Re(\partial_{x_t}\mathbf{J}_t^\top)\mathbf{M}_D\Im\mathbf{J}_t + \Re\mathbf{J}_t^\top\mathbf{M}_D\Im(\partial_{x_t}\mathbf{J}_t),\\ \partial_{x_t}(\Im\mathbf{J}_t^\top\mathbf{M}_D\Re\mathbf{J}_t) &= \Im(\partial_{x_t}\mathbf{J}_t^\top)\mathbf{M}_D\Re\mathbf{J}_t + \Im\mathbf{J}_t^\top\mathbf{M}_D\Re(\partial_{x_t}\mathbf{J}_t),\\ \partial_{x_t}(\Im\mathbf{J}_t^\top\mathbf{M}_D\Im\mathbf{J}_t) &= \Im(\partial_{x_t}\mathbf{J}_t^\top)\mathbf{M}_D\Im\mathbf{J}_t + \Im\mathbf{J}_t^\top\mathbf{M}_D\Im(\partial_{x_t}\mathbf{J}_t),\end{aligned}$$

and $\partial_{x_t}\mathbf{J}_t = \mathbf{U}\partial_{x_t}\mathbf{F}_t$. The (m,n)-th entry of the matrix $\partial_{x_t}\mathbf{F}_t$ is given by

$$(\partial_{x_t}\mathbf{F}_t)_{m,n} = \binom{n}{m}(n-m)z_t^{n-m-1}e^{im\theta_t}. \tag{6.19}$$

The derivatives $\partial_{y_t}\mathbf{T}_t(\mathbf{M}_D)$ and $\partial_{\theta_t}\mathbf{T}_t(\mathbf{M}_D)$ are calculated in the same way.

6.3 Numerical results

In this section, we perform computation of such experiments of tracking. We treat both the problem of full-view (subsection 6.3.1) and partial-view (subsection 6.3.2) settings.

6.3.1 Numerical experiments of tracking in the full-view setting

Here we show the performance of EKF in a full angle of view setting with the shape 'A' as target D, which has diameter 10 and is centered at the origin. The path (z_t, θ_t) is simulated according to the model (6.12) during a period of 10 seconds ($\Delta\tau = 0.01$ second), with parameters $\sigma_a = 2, \sigma_\theta = 0.5$, and the initial state $X_0 = (v_0, z_0, \theta_0)^\top = (-1, 1, 5, -5, 3\pi/2)^\top$. We make sure that the target is always included inside the measurement circle on which $N = 20$ sources/receivers are fixed, see Figure 6.1. The data stream $\mathbf{V}_t$ is generated by first calculating the MSR matrix corresponding to each $D_t, t \geq 0$ then adding a white noise.

Suppose that the CGPT of D is correctly determined by dictionary matching as described in chapter 5. Then we use the first two orders CGPT $\mathbf{M}_D$ of D in (6.16b), and take $(0, 0, 10, -0.5, 0)^\top$ as initial guess of X_0 for EKF.

We add 10% and 20% of noise to data, and show the results of tracking in Figure 6.2 (a) (c) and (e). We see that EKF can find the true system state, despite of the poor initial guess, and the tracking precision decays as the measurement noise level gets higher. The same experiment with small target (of same shape) of diameter 1 is repeated in Figure 6.2 (b) (d) and (f), where the tracking of position remains correct, on the contrary, that of orientation fails when the noise level is high. Such a result is in accordance with physical intuitions. In fact, the position of a small target can be easily localized in the far field, while its orientation can be correctly determined only in the near field.

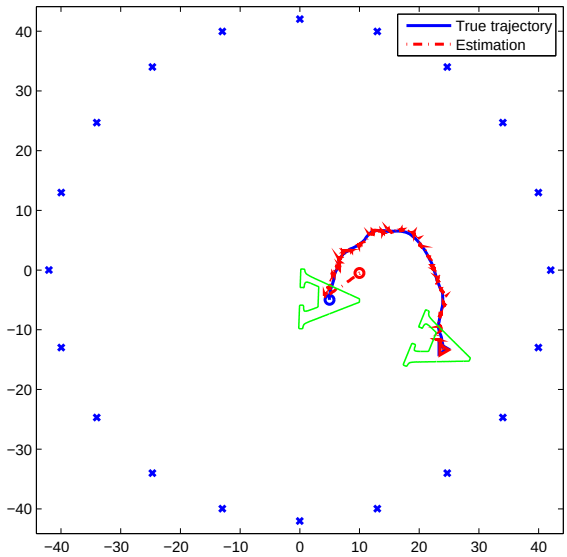

Figure 6.1: Trajectory of the letter 'A' and the estimation by EKF. The initial position is $(5, -5)$ while the initial guess given to EKF is $(10, -0.5)$. The crosses indicate the position of sources/receivers, while the circle and the triangle indicate the starting and the final position of the target, respectively. In blue is the true trajectory and in red the estimated one.

6.3.2 Tracking in the limited-view setting

The performance of the tracking algorithm can also be affected by the limited angle of view. We repeat the experiment of subsection 6.3.1 with $\delta = 10$, $\gamma = \pi$, and the same initial guess. In the first configuration, $N = 21$ sources/receivers are equally distributed between $[0, \gamma)$, see Figure 6.3 (a). The results of tracking by EKF presented in Figure 6.4 (a), (c) and (e) show large deviations in the estimation of position, and a totally wrong estimation of orientation. In the second configuration, we divide the sources/receivers into 5 groups placed in a nonuniform way on $[0, 2\pi)$, and each group covers only an angle range of 0.2π, see Figure 6.3 (b). Although the total angular coverages are the same in both configurations, the second one gives much better tracking results, as shown in Figure 6.4 (b), (d) and (f). These results clearly demonstrates the importance of a large angle of view (or a directional diversity) for the tracking problem.

6.4 Conclusion

In this chapter we have provided a location and orientation tracking of a mobile target from MSR measurements in the full- and limited-view settings. In the limited-view case, the effect of noise is severe on the tracking. However, if the arrays of receivers and transmitters offer a good directional diversity, then satisfactory results can be obtained. It would be interesting to generalize our algorithms for tracking mul-

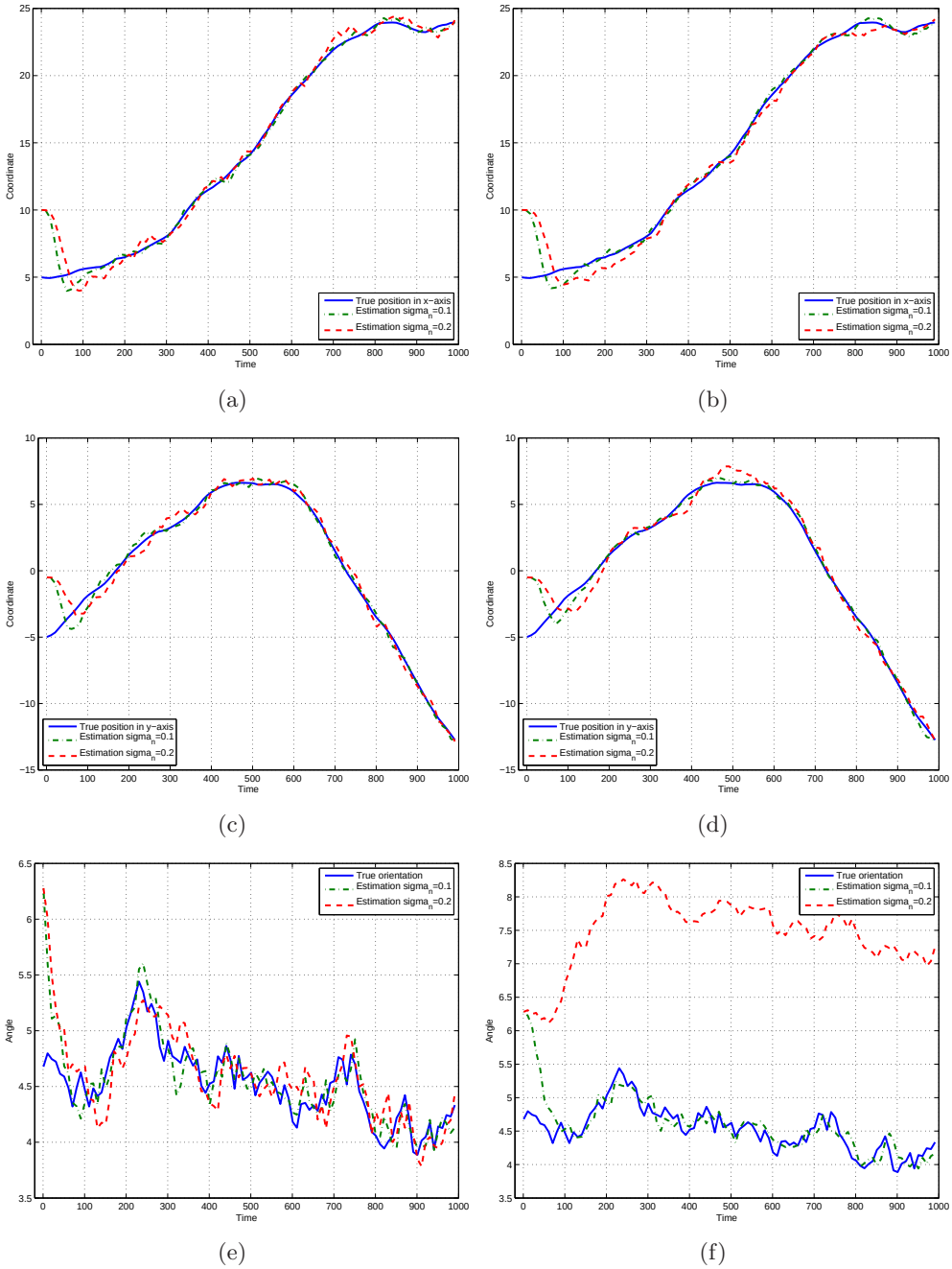

Figure 6.2: Results of tracking using the configuration of Figure 6.1 at different noise levels. First row: coordinate in x-axis. Second row: coordinate in y-axis. Last row: orientation. In the first column the target has size 10, while in the second column the target has size 1. The solid line always indicates the true system state.

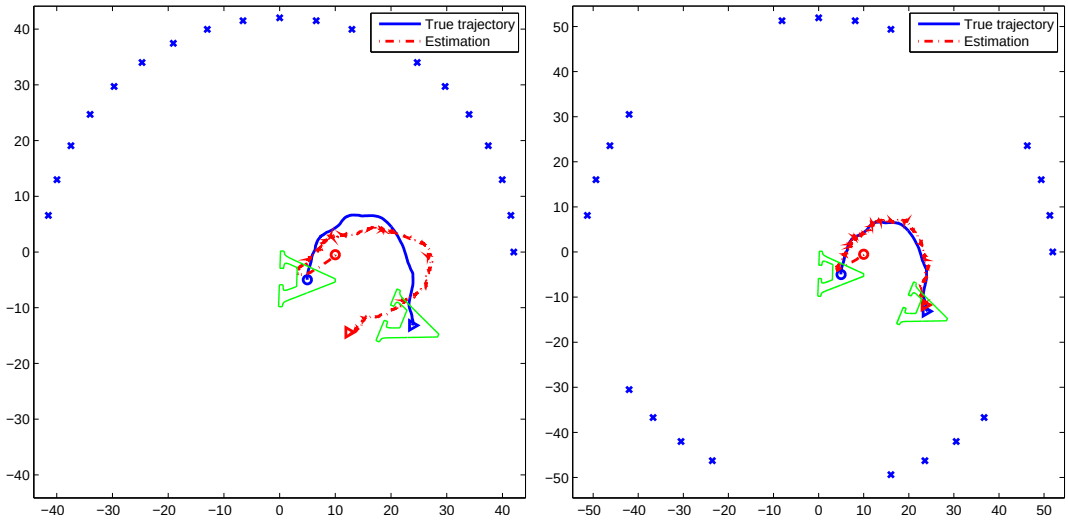

(a) (b)

Figure 6.3: Same experiment as in Figure 6.1, with a limited angle of view $\gamma = \pi$. In Figure(a) sources/receivers are equally distributed between $[0, \gamma)$, while in Figure(b) they are divided into 5 groups.

tiple targets. As a first step, a matching pursuit algorithm [80] would be appropriate for recognizing the targets.

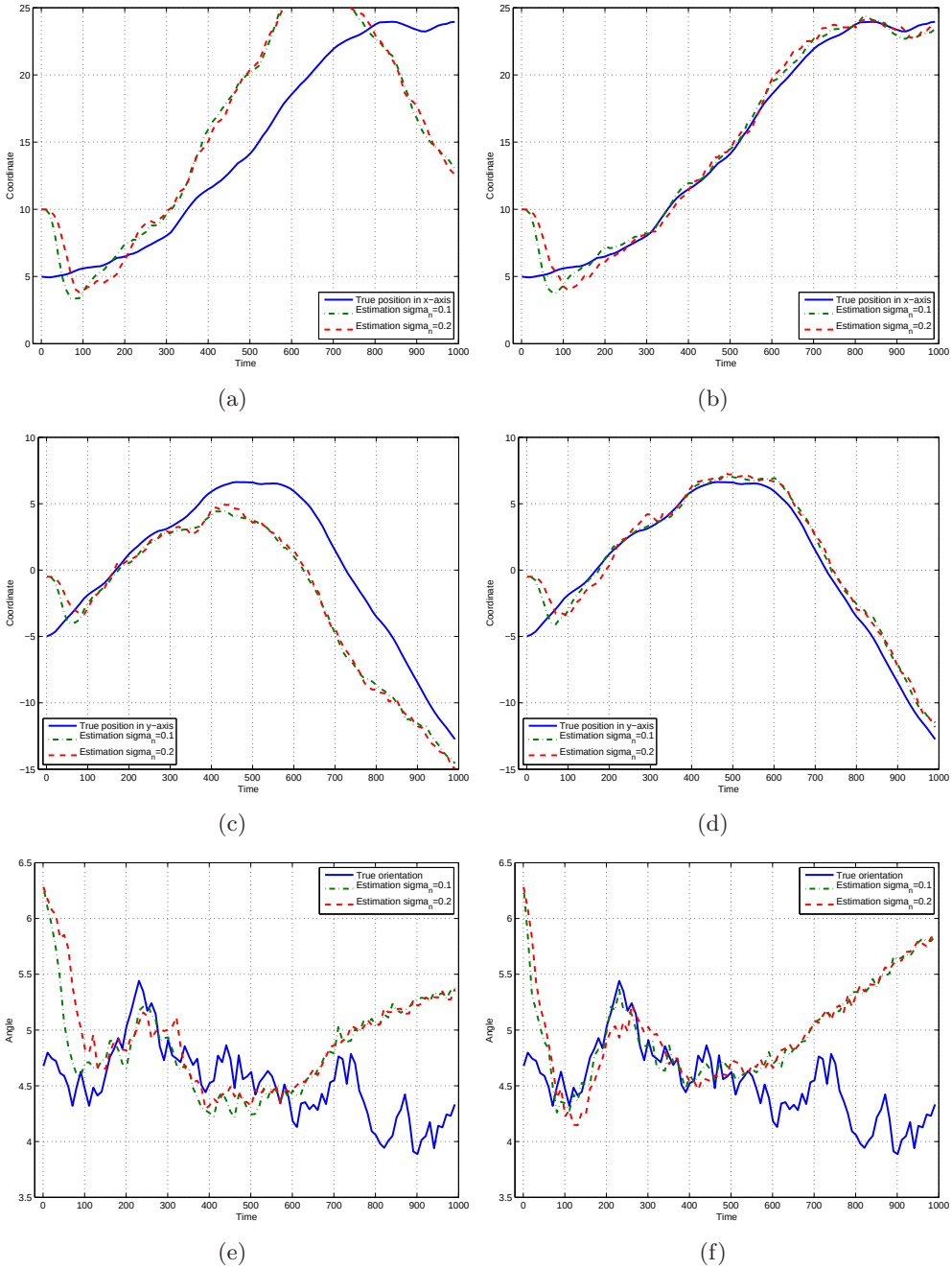

Figure 6.4: Results of tracking using the configuration of Figure 6.3 at different noise levels. First row: coordinate in x-axis. Second row: coordinate in y-axis. Last row: orientation. First and second column correspond to the configuration in Figure 6.3 (a) and (b), respectively.

CHAPTER 7

Shape Recognition and Classification in Electro-Sensing

The results of this chapter have been submitted in [6].

Abstract

In this chapter, we apply the previous results to explain how weakly electric fish might identify and classify a target, knowing by advance that the latter belongs to a certain collection of shapes. The electric fish would first locate the target using a specific location search algorithm (see chapter 3). Then it could extract, from the perturbations of the electric field, generalized (or high-order) polarization tensors of the target (see chapter 4). Computing, from the extracted features, invariants under rigid motions and scaling yields shape descriptors. Then, the fish might classify a target by comparing these invariants with those of a set of learned shapes (chapter 5).

On the other hand, when measurements are taken at multiple frequencies, the fish might exploit the shifts and use the spectral content of the generalized polarization tensors to dramatically improve the stability with respect to measurement noise of the classification procedure in electro-sensing. Surprisingly, it turns out that the first-order polarization tensor at multiple frequencies could be enough for the purpose of classification.

A procedure to eliminate the background field in the case where the permittivity of the surrounding medium can be neglected, and hence improve further the stability of the classification process, is also discussed.

7.1 Introduction

In this chapter, we tackle the challenging problem of shape recognition and classification. Hence, we come back to the model developped in chapter 2, which will be recalled in subsection 7.2.1. In order to explain how the shape information is encoded in measured data, we first adapt the multipolar expansion found in section 4.2.1 to the electrolocation problem. As stated before, this asymptotic expansion generalizes Rasnow's formula [91] in two directions: (i) it is a higher-order approximation of the effect of a nearby

target and it is valid for an arbitrary shape and admittivity contrast and (ii) it takes also into account the fish's body. As it has been proved in chapter 2, by postprocessing the measured data using layer potentials associated only to the fish's body, one can reduce the multipolar formula to the one in free space, *i.e.*, without the fish.

Then we show how to identify and classify a target, knowing by advance that the latter belongs to a dictionary of pre-computed shapes. The shapes considered in this paper have been experimentally tested and results reported in [110]. This idea comes naturally in mind when modeling behavioral experiments such as in [109, 111, 112]. The pre-computed shapes would then be a model for the fish's memory (trained to recognize specific shapes), and the experience of recognition presented here would simulate the discrimination exercises that are then imposed to them.

We develop two algorithms for shape classification: one based on shape descriptors while the second is based on spectral induced polarizations. We first extract, from the data, generalized (or high-order) polarization tensors of the target (GPTs) as in chapter 4. Note that the shape features are encoded in the high-order polarization tensors. The noise level in the reconstructed generalized polarization tensors depends on the angle of view. Larger is the angle of view, more stable is the reconstruction (shown in chapter 4). l_1-regularization techniques could be used, as seen in section 4.3.3. Then we compute from the extracted features invariants under rigid motions and scaling. Comparing these invariants with those in a dictionary of pre-computed shapes (see chapter 5), we successfully classify the target. Since the measurements are taken at multiple frequencies, we make use of the spectral content of the generalized polarization tensor in order to dramatically improve the stability with respect to measurement noise of the physics-based classification procedure. In fact, we show numerically that the first-order polarization tensor at multiple frequencies is enough for the purpose of classification.

This chapter is organized as follows. In section 7.2, we adapt the extraction of GPTs defined in chapter 4 to the physically relevant model for electrolocation derived in chapter 2. In section 7.3 we apply the algorithm of dictionary matching (which was the purpose of chapter 5). Finally, we illustrate our findings in section 7.4 with numerical experiments.

7.2 Feature extraction from induced current measurements

7.2.1 Electro-sensing model

Let us recall the nondimensionalized model of electro-sensing, detailed in chapter 2: the body of the fish is Ω (of size of order 1), an open bounded set in $\mathbb{R}^d, d = 2, 3$, of class $\mathcal{C}^{1,\alpha}$, $0 < \alpha < 1$, with outward normal unit vector ν. The electric organ is a dipole J placed at $x_0 \in \Omega$ or a sum of point sources inside Ω satisfying the neutrality condition. The non-dimensionalized model presented in chapter 2 lead us to consider that the conductivity of the background medium is 1 and that its permittivity is vanishing. Consider a target $D = z + \delta B$, where $\delta \ll 1$ is the characteristic size of D, z is its location, and B a smooth bounded domain containing the origin. We assume that D is of complex admittivity $k = \sigma + i\varepsilon\omega$, with ω being the operating frequency in the range $[1, 10]$ and σ and ε being respectively the conductivity and the permittivity of the target. It has been also shown in chapter 2 that, in the presence of D, the electric field u generated by the

fish is the solution of the following system:

$$\begin{cases} \Delta u = J & \text{in } \Omega, \\ \nabla \cdot (1 + (k-1)\chi_D)\nabla u = 0 & \text{in } \mathbb{R}^d \setminus \overline{\Omega}, \\ \left.\dfrac{\partial u}{\partial \nu}\right|_- = 0 & \text{on } \partial\Omega, \\ u|_+ - u|_- = \xi \left.\dfrac{\partial u}{\partial \nu}\right|_+ & \text{on } \partial\Omega \\ |u(x)| = O(|x|^{-d+1}), \ |x| \to \infty. \end{cases} \tag{7.1}$$

Here, χ_D is the characteristic function of D. Figure 7.1 shows isopotentials with and without a target with zero permittivity but different conductivity from the surrounding medium. Note that if the target's admittivity depends on the frequency (*i.e.*, if the permittivity is nonzero), then a phase shift in the electrical potential is induced.

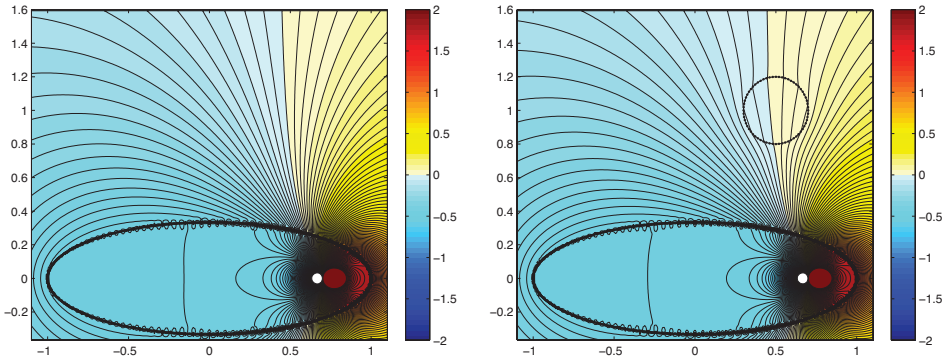

(a) (b)

Figure 7.1: Isopotentials without (a) and with (b) a target with $\sigma = 5$ and $\varepsilon = 0$.

In chapters 4 and 5, we have extracted the GPTs of a target by multistatic measurements using arrays of sources and receptors. These GPTs were then arranged and compared to a dictionary of already known shapes. This chapter aims at adapting this method to the electro-sensing problem. The same problem as in chapter 3 holds : the fish carries only one source, its electric organ J. Hence, in subsection 7.2.3 we will use the information given by its swimming patterns.

7.2.2 Asymptotic formalism

The first step is to compute the GPTs from the measurements. In this regard, the next result will be useful. Except when mentioned, we will fix in this section the frequency ω, leading to a fixed complex admittivity k. Recall that the Green's function, defined in (2.15), is given by

$$G(x) = \begin{cases} \dfrac{1}{2\pi} \ln |x|, & d = 2, \\ -\dfrac{1}{4\pi} \dfrac{1}{|x|}, & d = 3. \end{cases}$$

As defined in (2.14) and(2.17), we denote the single and double layer potentials of a function $\phi \in L^2(\partial\Omega)$ as $\mathcal{S}_\Omega[\phi]$ and $\mathcal{D}_\Omega[\phi]$, and the Neumann-Poincaré operator for Ω is denoted $\mathcal{K}^*_\Omega$.

We still assume that the target is away from the fish, *i.e.*, the distance between the fish and the target is much larger than the target's characteristic size but smaller than the range of the electrolocation which does not exceed two fish's body lengths. The following theorem adpats the multipolar expansion computed in section 4.2.1 to our problem.

Theorem 7.2.1. *Let us define the function $H : \mathbb{R}^d \to \mathbb{C}$ by*

$$H(x) = p(x) + \mathcal{S}_\Omega \left[\left. \frac{\partial u}{\partial \nu} \right|_+ \right] - \xi \mathcal{D}_\Omega \left[\left. \frac{\partial u}{\partial \nu} \right|_+ \right], \tag{7.2}$$

where p is the field created by the dipole J, i.e., $\Delta p = J$ in $\mathbb{R}^d$. Then, for every integer $K \geq 1$, the following expansion holds

$$u(x) = H(x) + \delta^{d-2} \sum_{|\alpha|=1}^{K} \sum_{|\beta|=1}^{K-|\alpha|+1} \frac{(-1)^{|\beta|} \delta^{|\alpha|+|\beta|}}{\alpha! \beta!} \partial^\alpha H(z) M_{\alpha\beta}(\lambda, B) \partial^\beta G(x-z) + O(\delta^{d+K}), \tag{7.3}$$

uniformly for $x \in \partial\Omega$.

Let us make a few remarks. First, the definition of the GPTs still holds for complex-valued λ. However, some properties are lost by this change; thus one has to study them more carefully in this situation. Second, the function H, which is computed from the boundary measurements, still depends on δ but this is not important for our present study. Indeed, formula (7.3) could have been derived - as in (2.51) - with U, the background solution in the absence of the target, instead of H and G_R - the Green function associated to Robin conditions on $\partial\Omega$ - instead of G, but it is much easier to compute $\partial^\alpha H(z)$ and $\partial^\beta G(x-z)$ once z is known. This leads us to the third remark: the location z is supposed to be known from the algorithm developed in chapter 3. Note that electrolocation algorithm could be also based on the fish's movement if only one frequency is used [75].

We will follow the proof of [19, Theorem 4.8]. In a first step, let us show the following formula.

Lemma 7.2.2. *For $x \in \mathbb{R}^d$,*

$$u(x) = H(x) + \mathcal{S}_D(\lambda I - \mathcal{K}_D^*)^{-1} \left[\left. \frac{\partial H}{\partial \nu} \right|_{\partial D} \right](x), \tag{7.4}$$

Proof. In section 2.5.1, it is shown that

$$u(x) = p(x) + \mathcal{S}_\Omega[\psi](x) + \mathcal{D}_\Omega[\phi](x) + \mathcal{S}_D[\phi](x),$$

see equation (2.58). Here the functions ψ, $\phi \in L^2(\partial\Omega)$ and $\phi \in L^2(\partial D)$ verify the system (2.59) that we recall here :

$$\begin{cases} \phi = -\xi\psi \quad \text{on } \partial\Omega, \\ \left(\frac{I}{2} - \mathcal{K}_\Omega^* + \xi \frac{\partial \mathcal{D}_\Omega}{\partial \nu}\right)[\psi] - \frac{\partial}{\partial \nu}(\mathcal{S}_D[\phi]) = \frac{\partial p}{\partial \nu} \quad \text{on } \partial\Omega, \\ -\frac{\partial}{\partial \nu}(\mathcal{S}_\Omega[\psi]) + \xi \frac{\partial}{\partial \nu}(\mathcal{D}_\Omega[\psi]) + (\lambda I - \mathcal{K}_D^*)[\phi] = \frac{\partial p}{\partial \nu} \text{ on } \partial D. \end{cases}$$

The third line gives us

$$\phi = (\lambda I - \mathcal{K}_D^*)^{-1} \left[\left. \frac{\partial H}{\partial \nu} \right|_{\partial D} \right],$$

and the jump formulas for the single and double layer potentials (2.16) give us

$$\psi = \left. \frac{\partial u}{\partial \nu} \right|_+ \quad \text{and } \phi = -u|_+ + u|_-,$$

so that, from the boundary conditions of the system (7.1), we obtain $p + \mathcal{S}_\Omega[\psi] + \mathcal{D}_\Omega[\phi] = H$ and the lemma is proved. □

We can now prove Theorem 7.2.1, using the arguments in [19, pp. 72-73]. Starting with formula (7.4), the proof relies on a Taylor expansion of H and the Green function involved in the single layer potential. Indeed, denoting

$$H_K(x) = \sum_{|\alpha|=0}^{K} \frac{1}{\alpha!} \partial^\alpha H(z)(x-z)^\alpha,$$

a Taylor expansion gives us

$$\left\| \frac{\partial H}{\partial \nu} - \frac{\partial H_K}{\partial \nu} \right\|_{L^2(\partial D)} \leq C\delta^K \left|\partial D\right|^{1/2},$$

and from [19, Formula (4.10)], we have for any $h \in L^2(\partial D)$ such that $\int_{\partial D} h = 0$:

$$\forall x \in \partial\Omega, \ \left|\mathcal{S}_D(\lambda I - \mathcal{K}_D^*)^{-1}[h](x)\right| \leq C\delta \left|\partial D\right|^{1/2} \left\|h\right\|_{L^2(\partial D)}.$$

Hence, using the fact that $|\partial D| = \delta^{d-1} |\partial B|$, we obtain

$$\begin{aligned} &\left\| \mathcal{S}_D(\lambda I - \mathcal{K}_D^*)^{-1} \left[\frac{\partial H}{\partial \nu} - \frac{\partial H_K}{\partial \nu} \right] \right\|_{L^\infty(\partial\Omega)} \\ &\qquad \leq C\delta \left|\partial D\right|^{1/2} \left\| \frac{\partial H}{\partial \nu} - \frac{\partial H_K}{\partial \nu} \right\|_{L^2(\partial D)} \leq C\delta^{d+K}. \end{aligned}$$

Plugging this inequality into (7.4) enables us to write, for $x \in \partial\Omega$,

$$u(x) = H(x) + \mathcal{S}_D(\lambda I - \mathcal{K}_D^*)^{-1} \left[\frac{\partial H_K}{\partial \nu} \right](x) + O(\delta^{d+K}).$$

By a change of variables $y' = (y-z)/\delta$, denoting $\phi_\alpha(y') = (\lambda I - \mathcal{K}_B^*)^{-1}[\nu \cdot \nabla w^\alpha](y')$ for $y' \in \partial B$ (where ν is here the outward normal unit vector to ∂B), we have (see for example the arguments in [12, Section 3])

$$u(x) - H(x) = \sum_{|\alpha|=0}^{K} \frac{1}{\alpha!} \partial^\alpha H(z) \delta^{|\alpha|+d-2} \int_{\partial B} G(x-z-\delta y')\phi_\alpha(y') d\sigma(y) + O(\delta^{d+K}).$$

We can now conclude by injecting a Taylor expansion of the Green function

$$G(x-z-\delta y) = \sum_{|\beta|=0}^{\infty} \frac{(-\delta)^{|\beta|}}{\beta!} \partial^\beta G(x-z) y^\beta,$$

in the integrand, giving

$$u(x) - H(x) = \delta^{d-2} \sum_{|\alpha|=0}^{K} \sum_{|\beta|=0}^{K-|\alpha|+1} \frac{(-1)^{|\beta|}\delta^{|\alpha|+|\beta|}}{\alpha!\beta!} \partial^\alpha H(z) \partial^\beta G(x-z) \int_{\partial B} y^\beta \phi_\alpha(y) d\sigma(y) + O(\delta^{d+K}).$$

The last term is $M_{\alpha\beta}(\lambda, B)$ by definition, see (4.9); it then suffices to show that the terms with $|\alpha| = 0$ or $|\beta| = 0$ vanish, which is the case because $\int_{\partial B} \phi_\alpha = 0$ and $\phi_\alpha = 0$ if $|\alpha| = 0$. Thus, Theorem 7.2.1 is proved. □

7.2.3 Data acquisition and reduction

As mentioned above, we will take advantage of the fact that the fish is swimming, in order to cop with the problem of having only one source. Let us suppose that the fish is moving, and let us take a sample of

$N_s \in \mathbb{N}^*$ different positions $(\Omega_s)_{1\leq s\leq N_s}$. This gives us $2N_s$ different functions $(u_s)_{1\leq s\leq N_s}$ and $(H_s)_{1\leq s\leq N_s}$, leading us to the following data matrix

$$\mathbf{V} := (V_{rs})_{1\leq s\leq N_s, 1\leq r\leq N_r} := \left(u_s(x_r^{(s)}) - H_s(x_r^{(s)})\right)_{1\leq r\leq N_s, 1\leq r\leq N_r}, \tag{7.5}$$

where $(x_r^{(s)} \in \partial\Omega_s)_{1\leq r\leq N_r}$ are the receptors of the fish being in the s^{th} position. The choices of indices emphasize then the fact that the different positions play the role of sources.

The goal of this subsection is to simplify this data set in order to extract the CGPTs (defined in (4.14)-(4.17)). Indeed, from (7.3), one has

$$V_{rs} = \delta^{d-2} \sum_{|\alpha|=1}^{K} \sum_{|\beta|=1}^{K-|\alpha|+1} (-1)^{|\beta|} \frac{\delta^{|\alpha|+|\beta|}}{\alpha!\beta!} \partial^\alpha H_s(z) M_{\alpha\beta}(\lambda, B) \partial^\beta G(x_r^{(s)} - z) + O(\delta^{d+K}). \tag{7.6}$$

As in chapter 4, we will express this formula in terms of CGPTs. From the definition of H, and with the help of formula (4.18), one can prove the following lemma.

Lemma 7.2.3. *Let the source J_s be a dipole of moment $\mathbf{p}_s$ placed at z_s:*

$$p_s(x) = \mathbf{p}_s \cdot \nabla G(x - z_s), \tag{7.7}$$

Then, for any $\alpha \in \mathbb{N}^2$, there exist two real numbers $A_{|\alpha|,s,z}$ and $B_{|\alpha|,s,z}$ such that

$$\frac{1}{\alpha!}\partial^\alpha H_s(z) = A_{|\alpha|,s,z} a_\alpha^{|\alpha|} + B_{|\alpha|,s,z} b_\alpha^{|\alpha|}.$$

Moreover, $A_{|\alpha|,s,z}$ and $B_{|\alpha|,s,z}$ can be expressed in the following way

$$\begin{aligned}
A_{m,s,z} &= \frac{(-1)^m}{2\pi} \mathbf{p}_s \cdot \begin{pmatrix} \phi_{m+1}(z - z_s) \\ \psi_{m+1}(z - z_s) \end{pmatrix} \\
&\quad - \frac{1}{2\pi m} \int_{\partial\Omega} \left.\frac{\partial u_s}{\partial \nu}\right|_+ (y) \phi_m(y - z) d\sigma(y), \\
&\quad - \frac{\xi}{2\pi} \int_{\partial\Omega} \begin{pmatrix} \phi_{m+1}(y - z) \\ \psi_{m+1}(y - z) \end{pmatrix} \cdot \nu_y \left.\frac{\partial u_s}{\partial \nu}\right|_+ (y)\, d\sigma(y), \\
B_{m,s,z} &= \frac{(-1)^m}{2\pi} \mathbf{p}_s \cdot \begin{pmatrix} \psi_{m+1}(z - z_s) \\ -\phi_{m+1}(z - z_s) \end{pmatrix} \\
&\quad - \frac{1}{2\pi m} \int_{\partial\Omega} \left.\frac{\partial u_s}{\partial \nu}\right|_+ (y) \psi_m(y - z) d\sigma(y) \\
&\quad - \frac{\xi}{2\pi} \int_{\partial\Omega} \begin{pmatrix} \psi_{m+1}(y - z) \\ -\phi_{m+1}(y - z) \end{pmatrix} \cdot \nu_y \left.\frac{\partial u_s}{\partial \nu}\right|_+ (y)\, d\sigma(y),
\end{aligned}$$

where the functions ϕ_m and ψ_m are defined for $x \in \mathbb{R}^2$, $x = (r_x, \theta_x)$ in the polar coordinates, by

$$\phi_m(x) = \frac{\cos m\theta_x}{r_x^m}, \quad \psi_m(x) = \frac{\sin m\theta_x}{r_x^m}.$$

Proof. Let us fix $\alpha \in \mathbb{N}^2$ and define $m = |\alpha|$. Let us recall the definition of H, given in (7.2)

$$H_s(x) = p_s(x) + \mathcal{S}_{\Omega_s}\left[\left.\frac{\partial u_s}{\partial \nu}\right|_+\right] - \xi \mathcal{D}_{\Omega_s}\left[\left.\frac{\partial u_s}{\partial \nu}\right|_+\right],$$

where $\Delta p_s = f_s$ in $\mathbb{R}^2$. From (7.7) it follows that

$$\partial^\alpha p_s(x) = \mathbf{p}_s \cdot \nabla \partial^\alpha G(x - z_s).$$

Hence, (4.18) yields

$$\begin{aligned}\frac{(-1)^{|\alpha|}}{\alpha!}\partial^\alpha p_s(z) = a_\alpha^m \left[\frac{-1}{2\pi m}\mathbf{p}_s \cdot \nabla\phi_m(z - z_s)\right] \\ + b_\alpha^m \left[\frac{-1}{2\pi m}\mathbf{p}_s \cdot \nabla\psi_m(z - z_s)\right].\end{aligned}$$

Moreover, we have

$$\nabla\phi_m = -m \begin{pmatrix} \phi_{m+1} \\ \psi_{m+1} \end{pmatrix}, \quad \nabla\psi_m = -m \begin{pmatrix} \psi_{m+1} \\ -\phi_{m+1} \end{pmatrix}.$$

In the same manner, from

$$\mathcal{S}_{\Omega_s}\left[\left.\frac{\partial u_s}{\partial \nu}\right|_+\right](x) = \int_{\partial\Omega_s} \left.\frac{\partial u_s(y)}{\partial \nu}\right|_+ G(y - x)d\sigma(y),$$

we can deduce

$$\begin{aligned}&\frac{1}{\alpha!}\partial^\alpha \mathcal{S}_{\Omega_s}\left[\left.\frac{\partial u_s}{\partial \nu}\right|_+\right](z) \\ &= \frac{1}{\alpha!}\int_{\partial\Omega_s} \left.\frac{\partial u_s}{\partial \nu}\right|_+ (y)(-1)^{|\alpha|}\partial^\alpha G(y - z)d\sigma(y) \\ &= a_\alpha^m \left(\int_{\partial\Omega_s} \frac{-1}{2\pi m} \left.\frac{\partial u_s}{\partial \nu}\right|_+ (y)\frac{\cos m\theta_{y-z}}{r_{y-z}^m}d\sigma(y)\right) \\ &+ b_\alpha^m \left(\int_{\partial\Omega_s} \frac{-1}{2\pi m} \left.\frac{\partial u_s}{\partial \nu}\right|_+ (y)\frac{\sin m\theta_{y-z}}{r_{y-z}^m}d\sigma(y)\right).\end{aligned}$$

Combining those two equations leads us to the desired result. □ From (7.6), the data matrix is then expressed as follows

$$\begin{aligned}Q_{rs} &= \sum_{|\alpha|+|\beta|=1}^{K+1} \left(A_{|\alpha|,s,z}a_\alpha^{|\alpha|} + B_{|\alpha|,s,z}b_\alpha^{|\alpha|}\right) \times M_{\alpha\beta}(\lambda, \delta B)\frac{-a_\beta^{|\beta|}\cos|\beta|\,\theta_{x_r^{(s)}-z} - b_\beta^{|\beta|}\sin|\beta|\,\theta_{x_r^{(s)}-z}}{2\pi\,|\beta|\,r^{|\beta|}_{x_r^{(s)}-z}} + O(\delta^{K+2}) \\ &= \sum_{m+n=1}^{K+1} \underbrace{\begin{pmatrix} A_{m,s,z} & B_{m,s,z} \end{pmatrix}}_{\mathbf{S}_{sm}} \underbrace{\begin{pmatrix} M_{mn}^{cc} & M_{mn}^{cs} \\ M_{mn}^{sc} & M_{mn}^{ss} \end{pmatrix}}_{M_{mn}} \times \underbrace{\begin{pmatrix} \cos n\theta_{x_r^{(s)}-z} \\ \sin n\theta_{x_r^{(s)}-z} \end{pmatrix}\frac{-1}{2\pi n r^n_{x_r^{(s)}-z}}}_{\mathbf{G^{(s)}}_{nr}} + \underbrace{O(\delta^{K+2})}_{E_{rs}}.\end{aligned} \tag{7.8}$$

Thus, defining the following matrices

$$\mathbf{M} = \begin{pmatrix} M_{11} & M_{12} & \cdots & M_{1K} \\ M_{21} & M_{22} & \cdots & M_{2K} \\ \cdots & \cdots & \ddots & \cdots \\ M_{K1} & M_{K2} & \cdots & M_{KK} \end{pmatrix}, \ \mathbf{E} = (E_{rs})_{1\le r\le R, 1\le s\le N_s}, \tag{7.9}$$

the problem is to recover the matrix $\mathbf{M}$ knowing the matrix

$$\mathbf{V} = L(\mathbf{M}) + \mathbf{E}, \tag{7.10}$$

where L is the linear operator defined by (7.8). We shall underline the similarity between notations (4.20)-(4.21) and (7.9)-(7.10).

Therefore, the CGPTs of the target D can be reconstructed as in chapter 4 from the least-squares solution of the above linear system, *i.e.*,

$$\mathbf{M}^{\text{est}} = \underset{\mathbf{M}\perp\ker(L)}{\operatorname{argmin}} \|\mathbf{V} - L(\mathbf{M})\|_F^2. \tag{7.11}$$

Let us remark that, in the case of multifrequency measurements $(\omega_1, \ldots, \omega_{N_f})$, we can reconstruct $\left(\mathbf{M}^{\text{est},f}\right)_{1\le f\le N_f}$ from $\left(\mathbf{V}^{(f)}\right)_{1\le f\le N_f}$ analogously.

Let us note that the invariances developped in chapter 5 really make sense here, since the fish is moving. It could also be related to the behavioral experiments that have shown that weakly electric fish categorize targets according to their shapes but not according to sizes, locations, or orientations [110].

7.3 Recognition and classification

Depending on whether we consider multifrequency measurements or not, we will not identify the CGPTs in the same way.

7.3.1 Fixed frequency setting: shape descriptor based classification

When only one frequency is available, we can act as if we were in a real complex-valued case and apply directly the identification algorithm based on shape descriptors $\mathcal{I}^{(1)}_{mn}(D)$ and $\mathcal{I}^{(1)}_{mn}(D)$ defined in section 5.3.2. Note that the definitions in (5.30) still hold for complex admittivities.

To be more precise, when the reconstruction order K is greater than 2, we compute the shape descriptors of D from (7.9), and apply algorithm 2, page 80.

7.3.2 Multifrequency setting: Spectral induced polarization based classification

When multiple frequencies are involved, we can use the shape descriptors $\mathcal{I}^{(1)}_{mn}(D)$ and $\mathcal{I}^{(2)}_{mn}(D)$ at frequencies $\omega_1, \ldots, \omega_F$ to enhance the stability of the classification. However, as it will be shown later, this does not yield a very stable classification procedure.

Here we rather focus on the first-order polarization tensor (PT), that is, the 2×2 complex matrix $\mathbf{M}(\lambda_f, D)$ associated with the target D and frequency f:

$$\mathbf{M}(\lambda_f, D) = \int_{\partial D} \left(\lambda_f I - \mathcal{K}_D^*\right)^{-1} [\nu] y \, d\sigma(y), \;\; \lambda_f = \frac{k_f + 1}{2(k_f - 1)},$$

for $f = 1, \ldots, N_f$. We will show that they are sufficient to identify efficiently the targets. Note that it is not possible to compute the shape descriptors $\mathcal{I}^{(1)}_{mn}(D)$ and $\mathcal{I}^{(2)}_{mn}(D)$ based only on first-order PT, because they require at least second-order polarization tensors. This limits the use of shape descriptors in the limited-view case where the reconstruction of higher-order GPTs is not accurate (see section 4.3.3).

Here we use the spectral content of the first-order PTs for recognition. We have the following properties [20].

Proposition 7.3.1. *For any scaling $\delta > 0$, rotation angle $\theta \in \mathbb{R}$ and translation vector $z \in \mathbb{R}^2$, let us denote*

$$D = z + \delta R_\theta B := \{x = z + \delta R_\theta u, \; u \in B\},$$

where

$$R_\theta := \begin{pmatrix} \cos\theta & -\sin\theta \\ \sin\theta & \cos\theta \end{pmatrix},$$

is the rotation matrix of angle θ. Then,

$$\mathbf{M}(\lambda_f, D) = \delta^2 R_\theta \mathbf{M}(\lambda_f, B) R_\theta^T. \tag{7.12}$$

Hence, if we denote by $\tau_1^{(f)}(D)$ and $\tau_2^{(f)}(D)$ the singular values of $\mathbf{M}(\lambda_f, D)$, we obtain

$$\forall j \in \{1, 2\},\ \tau_j^{(f)}(D) = \delta^2 \tau_j^{(f)}(B).$$

This gives an idea for two algorithms:

1. The first one, matching the singular values of all the first-order PT $(\mathbf{M}(\lambda_f, D))_{1 \leq f \leq N_f}$, would be dependent of the characteristic scale δ of the targets in the dictionary;

2. The second one, independent of the scale of the target, would match the following quantities

$$\mu_j^{(f)} = \frac{\tau_j^{(f)}}{\tau_j^{(N_f)}}, \tag{7.13}$$

for $j = 1, 2$ and $f = 1, \ldots, N_f - 1$.

Some comments are in order. First, the reason why we consider the first one, even if it is scale-dependent, is because it is far more stable. Also, in some biological experiments, two targets of different scales are considered as different [111]. A question raised was then: how is it possible to discriminate between a nearby small target and an extended one situated far away? With the second algorithm, we have an answer. The last remark concerns equation (7.13). We could have also considered other scale-dependent ratios, such as

$$\frac{\tau_j^{(f)}}{\tau_j^{(1)}} \text{ or } \frac{\tau_j^{(f)}}{\sum_{f'=1}^{N_f} \tau_j^{(f')}},$$

but since $\tau_j^{(N_f)}$ happens to be the largest one (the frequencies are sorted in increasing order), it is more stable to consider (7.13). It is worth mentioning that if there exists an integer $p > 2$ such that $R_{2\pi/p} D = D$, then $\mathbf{M}(\lambda_f, D)$ is proportional to identity (see subsection 5.3.1).

7.3.3 Background field elimination

We can also improve stability of reconstruction by eliminating the background field. Let us recall $U(x)$ to be the background electric field (*i.e.*, the solution of (7.1) with $k = 1$). Let us also recall formula (3.2), proved with proposition 2.4.1 and lemma 2.4.2 :

$$\mathcal{P}_\Omega \left(\left.\frac{\partial u_f}{\partial \nu}\right|_+ - \left.\frac{\partial U}{\partial \nu}\right|_+ \right) \approx \nabla U(z)^T \mathbf{M}(\lambda_f, D) \nabla_z \left(\frac{\partial G}{\partial \nu_x} \right), \tag{7.14}$$

where u_f is u associated with the f^{th} frequency, $\mathbf{M}(\lambda_f, D)$ is the first-order polarization tensor at the f^{th} frequency, and $\mathcal{P}_\Omega$ is the (real-valued) postprocessing operator given by

$$\mathcal{P}_\Omega := \frac{1}{2} I - \mathcal{K}_\Omega^* - \xi \frac{\partial \mathcal{D}_\Omega}{\partial \nu}.$$

Hence, if the emitted signal U is real-valued, then taking the imaginary part leads us to

$$\mathcal{P}_\Omega \left[\Im m \left(\left.\frac{\partial u_f}{\partial \nu}\right|_+ \right) \right] \approx \nabla U(z)^T \Im m\, \mathbf{M}(\lambda_f, D) \nabla_z \left(\frac{\partial G}{\partial \nu_x} \right). \tag{7.15}$$

Note that the restriction on U to be real is justified since the permittivities of water and the fish are negligible [39, 94]. Now, from (7.15), we can extract $\Im m\, \mathbf{M}(\lambda_f, D)$ by solving a least-squares problem similar to (7.11). Then, we have the singular values of the imaginary part of $\mathbf{M}(\lambda_f, D)$, which would be sufficient for shape recognition and classification. The goal of this procedure is to get rid off the computation of $\partial U/\partial \nu$ in (7.14), which is supposed to be performed numerically in real-world applications, thus subject to errors. Let us recall that the postprocessing operator $\mathcal{P}_\Omega$ makes the data independent of the shape of the fish's body.

Because of the following relation which follows from (7.12)

$$\mathbf{M}(\lambda_f, D) = O(\delta^2 \mathbf{M}(\lambda_f, B)),$$

taking the imaginary part would lead us to only compute $\nabla U(z)$ in (7.15) and hence, the error made here would be modulated by a factor of order δ^2.

7.4 Numerical illustrations

In this section, we illustrate the performance of the algorithms developed in the previous section. We use the CGPTs obtained in order to classify the targets. We present an example with fixed frequency, and another with multifrequency measurements. As it will be seen, the latter does not lead us to a significantly more stable classification in the presence of noise or for limited aperture. The errors in the reconstruction of the high-order polarization tensors due to measurement noise or the limited-view aspect deteriorate the stability of the proposed algorithm. However, when, at multiple frequencies, only the first-order polarization tensor is used, we arrive at a very robust and efficient classification procedure.

For the sake of clarity, and due to the large numbers of computations performed, the results are presented separatedly, see section 7.5.

7.4.1 Setup and methods

We describe the dictionary as well as the measurement systems. We consider two different shapes for the fish: ellipses and twisted ellipses. Note that this variety of shapes exists in nature. On the one hand, twisted ellipses would represent electric eels (*Electrophorus electricus*), whereas on the other hand straight ellipses would look like *Apteronotids* [84]. This simplified representation shows that the principle of our algorithms can be generalized to any kind of fish's shape (hence modeling, for example, electro-sensing for *Mormyrids* as well). It also enhances the fact that, for bio-inspired engineering applications, the shape of the robot is not determining. Moreover, as we will see later, our simplified representation is a good model to tackle aperture issues.

Dictionary

The dictionary $\mathcal{D}$ that we consider here is composed by 8 different targets: a disk, an ellipse, the letter 'A', the letter 'E', a rectangle, a square, a triangle, and an ellipse with different electrical parameters (see Figure 7.2). Indeed, all the other targets have conductivity $\sigma = 2$ and permittivity $\varepsilon = 1$ whereas the last one has conductivity $\sigma = 5$ and permittivity $\varepsilon = 2$. Note that this is not the dictionaries used in chapter 5 ; indeed, we want here to fit with real-world experiments done in [109, 110, 111]. Except when mentioned, the characteristic size of the target will not matter, and will be fixed to be of order 1.

Measurements

In each numerical experiment, one target of the dictionary is placed at the origin, while the fish swims around it. As it has been mentioned, we consider two different shapes for the fish's body: ellipses and

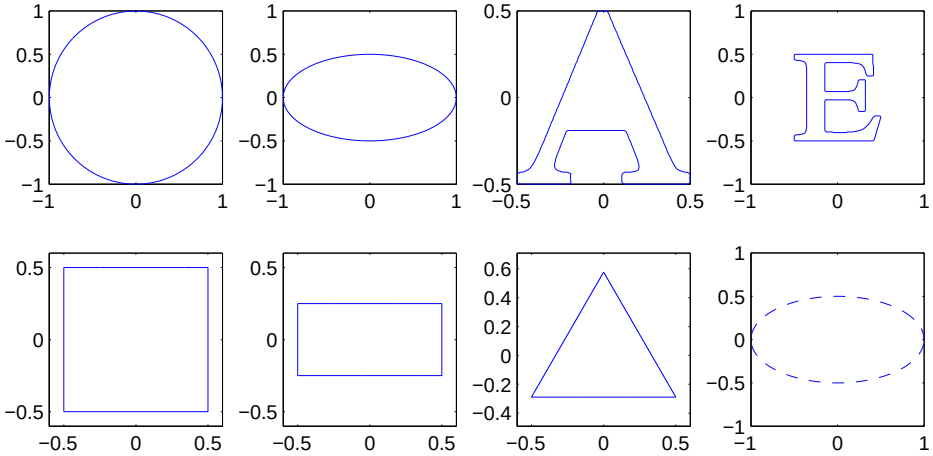

Figure 7.2: The 8 elements of the dictionary. The dotted lines indicate a target with different electrical parameters.

twisted ellipses. The measured data is built taking 20 positions of the fish around the target (see Figure 7.3).

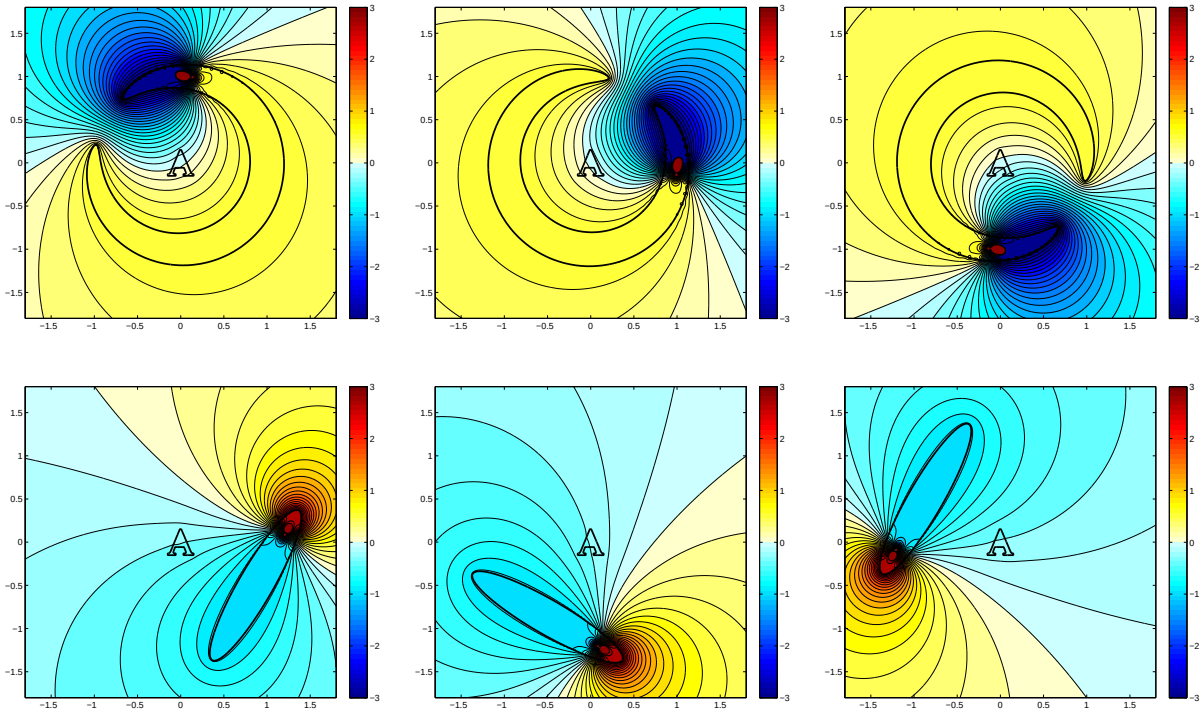

Figure 7.3: Two different kinds of experiences involve (on the top) a twisted-ellipse shape or (on the bottom) ellipse shape. The real part of the electric field is plotted, for 3 (out of 20) positions that the fish takes around the target (placed at the origin).

In Figure 7.4, a smaller aperture than the one in Figure 7.3 is considered.

The typical size of the target is $\delta = 0.3$ while the fish is turning around a disk of radius $R = 1$; the twisted ellipse's semi-axes are $a = 1.8$ and $b = 0.2$ while the straight ellipse's semi axis are $a = 1$ and $b = 0.2$. The effective thickness of the skin is set at $\xi = 0$. The fish has 2^7 receptors uniformly distributed on its skin, and the electric organ emits $N_f = 10$ frequencies, equally distributed from $\omega_0 := 1$ to $N_f\omega_0$.

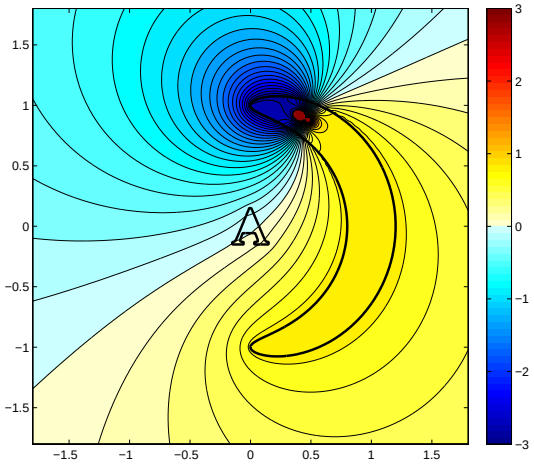

Figure 7.4: A fish having the shape of a twisted ellipse with a smaller aperture than in Figure 7.3.

Classification

The recognition process is as follows. When measurements are acquired, we perform least-square reconstruction of the (first- or second-order) CGPT of the targets. From this CGPT, we compute quantities of interest q (*i.e.* Shape Descriptors or singular values or ratios of singular values). Then, for each element n in the dictionary $\mathcal{D}$, we compute $\|q - q_n\|$, where q_n is the - pre-computed - quantity of interest for the nth shape. This process is summarized in algorithm 3. This leads us to charts such as the ones presented in Figures 7.5(a), 7.5(b), and 7.5(c).

Algorithm 3 Classification algorithm.

Input: the quantities of interest $\left(q^{(f)}\right)_{1\leq f\leq N_f}$ calculated from the measurement of an unknown shape D;

for $B_n \in \mathcal{D}$ **do**
$e_n \leftarrow \sum_{1\leq f\leq N_f} \|q(B_n)^{(f)} - q^{(f)}\|^2$ where $\left(q(B_n)^{(f)}\right)_{1\leq f\leq N_f}$ is the same type of quantities of interest of the shape B_n;
$n \leftarrow n + 1$;
end for
Output: the true dictionary element $n^* \leftarrow \text{argmin}_n e_n$.

Stability analysis

First, let us explain what kind of noise is considered. We will add a random matrix (with Gaussian entries) to the data matrix $\mathbf{V}$ defined in (7.5). More precisely, we will consider

$$\tilde{\mathbf{V}} := \mathbf{V} + \varepsilon \mathbb{W},$$

where $\mathbb{W}$ is a $N_s \times R$ matrix whose coefficients follow a Gaussian distribution with mean 0 and variance 1. The real number ε is the strength of the noise, and will be given in percentage of the fluctuations of $\mathbf{V}$, (*i.e.*, $\max_{s,r} Q_{sr} - \min_{s,r} Q_{sr}$). The recognition procedure remains the same.

Stability analysis was then carried out empirically: for each noise level, we performed N_{stabil} independent recognition process (with N_{stabil} being precised for each experiment), and computed the ratio of good detection. The computation ends when we reach the threshold of 12.5% probability of detection that corresponds to a uniform random choice of the object. This gives us Figures 7.6(a) to 7.8(b).

7.4.2 Results and discussion

In this subsection, we compare the respective stability of our algorithms. Due to the large number of situations and computations, only significant figures were plotted, giving the following classification of recognition processes, according to their range of application.

Fixed frequency setting: shape descriptors

If only one frequency is accessible for the measurements, then the only algorithm possible is classification based on shape descriptors. Indeed, first-order PTs are not enough to discriminate between objects [35]. However, the use of shape descriptors is limited to the twisted-ellipse case with nearly full aperture (see Figures 7.5(b) and 7.5(c), where some targets are not recognized, such as the ellipse in Figure 7.5(b) or the disk in Figure 7.5(c)). Moreover, its stability with respect to measurement noise is quite poor (see Figure 7.6(a)).

Multifrequency setting: spectral content of PTs

In the case of multifrequency measurements, shape descriptors do not increase their stability enough compared to singular values (see Figure 7.6(b)). Hence, it is better to use singular values of the PTs (see Figures 7.7(c) to 7.7(b)). One can see that:

- considering all singular values (Figures 7.7(c) and 7.7(a)) is much more stable than considering ratios of singular values (Figures 7.7(d) and 7.7(b));
- the aperture does not change very much the stability.

In this regard, the most stable algorithm is to recognize all singular values when the fish is a twisted ellipse (Figure 7.7(c)), leading us to a probability of detection superior to 90% with noise level of 125%. This is a huge gap when compared to the recognition process with shape descriptors, allowing only a few percents of noise. Note that the noise level is computed with respect to the perturbation in the measurements $\mathbf{V}$ given by (7.5), which is of order of the target volume, see (7.6). Hence, a noise level of 125% remains small compared to the actual transdermal potential u.

Background field elimination

We can see in Figures 7.8(a) and 7.8(b) that taking the imaginary part of the measurements in order to avoid the computation of the background field does not significantly decrease the stability of the reconstruction based on spectral content. Since the reconstruction of CGPTs is very fast, the background field elimination technique would yield to real-time imaging.

7.5 Figures

In this section, we numerically illustrate the main findings in this chapter and show the potential of electrosensing for shape recognition and classification (see pages 114-117).

7.6 Concluding remarks

In this chapter, we have successfully exhibited the physical mechanism underlying shape recognition and classification in active electrolocation. We have shown that extracting generalized polarization tensors from the data and comparing invariants with those of learned elements in a dictionary yields a classification

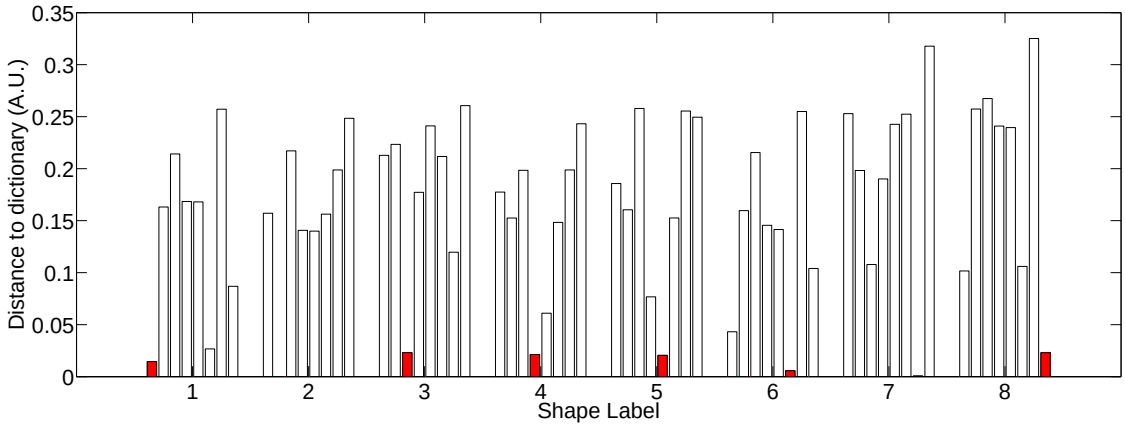

(a) Twisted ellipse

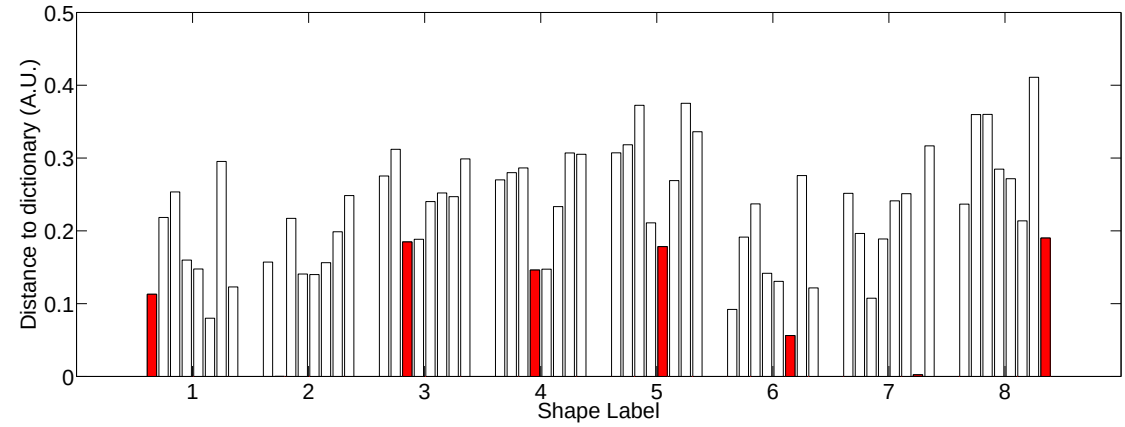

(b) Straight ellipse

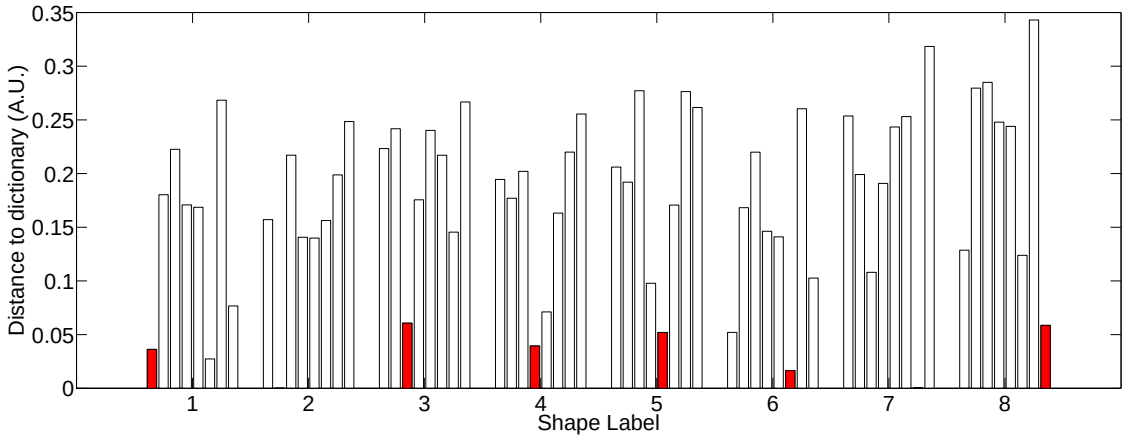

(c) Twisted ellipse with smaller aperture

Figure 7.5: Results of the matching with the dictionary (differences between shape descriptors). The red bar represents the bar of the target being identified. In the x-coordinates, 1 stands for the disk, 2 for the ellipse, 3 for the letter A, 4 for the letter E, 5 for the square, 6 for the rectangle, 7 for the triangle and 8 for the ellipse with different electrical parameters. In the y-coordinates, the distance between the shape descriptor of the target - computed from measurements - and the shape descriptors of the dictionary.

procedure with a good performance in the full-view case and with moderate measurement noise level. However, this shape descriptor based classification is instable in the limited-view case and for higher noise

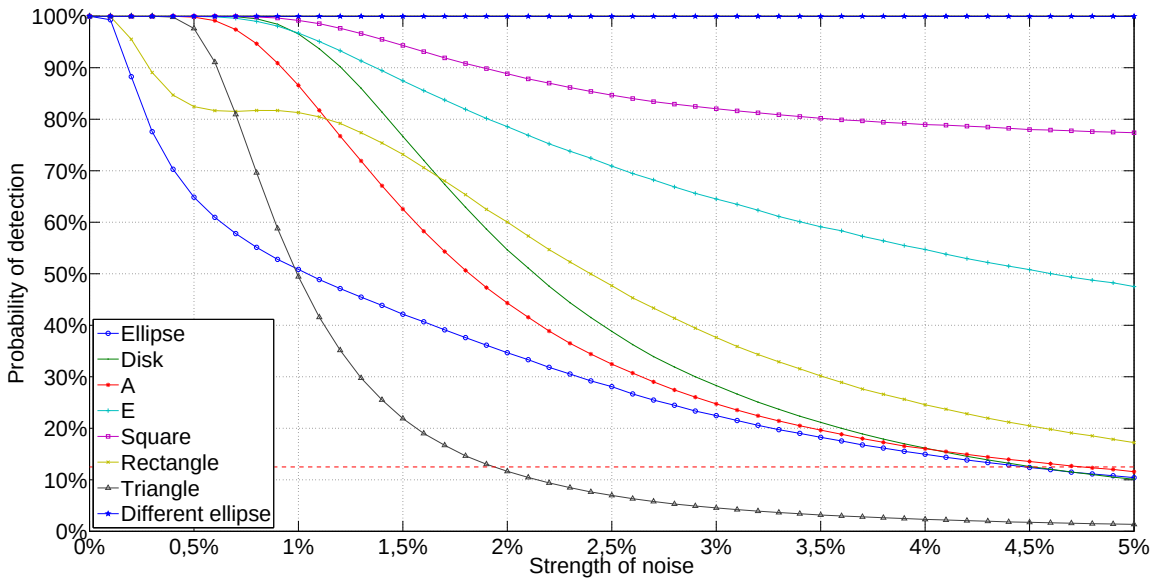

(a) One frequency (the smallest one) considered, $N_{\text{stabil}} = 10^5$.

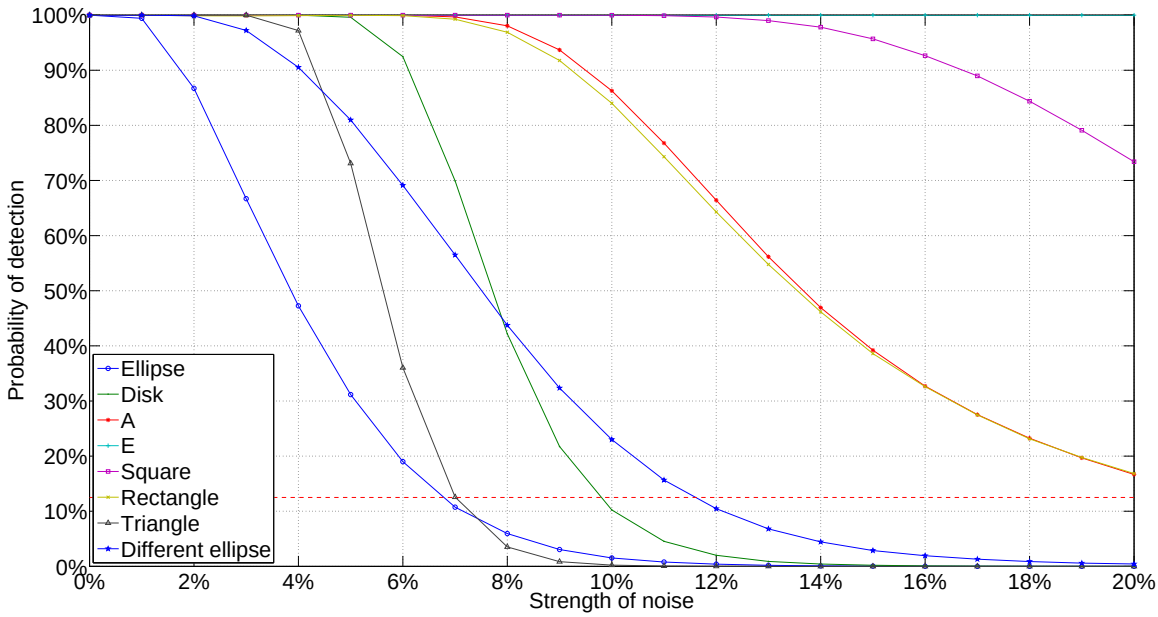

(b) All frequencies are considered, $N_{\text{stabil}} = 5.10^4$.

Figure 7.6: Stability of classification based on Shape Descriptors, when the fish is a twisted ellipse. The threshold of 12.5% that corresponds to a randomly chosen target is represented in red dotted line.

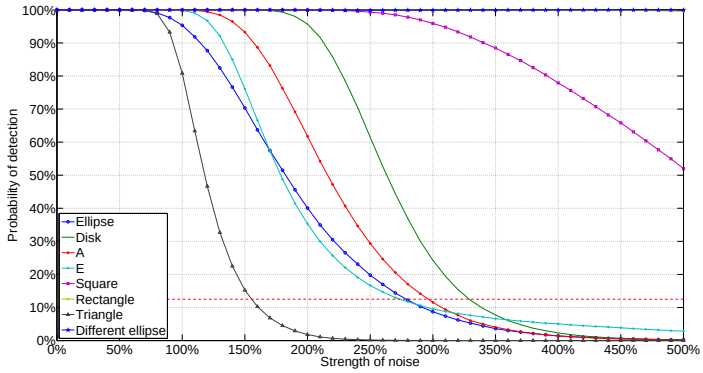

(a) Straight ellipse, all SVs.

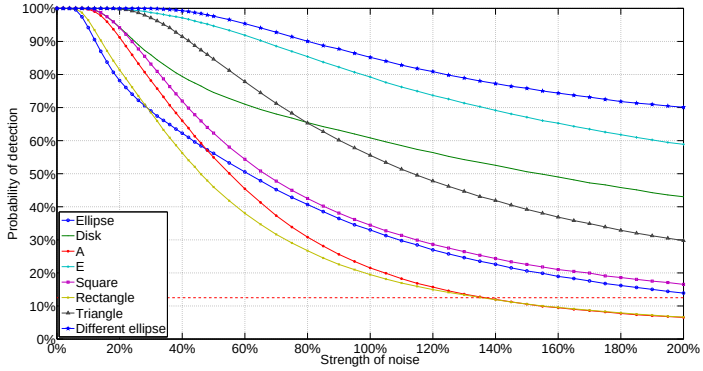

(b) Straight ellipse, ratios of SVs.

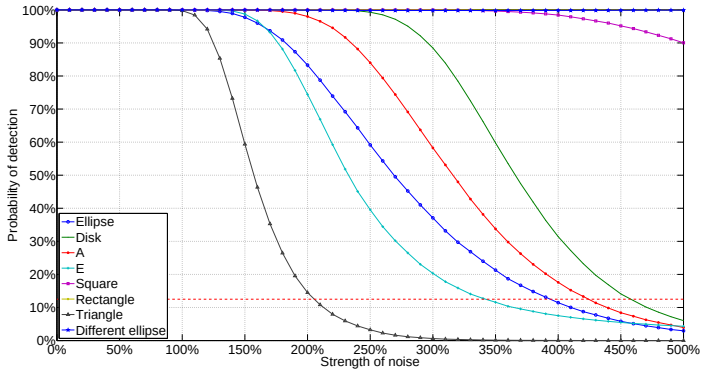

(c) Twisted ellipse, all SVs.

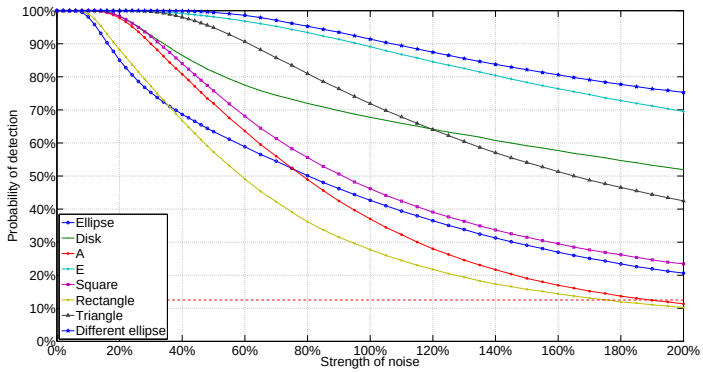

(d) Twisted ellipse, ratios of SVs.

Figure 7.7: Stability of classification based on singular values of PTs. When all SVs (singular values) are considered, the characteristic size of the target is supposed to be known. Here, for all these figures, $N_{\text{stabil}} = 5.10^4$

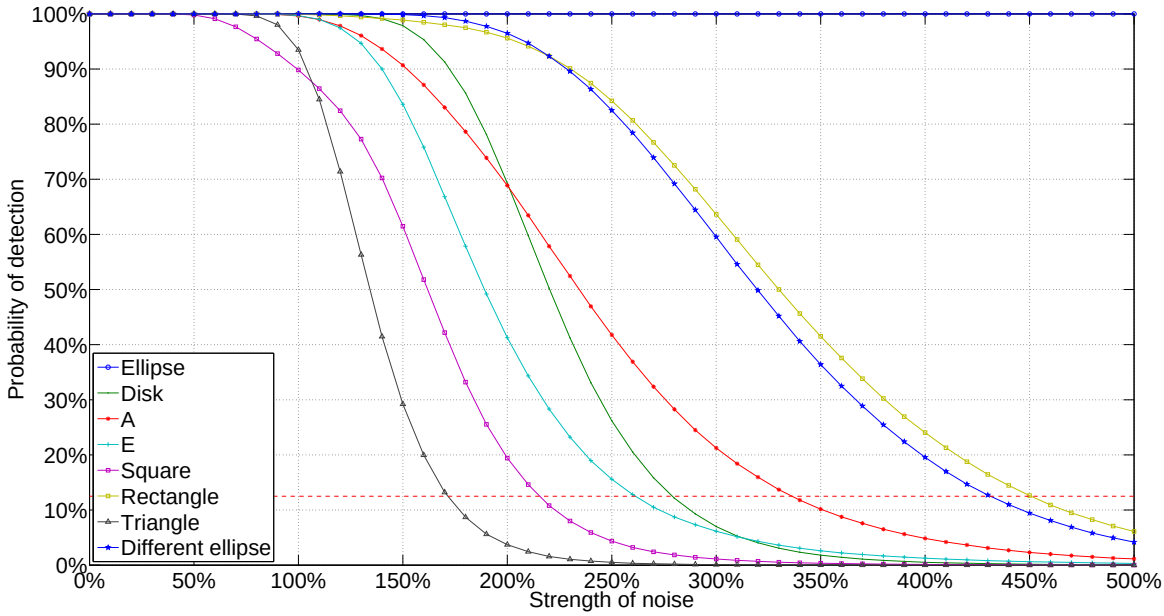

(a) All singular values.

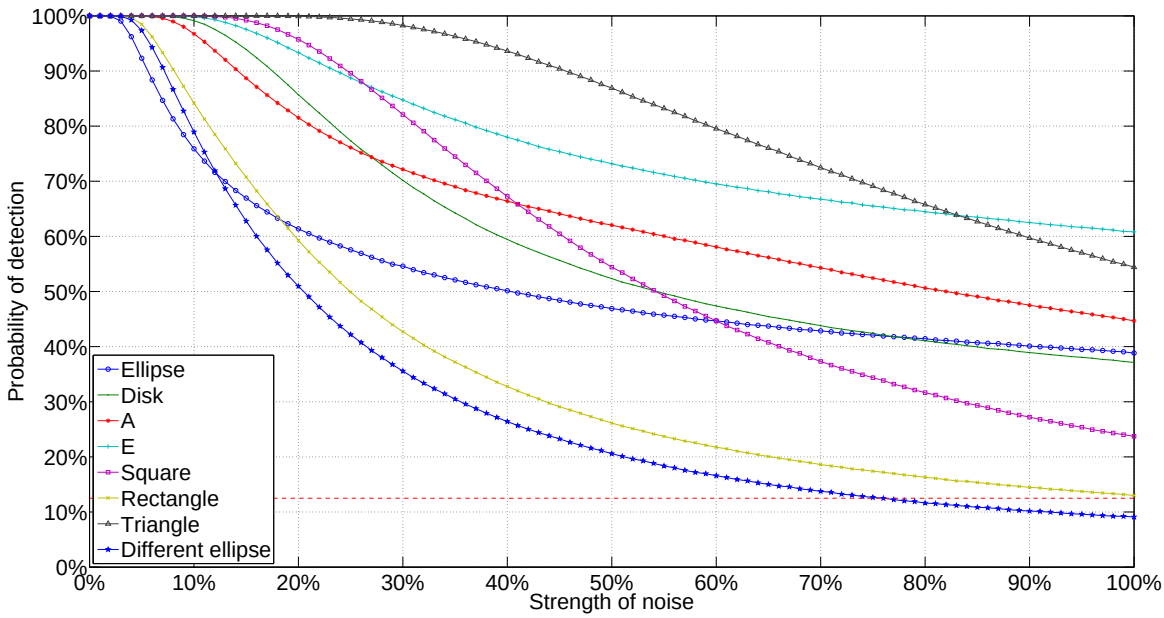

(b) Ratios of singular values.

Figure 7.8: Classification with imaginary part of the PT, when the fish is a straight ellipse. Here, $N_{\text{stabil}} = 10^5$.

level. When measurements at multiple frequencies are used, the stability of our classification approach is significantly improved by using phase shifts and keeping only the first-order polarization tensor. The resulting spectral induced polarization based classification is very robust.

CHAPTER 8

Conclusion and Perspectives

Let us summarize the work that has been done. From the mathematical model in chapter 2 and the localization algorithm in chapter 3, we have decided to develop a way to extract the GPTs of a target chapter 4, leading to identification (chapter 5) and tracking (chapter 6). This gives us tools to better understand how weakly electric fishes could discriminate two objects of different shapes (chapter 7). The research path taken has then shown to be applicable to other imaging process, making easier the bio-inspiration process.

Our results open the door for the application of the extended Kalman filter developed in chapter 6 to show the feasibility of a tracking of both location and orientation of a target from perturbations of the electric field on the skin surface of the fish. It also remains to understand to what extent the spectral induced polarization approach could help us retrieve the electric parameters of the target or locate and recognize multiple targets.

The plan for future research would be to continue the study of imaging, in a broad sense. That means not only computational inverse problems arising in industry or medical imaging, but also computer vision, of artifical intelligence for robotics. Here are some projects in progress.

In the context of eletrolocation, a work in common has begun with F. Boyer from École des Mines de Nantes, who is working on an electric robotic fish. He has designed with his team an electric sensor that is able to navigate throught obstacles, but it does not recognize these objects (see [74] and references therein). The aim of this collaboration would be to give detection and identification features to this robot.

In this regard, giving the robot a sense of learning (supervised or unsupervised) would be very interseting. In a project involving S. Mallat [80] and his team we started to apply machine learning theory to the classification of targets in electro-sensing.

Appendices

APPENDIX A

Several Technical Estimates

A.1 The truncation error in the MSR expansion

Recall the expansion of the element in the MSR matrix (4.11). We prove the following estimate of the truncation error.

Proposition A.1.1. *Let E_{rs} be as in* (4.11). *Set $\rho = \delta/R$, the ratio between the typical length scale of the inclusion D and the distance of the receivers (sources) from the inclusion. Assume also that ρ is much smaller than one. Then*

$$|E_{rs}| \lesssim \rho^{K+2}. \tag{A.1}$$

Proof. From the Taylor expansion of multivariate functions ([**?**], Chapter 1), we verify that the truncation error E_{rs} can be written as

$$\int_{\partial D} e_K(y; x_r, z)(\lambda I - \mathcal{K}_D^*)^{-1}\left[\frac{\partial G(\cdot - x_s)}{\partial \nu}\right](y)ds(y) + \int_{\partial D} G_K(y; x_r, z)(\lambda I - \mathcal{K}_D^*)^{-1}\left[\frac{\partial}{\partial \nu} e_K(\cdot; z, x_s)\right](y)ds(y).$$

Here, $G_K(y; x_r, z)$ and $e_K(y; x_r, z)$ (and similarly $e_K(y; z, x_s)$) are given by

$$G_K(y; x_r, z) = \sum_{k=1}^{K} \sum_{|\alpha|=k} \frac{(-1)^{|\alpha|}}{\alpha!} \partial^\alpha G(x_r - z)(y - z)^\alpha,$$

$$e_K(y; x_r, z) = \sum_{|\alpha|=K+1} \Big(\frac{1}{\alpha!}\int_0^1 (1-s)^K \partial^\alpha G(x_r - z - s(y-z))ds\Big)(y-z)^\alpha.$$

Due to the invariance relation (5.7), the operator $(\lambda I - \mathcal{K}_D^*)^{-1}$, as an operator from the space $L^2(\partial D)$ to itself, is bounded uniformly with respect to the scaling of D. Consequently, the first term in E_{rs} is bounded by

$$C\|e_K(\cdot; x_r, z)\|_{L^\infty(\partial D)} \|\frac{\partial G(\cdot - x_s)}{\partial \nu}\|_{L^2(\partial D)} |\partial D|^{\frac{1}{2}} \leq C\|e_K\|_{L^\infty(\partial D)} \|\frac{\partial G(\cdot - x_s)}{\partial \nu}\|_{L^\infty(\partial D)} |\partial D|.$$

Assume that $z \in D$; the distance between $\overline{D}$ and the receivers (sources) is of order R. From the above expression of e_K, the explicit form of $\partial^\alpha G$ in (4.18), and the fact that $|y-z| \le C\delta$ for $y \in \overline{D}$, we have

$$|e_K(y;x_r,z)| \le C\left(\sum_{|\alpha|=K+1}\frac{1}{\alpha!}\|\partial^\alpha G_r(x_r-\cdot)\|_{\mathcal{C}(\overline{D})}\right)|y-z|^{K+1} \le C\left(\frac{\delta}{R}\right)^{K+1}.$$

Similarly, we have $\|\partial_\nu G(\cdot - x_s)\|_{L^\infty(\partial D)} \le CR^{-1}$. The measure $|\partial D|$ in dimension two is of order δ. Substituting these estimates into the bound for the first term in E_{rs}, we see that it is bounded by $C\rho^{K+2}$.

The second term can be bounded from above by

$$C\|G_K\|_{L^\infty(\partial D)}\|\frac{\partial e_K(\cdot;z,x_s)}{\partial \nu}\|_{L^\infty(\partial D)}|\partial D|.$$

We have $\|G_K(\cdot;x_r,z)\|_{L^\infty(\partial D)} \le C\rho$, which is the order of the leading term. Further, from the explicit form of e_K, we verify that

$$\|\frac{\partial e_K(\cdot;z,x_s)}{\partial \nu}\|_{L^\infty(\partial D)} \le C\left(\|G(\cdot-x_s)\|_{\mathcal{C}^{K+2}(\overline{D})}\delta^{K+1} + \|G(\cdot-x_s)\|_{\mathcal{C}^{K+1}(\overline{D})}\delta^K\right) \le C\frac{\delta^K}{R^{K+1}}.$$

As a result, the above upper bound for the second term in E_{rs} is of order ρ^{K+2} as well. This proves (A.1). □

Proposition A.1.2. *The solution $u_s(x)$ defined by the transmission problem (4.2) satisfies the symmetry property*

$$u_s(x_r) = u_r(x_s). \tag{A.2}$$

Proof. Let Ω_s^ρ be the the ball of radius ρ centered at x_s, and Ω_r^ρ the ball of radius ρ centered at x_r. Let Ω_ρ be the domain $B_R\backslash(\Omega_r^\rho \cup \Omega_s^\rho \cup D)$ where B_R is a sufficiently large ball with radius R. Then we have

$$\begin{aligned}
0 &= \int_{\Omega_\rho}\Big(u_s(x)\Delta u_r(x) - u_r(x)\Delta u_s(x)\Big)dx = \int_{\partial\Omega_\rho}\left(u_s(x)\frac{\partial u_r}{\partial n}(x) - u_r(x)\frac{\partial u_s}{\partial n}(x)\right)ds(x)\\
&= -\int_{\partial\Omega_s^\rho}\left(u_s(x)\frac{\partial u_r}{\partial n}(x) - u_r(x)\frac{\partial u_s}{\partial n}(x)\right)ds(x) - \int_{\partial\Omega_r^\rho}\left(u_s(x)\frac{\partial u_r}{\partial n}(x) - u_r(x)\frac{\partial u_s}{\partial n}(x)\right)ds(x)\\
&\quad - \int_{\partial D}\left(u_s(x)\frac{\partial u_r}{\partial n}(x)\Big|_+ - u_r(x)\frac{\partial u_s}{\partial n}(x)\Big|_+\right)ds(x) + \int_{\partial B_R}\left(u_s(x)\frac{\partial u_r}{\partial n}(x)\Big|_+ - u_r(x)\frac{\partial u_s}{\partial n}(x)\Big|_+\right)ds(x)\\
&= J_s^\rho + J_r^\rho + J_D + J_R.
\end{aligned}$$

For J_D, thanks to the jump conditions in (4.2), we have that

$$J_D = \kappa\int_{\partial D}\left(u_r(x)\frac{\partial u_s}{\partial n}(x)\Big|_- - u_s(x)\frac{\partial u_r}{\partial n}(x)\Big|_-\right)ds(x) = \kappa\int_D\Big(u_r(x)\Delta u_s(x) - u_s(x)\Delta u_r(x)\Big)dx = 0.$$

The other two terms J_s^ρ and J_r^ρ can be treated similarly; hence we focus on the first item. We've shown that $u_s(x) = G(x-x_s) + \mathcal{S}_D[\phi_s]$. In a neighborhood of Ω_s^ρ, we have

$$\|u_r\|_{L^\infty} + \|\nabla u_r\|_{L^\infty} + \|\mathcal{S}_D[\phi_s]\|_{L^\infty} + \|\nabla\mathcal{S}_D[\phi_s]\|_{L^\infty} \le C.$$

Consequently,

$$\left|\int_{\partial\Omega_s^\rho}u_s(x)\frac{\partial u_r}{\partial n}(x)\right| \le C\int_{\partial B_\rho(x_s)}(1+|\log\rho|)ds(x) \le C\rho|\log\rho|.$$

$$\left|\int_{\partial\Omega_s^\rho}u_r(x)\left(\frac{\partial u_s}{\partial n}(x) - \frac{\partial G}{\partial n}(x-x_s)\right)\right|ds(x) \le \left|\int_{\partial\Omega_s^\rho}u_r(x)\frac{\partial\mathcal{S}_D[\phi_s]}{\partial n}(x)ds(x)\right| \le C\rho.$$

These estimates imply that

$$\lim_{\rho\to 0} J_s^\rho = \lim_{\rho\to 0}\int_{\partial B_\rho(x_s)} u_r(x_s+y)\frac{\partial G}{\partial n}(y)ds(y) = \lim_{\rho\to 0}\frac{1}{2\pi\rho}\int_0^{2\pi}\rho u_r(x_s+\rho\theta)d\theta = u_r(x_s).$$

The same analysis applied to J_r^ρ shows that $\lim_{\rho\to 0} J_r^\rho = -u_s(x_r)$.

To control J_R, we recall the fact that $\mathcal{S}_D[\phi]$ decays as $|x|^{-1}$ and $\nabla\mathcal{S}_D[\phi]$ decays as $|x|^{-2}$ for $\phi\in L^2(\partial D)$ satisfying $\int_{\partial D}\phi ds = 0$; these estimates imply that the logarithmic part of u_s dominates. Therefore,

$$\lim_{R\to\infty} J_R = \lim_{R\to\infty}\int_{\partial B_R}\log|x-x_s|\frac{\langle\nu_x, x-x_r\rangle}{|x-x_r|^2} - \log|x-x_r|\frac{\langle\nu_x,x-x_s\rangle}{|x-x_s|^2}ds(x).$$

The integrand above can be written as

$$\left(\log\frac{|x-x_s|}{|x-x_r|}\right)\frac{\langle\nu_x,x-x_r\rangle}{|x-x_r|^2} + \log|x-x_r|\left[\frac{\langle\nu_x,x-x_r\rangle}{|x-x_r|^2} - \frac{\langle\nu_x,x-x_s\rangle}{|x-x_s|^2}\right].$$

We verify that the first term is of order $o(\frac{1}{R})$; its contribution to the limiting integral is hence negligible. The second term in the integrand can be further written as

$$\log|x-x_r|\left[\langle\nu_x,x-x_r\rangle\left(\frac{1}{|x-x_r|^2}-\frac{1}{|x-x_s|^2}\right) + \frac{\langle\nu_x,x-x_r-(x-x_s)\rangle}{|x-x_s|^2}\right].$$

From

$$\frac{1}{|x-x_r|^2}-\frac{1}{|x-x_s|^2} = \frac{|x_s|^2-|x_r|^2+2\langle x,x_r-x_s\rangle}{|x-x_r|^2|x-x_s|^2},$$

we verify that the second term in the integrand is of order $O(\log R/R^2)$; hence its contribution to the limiting integral is also zero. To summarize, we have $\lim_{R\to\infty} J_R = 0$.

From the above analysis, we take the limit $\rho\to 0, R\to\infty$ on the equality $0 = J_s^\rho + J_r^\rho + J_D + J_R$ and conclude that (A.2) holds. □

A.2 Proof of formula (4.18)

Formula (4.18) is well-known. We include a proof for reader's sake.

In order to prove (4.18), we need to find the derivative of the function $\log|x|$. To this end, we consider the Taylor expansion of the logarithmic function around the point x. The most convenient method for this expansion is to view the space variables as complex numbers. For a small perturbation z of the point x ($x, z\in\mathbb{C}$), we calculate

$$\log|x-z| - \log|x| = \frac{1}{2}\left([\log(x-z)-\log x] + [\log(\overline{x}-\overline{z})-\log\overline{x}]\right).$$

To expand the first item on the right-hand side of the above equality, we write it as $\log(1-\frac{z}{x})$, and since $|\frac{z}{x}|<1$ we obtain the expansion

$$\log(1-\frac{z}{x}) = -\sum_{j=1}^{\infty}\frac{1}{j}\left(\frac{z}{x}\right)^j = -\sum_{j=1}^{\infty}\frac{1}{j}\left(\frac{r_z e^{i\theta_z}}{r_x e^{i\theta_x}}\right)^j.$$

Taking the conjugate, we obtain the expansion for $\log(\overline{x}-\overline{z})-\log\overline{x}$. Consequently, we have

$$\begin{aligned}\log|x-z|-\log|x| &= -\frac{1}{2}\sum_{j=1}^{\infty}\frac{1}{j}\left[\left(\frac{r_z e^{i\theta_z}}{r_x e^{i\theta_x}}\right)^j+\left(\frac{r_z e^{-i\theta_z}}{r_x e^{-i\theta_x}}\right)^j\right]\\ &= -\sum_{j=1}^{\infty}\frac{1}{j}\left(\frac{\cos j\theta_x}{r_x^j}[r_z^j\cos j\theta_z]+\frac{\sin j\theta_x}{r_x^j}[r_z^j\sin j\theta_z]\right)\\ &= -\sum_{j=1}^{\infty}\frac{1}{j}\left(\frac{\cos j\theta_x}{r_x^j}\sum_{|\alpha|=j}a_\alpha^j z^\alpha+\frac{\sin j\theta_x}{r_x^j}\sum_{|\alpha|=j}b_\alpha^j z^\alpha\right).\end{aligned}$$

In the last equality, we understood the variable z as real variable and used the representation (4.13). Compare the last term of the above formula with the (real-variable) multivariate expansion of $\log|x-z|-\log|x|$, we observe that

$$\sum_{|\alpha|=j}\frac{(-1)^j}{\alpha!}(\partial_x^\alpha\log|x|)z^\alpha=-\sum_{|\alpha|=j}\frac{1}{j}\left(\frac{\cos j\theta_x}{r_x^j}a_\alpha^j+\frac{\sin j\theta_x}{r_x^j}b_\alpha^j\right)z^\alpha.$$

For each double index α, we get (4.18).

A.3 Proof of formula (4.25)

The proof is a straightforward computation. The elements of the matrix $\mathbf{C}^t\mathbf{C}$ correspond to inner products of columns of the matrix $\mathbf{C}$, that is, the inner products of vectors formed by evaluating sin and cos functions at $(k_1\theta_1,\ldots,k_1\theta_N)$ and at $(k_2\theta_1,\ldots,k_2\theta_N)$, where $k_1,k_2=1,2,\ldots,K$, $k_1+k_2\le 2K<N$, and $\theta_j=2\pi j/N$, $j=1,2,\ldots,N$. When two cos vectors are chosen, the inner product becomes

$$\sum_{j=1}^{N}\cos k_1\theta_j\cos k_2\theta_j=\frac{1}{4}\sum_{j=1}^{N}\left(e^{i\frac{2\pi(k_1+k_2)j}{N}}+e^{-i\frac{2\pi(k_1+k_2)j}{N}}+e^{i\frac{2\pi(k_1-k_2)j}{N}}+e^{-i\frac{2\pi(k_1-k_2)j}{N}}\right).$$

Since k_1+k_2 is an integer less than N, the first two sums always vanish because

$$\sum_{j=1}^{N}e^{i\frac{2\pi(k_1+k_2)j}{N}}=\frac{1-e^{i2\pi(k_1+k_2)}}{1-e^{i\frac{2\pi(k_1+k_2)}{N}}}=0.$$

When $k_1=k_2$, the last two sums contribute and the overall result is $N/2$. When $k_1\neq k_2$, the inner products under estimation is zero according to the above observation.

The case of inner product with sin and sin or cos and cos vectors can be similarly analyzed, and it can be easily seen that (4.25) holds.

APPENDIX B

Kalman Filters

B.1 Kalman Filter

The KF is a recursive method that uses a stream of noisy observations to produce an optimal estimator of the underlying system state [63]. Consider the following time-discrete dynamical system ($t \geq 1$):

$$X_t = F_t X_{t-1} + W_t, \tag{B.1}$$

$$Y_t = H_t X_t + V_t. \tag{B.2}$$

where

- X_t is the vector of *system state*;
- Y_t is the vector of *observation*;
- F_t is the state transition matrix which is applied to the previous state X_{t-1};
- H_t is the observation matrix which yields the (noise free) observation from a system state X_t;
- $W_t \sim \mathcal{N}(0, Q_t)$ is the process noise and $V_t \sim \mathcal{N}(0, R_t)$ is the observation noise, with respectively Q_t and R_t the covariance matrix. These two noises are independent between them. Further, we assume that, for $t \neq \tau$, W_t and W_τ are also independent (the same holds for V_t and V_τ).

Suppose that X_0 is Gaussian. Then it follows that the process $(X_t, Y_t)_{t \geq 0}$ is Gaussian. The objective is to estimate the system state X_t from the accumulated observations $Y^{(2)} := [Y_1 \dots Y_t]$.

The optimal estimator (in the least-squares sense) of the system state X_t given the observations $Y^{(2)}$ is the conditional expectation

$$\hat{x}_{t|t} = \mathbb{E}[X_t | Y^{(2)}]. \tag{B.3}$$

Since the joint vector $(X_t, Y^{(2)})$ is Gaussian, the conditional expectation $\hat{x}_{t|t}$ is a linear combination of $Y^{(2)}$, which can be written in terms of $\hat{x}_{t-1|t-1}$ and Y_t only. The purpose of the KF is to calculate $\hat{x}_{t|t}$ from $\hat{x}_{t-1|t-1}$ and Y_t.

We summarize the algorithm in the following.

Initialization:

$$\hat{x}_{0|0} = \mathbb{E}[X_0],\ P_{0|0} = \mathrm{cov}(X_0). \tag{B.4}$$

Prediction:

$$\hat{x}_{t|t-1} = F_t \hat{x}_{t-1|t-1}, \tag{B.5}$$
$$\tilde{Y}_t = Y_t - H_t \hat{x}_{t|t-1}, \tag{B.6}$$
$$P_{t|t-1} = F_t P_{t-1|t-1} F_t^T + Q_t. \tag{B.7}$$

Update:

$$S_t = H_t P_{t|t-1} H_t^T + R_t, \tag{B.8}$$
$$K_t = P_{t|t-1} H_t^T S_t^{-1}, \tag{B.9}$$
$$\hat{x}_{t|t} = \hat{x}_{t|t-1} + K_t \tilde{Y}_t, \tag{B.10}$$
$$P_{t|t} = (I - K_t H_t) P_{t-1|t-1}. \tag{B.11}$$

To apply the KF algorithm the covariance matrices Q_t, R_t must be known.

B.2 Extended Kalman Filter

Consider now a nonlinear dynamical system:

$$X_t = f_t(X_{t-1}, W_t), \tag{B.12}$$
$$Y_t = h_t(X_t, V_t), \tag{B.13}$$

where X_t, Y_t, W_t, V_t are the same as in the KF, while the functions f_t, h_t are nonlinear and differentiable. Nothing can be said in general on the conditional distribution $X_t|Y^{(2)}$ due to the nonlinearity. The EKF calculates an approximation of the conditional expectation (B.3) by an appropriate linearization of the state transition and observation models, which makes the general scheme of KF still applicable [114]. However, the resulting algorithm is no more optimal in the least-squares sense due to the approximation.

Let $F_X = \partial_X f(\hat{x}_{t-1|t-1}, 0), F_W = \partial_W f(\hat{x}_{t-1|t-1}, 0)$, the partial derivatives of f (with respect to the system state and the process noise) evaluated at $(\hat{x}_{t-1|t-1}, 0)$, and let $H_X = \partial_X h(\hat{x}_{t|t-1}, 0), H_V = \partial_V h(\hat{x}_{t|t-1}, 0)$ be the partial derivatives of h (with respect to the system state and the observation noise) evaluated at $(\hat{x}_{t|t-1}, 0)$. The EKF algorithm is summarized below.

Initialization:

$$\hat{x}_{0|0} = \mathbb{E}[X_0],\ P_{0|0} = \mathrm{cov}(X_0). \tag{B.14}$$

Prediction:

$$\hat{x}_{t|t-1} = f(\hat{x}_{t-1|t-1}, 0), \tag{B.15}$$
$$\tilde{Y}_t = Y_t - h(\hat{x}_{t|t-1}, 0), \tag{B.16}$$
$$P_{t|t-1} = F_X P_{t-1|t-1} F_X^T + F_W Q_t F_W^T. \tag{B.17}$$

Update:

$$S_t = H_X P_{t|t-1} H_X^T + H_V R_t H_V^T, \tag{B.18}$$
$$K_t = P_{t|t-1} H_X^T S_t^{-1}, \tag{B.19}$$
$$\hat{x}_{t|t} = \hat{x}_{t|t-1} + K_t \tilde{Y}_t, \tag{B.20}$$
$$P_{t|t} = (I - K_t H_X) P_{t-1|t-1}. \tag{B.21}$$

Bibliography

[1] R.K. Adair, R.D. Astumian, and J.C. Weaver. Detection of weak electric fields by sharks, rays, and skates. *Chaos: An Interdisciplinary Journal of Nonlinear Science*, 8(3):576–587, 1998. [cited at p. 12]

[2] J. Albert and W. Crampton. Diversity and phylogeny of neotropical electric fishes (gymnotiformes). *Electroreception*, pages 360–409, 2005. [cited at p. 12]

[3] G. Allaire. *Numerical analysis and optimization*. Numerical Mathematics and Scientific Computation. Oxford University Press, Oxford, 2007. [cited at p. 25]

[4] H. Ammari, T. Boulier, and J. Garnier. Modeling active electrolocation in weakly electric fish. *SIAM Journal on Imaging Sciences*, 6(1):285–321, 2013. [cited at p. 19, 41]

[5] H. Ammari, T. Boulier, J. Garnier, W. Jing, H. Kang, and H. Wang. Target identification using dictionary matching of generalized polarization tensors. *Submitted to Foundations of Computational Mathematics (arXiv:1204.3035)*, 2012. [cited at p. 55, 62, 73]

[6] H. Ammari, T. Boulier, J. Garnier, H. Kang, and H. Wang. Shape identification and classification in active electrolocation. *Submitted to Proceedings of the National Academy of Sciences (USA) (arXiv:1302.6384v1)*, 2012. [cited at p. 101]

[7] H. Ammari, T. Boulier, J. Garnier, H. Kang, and H. Wang. Tracking of a mobile target using generalized polarization tensors. *Accepted for publication in SIAM Journal on Imaging Sciences (arXiv:1212.3544)*, 2012. [cited at p. 55, 91]

[8] H. Ammari, D. Chung, H. Kang, and H. Wang. Invariance properties of generalized polarization tensors and design of shape descriptors in three dimensions. *arXiv preprint arXiv:1212.3519*, 2012. [cited at p. 87]

[9] H. Ammari, P. Garapon, F. Jouve, H. Kang, M. Lim, and S. Yu. A new optimal control approach for the reconstruction of extended inclusions. *To appear in SIAM Journal on Control and Optimization*, 2013. [cited at p. 74]

[10] H. Ammari, J. Garnier, and V. Jugnon. Detection, reconstruction, and characterization algorithms from noisy data in multistatic wave imaging, 2011. [cited at p. 56, 68]

[11] H. Ammari, J. Garnier, H. Kang, M. Lim, and K. Sølna. Multistatic imaging of extended targets. *SIAM Journal on Imaging Sciences*, 5(2):564–600, 2012. [cited at p. 74]

[12] H. Ammari, J. Garnier, H. Kang, M. Lim, and S. Yu. Generalized polarization tensors for shape description. *To appear in Numerische Mathematik*, 2012. [cited at p. 73, 75, 81, 83, 105]

[13] H. Ammari, J. Garnier, H. Kang, W.K. Park, and K. Sølna. Imaging schemes for perfectly conducting cracks. *SIAM Journal on Applied Mathematics*, 71(1):68–91, 2011. [cited at p. 41]

[14] H. Ammari, J. Garnier, and K. Sølna. Resolution and stability analysis in full-aperture, linearized conductivity and wave imaging. In *To appear in Proc. Amer. Math. Soc., to appear*, volume 2, 2012. [cited at p. 87]

[15] H. Ammari, R. Griesmaier, and M. Hanke. Identification of small inhomogeneities: asymptotic factorization. *Mathematics of computation*, 76(259):1425, 2007. [cited at p. 42]

[16] H. Ammari, E. Iakovleva, and D. Lesselier. A music algorithm for locating small inclusions buried in a half-space from the scattering amplitude at a fixed frequency. *Multiscale Modeling & Simulation*, 3(3):597–628, 2005. [cited at p. 41]

[17] H. Ammari and H. Kang. High-order terms in the asymptotic expansions of the steady-state voltage potentials in the presence of conductivity inhomogeneities of small diameter. *SIAM J. Math. Anal.*, 34(5):1152–1166, 2003. [cited at p. 34, 55]

[18] H. Ammari and H. Kang. Properties of generalized polarization tensors. *SIAM Multiscale Model. Simul.*, 1:335–348, 2003. [cited at p. 55]

[19] H. Ammari and H. Kang. *Reconstruction of small inhomogeneities from boundary measurements*. Number 1846. Springer Verlag, 2004. [cited at p. 34, 35, 41, 46, 53, 55, 56, 57, 58, 73, 104, 105]

[20] H. Ammari and H. Kang. *Polarization and moment tensors: with applications to inverse problems and effective medium theory*. Springer Verlag, 2007. [cited at p. 23, 24, 25, 34, 35, 41, 42, 43, 53, 56, 58, 60, 68, 69, 73, 77, 108]

[21] H. Ammari, H. Kang, E. Kim, and J.-N. Lee. The generalized polarization tensors for resolved imaging part ii: Shape and electromagnetic parameters reconstruction of an electromagnetic inclusion from multistatic measurements. *Mathematics of Computation*, 81(278):839, 2011. [cited at p. 87]

[22] H. Ammari, H. Kang, E. Kim, K. Louati, and M.S. Vogelius. A music-type algorithm for detecting internal corrosion from electrostatic boundary measurements. *Numerische Mathematik*, 108(4):501–528, 2008. [cited at p. 41, 42]

[23] H. Ammari, H. Kang, and H. Lee. *Layer potential techniques in spectral analysis*. Mathematical Surveys and Monographs, vol. 53. American Mathematical Society, Providence, RI, 2009. [cited at p. 24]

[24] H. Ammari, H. Kang, H. Lee, and M. Lim. Enhancement of near cloaking using generalized polarization tensors vanishing structures. part i: The conductivity problem. *Comm. Math. Phys.*, to appear. [cited at p. 55, 56, 59]

[25] H. Ammari, H. Kang, M. Lim, and H. Zribi. Conductivity interface problems. part i: small perturbations of an interface. *Transactions of the American Mathematical Society*, 362(5):2435–2449, 2010. [cited at p. 27, 28, 73, 77]

[26] H. Ammari, H. Kang, and K. Touibi. Boundary layer techniques for deriving the effective properties of composite materials. *Asymptotic Analysis*, 41(2):119–140, 2005. [cited at p. 55]

[27] C. Assad. *Electric field maps and boundary element simulations of electrolocation in weakly electric fish*. PhD thesis, California Institute of Technology, 1997. [cited at p. 16, 19]

[28] C. Assad, B. Rasnow, and P.K. Stoddard. Electric organ discharges and electric images during electrolocation. *Journal of experimental biology*, 202(10):1185–1193, 1999. [cited at p. 15]

[29] C. Assad, B. Rasnow, P.K. Stoddard, and JM Bower. The electric organ discharges of the gymnotiform fishes: Ii. eigenmannia. *Journal of Comparative Physiology A: Neuroethology, Sensory, Neural, and Behavioral Physiology*, 183(4):419–432, 1998. [cited at p. 15, 17, 21]

[30] D. Babineau, A. Longtin, and J.E. Lewis. Modeling the electric field of weakly electric fish. *Journal of experimental biology*, 209(18):3636, 2006. [cited at p. 16]

[31] M Bacher. A new method for the simulation of electric fields, generated by electric fish, and their distorsions by objects. *Biological cybernetics*, 47(1):51–58, 1983. [cited at p. 14, 15]

[32] C.C. Bell, J. Bradbury, and C.J. Russell. The electric organ of a mormyrid as a current and voltage source. *Journal of Comparative Physiology A: Neuroethology, Sensory, Neural, and Behavioral Physiology*, 110(1):65–88, 1976. [cited at p. 21]

[33] E. Beretta and E. Francini. Lipschitz stability for the electrical impedance tomography problem: the complex case. *Communications in Partial Differential Equations*, 36(10):1723–1749, 2011. [cited at p. 41]

[34] G.A. Boulenger and L. Loat. *The fishes of the Nile*. Wheldon & Wesley, 1965. [cited at p. 8]

[35] M. Brühl, M. Hanke, and M.S. Vogelius. A direct impedance tomography algorithm for locating small inhomogeneities. *Numer. Math.*, 93(4):635–654, 2003. [cited at p. 41, 42, 113]

[36] R. Budelli and A.A. Caputi. The electric image in weakly electric fish: perception of objects of complex impedance. *Journal of Experimental Biology*, 203(3):481, 2000. [cited at p. 16]

[37] T.H. Bullock, C.D. Hopkins, A.N. Popper, and R.F. Richard, editors. *Electroreception*. Springer-Verlag, New York, 2005. [cited at p. 7, 16]

[38] Y. Capdeboscq, A.B. Karrman, and J.-C. Nédélec. Numerical computation of approximate generalized polarization tensors. *Applicable Analysis*, 91(6):1189–1203, 2012. [cited at p. 73]

[39] A. A. Caputi, R. Budelli, K. Grant, and C. C. Bell. The electric image in weakly electric fish: physical images of resistive objects in gnathonemus petersii. *Journal of experimental biology*, 201(14):2115, 1998. [cited at p. 16, 21, 110]

[40] D.J. Cedio-Fengya, S. Moskow, and M.S. Vogelius. Identification of conductivity imperfections of small diameter by boundary measurements. continuous dependence and computational reconstruction. *Inverse Problems*, 14:553, 1998. [cited at p. 34, 55]

[41] D.H. Chambers and J.G. Berryman. Target characterization using decomposition of the time-reversal operator: electromagnetic scattering from small ellipsoids. *Inverse Problems*, 22(6):2145, 2006. [cited at p. 41]

[42] L. Chen, J. L. House, R. Krahe, and M.E. Nelson. Modeling signal and background components of electrosensory scenes. *Journal of Comparative Physiology A: Neuroethology, Sensory, Neural, and Behavioral Physiology*, 191(4):331–345, 2005. [cited at p. 16]

[43] M. Cheney. The linear sampling method and the music algorithm. *Inverse Problems*, 17(4):591, 2001. [cited at p. 41]

[44] M. Cheney and B. Borden. Imaging moving targets from scattered waves. *Inverse problems*, 24(3):035005, 2008. [cited at p. 91]

[45] D. Clark, I.T. Ruiz, Y. Petillot, and J. Bell. Particle phd filter multiple target tracking in sonar image. *Aerospace and Electronic Systems, IEEE Transactions on*, 43(1):409–416, 2007. [cited at p. 91]

[46] G. Dassios and R. Kleinman. *Low frequency scattering*. Oxford University Press, USA, 2000. [cited at p. 55]

[47] D. Davies, P. Palmer, and M. Mirmehdi. Detection and tracking of very small low contrast objects. In *Proc. BMVC*, pages 60.1–60.10, 1998. [cited at p. 91]

[48] E.A. Davis and C.D. Hopkins. Behavioural analysis of electric signal localization in the electric fish, *Gymnotus carapo* (gymnotiformes). *Animal behaviour*, 36(6):1658–1671, 1988. [cited at p. 12]

[49] A. J. Devaney. Super-resolution processing of multi-static data using time reversal and music. *J. Acoust. Soc. Am*, 2004. [cited at p. 42]

[50] L. Escauriaza, E.B. Fabes, and G. Verchota. On a regularity theorem for weak solutions to transmission problems with internal Lipschitz boundaries. *Proc. Amer. Math. Soc.*, 115(4):1069–1076, 1992. [cited at p. 24]

[51] W. Feldberg and A. Fessard. The cholinergic nature of the nerves to the electric organ of the torpedo (torpedo marmorata). *The Journal of physiology*, 101(2):200–216, 1942. [cited at p. 8]

[52] S. Finger and M. Piccolino. *The Shocking History of Electric Fishes: From Ancient Epochs to the Birth of Modern Neurophysiology*. Oxford University Press, USA, 2011. [cited at p. 8]

[53] A. Friedman and M.S. Vogelius. Identification of small inhomogeneities of extreme conductivity by boundary measurements: a theorem on continuous dependence. *Archive for Rational Mechanics and Analysis*, 105(4):299–326, 1989. [cited at p. 55]

[54] C. Graff, G. Kaminski, M. Gresty, and T. Ohlmann. Fish perform spatial pattern recognition and abstraction by exclusive use of active electrolocation. *Current biology*, 14(9):818–823, 2004. [cited at p. 10]

[55] E. Haber, U.M. Ascher, and D. Oldenburg. On optimization techniques for solving nonlinear inverse problems. *Inverse problems*, 16(5):1263, 2000. [cited at p. 74]

[56] C.D. Haworth, Y. De Saint-Pern, D. Clark, E. Trucco, and Y. Petillot. Detection and tracking of multiple metallic objects in millimetre-wave images. *International Journal of Computer Vision*, 71(2):183–196, 2007. [cited at p. 91]

[57] W. Heiligenberg. Theoretical and experimental approaches to spatial aspects of electrolocation. *Journal of Comparative Physiology A: Neuroethology, Sensory, Neural, and Behavioral Physiology*, 103(3):247–272, 1975. [cited at p. 15]

[58] C. Hopkins. Passive electrolocation and the sensory guidance of oriented behavior. *Electroreception*, pages 264–289, 2005. [cited at p. 12]

[59] N. Hoshimiya, K. Shogen, T. Matsuo, and S. Chichibu. The apteronotus eod field: Waveform and eod field simulation. *Journal of Comparative Physiology A: Neuroethology, Sensory, Neural, and Behavioral Physiology*, 135(4):283–290, 1980. [cited at p. 15, 16]

[60] G.J. Howes. The phylogenetic relationships of the electric catfish family malapteruridae (teleostei: Siluroidei). *Journal of natural history*, 19(1):37–67, 1985. [cited at p. 8]

[61] J.S. Jaffe. Target localization for a three-dimensional multibeam sonar imaging system. *The Journal of the Acoustical Society of America*, 105:3168, 1999. [cited at p. 91]

[62] B. Jawad, P.-B. Gossiaux, F. Boyer, V. Lebastard, F. Gomez, N. Servagent, S. Bouvier, A. Girin, and M. Porez. Sensor model for the navigation of underwater vehicles by the electric sense. In *Proc. of 2010 IEEE International Conference on Robotics and Biomimetics (ROBIO)*, pages 879–884, 2010. [cited at p. 17]

[63] R.E. Kalman. A new approach to linear filtering and prediction problems. *Journal of basic Engineering*, 82(1):35–45, 1960. [cited at p. 127]

[64] A.J. Kalmijn. Detection of weak electric fields. *Sensory biology of aquatic animals*, pages 151–186, 1988. [cited at p. 12]

[65] H. Kang. Layer potential approaches to interface problems. In *États de la Recherche : Problèmes Inverses et Imagerie*, 2013, february, 20-22. [cited at p. 53]

[66] H. Kang and J.K. Seo. The layer potential technique for the inverse conductivity problem. *Inverse Problems*, 12(3):267–278, 1996. [cited at p. 24]

[67] T. Kato. *Perturbation theory for linear operators*. Springer-Verlag, Berlin, second edition, 1976. Grundlehren der Mathematischen Wissenschaften, Band 132. [cited at p. 44]

[68] O.D. Kellogg. *Foundations of potential theory*, volume 31. Dover Publications, 2010. [cited at p. 24]

[69] A. Khelifi and H. Zribi. Asymptotic expansions for the voltage potentials with two-dimensional and three-dimensional thin interfaces. *Mathematical Methods in the Applied Sciences*, 34(18):2274–2290, 2011. [cited at p. 26]

[70] A. Kirsch. Characterization of the shape of a scattering obstacle using the spectral data of the far field operator. *Inverse problems*, 14(6):1489, 1999. [cited at p. 41]

[71] M.J. Lannoo and S.J. Lannoo. Why do electric fishes swim backwards? an hypothesis based on gymnotiform foraging behavior interpreted through sensory constraints. *Environmental biology of fishes*, 36(2):157–165, 1993. [cited at p. 13]

[72] M. Lanza de Cristoforis and L. Rossi. Real analytic dependence of simple and double layer potentials upon perturbation of the support and of the density. *J. Integral Equations Appl.*, 16(2):137–174, 2004. [cited at p. 27, 28, 29]

[73] C.L. Lawson and R.J. Hanson. *Solving least squares problems*, volume 15. SIAM, 1995. [cited at p. 60]

[74] V. Lebastard, F. Boyer, C. Chevallereau, and N. Servagent. Underwater electro-navigation in the dark. In *Robotics and Automation (ICRA), 2012 IEEE International Conference on*, pages 1155–1160. IEEE, 2012. [cited at p. 119]

[75] V. Lebastard, C. Chevallereau, A. Amrouche, B. Jawad, A. Girin, F. Boyer, and P.-B. Gossiaux. Underwater robot navigation around a sphere using electrolocation sense and kalman filter. In *2010 IEEE/RSJ International Conference on Intelligent Robots and Systems (IROS)*, pages 4225–4230, 2010. [cited at p. 104]

[76] H.W. Lissmann. On the function and evolution of electric organs in fish. *Journal of Experimental Biology*, 35(1):156–191, 1958. [cited at p. 12]

[77] H.W. Lissmann and K.E. Machin. The mechanism of object location in gymnarchus niloticus and similar fish. *Journal of Experimental Biology*, 35(2):451–486, 1958. [cited at p. 7, 13, 14, 15]

[78] M.A. MacIver. *The computational neuroethology of weakly electric fish: body modeling, motion analysis, and sensory signal estimation*. PhD thesis, Citeseer, 2001. [cited at p. 16]

[79] M.A. MacIver, N.M. Sharabash, and M.E. Nelson. Prey-capture behavior in gymnotid electric fish: motion analysis and effects of water conductivity. *Journal of Experimental Biology*, 204(3):543, 2001. [cited at p. 21]

[80] S. Mallat. *A wavelet tour of signal processing*. Academic press, 1999. [cited at p. 98, 119]

[81] E. Margolis and Y.C. Eldar. Nonuniform sampling of periodic bandlimited signals. *Signal Processing, IEEE Transactions on*, 56(7):2728–2745, 2008. [cited at p. 66]

[82] A. Migliaro, A.A. Caputi, and R. Budelli. Theoretical analysis of pre-receptor image conditioning in weakly electric fish. *PLoS computational biology*, 1(2):e16, 2005. [cited at p. 16]

[83] G.W. Milton. *The theory of composites*, volume 6. Cambridge University Press, 2002. [cited at p. 43, 55]

[84] P. Moller. *Electric fishes: history and behavior*, volume 17. Chapman & Hall London, 1995. [cited at p. 7, 8, 9, 11, 12, 13, 20, 21, 33, 42, 110]

[85] J.C. Mosher and R.M. Leahy. Source localization using recursively applied and projected (rap) music. *Signal Processing, IEEE Transactions on*, 47(2):332–340, 1999. [cited at p. 46]

[86] J.-C. Nédélec. Integral equations with non integrable kernels. *Integral equations and operator theory*, 5(1):562–572, 1982. [cited at p. 36]

[87] M.E. Nelson. Target detection, image analysis, and modeling. *Electroreception*, pages 290–317, 2005. [cited at p. 16]

[88] J. Okedi. The food and feeding habits of the small mormyrid fishes of lake victoria, east africa. *A. J. Trop. Hydrobiol. Fish.*, 1(1):1–12, 1971. [cited at p. 12]

[89] G. Pólya and G. Szego. Isoperimetric inequalities in mathematical physics. *Annals of Mathematical Studies*, 27, 1951. [cited at p. 55]

[90] B. Rasnow. The effects of simple objects on the electric field of apteronotus. *Journal of Comparative Physiology A: Neuroethology, Sensory, Neural, and Behavioral Physiology*, 178(3):397–411, 1996. [cited at p. 14]

[91] B. Rasnow. The effects of simple objects on the electric field of apteronotus. *J Comp. Physiol. A*, 178:397–411, 1996. [cited at p. 101]

[92] B. Rasnow, C. Assad, M.E. Nelson, and J.M. Bower. Simulation and measurement of the electric fields generated by weakly electric fish. In *Advances in neural information processing systems 1*, pages 436–443. Morgan Kaufmann Publishers Inc., 1989. [cited at p. 16]

[93] H. Rouvière, A. Delmas, and V. Delmas. Anatomie humaine descriptive, topographique et fonctionnelle tome 4: système nerveux central, voies & centres nerveux. 2002. [cited at p. 11]

[94] H. Scheich, T.H. Bullock, and R.H. Hamstra. Coding properties of two classes of afferent nerve fibers: high-frequency electroreceptors in the electric fish, eigenmannia. *Journal of Neurophysiology*, 36(1):39, 1973. [cited at p. 21, 110]

[95] R. Schmidt. Multiple emitter location and signal parameter estimation. *Antennas and Propagation, IEEE Transactions on*, 34(3):276–280, 1986. [cited at p. 42]

[96] B. Scholz. Towards virtual electrical breast biopsy: space-frequency music for trans-admittance data. *Medical Imaging, IEEE Transactions on*, 21(6):588–595, 2002. [cited at p. 42]

[97] O. Steinbach. *Numerical approximation methods for elliptic boundary value problems: finite and boundary elements*. Springer Verlag, 2008. [cited at p. 36]

[98] P.K. Stoddard and M.R. Markham. Signal cloaking by electric fish. *Bioscience*, 58(5):415, 2008. [cited at p. 10]

[99] P.K. Stoddard, B. Rasnow, and C. Assad. Electric organ discharges of the gymnotiform fishes: Iii. brachyhypopomus. *Journal of Comparative Physiology A: Neuroethology, Sensory, Neural, and Behavioral Physiology*, 184(6):609–630, 1999. [cited at p. 21]

[100] A. Tarantola. *Inverse problem theory and methods for model parameter estimation*. Society for Industrial and Applied Mathematics, 2005. [cited at p. 74]

[101] M.E. Taylor. *Partial differential equations. I*, volume 115 of *Applied Mathematical Sciences*. Springer-Verlag, New York, 1996. Basic theory. [cited at p. 31]

[102] M.-J. Toerring and P. Belbenoit. Motor programmes and electroreception in mormyrid fish. *Behavioral Ecology and Sociobiology*, 4(4):369–379, 1979. [cited at p. 13]

[103] M.-J. Toerring and P. Moller. Locomotor and electric displays associated with electrolocation during exploratory behavior in mormyrid fish. *Behavioural brain research*, 12(3):291–306, 1984. [cited at p. 14]

[104] U. van Rienen. *Numerical methods in computational electrodynamics*, volume 12 of *Lecture Notes in Computational Science and Engineering*. Springer-Verlag, Berlin, 2001. Linear systems in practical applications. [cited at p. 20]

[105] G. Verchota. Layer potentials and regularity for the Dirichlet problem for Laplace's equation in Lipschitz domains. *J. Funct. Anal.*, 59(3):572–611, 1984. [cited at p. 24]

[106] C.R. Vogel. *Computational methods for inverse problems*, volume 23. Society for Industrial and Applied Mathematics, 1987. [cited at p. 74]

[107] A. Volta. On the electricity excited by the mere contact of conducting substances of different kinds. in a letter from mr. alexander volta, frs professor of natural philosophy in the university of pavia, to the rt. hon. sir joseph banks, bart. kbprs. *Philosophical Transactions of the Royal Society of London*, 90:403–431, 1800. [cited at p. 11]

[108] G. von der Emde. Electrolocation of capacitive objects in four species of pulse-type weakly electric fish: Ii. electric signalling behaviour. *Ethology*, 1992. [cited at p. 13]

[109] G. von der Emde. Active electrolocation of objects in weakly electric fish. *Journal of experimental biology*, 202(10):1205, 1999. [cited at p. 13, 102, 110]

[110] G. von der Emde. Distance and shape: perception of the 3-dimensional world by weakly electric fish. *Journal of Physiology Paris*, 98:67–80, 2004. [cited at p. 13, 102, 108, 110]

[111] G. von der Emde and S. Fetz. Distance, shape and more: recognition of object features during active electrolocation in a weakly electric fish. *Journal of Experimental Biology*, 210(17):3082, 2007. [cited at p. 102, 109, 110]

[112] G. von der Emde, S. Schwarz, L. Gomez, R. Budelli, and K. Grant. Electric fish measure distance in the dark. *Nature*, 235:890–894, 1998. [cited at p. 13, 102]

[113] L. Wang, M. Cheney, and B. Borden. Multistatic radar imaging of moving targets. In *Radar Conference, 2010 IEEE*, pages 391–396. IEEE, 2010. [cited at p. 91]

[114] G. Welch and G. Bishop. An introduction to the kalman filter. Technical Report TR 95-041, University of North Carolina, University of North Carolina, Department of Computer Science, 1995. [cited at p. 91, 128]

[115] R. Williams, B. Rasnow, and C. Assad. Hypercube simulation of electric fish potentials. In *Proc. DMCC5 (Distributed Memory Computing Conference), Charleston, SC. Citeseer*, 1990. [cited at p. 16]

[116] R. Williams, B. Rasnow, and C. Assad. Hypercube simulation of electric fish potentials. In *Proc. DMCC5 (Distributed Memory Computing Conference), Charleston, SC*. Citeseer, 1990. [cited at p. 19, 23]

[117] H.H. Zakon. The electroreceptive periphery. *Electroreception. Wiley, New York*, pages 103–156, 1986. [cited at p. 21]

[118] H. Zribi. *La Méthode des Équations Intégrales pour des Analyses de Sensitivité.* PhD thesis, Ecole Polytechnique, 2005. [cited at p. 26, 27, 28, 29]

[119] A. Zygmund. *Trigonometric series*, volume 1. Cambridge university press, 2003. [cited at p. 65, 66]